Nanoscale
Horizons

ROYAL SOCIETY
OF CHEMISTRY

REVIEW

View Article Online
View Journal | View Issue

Check for updates

Cite this: *Nanoscale Horiz.*, 2024, **9**, 2085

Received 22nd May 2024,
Accepted 19th August 2024

DOI: 10.1039/d4nh00226a

rsc.li/nanoscale-horizons

# Plasmonic nanoparticle sensors: current progress, challenges, and future prospects

Krishna Kant,[ab] Reshma Beeram,[c] Yi Cao,[d] Paulo S. S. dos Santos,[e] Lara González-Cabaleiro,[a] Daniel García-Lojo,[a] Heng Guo,[f] Younju Joung,[g] Siddhant Kothadiya,[hi] Marta Lafuente,[jk] Yong Xiang Leong,[l] Yiyi Liu,[m] Yuxiong Liu,[m] Sree Satya Bharati Moram,[c] Sanje Mahasivam,[n] Sonia Maniappan,[o] Daniel Quesada-González,[p] Divakar Raj,[q] Pabudi Weerathunge,[n] Xinyue Xia,[r] Qian Yu,[g] Sara Abalde-Cela,[s] Ramon A. Alvarez-Puebla,[tu] Rizia Bardhan,[hi] Vipul Bansal,[n] Jaebum Choo,[g] Luis C. C. Coelho,[ev] José M. M. M. de Almeida,[ew] Sergio Gómez-Graña,[a] Marek Grzelczak,[x] Pablo Herves,[a] Jatish Kumar,[o] Theobald Lohmueller,[y] Arben Merkoçi,[pz] José Luis Montaño-Priede,[x] Xing Yi Ling,[l] Reyes Mallada,[jkaa] Jorge Pérez-Juste,[a] María P. Pina,[jkaa] Srikanth Singamaneni,[m] Venugopal Rao Soma,[cab] Mengtao Sun,[d] Limei Tian,[f] Jianfang Wang,[r] Lakshminarayana Polavarapu*[a] and Isabel Pastoriza Santos*[a]

Plasmonic nanoparticles (NPs) have played a significant role in the evolution of modern nanoscience and nanotechnology in terms of colloidal synthesis, general understanding of nanocrystal growth mechanisms, and their impact in a wide range of applications. They exhibit strong visible colors due to localized surface plasmon resonance (LSPR) that depends on their size, shape, composition, and the surrounding dielectric environment. Under resonant excitation, the LSPR of plasmonic NPs leads to a strong field enhancement near their surfaces and thus enhances various light–matter interactions. These

---

[a] *CINBIO, Department of Physical Chemistry, Universidade de Vigo, 36310 Vigo, Spain. E-mail: pastoriza@uvigo.gal, lakshmi@uvigo.gal*
[b] *Department of Biotechnology, School of Engineering and Applied Sciences, Bennett University, Greater Noida, UP, India*
[c] *Advanced Centre of Research in High Energy Materials (ACRHEM), DRDO Industry Academia – Centre of Excellence (DIA-COE), University of Hyderabad, Hyderabad 500046, Telangana, India*
[d] *School of Mathematics and Physics, University of Science and Technology Beijing, Beijing 100083, P. R. China*
[e] *INESC TEC—Institute for Systems and Computer Engineering, Technology and Science, Rua Dr Alberto Frias, 4200-465 Porto, Portugal*
[f] *Department of Biomedical Engineering, and Center for Remote Health Technologies and Systems, Texas A&M University, College Station, TX 77843, USA*
[g] *Department of Chemistry, Chung-Ang University, Seoul 06974, South Korea*
[h] *Department of Chemical and Biological Engineering, Iowa State University, Ames, IA 50011, USA*
[i] *Nanovaccine Institute, Iowa State University, Ames, IA 50012, USA*
[j] *Department of Chemical & Environmental Engineering, Campus Rio Ebro, C/Maria de Luna s/n, 50018 Zaragoza, Spain*
[k] *Instituto de Nanociencia y Materiales de Aragón (INMA), CSIC-Universidad de Zaragoza, 50009 Zaragoza, Spain*
[l] *Division of Chemistry and Biological Chemistry, School of Chemistry, Chemical Engineering and Biotechnology, Nanyang Technological University, Singapore 637371, Singapore*
[m] *Department of Mechanical Engineering and Materials Science, Washington University in St. Louis, St. Louis, MO, 63130, USA*
[n] *Sir Ian Potter NanoBioSensing Facility, NanoBiotechnology Research Laboratory, School of Science, RMIT University, Melbourne, VIC 3000, Australia*
[o] *Department of Chemistry, Indian Institute of Science Education and Research (IISER) Tirupati, Tirupati 517 507, India*
[p] *Catalan Institute of Nanoscience and Nanotechnology (ICN2), CSIC and BIST, Campus UAB, Bellaterra, 08193, Barcelona, Spain*
[q] *Department of Allied Sciences, School of Health Sciences and Technology, UPES, Dehradun, 248007, India*
[r] *Department of Physics, The Chinese University of Hong Kong, Shatin, Hong Kong SAR 999077, China*
[s] *International Iberian Nanotechnology Laboratory (INL), 4715-330 Braga, Portugal*
[t] *Department of Physical and Inorganic Chemistry, Universitat Rovira i Virgili, Tarragona, Spain*
[u] *ICREA—Institució Catalana de Recerca i Estudis Avançats, 08010, Barcelona, Spain*
[v] *FCUP, University of Porto, Rua do Campo Alegre, 4169-007 Porto, Portugal*
[w] *Department of Physics, University of Trás-os-Montes e Alto Douro, 5001-801 Vila Real, Portugal*
[x] *Centro de Física de Materiales (CSIC-UPV/EHU) and Donostia International Physics Center (DIPC), Paseo Manuel de Lardizabal 5, 20018 Donostia San-Sebastián, Spain*
[y] *Chair for Photonics and Optoelectronics, Nano-Institute Munich, Department of Physics, Ludwig-Maximilians-Universität (LMU), Königinstraße 10, 80539 Munich, Germany*
[z] *Catalan Institution for Research and Advanced Studies (ICREA), Passeig de Lluís Companys, 23, Barcelona, 08010, Spain*
[aa] *Networking Research Center on Bioengineering, Biomaterials and Nanomedicine, CIBER-BBN, 28029 Madrid, Spain*
[ab] *School of Physics, University of Hyderabad, Hyderabad 500046, Telangana, India*

unique optical properties of plasmonic NPs have been used to design chemical and biological sensors. Over the last few decades, colloidal plasmonic NPs have been greatly exploited in sensing applications through LSPR shifts (colorimetry), surface-enhanced Raman scattering, surface-enhanced fluorescence, and chiroptical activity. Although colloidal plasmonic NPs have emerged at the forefront of nanobiosensors, there are still several important challenges to be addressed for the realization of plasmonic NP-based sensor kits for routine use in daily life. In this comprehensive review, researchers of different disciplines (colloidal and analytical chemistry, biology, physics, and medicine) have joined together to summarize the past, present, and future of plasmonic NP-based sensors in terms of different sensing platforms, understanding of the sensing mechanisms, different chemical and biological analytes, and the expected future technologies. This review is expected to guide the researchers currently working in this field and inspire future generations of scientists to join this compelling research field and its branches.

## 1. Introduction

The development of sensors for ultrasensitive detection of biologically active molecules and chemical substances (organic and inorganic) is crucial for early diagnosis, probing biological processes, and environmental safety.[1–16] Early diagnosis is critical for the prevention of spreading the disease to other parts of the body or other people.[17–21] For instance, we witnessed the fast contagion of COVID-19 and its impact on the health system across the globe.[22] The early detection of the virus has played a significant role in the prevention of its spreading.[23,24] Similarly, the early detection of diseases like cancer not only prevents mortality but also reduces the treatment cost.[21] In connection with this, various molecular diagnostics techniques have been developed based on the detection and quantification of nucleic acids (DNA and RNA), proteins, peptides, or antibodies using polymerase chain reaction (PCR),[25] enzyme-linked immunosorbent assays (ELISA),[26] immunofluorescence,[27] *etc.* On the other hand, various analytical chemistry techniques such as gas/liquid chromatography, mass spectrometry, nuclear magnetic resonance spectroscopy, and atomic/emission absorption spectroscopy have been developed for the detection of chemical contaminants in water or air.[28] Although modern analytical and molecular diagnostics techniques are precise and reliable, they are expensive and time-consuming due to complex instrumentation. Nevertheless, in the last three decades, various types of nanoparticles (NPs) have been extensively exploited in analytical chemistry, molecular diagnostics. This has led to the development of new research fields so-called nanosensors and nanobiosensors, where the sensing platforms are constructed using nanomaterials.[29–33] Generally, nanoparticles act as optical or electrochemical sensors, offering efficiency, ease of use, and cost-effectiveness.

Among all, plasmonic NPs are one of the most studied materials over the last three decades in the field of nanoscience and nanotechnology and have emerged at the forefront of chemical and biosensors with a detection capability of fast, efficient, point-of-care, and cost-effective.[34–36] In particular, gold (Au) and silver (Ag) NPs have received significant attention due to their tunable optical properties in the visible to near-infrared (NIR) range.[10,37–40] Over the years, plasmonic NPs have been greatly exploited in a wide range of applications including photonics, light harvesting, chemical and biological sensing, imaging, and therapy.[34,35,41] They exhibit unique optical properties due to strong localized surface plasmon resonance (LSPR) that arises at the surface of NPs. LSPR refers to the collective oscillations of conduction band electrons at the interface of plasmonic NPs and their surrounding medium (typically dielectric) upon their interaction with electromagnetic radiation.[38,40] The electron cloud oscillations confine on plasmonic NPs according to their dimensions and thus the wavelength of the LSPR band in the extinction spectra of the NPs strongly depends on their size, shape, composition, interparticle distance, and refractive index of the surrounding medium.[37,40] Because of intense efforts from researchers across the globe, currently, we are in a position to precisely control the size, shape and composition of plasmonic NPs through colloid chemistry.[42–45] A few milestones of the colloidal synthesis of plasmonic NPs include the Turkevich synthesis method,[46,47] seed-mediated synthesis of Au & Ag nanorods (NRs),[48,49] polyol synthesis of Ag nanocubes (NCs),[50] Ag nanoplates (NPTs),[51] Au nanoshells,[52] Au nanostars (NSTs),[53,54] *etc.* have opened doors for precise shape control of plasmonic NPs. The developments in the colloidal synthesis of plasmonic NPs have enabled the tunability of their LSPR in the visible to NIR. Recently, there has been growing interest in obtaining plasmonic NPs with chiroptical response by shaping or assembling them into chiral morphology (twisted or helical).[55,56] Such chiral NPs exhibit circular dichroism signals at their LSPR position, which are tunable from visible to NIR.

The LSPR strongly enhances the light–matter interactions on the surface of NPs by focusing the incident light at a nanometer scale through the incident enhancement of electromagnetic field by several orders of magnitude. These properties have made the plasmonic NPs highly attractive for ultrasensitive optical sensing of various analytes ranging from inorganic ions and small organic molecules to biomacromolecules by refractive index sensitivity, colorimetry (based on an analyte-induced aggregation of NPs), and LSPR-enhanced techniques such as surface enhanced Raman scattering (SERS) and surface enhanced fluorescence (SEF).[10,37–40,57,58] The first breakthrough study of DNA–Au NP interactions was published in 1996 by

Mirkin *et al.*[59] and Alivisatos *et al.*,[60] reporting the reversible aggregation of oligonucleotides-capped Au NPs by the addition of complementary DNA. These reports have laid the foundation for not only DNA sensing but also sensing of other biomolecules using plasmonic NPs. The sensing is usually based on the change in LSPR of plasmonic NPs by selective aggregation of NPs or change in surrounding dielectric constant upon binding to a target molecule.[61] As the plasmonic NPs exhibit intense colors in the visible region due to high extinction coefficients, the change in color (usually red to blue or violet for Au NPs) upon analyte-induced aggregation makes them suitable for naked-eye detection.[61]

On the other hand, SERS has evolved as one of the most sensitive analytical techniques for ultrasensitive detection (even quantification to some extent) of various analytes.[13,62–64] Previous studies have demonstrated the capability of detecting signals from single molecules by SERS.[65–68] Moreover, it is a non-invasive technique, and it doesn't require specific binding of analytes to plasmonic NPs. It is based on enhanced Raman scattering of molecules that are placed near or on the surface of NPs mainly due to the electric field enhancement caused by LSPR. This technique has been extensively investigated in the last two decades for sensing a wide range of analytes using plasmonic NPs of different shapes and their assemblies.[13] Besides, SEF has also gained significant attention for enhancing signal-to-noise ratio and improving the sensitivity of fluorescence-based bioassays, where the fluorescence enhancement strongly depends on the size of plasmonic NPs.[57,69] Due to their interesting optical properties, plasmonic NPs have emerged at the forefront of materials for chemical and bio-sensing.[35] Over the yars, numerous review articles have already been published on various aspects of plasmonic NP sensors, especially focusing on SERS, LSPR shifts, and colorimetric-based sensing.[6,9–11,13,35,36,64,66,70–75] However, as the field is well-established, there is a need to discuss the current progress in terms of fundamental understanding, technological advances, and challenges remaining to be addressed, along with prospects in different aspects of plasmonic sensors. Therefore, researchers of different expertise in plasmonic sensors have joined to provide a state-of-the-art overview of various subtopics of plasmonic sensors. As outlined in Scheme 1, this review covers the research progress on different aspects of plasmon NP-based sensors: (1) shape-controlled synthesis of plasmonic NPS with tunable optical properties, (2) different methods of sensing using the plasmonic NPs, (3) SERS (fundamentals, different types of substrates, and sensing different analytes and sensing reaction intermediates), (4) LSPR sensing (fundamentals, methods and different analytes), (5) colorimetric sensing, and (6) plasmonic chiroptical sensors. Finally, a brief outlook is provided on the challenges that need to be addressed soon to realize the real-world applications of plasmonic NP-based sensors.

## 2. Methods of plasmonic sensing

This section provides a brief overview of different techniques used for plasmonic sensing, including SERS, SEFSEF, LSPR,

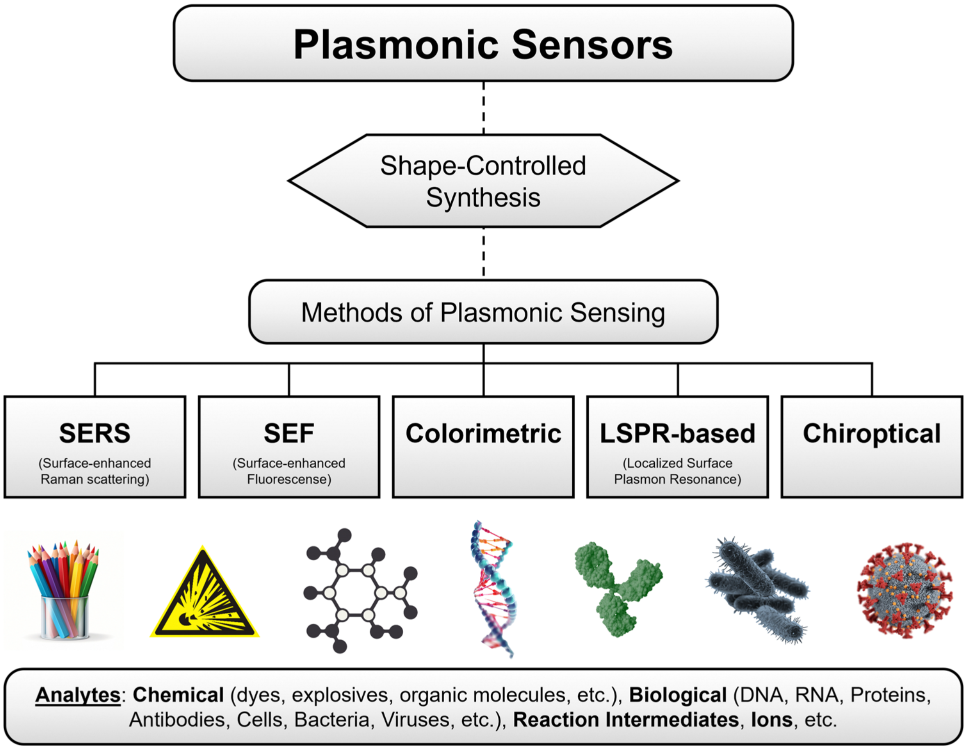
Plasmonic Sensors
Shape-Controlled Synthesis
Methods of Plasmonic Sensing
SERS
(Surface-enhanced Raman scattering)
SEF
(Surface-enhanced Fluorescense)
Colorimetric
LSPR-based
(Localized Surface Plasmon Resonance)
Chiroptical
**Analytes**: **Chemical** (dyes, explosives, organic molecules, etc.), **Biological** (DNA, RNA, Proteins, Antibodies, Cells, Bacteria, Viruses, etc.), **Reaction Intermediates**, **Ions**, etc.

Scheme 1 Overview of the contents of the review, which includes research progress of shape-controlled synthesis followed by different methods of sensing for sensing different analytes.

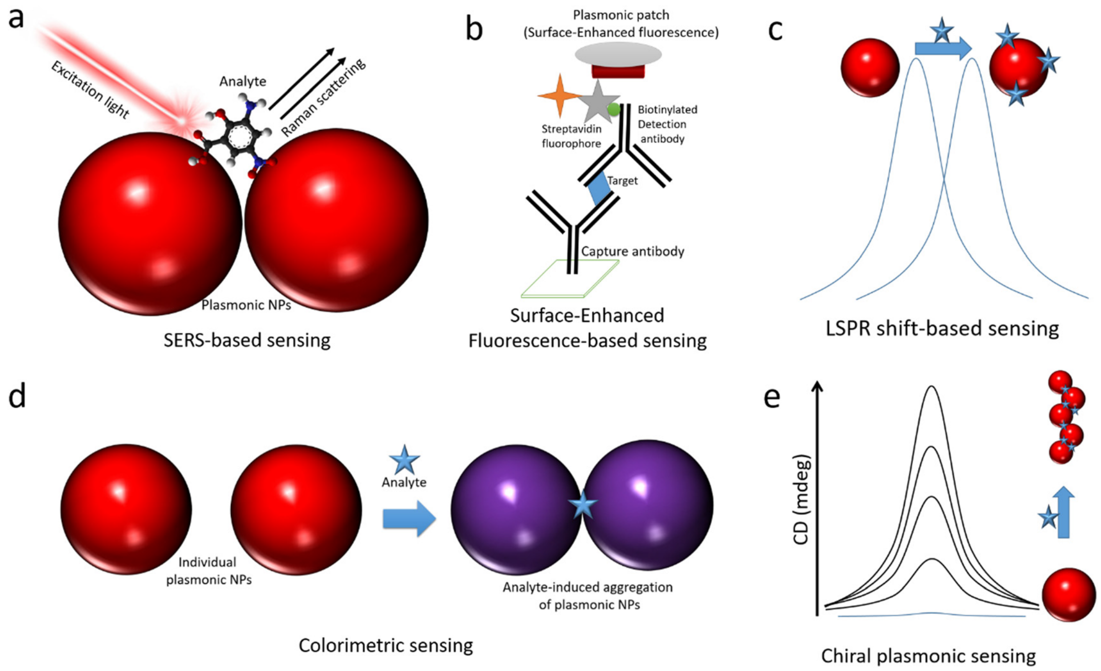

Fig. 1 Schematic illustrations of different types of optical sensing methods using plasmonic NPs. (a) Surface enhanced Raman scattering, in which the plasmonic NPs enhance the Raman signals of analytes by several orders of magnitude. (b) Surface-enhanced fluorescence, in which the plasmonic NPs significantly enhance the fluorescence of fluorophores linked to their surface, and then they act as bright fluorescent labels for the ultrasensitive detection of analytes in standard bioassays. (c) LSPR shift, which is based on an analyte-induced shift in the extinction spectra of plasmonic NCs due to changes in refractive index or coupling between particles. (d) Colorimetric sensing, which is based on the analyte-induced color change of colloidal plasmonic NP through aggregation. (e) Chiroptical sensing, which is based on inducing or increasing the CD signal of plasmonic NPs upon their interaction with chiral molecules.

colorimetric, and chiroptical methods. The basic working principles of these methods are schematically illustrated in Fig. 1. For each method, we briefly describe the working principle and various sensing strategies and substances. A detailed overview and state of the art for each method are provided in the following sections.

### SERS

It is one of the most extensively exploited methods in the field of plasmonic sensors.[13,76,77] This is based on the enhancement of inelastic scattering of molecules by several orders of magnitude ($10^6$–$10^9$ or more) through strong electric field enhancement when they are adsorbed on the surface of plasmonic NPs (Fig. 1a).[13] SERS was first observed from pyridine adsorbed on rough silver electrodes by Fleischmann *et al.* in 1974.[78] The enhancement was attributed to a surface area-related phenomenon. Later, this was observed independently by Jeanmaire *et al.* and Albrecht *et al.* in 1977.[79,80] The enhancement was assigned to the resonant Raman scattering of molecules adsorbed on rough metal surfaces by the interaction with surface plasmons. The detailed history of the discovery of SERS was discussed in previous reviews.[13,64,66,81,82] Following these early works, SERS has been greatly studied in terms of fundamental understanding of the enhancement mechanisms, optimization of enhancement factors, exploring various shapes and sizes of plasmonic NPs, development of different substrates, and sensing a wide range of analytes.[13,64,82] The SERS enhancement factors are strongly dependent on the chemical composition of plasmonic NPs, the distance between the surface of NPs and the analyte molecule, the excitation wavelength, the position of LSPR, and the resonance of the analyte with the excitation light.[83] The sensitivity of this technique can be as high as single molecule detection in some cases.[65,66,68,84,85] Over the years, researchers have found that the aggregated NPs and the NPS with sharp tips exhibit strong electric field enhancements and thus better SERS signals at the resonant excitation wavelength. SERS sensing can be performed in different ways, such as in a solution phase, on a solid substrate, in a microfluidic flow channel, and inside a tissue, depending on the type of analyte and the plasmonic substrate.[13,14,61,64,86]

### SEF

The concept SEF is similar to that of SERS, however, instead of the Raman signals, the fluorescence of molecules significantly increases upon placing them in proximity to a plasmonic NP surface.[57,69,87–95] The enhancement is caused by the interaction of fluorophores with surface plasmons, and thus the fluorophores experience a strong electric field enhancement, leading to enhanced fluorescence intensity. This phenomenon is also called metal-enhanced fluorescence or plasmon-enhanced fluorescence.[90,93,94] The enhancement of fluorescence is strongly dependent on the overlap of the optical absorption spectra of fluorophore and extinction spectra of NPs, size of NPs, and the distance between the fluorophore and metal NP surface to overcome the quenching by Főrster resonance energy transfer (FRET).[87,94] In addition, plasmonic NPs enhance the intrinsic radiative decay of fluorophores and thus a reduction in lifetime. The mechanisms of surface-enhanced fluorescence have been greatly studied by Lakowicz and co-workers, and they proposed strategies for radiative decay engineering of fluorophores using metal surfaces. SEF has been greatly exploited in the sensing of various analytes.[96–99] The working principle of a typical SEF-based sensor is illustrated in Fig. 1c.[69,87,95] It is based on the enhancement of the fluorescence intensity of fluorophores that are used as labels in recognizing the binding, thus SEF significantly improves the sensitivity of the biosensors. This has been widely used in fluorescence-linked immunoassays and is compatible with other immunoassays, flow cytometry, *etc.*[69,95,100,101] Moreover, it can shorten overall assay times and lower sample volumes, and it can be combined with lateral flow techniques. In addition, SEF has been explored in single-molecular spectroscopy, bioimaging, DNA hybridization sensing, and beyond.[102–105] However, one of the major challenges is to control the interactions between plasmonic NPs and fluorophores to overcome the quenching effect.

### LSPR-shift

The extinction spectra of plasmonic NPs not only dependent on the morphology but also the dielectric constant of the surrounding medium.[39,40] Thus, the change in the surrounding medium leads to a redshift or blue shift of the LSPR peak.[39,58,106–108] This has been exploited to detect the molecular interactions near the nanoparticle surface, as illustrated in Fig. 1c.[38,39,58,108,109] The NPs either in colloidal form or on a substrate exhibit LSPR shifts upon interacting with target analyte molecules.[37,39,108] The interactions can be specific or non-specific depending on the experimental configuration. The extent of LSPR shift depends on the concentration of the molecules that interact with the NP surface.[15] Based on the LSPR shifts, a range of analytes have been detected in different sensing configurations. Among all, LSPR-shift-based immunoassays,[110] LSPR optical fiber sensors[110] and label-free sensing techniques have received significant attention.[37,109]

### Colorimetric sensing

Sensing based on analyte-induced color changes of probe materials has been significantly explored in modern science and technology due to its low cost and point-of-care testing ability.[111–115] Moreover, it doesn't require sophisticated instrumentation and skilled manpower. One of the most interesting features that makes colloidal plasmonic NPs highly attractive is their visible colors due to strong surface plasmon resonance. Their extinction coefficients are 1000 times higher than those of conventional organic dye molecular probes used in colorimetric sensing, thus making them highly attractive as colorimetric probes for high-sensitivity detection.[116,117] The colorimetric plasmonic sensing is based on the selective aggregation of gold NPs upon binding to an analyte (Fig. 1d), the colloidal solution color changes from red to blue due to surface plasmon coupling between particles in the aggregate.[61,118–120] Thus, plasmonic NPs offer naked-eye detection of analytes, and the color changes can be quantified using a mobile device to obtain quantitative information about the analytes.[121] The colorimetric plasmonic sensing can be either through specific or non-specific interaction with the analyte.[119,122–127] This method has been extensively applied for the detection of metal ions, biomolecules, and proteins.[120,123,127]

### Chiral plasmonic sensing

Chirality, a commonly observed feature in biological systems, is one of the most fascinating properties that nature has given us.[128] On the one hand, organic chiral molecules are being greatly exploited regarding their synthesis and applications, and inorganic chiral nanomaterials have received significant attention in the last decade.[129–131] Chirality in inorganic NPs arises due to their morphology which has no mirror or inversion symmetry.[129–134] Thus, they exhibit higher dissymmetry (g) factors ($\sim 0.2$) compared to organic systems ($\sim 10^{-3}$).[131,134] Among all, chiral plasmonic NRs have received significant attention due to their tunable chiroptical signal in the visible range and the g-factors.[134] Chirality in plasmonic NPs has been achieved either by shaping them into helical/twisted morphology or through chiral self-assembly using chiral templates.[134,135] The strength of chirality (g-factor) strongly depends on the helicity of the individual or assembled NPs.[134,136] Thus, chiral plasmonic sensing is generally based on the analyte-induced chirality of plasmonic NPs, as illustrated in Fig. 1e.[137,138] The chiroptical activity increases with increasing the analyte concentration, thus enabling its quantitative determination.

## 2.1. Different types of plasmonic metal NPs used in sensing

The shape of plasmonic metal NPs, which are mostly made of Au and Ag, is determined by their crystalline structure, facet, and anisotropy.[139] High uniformity in size and shape can ensure the investigation of the physical properties and wide applications of plasmonic NPs. The bottom-up chemical synthesis methods, including chemical reduction, electrochemical deposition, photochemical reaction, and multiphase-based synthesis, have been well-developed for the preparation of high-quality NPsP with superior plasmonic properties. Among the chemical reduction methods, seed-mediated growth is the most common technique for synthesizing high-quality NPs. Two steps are involved in this method: nucleation of nanoscale seeds and atomistic growth of the seeds to give final NPs.[140] Once the nucleated clusters lock into well-defined structures, the nanoscale seeds are formed.[140] Different nanoscale seeds can be classified according to their crystalline structure, defects, and shape. The typical diameters of nanoscale seeds are in the range of $\sim$1–15 nm. There are three major categories of nanoscale seeds: single-crystalline, multiply twinned, and plate-like (Fig. 2a, top). Single-crystalline seeds are made of the face-centered cubic lattice (fcc) and are typically by eight {111}and six {100} facets. Due to their small size, their facets are usually difficult to identify and lack defects. Multiply twinned seeds are enclosed typically by {111} facets with multiple twin boundaries in a decahedral shape. When a layer of the fcc lattice is missed or added in stacking order, plate-like seeds are formed. By controlling the concentration of nanoscale seeds, the type and concentration of the capping agent, and the reaction conditions, differently shaped NCs can be synthesized even from the same

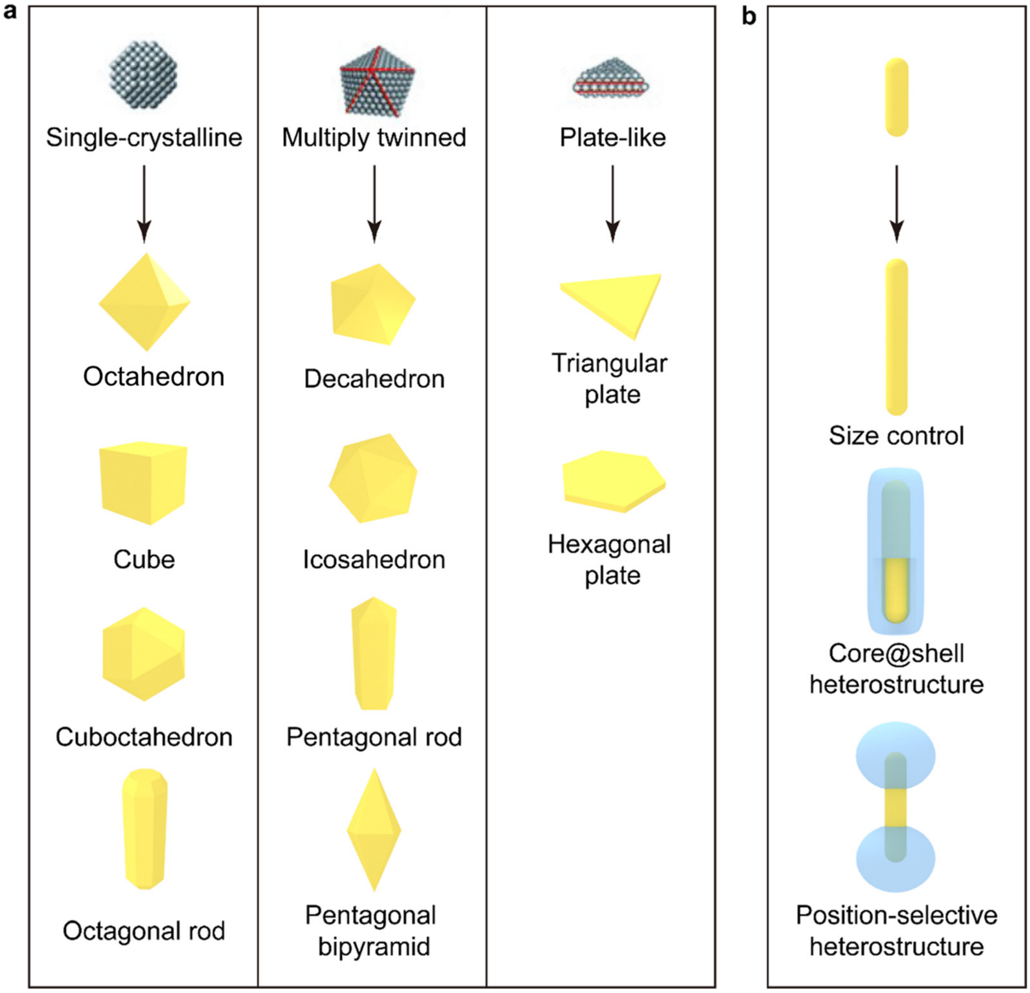

Fig. 2 Seed-mediated growth of plasmonic metal NPs. (a) Schematics of three representative types of nanoscale seeds (top) and the faceted NCs (bottom) produced from the seeds by seed-mediated growth. The red lines in the nanoscale seeds indicate twin boundaries and stacking faults.[140,141] Reproduced from ref. 140 with permission from Wiley-VCH publisher, copyright 2009. (b) Schematics showing the overgrowth of homo- and heterostructures with the faceted NPs as seeds. Metal nanorods are used as a representative example for controlling sizes and constructing core@shell and position-selective heterostructures. The illustrated plasmonic NPs are typically made of Au and Ag.

type of nanoscale seed. The typical shapes of final plasmonic metal NCs obtained from single-crystalline seeds include octahedron, cube, cuboctahedron, and octagonal rod (Fig. 2a, left panel). The shape of final NCs is highly impacted by the defect of nanoscale seeds as well. The defect generated in nanoscale seeds broadens the diversity of final NCs. Decahedron, icosahedron, pentagonal rod, and pentagonal bipyramid can be synthesized from multiply twinned nanoscale seeds (Fig. 2a, middle panel). Plate-like nanoscale seeds enable the growth of two-dimensional-like NCs, such as triangular and hexagonal plates (Fig. 2a, right panel).

The obtained large metal NCs equipped with unique stacking order and facets can be used as seeds for the further overgrowth of homogeneous and heterogeneous components. Size control is one of the purposes (Fig. 2b, top). In order to maintain high uniformity in size and shape and avoid the production of byproducts, nanoparticles up to hundreds of nanometers in size are synthesized step by step by controlling the concentrations of the seeds and the metal salt precursor.[142–144] The obtained metal NCs can also be used to construct heterostructures through seed-mediated growth. Core–shell A@B heterostructures (Fig. 2b, middle) have been designed to satisfy diverse demands, such as plasmon-assisted biomedical applications, solar energy harvesting and photocatalysis. The shell can be made of another plasmonic nanoparticle, semiconductor (metal oxides, metal sulfides, metal selenides), silica, polymer, lanthanide-doped nanomaterial, or metal–organic framework.[145] Moreover, the shell component can also be selectively deposited at different positions on the plasmonic metal core where the plasmonic near-field enhancement reaches maximum to optimize the effect of the plasmonic enhancement by the metal core. The position-selective heterostructures can also allow both components to interact with the surrounding environment. As shown in Fig. 2b (bottom), dumbbell-like heterostructures are the most common position-selective heterostructures. However, limited types of position-selective heterostructures have so far been prepared because the conditions to control the deposition location is usually very delicate.[145]

Shape and size are the most important factors affecting the plasmon properties of metal NPs. The incident light can be confined to different regions on the plasmonic NP surface because of their specific morphology. Specific plasmon modes (LSPR) can be supported on plasmonic metal NPs and interestingly the wavelengths of these plasmon modes can be precisely tuned by varying the morphology and size. The optical properties of these plasmonic NPs determine their applications. Nanospheres (NSs) have attracted the most attention during the past decades among diverse nanoparticles owing to their simplicity in synthesis, spherical symmetry, and readiness in assembly.[146] The isotropic spherical geometry of NSs also allows for the easy analytical solving of Maxwell's equations and the calculation of the absorption, scattering, and extinction cross-sections of NSs, which is known as Mie theory.[146] Taking Au NSs as an example. They can be synthesized uniformly by seed-mediated growth, as shown in Fig. 3a.[147] The dipolar plasmon mode (Fig. 4, solid yellow line) can be tuned from 500 nm to 600 nm by precisely controlling the diameter of Au NSs from 24 nm to 103 nm. With a diameter larger than 130 nm, both quadrupolar and dipolar plasmon modes can be sustained. However, the spectral tunability of the plasmon modes is limited for metal NSs. Nanocubes (NCs), another type of highly symmetric structure, are formed when the round surfaces of an NS are evenly transformed into four flat faces (Fig. 3b). In comparison to NSs, the dipolar plasmon mode of Ag NCs split into two peaks (Fig. 4, solid pink line) owing to their sharp corners.[148] In addition, complex plasmon modes can be localized not only to the edges of nanocubes but also to the sharp corners and flat faces when nanocubes are deposited on both dielectric and metallic substrates. The corner plasmon modes of NCs can even split into distal and proximal ones in the presence of a substrate.[149]

Anisotropic structures are highly desired because they provide extra size parameters to control the plasmon modes. When NSs are elongated along one direction, NRs are obtained. NRs have longer lengths than diameters, giving rise to an anisotropic shape and a specific length-to-diameter aspect ratio (Fig. 3c). The wavelengths of the plasmon modes are highly sensitive to the aspect ratio of NRs (Fig. 4, solid and dotted purple lines). The longitudinal plasmon wavelength of plasmonic metal NRs can be synthetically varied from the visible to the IR region. Another attractive property of NRs is their different responses to incident light linearly polarized along the transverse and longitudinal directions. The odd and even longitudinal multipolar plasmon modes have been observed on Ag NRs with high aspect ratios. The multipolar plasmon modes can endow NRs with a color routing capability.[159] With emitters sandwiched between Ag NRs and a dielectric substrate, the emission of two-dimensional (2D) excitons was found to be routed to the two ends by the multipolar plasmon modes.[160]

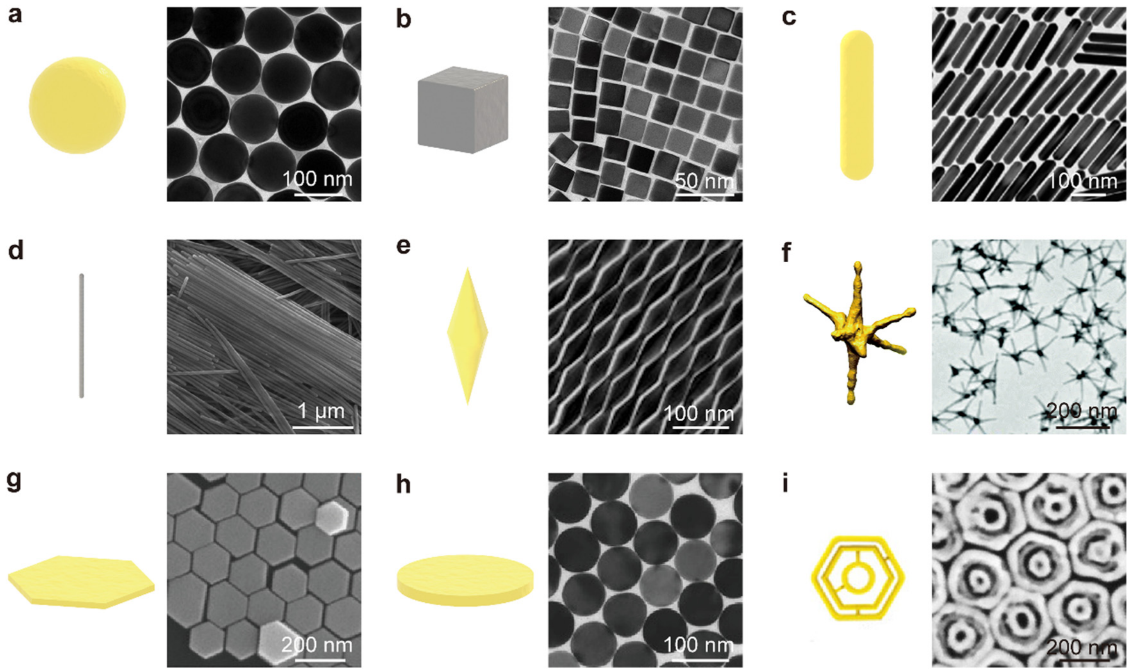

Fig. 3 Schematics of representative individual NPs and their corresponding transmission electron microscopy (TEM)/scanning electron microscopy (SEM) images. (a) Au NSs, TEM. Reproduced from ref. 147 with permission from Wiley-VCH publisher, Copyright 2014. (b) Ag@Au NCs, TEM. Reproduced from ref. 150 with permission from ACS publisher, Copyright 2019 (c) Au NRs, TEM Reproduced from ref. 151 with permission ACS publisher, Copyright 2015 (d) Ag NWs, SEM. Reproduced from ref. 152 with permission from ACS publisher, Copyright 2015 (e) Au NBPs, TEM. Reproduced from ref. 153 with permission from Springer Nature publisher, Copyright 2015 (f) Au nanostars, TEM. Reproduced from ref. 154 with permission from RSC publisher, Copyright 2019 (g) hexagonal Au NPLs, SEM. Reproduced from ref. 144 with permission from Wiley-VCH publisher, Copyrights 2016 (h) Circular Au NPLs, TEM. Reproduced from ref. 155 with permission from Wiley-VCH publisher, Copyrights 2018 (i) Intertwined triple Au nanoscale rings, SEM. Reproduced from ref. 156 with permission from ACS publisher, Copyright 2021.

Nanowires (NWs) are obtained when the aspect ratio is further increased (Fig. 3d). The excellent electrical conductivity and transparency of plasmonic metal NWs make them useful as transparent conductive electrodes for flexible optoelectronics.[161] At the longitudinal plasmon resonance, the field enhancement is localized at the two ends for one-dimensional nanostructures. The electromagnetic (EM) enhancement around the ends is limited because of the hemispherical shape. By sharpening the ends of NRs, nanobipyramids (NBPs) (Fig. 3e) are formed. Higher-order longitudinal plasmon resonances (Fig. 4, solid and dotted blue lines) can be sustained on NBPs owing to the sharp ends.[157] Such sharp ends induce electric field enhancement about three times larger than that of NRs, promoting the generation of hot electrons.[162] The local temperature around the tip has been proven to reach dozens of degrees Celsius because of the enhanced near-field.[163] To fully use the advantages offered by the sharp ends, nanostars of different types have been developed. Nanostars typically have more than three sharp branches (Fig. 3f). Their plasmon modes are dependent on the number and length of their branches, among other parameters. The drastic electric field enhancement occurs around the sharp ends and tips at the LSPR for NBPs and nanostars, which allows them to be used in SERS, sensing, and photocatalysis.[162,164] The sharp ends and tips of NBPs and NSTs can also induce local strain on 2D semiconductors in contact with the NPs, leading to the development of single-photon quantum emitters.[165] When NSs are compressed along a certain direction, 2D nanostructures such as hexagonal (Fig. 3g) and circular (Fig. 3h) nanoplates (NPLs) are produced. Hexagonal NPLs can be synthesized by controlling the concentrations of the metal salt precursor and the seeds. Circular NPLs with different diameters can be produced through chemical etching on hexagonal NPLs by adjusting the etching time.[144]

The thickness is barely affected during the etching process. NPLs, therefore, provide a more flexible method for tuning the plasmon mode by independently varying their thickness and diameter (Fig. 4, solid and dotted green lines). Benefiting from the large atomically flat facets in the lateral direction, the EM field can be confined into a large face-contact area between NPLs and substrates.[166] Especially in NPL-on-mirror structures, rich optical properties, including magnetic and anapole plasmon resonances, have been observed within the dielectric layer sandwiched between the NPL and the metal film.[166] Fabry–Pérot nanoresonators constructed out of Au NPLs and an Au film sandwiched with a high-refractive-index dielectric layer possess high quality factors of up to 76. They also benefit from the atomically flat surface of Au NPLs.[167] To combine the maximized field enhancement regions of 2D nanostructures and strongly amplified near-field focusing in dimers, trimers, and multimers, complex plasmonic nanostructures have recently been designed and synthesized. For example, Fig. 3i, displays intertwined triple ring structures whose near-field focusing can be tailored through the variation of the intragap distance between the nanoscale rings. Such complex 2D nanostructures have enabled single-particle SERS with large enhancement factors (EF) up to $\sim 10^9$.[156]

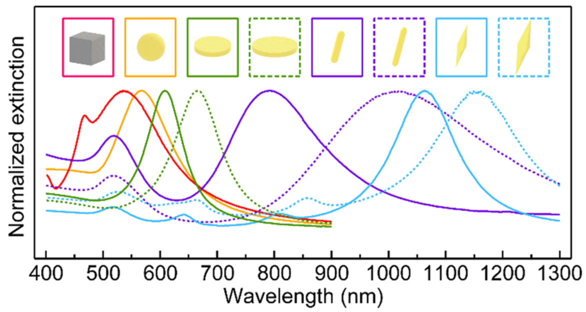

Fig. 4 Representative extinction spectra for Ag NCs (73 nm in edge length, solid pink line), Au NSs (88 nm in diameter, solid yellow line), circular Au NPLs (79 nm in diameter, 22 nm in thickness, solid green line; 99 nm in diameter, 22 nm in thickness, dotted green line), Au NRs (14 nm in diameter, 59 nm in length, solid purple line; 10 nm in diameter, 63 nm in length, dotted purple line), Au NBPs (59 nm in waist diameter, 230 nm in length, solid blue line; 70 nm in waist diameter, 276 nm in length, dotted blue line). All samples are dispersed in aqueous solutions for extinction measurements. The data of Au NSs, Au NPLs and Au NBPs are reproduced from ref. 146, 155, 157 with permission from Wiley-VCH publisher, Copyright 2014, 2018 and 2015, respectively. The data of Au NRs are reproduced from ref. 158 with permission from ACS publisher, Copyright 2006.

## 3. Plasmonic metal nanoparticles-based SERS sensing

### 3.1. Fundamentals of SERS

SERS spectroscopy is based on the amplification of Raman signals from molecules sorbed on plasmonic surface, usually gold or silver.[168] The discovery of the SERS effect can be attributed to Fleischman, Hendra, and McQuillan in 1974.[78] They observed an unusually strong Raman signal from pyridine molecules absorbed on a roughened silver electrode. These authors interpreted the effect as a local increase of the surface concentration of the analyte due to the increase of the surface area of the electrode due to its deterioration because of the consecutive reduction–oxidation cycles. Consequently, the physical effect was incorrectly named SERS spectroscopy. However, subsequent independent reports by Jean Maire and Van Duyne,[80] Albrecht and Creighton,[79] both published in 1977, together with the seminal work by Moskovits[169] demonstrated that this intensity could not be accounted for an increased surface. Conversely, they reported SERS as an eminent electromagnetic (EM) effect derived from the excitation of LSPRs upon their excitation when illuminating nanostructured metals with the appropriate light, as previously theorized by Bohm[170] and demonstrated by Otto,[86] as a solution of the Maxwell equations. Also, they highlighted that the scattering intensity from the adsorbed molecules was $10^5$–$10^6$ times stronger than the conventional Raman signal. Notably, until 1979, all SERS experiments were carried out only on electrodes being Creighton, Blatchford, and Albrecht[171] the first in report SERS experiments in colloidal Au and Ag nanostructures. In 1980 Otto reported the effect of the charge transfer and the resonance at the surface, the so-called chemical effects on the intensification of the SERS signal.[172] In 1983/84 the surface selection rules were developed independently by Creighton[173] and Moskovits.[174] No matter these advances and as reported by Moskovits in one of the most influential reviews in SERS,[63] the research and use of this technique became mostly academic until 1997. In that year, two different papers demonstrated the capability of SERS for the detection of single molecules.[68,85] This fact not only fueled the fundamental research in the field but also in closed areas such as nanofabrication optical theory and the development of applications in biology, medicine, environmental science, or catalysis. Thus, today an extraordinary effort led by a myriad of research groups is performed to transform SERS into a real live tool especially in the field of biosciences.

The fundamental components in SERS include a molecule, a plasmonic material, and EM radiation. The adsorption of the molecule onto the plasmonic surface is typically classified according to the strength of bonding into either physisorption (weak interaction) or chemisorption (chemical bonding). When this molecule-nanoparticle system is illuminated by EM radiation, the incident photons can induce substrate excitations such as electron–hole pairs, surface plasmons, or surface phonons that contribute to the enhancement. In particular, the nanostructure's absorption of light can generate potent local electric fields at the location of the adsorbed molecular species. This local field significantly influences the optical properties of the adsorbate, thereby causing the SERS enhancement. Moreover, the interaction between the incident radiation and the adsorbed molecule may result in photodissociation, photoreactions, or photo-desorption, each of which leaves unique traces in the resultant SERS spectrum. On the other hand, the interaction of light with the metallic nanostructure depends on the value of the complex dielectric function at the excitation wavelength, which determines the enhancement observed at a given excitation frequency. Particle absorption and scattering are influenced by the shape and size of the metal nanostructure, thus affecting SERS intensities. Furthermore, the excitations in nanostructures are strongly influenced by the medium's dielectric constant. The absorption and scattering of light by metallic nanoparticles (smaller than the wavelength of the incident light) are crucial properties that yield SERS and provide the theoretical basis for the explanation of the EM enhancement.[62,83,86,175–180] Although LSPR of nanostructures is necessary for large enhancement factors of SERS, the chemical interactions between analytes and substrates can lead to Raman enhancement *via* the chemical enhancement mechanism that has often been observed for semiconductor substrates.[13,181]

For a single isolated plasmonic sphere (Fig. 5a), the extinction and scattering can be fully explained by the Mie theory.[182,183] When the light resonates with the LSPR, the metal sphere emits its dipolar field ($E_{\mathrm{SP}}$). The magnitude of that field at a nearby molecule depends on the sphere's radius ($r$), its distance ($d$) from the molecule, the dielectric constants of the metal ($\varepsilon$) and the surrounding medium ($\varepsilon_0$), as well as the strength of the incident field ($E_0$). Therefore, the molecule experiences an enhanced local field ($E_{\mathrm{M}}$) which includes both electric-field magnitudes: $E_0 + E_{\mathrm{SP}}$. The light field enhancement $A(\nu)$ is determined by the ratio of the field at the molecule's position to the incoming field.

$$A(\nu) = \frac{E_{\mathrm{M}}(\nu)}{E_0(\nu)} \approx \frac{\varepsilon - \varepsilon_0}{\varepsilon + 2\varepsilon_0} E_0 \left(\frac{r}{r+d}\right)^3 \qquad (1)$$

Here, $A(\nu)$ is particularly strong when the real part of $\varepsilon(\nu)$ is equal to $-2\varepsilon_0$. Additionally, for a significant EM enhancement, the imaginary part of the dielectric constant needs to be small. These conditions describe the resonant excitation of localized surface plasmons for a metal sphere.[184] Similarly, the scattered field will be enhanced if it is in resonance with the particle LSPR. Therefore, considering the enhancing effects for both the laser and the Stokes field, the EM SERS enhancement factor, $G^{\mathrm{SERS}}(\nu_{\mathrm{S}})$, can be expressed as:

$$G^{\mathrm{SERS}}(\nu_{\mathrm{S}}) = \left|A_{(\nu_{\mathrm{L}})}\right|^2 \left|A_{(\nu_{\mathrm{S}})}\right|^2 = \left|\frac{\varepsilon_{(\nu_{\mathrm{L}})} - \varepsilon_0}{\varepsilon_{(\nu_{\mathrm{L}})} + 2\varepsilon_0}\right|^2 \left|\frac{\varepsilon_{(\nu_{\mathrm{S}})} - \varepsilon_0}{\varepsilon_{(\nu_{\mathrm{S}})} + 2\varepsilon_0}\right|^2 \left(\frac{r}{r+d}\right)^{12} \qquad (2)$$

This equation indicates that the enhancement scales with the fourth power ($|E|^4$) of the local field of the metallic nanostructure, and that it is particularly strong when excitation and scattered fields are in resonance with LSPRS. On the other hand, the EM predicts that SERS does not require direct contact between the molecule and the metal, but it is necessary a certain sensing volume. This is because, as shown in eqn (1) and (2), the EM enhancement factor strongly decreases with the distance from the metal surface due to the decay of the dipolar field $[1/d]^3$ to the fourth power, resulting in $[1/d]^{12}$.

Maximum values for EM enhancement in spherical isolated nanoparticles are on the order of $10^6$. Theory predicts stronger EM enhancement for regions with sharp features and large curvatures, which may exist on silver and gold nanostructures. For instance, the EM SERS enhancement factor can be increased up to $10^{11}$ when the particle presents sharp tips or edges. These features localize the electric field within confined regions, enabling extremely high enhancement factors.[185,186] Additionally, closely spaced interacting NPs can provide further field enhancement. EM enhancement factors up to $10^{11}$ have been estimated for dimers of Ag NPs.[187] These substantial enhancements are typically attributed to highly concentrated EM fields associated with strong LSPRs at interstitial sites (often referred to as EM or SERS hotspots) in nanostructures consisting of two or more coupled nanostructured surfaces with closely spaced features. The size of these hotspots is as small as a few nanometers, and the EM field concentration on them strongly depends on the geometry of the nanostructured site where the probed molecules reside, the wavelength, and the polarization of the incident light.[185] When optical excitation is localized in such small hot spots, extraordinarily large EM SERS enhancements (proportional to field enhancement to the fourth power) up to $10^{12}$ have been theoretically predicted.[62]

While the EM mechanism is the primary contributor to the SERS signal, early observations noted a dependence of the scattering signal on the electrode potential,[188] suggesting an electronic coupling between the molecule and the metal. In addition, the presence of metal in the system can alter the polarizability of adsorbed molecules, thereby potentially increasing the Raman scattering efficiency. On the other hand, experimental observations, such as the effect's dependence on the chemical nature of the molecule and strong molecular

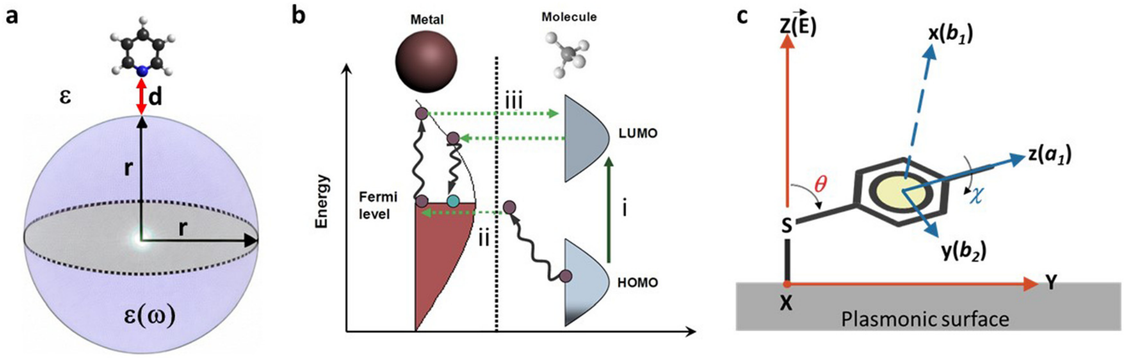

Fig. 5 (a) EM mechanism for SERS enhancement for a single isolated sphere. (b) Energy level diagram for a "molecule-metal system" showing a possible charge transfer involving molecular states (path (i)) and molecular and metallic states (paths (ii), (iii)). (c) Model for the estimation of the molecular orientation. Absolute orientation of the molecule on the surface and relative orientation of the ring over the surface are represented by *XYZ* and *xyz* axes, respectively.

selectivity, provide clear indications for the existence of an additional chemical SERS enhancement. Moreover, the best EM SERS enhancement factors ($10^{12}$) leave a gap of about two or three orders of magnitude to the highest experimentally observed non-resonant SERS enhancement factors on the order of $10^{15}$,[189] which suggests the existence of additional enhancement mechanism(s) accounting for the missing factors.

Different mechanisms have been proposed to account for the chemical SERS effect, sometimes also referred to as the first-layer effect, as it necessitates direct contact between the molecule and the metal. The electronic coupling between the molecule and metal and the formation of a surface complex can lead to charge transfer (CT) from the metal to the molecule, or *vice versa*, and within the adsorbed molecule itself, resulting in an increased Raman signal. Fig. 5b displays a typical energy level diagram for a molecule-metal system, where the energies of the highest occupied molecular orbital (HOMO) and the lowest unoccupied molecular orbital (LUMO) are roughly symmetric relative to the Fermi level of the metal, alongside possible CT processes involving molecular states (path (i)) and molecular and metallic states (paths (ii) and (iii)). Generally, the chemical SERS enhancement factor is believed to contribute enhancement factors on the order of 10–$10^3$, coexisting with EM enhancement.

The surface selection rules, formulated by Moskovits in the 80's,[174] explore the alteration of the relative intensity of bands within a given SERS spectrum as a result of the orientation of the molecule being studied in relation to the plasmonic surface. For example, when considering mercaptobenzene (Fig. 5c),[190] and a $C_{2v}$ symmetry for the mercaptobenzene group, its vibrational modes can be classified into in-plane (ip) $a_1$ and $b_2$ modes and out-of-plane (oop) $a_2$ and $b_1$ modes. On the other hand, assuming that the surface electric field, $E$, effectively has only a normal component ($Z$ direction in Fig. 5c),[191] the intensity of a vibrational mode is proportional to the square of the scalar product of the electric field and the dipole moment derivative of the mode, $\mathrm{d}\vec{\mu}/\mathrm{d}Q$.[192,193]

$$I \propto \left|\frac{\mathrm{d}\vec{\mu}}{\mathrm{d}Q}\vec{E}\right|^2 = \left|\frac{\mathrm{d}\vec{\mu}}{\mathrm{d}Q}\right|^2 \quad \left|\vec{E}\right|^2 \cos^2\alpha \qquad (3)$$

where $a$ is the angle between $\vec{E}$ and $\mathrm{d}\vec{\mu}/\mathrm{d}Q$. Defining $\theta$ as the tilt angle of the $z$ axis of the mercaptobenzene unit with the surface normal ($Z$), and $c$ as the twist angle of the molecular plane around the $z$ axis (which is 0° when $y$ is parallel to the surface). Then, by considering that the ip $a_1$ and $b_2$ modes have dipole moment derivatives along $z$ and $y$ axes, respectively, and the oop $b_1$ modes have dipole moment derivatives perpendicular to the phenyl ring (along $x$ axis), the molecular-fixed axis system $xyz$ can be correlated with the experimental axis system $XYZ$ by the two Eulerian angles, $\theta$ and $\chi$. The intensities of $a_1$, $b_1$ and $b_2$ can be then represented as follows from the above equation:[38]

$$I(a_1) \propto \cos^2\theta\, I^0(\alpha_1) \qquad (4)$$

$$I(b_1) \propto \sin^2\theta\, \mathrm{con}^2\chi\, I^0(b_1) \qquad (5)$$

$$I(b_2) \propto \sin^2\theta\, \sin^2\chi\, I^0(b_1) \qquad (6)$$

here $I^0$ represents the intrinsic intensity of the corresponding mode without the surface effects (*i.e.*, normal Raman spectrum). Thus $\theta + 90°$, which describes the angle metal surface-S-$\chi$, and $\chi$, which describes the orientation of the phenyl ring against the silver surface, can be calculated as follows:

$$\tan^2\chi = \frac{I(b_2)}{I(b_1)}\frac{I^0(b_1)}{I^0(b_2)} \qquad (7)$$

$$\tan^2\theta = \frac{I(b_1)}{I(a_1)}\frac{I^0(a_1)}{I^0(b_1)}\frac{1}{\cos^2\chi} \qquad (8)$$

Thus, by assigning the $a_1$, $b_1$ and $b_2$ vibrational modes in the SERS spectra, usually by computational density functional theory (DFT) methods, before and after the coupling, it is possible to know the tilt and twist angles. The deformation of these angles is, however, restricted by the fact that the chemoreceptor is chemically bound to the surface and requires very large analytes to be effective.

### 3.2. SERS sensing platforms

SERS-based detection of chemical and biological analytes at the trace or single molecule level is extremely desirable in a variety of scientific and technological domains, including analytical chemistry,[194] materials science,[195] forensics,[196] life science,[197] food industry,[198] explosive detection[199] and biomedical diagnostics.[200] The advancement of nanofabrication techniques, the ability to obtain desired plasmonic substrates, the tunability of LSPR of plasmonic substrates according to the requirements, and the sensitivity of SERS spectroscopy brought down the detection limits to a single molecule level. In particular, the design and fabrication of SERS substrates using desired plasmonic substrates is a key factor in achieving high-sensitivity detection.[201] A wide range of SERS substrates have been reported in the literature with the specific goal of controlling plasmonic hotspots and thus achieving high sensitivity.[202] SERS substrates can be broadly classified into two types depending on how the plasmonic NPs are being used in sensing analytes: (1) plasmonic NPs deposited on solid substrates in a controlled manner (2) colloidal solutions of plasmonic NPs with or without Raman reporters decorated on their surface.[203,204] To fabricate efficient SERS solid substrates various nanofabrication techniques such as focused ion beam technique,[205] soft lithography,[206] electron beam lithography,[207] stamping,[208] nanosphere lithography,[209] optical lithography,[210] molecular assembly-based lithography, and colloidal self-assembly have been employed.[211] Despite tremendous progress in the field, developing reliable and reproducible SERS solid substrates has been challenging. Extensive research has been conducted to optimize SERS substrates by close packing of NPs, using different shapes that exhibit strong field enhancements, positioning the analyte in the hotspot, and integrating SERS spectroscopy with other analytical systems (*e.g.*, microfluidic, optofluidic, and paper-based) to achieve ultrahigh detection sensitivity.[212–214] On the other hand, sensing in a liquid medium can performed using SERS tags or pure plasmonic NPs. In particular, SERS tags have been extensively used in the ultrasensitive quantitative detection of a wide range of analytes. SERS tags are commonly prepared by first functionalizing the surface of Au or Ag NPs of different shapes with molecules (Raman reporters) that exhibit strong intrinsic Raman scattering, followed by coating a biocompatible shell, usually a polymer or $SiO_2$. The shell can then be functionalized with a biorecognition system such as an antibody for specific binding to a target analyte. The SERS tags can also be used in solid substrate-based sensing platforms. Besides, the colloidal solutions of bare plasmonic NCs, with or without a biorecognition system have been used for specifically or nonspecifically binding to analytes to induce SERS signals. In the colloidal solution, the SERS detection is also influenced by the Brownian motion of analytes or metal NPs, and it is often used to attain quantitative analysis, but it has a low LOD.[215] In some cases, SERS substrates can be one or a few particles that enable the detection of single molecules through strong EM enhancements. On the other hand, they can also be rigid or flexible solid substrates (glass, silicon, paper, plastic, *etc.*) in which plasmonic NPs are chemically or physically immobilized. The substrates can also be integrated with other technologies such as microfluidics, electrocatalysis, and beyond. In the following section, the detection of various analytes using different types of SERS substrates has been discussed.

### 3.3. Single-molecule SERS (SM-SERS) approaches and requirements

Numerous comprehensive reviews have extensively covered substrates and methodologies aimed at acquiring Raman spectra from individual molecules. Here, our focus shifts towards discussing and highlighting some of the latest advancements and promising strategies in fabricating dependable probes for single-molecule (SM)-SERS in a reproducible manner. Several critical conditions must be met for successful SM-SERS, including the design of a nanostructure capable of sufficiently enhancing the EM field.[216] In SERS, both incident and scattered light undergo enhancement. The signal amplification thus scales approximately with the fourth power of the electric field intensity ($\sim|E|^4$).[217,218] For single-molecule measurements, an EM-field enhancement of at least on the order $10^7$–$10^{10}$ is required.[219]

The most common approach to obtaining sufficient enhancement factors takes advantage of the electromagnetic "hotspot" formed in the gap between two adjacent Au or Ag NPs. Plasmonic coupling at the particle junction results in a highly localized, strong electromagnetic field if the dimer is excited with light at a wavelength matching the coupled plasmon resonance.[220] However, the SERS enhancement obtained from plasmonic dimers is inversely proportional to the interparticle distance. For NSs, this typically requires distances on the order of 1–2 nm. Top-down nanolithography methods such as e-beam lithography or focussed ion beam milling are capable of fabricating nanostructures with such high precision. Nevertheless, benefiting from the EM enhancement requires precise localization of a single analyte in the hotspot region, a task that can be challenging and reliant on a suitable localization strategy.

Bottom-up approaches represent an alternative method, where the analyte is directly assembled together with the NP dimer. For instance, Lim *et al.* reported the formation of Au NS dimers with a DNA tether, that simultaneously enabled the localization of a single Raman-active dye at the particle junction.[221] Growing a Ag shell on the Au particle surface further reduced the interparticle spacing and increased enhancement. However, nanospheres formed by reduction chemistry or metal overgrowth are typically not perfectly spherical and may exhibit facets or edges. This variability can result in variations in the hotspot size, thus hindering quantitative measurements. A strategy for synthesizing nearly perfect spheres through chemical etching was reported by the Schlücker group.[222] Structural uniform dimers of ideal spheres were formed by the substrate-supported assembly and exhibited excellent and reproducible plasmonic properties for reliable measurements.[223] Nanodimer formation using alkanethiol[224] or DNA-linker[225] has proven useful for assembling spherical particles. A more versatile approach to dimer formation, with a defined gap size and hotspot targeting, is offered by DNA origami technology. DNA origami is a nanofabrication method that allows the design of three-dimensional structures with nanoscale precision.[226] This technique has been employed to assemble complex and multi-functional plasmonic nanostructures, enabling the study of enhanced light–matter interactions in various scientific applications, including SM-SERS.[227]

The first reports on DNA-origami assembled plasmonic dimers for SERS were published almost ten years ago. Interestingly, all reports employed different structural designs, illustrating the great design flexibility of DNA nanotechnology. For example, Prinz *et al.* designed gold dimers on triangular DNA origami scaffolds.[228] Thacker *et al.* developed a design to obtain strong plasmonic coupling between two 40 nm gold nanoparticles reproducibly held with gaps of 3.3 ± 1 nm on a porous DNA sheet.[229] Kühler *et al.* utilized gold nanodimers linked by a three-layered DNA origami spanning the plasmonic "hotspot".[230] Pilo-Pais *et al.* employed a DNA origami template where Au NPs were selectively placed on the corners of rectangular origami and subsequently enlarged *via* solution-based metal deposition.[231]

In recent years, further origami designs, such as nanoforks[232] and funnel-spacers,[233] have been devised, expanding the methodology towards successful SM measurements. In the first demonstration of SM-SERS with DNA-Origami assembled Au dimer nanoantennas, Simoncelli *et al.*, employed optothermal-induced shrinking of a DNA template to reduce the gap sizes between two 40 nm Au NSs.[233] By shrinking the plasmonic hotspot, SERS spectra from single molecules positioned in the NP gap were obtained. However, plasmonic heating is generally not wanted during the measurement. Along with hot carrier generation, high temperatures could lead to carbonization of the analyte.[234,235] Carbonization is characterized by the emergence of a broad carbon D-band at $\sim$1350 cm$^{-1}$ and a stronger G-band at $\sim$1580 cm$^{-1}$ that dominates the time-averaged spectrum. Strategies to avoid carbonization have been demonstrated, with gold being less prone to induce carbon formation compared to silver,[236] and carbonization tends to be further suppressed when SERS measurements are conducted in water.[237] As briefly mentioned earlier, the strength of DNA origami lies in its flexibility to realize alignments of particles with different shapes and materials. This flexibility allows for the creation of large hotspots capable of accommodating sizable molecules and proteins while still providing sufficient field enhancement. Nanostars and bowtie antennas formed by Au nanotriangles have emerged as alternatives to nanosphere dimers to achieve strong field enhancement with wider gaps. Au NSTs feature sharp tips where the electromagnetic field is concentrated at resonant excitations.[238] Recently, Kanehira *et al.* reported that dimers formed with "nanoflower" particles outperform spheres on "nanofork"-DNA origami nanoantennas.[239] Single protein SERS was demonstrated by Tanwar *et al.*, where thrombin was bound to a DNA template and then sandwiched between two bimetallic NSTs (Fig. 6a).[240] However, aligning NSTs precisely tip-to-tip can be challenging, even with DNA origami. Furthermore, the sharp tips of nanostars exhibit limited stability under resonant excitation and are prone to melting during measurement. Other methodologies have therefore been explored and reported. Heck *et al.* demonstrated SM-SERS on biotin/streptavidin with self-assembled "nanolenses" made of silver particles (Fig. 6b).[241] Tapoi *et al.* demonstrated SM-SERS of cytochrome *c* with DNA origami nanofork antennas (Fig. 6c).[232] Zhang *et al.* demonstrated non-resonant SERS of Cy5 in 5 nm gaps between gold triangles on DNA origami.[67]

A general limitation of most of these DNA origami approaches is a single dye or biomolecule must first be attached to the DNA origami. Subsequently, the plasmonic NPs are assembled around the analyte in a second step prior to measurements. This strategy may not be viable for typical sensing applications, where proteins or biomolecules must be identified from a liquid sample. Ideally, a SERS probe would enable the capture of analytes from the solution. Recently, a DNA origami scaffold with control over the tip-to-tip alignment of Au NRs with an average gap size of 8 nm has been reported (Fig. 6d).[243] These gaps were accessible for proteins captured using specific anchoring sites located in the hotspot region. The capability to target specific biologically relevant proteins may facilitate future *in situ* or *in vivo* measurements, for example, Sharma *et al.*[244] have reported the SERS detection of single epidermal growth factor (EGF) receptors using DNA origami-assembled gold nanorod dimer nanoantennas. To stabilize the structure during measurements, the origami template could additionally be protected *via* site-specific silanization without hindering any analyte binding.[245] In combination with recent implementations of machine learning for SERS data analysis,[246] the design for DNA origami assembled nanostructures for SM-SERS will pave the way for their wider use in biodiagnostics and personalized medicine.

As discussed above placing the analyte in the hotspot is critical for SM-SERS. Another approach that has been exploited for SM-SERS is tip-enhanced Raman spectroscopy (TERS, see Section 3.6 for more details), in which analyte molecules are placed in between the plasmonic tip and substrates.[247–249] The apex of the tip localizes the EM field in a confined space through the lightning rod effect.[250,251] Thus, the strong coupling between the tip and substrate results in strong EM field enhancement so the SERS EF. The spectral overlap of the SPR of the hotspot and the electronic transition of the analyte is an important factor for SM-SERS.[250] This technique has been used in the chemical mapping of single molecules with atomic precision,[252] *in situ* probing of catalytic reactions at the SM level, molecular conformations in molecular electronics where SM junctions are used,[253] and detection of biomolecules (viruses, DNA, and RNA)[248,251,254] with SM precision. Despite significant progress in recent years, the practical applications of SM sensing are yet to be realized. It is still challenging to prove whether the SERS signals come from SM. Moreover, the degradation of analytes under laser beam effects the reproducibility of SM SERS spectra.

### 3.4. Target analytes

In direct SERS, target analytes are molecules/ions that exhibit Raman active vibrational transitions, undergoing changes in polarizability during these vibrations. Moreover, it is more suitable for molecules with unsaturated bonds and aromatic rings (high polarizability) like polyaromatic hydrocarbons (PAHs), dyes, *etc.* Nevertheless, other analytes show low Raman cross-section (Raman efficiency) like some gas species, proteins, *etc* so an indirect SERS methodology is applied for its detection. This type of detection implies using plasmonic substrates/NP functionalized with a Raman active molecule

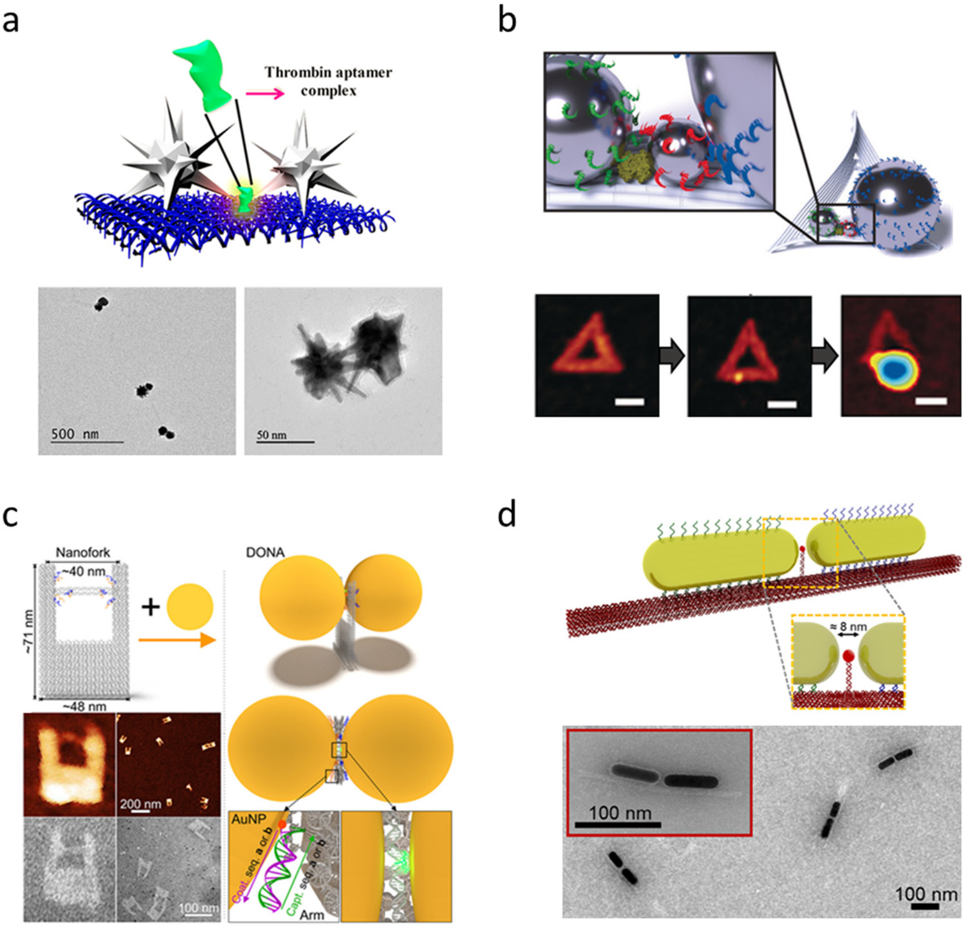

Fig. 6 Examples of plasmonic DNA origami nanoantennas for single protein measurements. (a) Schematic of gold/silver nanostar dimers formed around thrombin on a rectangular DNA origami sheet. TEM images of the nanostar dimer structure (Reproduced from ref. 240 with permission from ACS publisher, Copyright 2021). (b) A single streptavidin molecule is positioned in the gap between silver nanoparticles of different sizes, forming a so-called "nanolens". Reproduced from ref. 241 with permission from Wiley-VCH publisher, Copyright 2018. The sequence of AFM images shows the DNA origami template, the template with streptavidin attached, and the finally formed plasmonic structure. (c) DNA origami nanofork antenna structure. An analyte molecule is tethered to a DNA bridge spanning the particle gap reproduced from ref. 232 with permission from ACS publisher, Copyright 2021 (d) gold nanorods assembled by a DNA origami beam. A capturing strand is located between the nanorod tips to bind single proteins from the solution. Reproduced from ref. 242 with permission from Nature Publisher, Copyright 2023.

(typically with a large Raman scattering cross section and called SERS tag). Thus, in indirect SERS the interaction of the SERS tag with the target analyte produces a change in the Raman intensity or in the Raman shift. In the section, we summarize the detection of some of the most relevant target analytes, covering explosives and chemical warfare agents, ionic and gaseous species or biomolecules.

**3.4.1. Explosive molecules and chemical warfare agents and simulants.** Studies on synthesizing and detecting various explosives and their compositions are in vogue (*e.g.*, organic, inorganic, plastic-bonded, mixtures, metal NPs, improvised explosives, $\alpha$ and $\beta$ 1,3,5,7-tetranitro-1,3,5,7-tetrazocane (HMX), *etc.*). Generally, they exist in powder (solid) and liquid forms. Their extremely low vapor pressures (*e.g.*, 1,3,5-trinitro-1,3,5-triazinane (RDX) $\sim 10^{-9}$ torr and 2,4,6-trinitrotoluene (TNT) $\sim 10^{-6}$ torr) challenge their detection using conventional techniques. Further, in the real world, dynamic backgrounds will interfere with explosive detection, for instance, trace explosives on various surfaces (paper, wood, luggage), hidden explosives mixed with other materials, and buried explosives (in the case of buried land mines/improvised explosive devices). For these reasons, the trace detection of explosives, such as 2,4-dinitrotoluene (DNT), TNT, pentaerythritol tetranitrate (PETN), RDX (1,3,5-trinitro-1,3,5-triazinane) and HMX, *etc.*, gained extensive research interest in recent years.

Tremendous work has been performed to focus on challenges concerning trace explosives detection, such as innovations in flexible substrates that facilitate swabbing or wiping from surfaces, vapor detection, and making cost-effective, durable plasmonic structures. The molecular formula and structure of various explosives and chemical warfare simulants are provided in Fig. 7. Using tagged Au NRs, trace quantification of HMX and RDX has been reported recently based on the nitrite derived during hydrolysis. The study by Guven *et al.* has also been extended to real-world soil samples for simultaneous detection of HMX and RDX and achieving a recovery of greater than 90%.[255] With a novel 2D transition metal nitride substrate

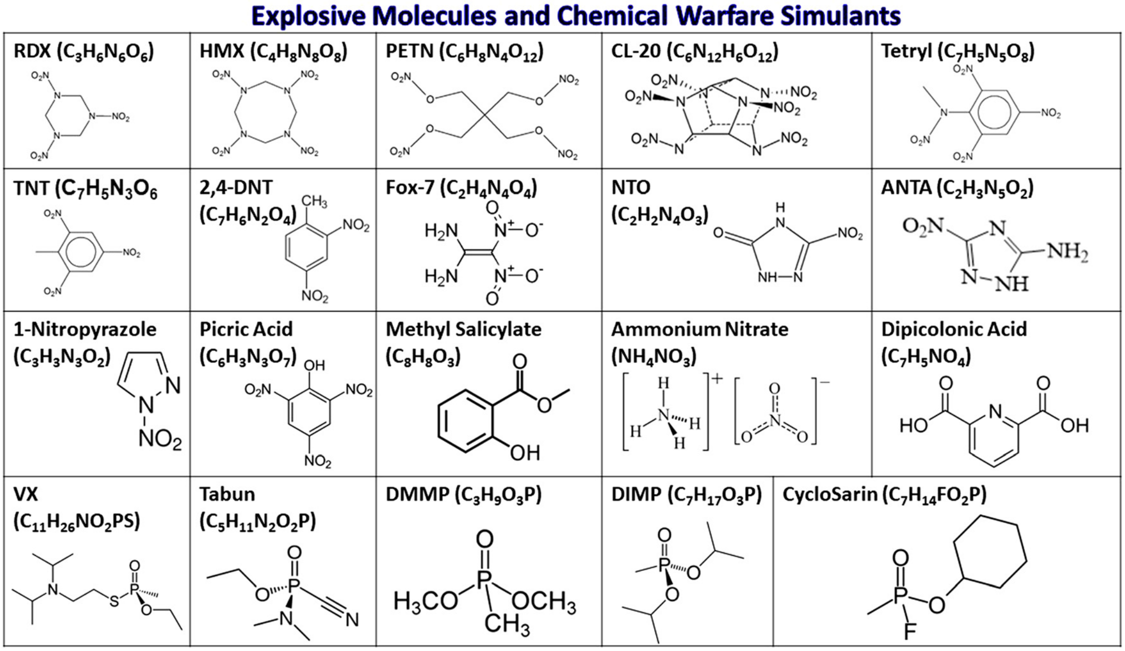
Explosive Molecules and Chemical Warfare Simulants
RDX ($C_3H_6N_6O_6$)
HMX ($C_4H_8N_8O_8$)
PETN ($C_6H_8N_4O_{12}$)
CL-20 ($C_6N_{12}H_6O_{12}$)
Tetryl ($C_7H_5N_5O_8$)
TNT ($C_7H_5N_3O_6$)
2,4-DNT ($C_7H_6N_2O_4$)
Fox-7 ($C_2H_4N_4O_4$)
NTO ($C_2H_2N_4O_3$)
ANTA ($C_2H_3N_5O_2$)
1-Nitropyrazole ($C_3H_3N_3O_2$)
Picric Acid ($C_6H_3N_3O_7$)
Methyl Salicylate ($C_8H_8O_3$)
Ammonium Nitrate ($NH_4NO_3$)
Dipicolonic Acid ($C_7H_5NO_4$)
VX ($C_{11}H_{26}NO_2PS$)
Tabun ($C_5H_{11}N_2O_2P$)
DMMP ($C_3H_9O_3P$)
DIMP ($C_7H_{17}O_3P$)
CycloSarin ($C_7H_{14}FO_2P$)

Fig. 7 Molecular formula and structure of various explosive molecules and chemical warfare simulants covered in this review.

as plasmonic material, explosive molecules like PETN, RDX, and HMX were detected on three base substrates: silicon, glass, and paper. Soundiraraju *et al.* have observed that the paper substrate has outperformed the other two substrates and a commercial substrate in enhancement.[256] Similarly, 2D hybrid graphene oxide (GO) and Ag NPs substrates fabricated by laser ablation were used to detect RDX and HMX using SERS with a sensitivity in the order of picomolar concentration.[257] Singh and co-workers were ableable to detect DNT and picric acid (PA), and dipicolinic acid (DPA) with nanomolar sensitivity using ultra-thin GO doped with nitrogen and nitrogen sulfur and decorated with Ag NPs.[258] Further, Naqvi *et al.* have achieved laser-ablated AgNP/GO substrates with a dual benefit of chemical and electromagnetic enhancements.[259] Ag-NPs embedded in GO have also been used for TNT sensing.[260] Liyanage *et al.* have used flexible gold NTs-based plasmonic sensor for the trace detection of RDX, TNT, and PETN, with a remarkable platforms for reproducibility of 4%, LOD of 56 parts-per-quadrillions and enhancements of EF $\sim 10^6$. The selectivity of the performance has also been analyzed by detecting explosives directly from fingerprints transferred to the sensor using a benchtop Raman system.[261] Silver NTs have also been shown to be advantageous in the trace detection PA with μM sensitivity by Wang *et al.*[262] Different papers (sandpaper, filter paper, and printing paper) loaded with picosecond ablated AgAu alloy NPs were used to detect RDX with enhancement factors $10^5$. Byram and co-workers have demonstrated sample collection through swabbing promising real-world applications in surface examinations.[263] Fan and co-workers have utilized plasmonic sticky and flexible SERS substrates to detect HNX, TATB, LLM-105, RDX, HMX, FOX-7, and TNT molecules. HNX traces on bags and fingerprints were also analyzed using the same substrate.[264] Gao *et al.* investigated a novel wrinkled, flexible Au-coated polyester (PET) film prepared by lithography and plasma etching and used it to detect TNT.[265] A flexible polydimethylsiloxane (PDMS)-based SERS substrate with Ag NPs has demonstrated TNT detection by wiping a cloth bag by Gao *et al.*[266] Moram *et al.* have used NaCl as an aggregation agent for AgAu alloy NPs and encompassed them in simple filter papers. The detection of NTO and DNT was achieved by systematically optimizing the soaking time of the filter paper and studying the effects of the concentration of the NaCl.[267] Explosive vapor detection using SERS is still a challenge because of the poor adsorption of molecules on the SERS substrate. Overcoming the challenge, gold NCs were used by Ben-Jaber *et al.* for the trace vapor detection of DNT and RDX, achieving an enhancement factor of $10^{10}$, the highest reported for the vapors so far.[268] Vapor detection of TNT, RDX, and PETN has been reported with ng sensitivity using a handheld Raman spectrometer.[269] A multiscale SERS substrate composed of photonic crystals and Au–silica NPs with core–shell morphology that can detect trace-level vapors rapidly (3 minutes) of DNT with 1 ppm sensitivity using a portable Raman spectrometer.[270] Sputtered gold and silver alloy on roughened glass, along with principal component analysis (PCA), has been used for the selective detection of three explosives, TNT, RDX, and PETN.[271] Anisotropic and cost-effective Ag dendrites prepared by electrochemical etching were used to detect RDX and AN with an enhancement of $10^4$ and RSD of 9%.[272] The study has been further extended using Au-decorated Ag dendrites, which have enhanced $10^6$ times and lower LOD of $\sim$nM.[273] Femtosecond laser ablation patterned micro square arrays on the Si surface. It was applied for trace detection of PA, RDX, and DNT using AgAu alloy NPs as plasmonic material. Their study found that the nanostructure at a particular fluence has yielded higher enhancement in the order of $10^6$ for PA and $10^4$ for RDX. The substrate also demonstrated efficiency in multiplexing along with PCA.[274] Picomolar detection of TNT, RDX, and HMX was reported using Au nanogap substrates.[275] Trimetallic AgAuCu nanostructures obtained *via* femtosecond Bessel beam ablation was tested for the trace detection of PETN and TNT in the nanomolar regime. The nanostructures forming a ladder-like periodic structure showed advantagesadvantages over thethe conventional Gaussian beam-structured surfaces.[276] Podagatlapalli *et al.* have employed Bessel beam ablated Ag nanostructures obtained in water for the sensing of hexanitrohexaazaisowurtzitane (CL-20) with an EF of $10^6$.[277] Laser-ablated Si nanostructures, which yielded periodic structures on the surface, effectively detected 100 nM of 5-amino-3-nitro-1*H*-1,2,4-triazole (ANTA) after coating with gold.[278] Simultaneous detection of explosives mixtures [PA+ 3-nitro-1,2,4- triazole-5-one (NTO) and PA + DNT] has also been reported using picosecond laser structured SERS substrates by Byram and co-workers. Unique Ag nanoribbons were observed during picosecond laser ablation of Ag under cylindrical focusing at a particular fluence, which was further used for explosive sensing with nanomolar sensitivity.[279] Ag NSs fabricated for different angles of incidence during laser ablation have demonstrated femtomolar detection of 1-nitropyrazole (NPZ).[280] Superhydrophobic substrates with Si pillars decorated with ZnO–Ag NPTs were used for the detection of NTO ($\sim 10^{-12}$ M), TNT ($\sim 10^{-12}$ M), and FOX-7 ($10^{-10}$ M), extending their studies to natural samples as well.[281] Ag-decorated ZnO structures were also used to detect ANTA, FOX-7, and CL-20.[282] Syed *et al.* have prepared reusable and cost-effective Cu NSs fabricated by femtosecond and picosecond ablation and have demonstrated trace detection efficiency for CL-20, FOX-7, and ANTA with an EF of $10^5$.[283] Subsequently, hybrid nanoparticles, formed by combining laser-induced nanoparticle-embedded periodic surface structures (LINEPSS) on Si *via* femtosecond (fs) laser ablation followed by 20 nm Ag coating, further improved the EF to $\sim 10^7$ in the detection of ANTA molecule, further improved the EF to $\sim 10^7$ in the detection of ANTA molecule.[284] Using a combination of laser-ablated structures and chemically synthesized gold NSTs, SERS-based detection of ammonium nitrate (AN) has been reported by Rathod *et al.* with μM sensitivity.[285] The mixture of pesticide molecules (thiram and tetrabenazine (TBZ)) was detected using fs laser patterned Si with Au NSTs.[286] Bharti *et al.* have synthesized alloy NPs by a two-step method of laser ablation followed by irradiation, and they were used for the successful detection of PA and AN with EFs ranging from $10^4$ to $10^7$.[287] Core–shell Au@Pd NPs synthesized using the same method were used to detect AN and PA.[288] Xiao *et al.* have used 1-D SPP-supported Ag nanostructures.[289] In contrast, hybrid, recyclable SERS substrates based on $TiO_2$ NRs decorated with Au NRs were used by Samransuksamer *et al.* for the detection of TNT.[290] A new method to enhance the sensitivity of detection using a contactless approach with vigorous dielectric microspheres (DMs) embedded within a PDMS film has been proposed. The method was evaluated using 4-aminothiophenol (4-ATP) as the Raman probe. It significantly improved the detection of dipicolinic acid (DPA), an anthrax biomarker, with a 5.7-fold sensitivity improvement on a solid substrate.[291] A multi-color fluorescent nanoprobe based on $Tb^{3+}$ ion with Au nanoclusters was synthesized to detect DPA with a sensitivity of 3.4 nM and high specificity, making it effective, convenient, simple to operate, and possessing broad application prospects.[292] Low-cost, scalable polyvinylidene fluoride (PVDF)-based Ag NP decorated SERS substrate has been used to detect DPA with a sensitivity of 1 ppm.[293] Femtosecond laser ablated Au NSs decorated with Au NPs were used to detect DPA, DNT, and PA with LODs 0.83 pg $L^{-1}$, 3.6 pg $L^{-1}$, and 2.3 pg $L^{-1}$.[294] Bai *et al.* reported that papain-capped Au NPs tend to undergo well-regulated aggregation upon adding $Hg^{2+}$ ions and DPA, resulting in ultrasensitive detection of DPA without sample pre-treatment and a low LOD of 67.25 pM.[295] A microporous Si substrate coated with an optimized layer of Au was developed by Singh and co-workers for trace detection of PA with LOD in the nM regime, and the enhancement was attributed to the presence of dense hotspot network resulting in coupling between both localized and extended plasmons.[296] Kong *et al.* have demonstrated a highly sensitive photonic crystal-based substrate with diatom frustule and Ag NPs for detecting TNT with $10^{-10}$ M sensitivity. Nanolitre of the analyte molecules was carefully delivered to the hotspot area using inkjet printing, resulting in superior sensitivity.[297] SERS coupled with digital microfluidics (SERS-DMF) has been proposed for highly sensitive and automated detection of explosives with better reproducibility and efficiency with proof of the concept for TNT and NTO with LODs of $10^{-7}$ and $10^{-8}$ M, respectively, by Liu *et al.*[298] Using a simple, inexpensive hydrophobic condensation strategy, biomimetic super-hydrophobic Ag micro/nano-pillar array surfaces were prepared as SERS substrates for ultrasensitive sensing of PA and NTO with picomolar sensitivity.[299] Chemically produced Ag NWs were used to detect perchlorates, chlorates, nitrates, picric acid, and 2,4-dinitrophenol.[300] Monoethanolamine (MEA) based Au NPs were employed to selectively and sensitively detect TNT in real-world samples such as envelopes, luggage, lake water, and clothing, with a detection limit of 21.47 pM by Lin *et al.*[301] AuNR@Ag NCs loaded into bacterial cellulose aerogels were used by Wu *et al.* for sensitive detection of TNT with enhanced selectivity achieved by using 4-ATP resulting in EF of $10^8$.[302] Exotic waxberry-like Au NPs decorated on PDA were fabricated using seed-mediated growth and further used for the detection of DNT by Chen *et al.*[303] Based on Janowsky complex formation of explosives and the SERS of the derivatives, TNT, HNS, and tetryl (2,4,6-trinitrophenyl-n methylnitramine) were detected with a sensitivity of 6.81 ng $mL^{-1}$, 135.1 ng $mL^{-1}$, 17.2 ng $mL^{-1}$, respectively, by Milligan *et al.*[304] To overcome the signal fluctuations in SERS, a deep learning model called neural network-aided SERS has been proposed to bridge the gap between lab and field applications.[305] The model employed a signal-to-noise ratio approach to label the spectra, which were further classified by the model, and accurate predictions were made in out-of-sample testing. With the goal of quantification of trace explosives, a low-cost hydrophobic filter paper has been proposed, coated with silicone oil and using laser-ablated Au NPs. The authors have used PCA and support vector regression to quantify traces of PA with an accuracy of 94% within 10 s.[306] Working under resonance Raman scattering conditionsconditions of an explosive molecule, PA, trace detection (100 nM) was achieved using AgAu nanostructures.[307] Deep learning method based onon the FAB-ResNet and (NLSTM) networks in the successful detection of explosive residues.[308] Detection of bio-hazardous materials has also been reported using SERS-based sensing. With the help of Au-coated Si, nanopillars functionalized with a chemical nerve agent antidote, 4-pyridine amide oxime, selectively and sensitively detect nerve agents Tabun, Cyclosarin, and VX in aqueous solutions. The SERS signals of the analytes distinctly discriminate between specific and non-specific binding down to sub-ppm levels, with binding specific SERS response decreasing in the order of Tabun > VX > Cyclosarin.[309] Self-assembled Au NPs coated with a citrate layer that acted as a trap for probe molecules were used by Lafuente *et al.* for the detection of dimethyl methyl phosphonate (DMMP) in the gas phase, achieving a sensitivity of 130 parts-per-billion.[310] The core–shell structure Au@$ZrO_2$ has also demonstrated excellent applicability for detecting DMMP with an RSD of 6.8% and a durability of 30 days.[311] Using high droplet adhesion that led to a high density of hotspots, femtomolar detection of two nerve agents, VX and Tabun, has been reported by Hakonen *et al.* using flexible Au decorated Si nanopillars and a handheld Raman system.[312] Gas phase detection of DMMP was reported by Lafuente and co-workers using Ag nanoplates on different substrates like Si, stainless steel mesh, and graphite foils with sensitivity down to 2.5 ppmV using a portable Raman spectrometer.[313] Huang *et al.* have demonstrated flexible, uniform cotton swabs coated with Ag NPs that were tagged to detect DMMP specifically have shown good reproducibility of 5.6%, implying practical usage.[314] Electrochemically roughened silver foil has been used to detect two nerve agents, DMMP and DIMP in the vapor phase.[315] Wang *et al.* have shown that by concentrating the molecules in the vital hotspot areas on the SERS substrates, a thin water film-confined SERS strategy was proposed, allowing for the successful detection of DMMP molecules weakly interacting with SERS-active substrates.[316] Wang and co-workers have achieved sensitive and flexible AuNPs@polyimide SERS heating chips and successfully detected nM TNT.[317] There are a few earlier review articles on the technique and materials used for SERS.[318–326]

Trace-level liquid/solid phase detection is essential and highly beneficial for chemical and explosive sensing applications. However, detecting vapor-phase chemicals and explosive compounds is a better solution to overcome the drawbacks of existing physical probing approaches in the present and foreseeable future. It is imperative to create essential technology that facilitates vapor-phase detection of explosive molecules economically with better sensitivity and stability. Explosive vapor sensing has been demonstrated by a few researchers in recent years.[327] The small quantity of DNT that emanates from TNT dominates the vapor headspace and aids as a natural tracer for TNT vapor detection. Therefore, detecting volatile impurities of TNT, such as 2,4-DNT, 2,6-DNT, and 1,3-DNB, is desirable. SERS-active substrates' response time and sensitivity are essential for superior DNT vapor detection. TNT vapor detection is limited due to low vapor pressure. Adhikari *et al.* have achieved rapid and sensitive vapor-phase detection of TNT, DNT, and PETN using nanogap SERS-substrate produced by Au NPs decoration on $SiO_2$ nanopillars and Au layers. The detection capability of TNT, PETN, and DNT for $10^{-9}$ atm., $10^{-11}$ atm., and $10^{-7}$ atm. vapor pressure was estimated at a lower laser power of 0.2 mW, and room temperature.[328] Shabtai and co-workers demonstrated the utility of Au NPs modified quartz fibers for gas phase detection of VX and HD. They reported the least detection for VX, and HD at $\sim$8 ppbv, and $\sim$0.73 ppbv, respectively.[329]

Detection of airborne chemicals and explosive molecules using SERS at a standoff distance (unlike the Raman technique) is challenging owing to the confinement of near-field enhancement. Consequently, very few reports on the SERS studies using standoff configurations exist in the literature. Phan-Quang and co-workers have recently demonstrated the 'first' in-air SERS detection in a standoff configuration (at a distance of 200 cm).[330] They have utilized aerosolized plasmonic colloidosomes as airborne plasmonic hotspots. They prepared a 3D plasmonic cloud (containing $\sim 10^9$ Ag NCs $cm^{-3}$) to detect airborne species (methylbenzenethiol (MBT), rhodamine 6G (Rh6G)), and methylene blue (MB). Zhang *et al.* have demonstrated the possibility of remote chemical detection (4-ATP) using fiber-based SERS substrates. Such studies can be extended to explosives and other hazardous materials.[331] Another exciting work demonstrates the possibility of detecting buried explosives. In this case, they could detect buried explosives (2,4-dinitrotoluene) in simulated field conditions.[332] They claim that the explosives used in landmines are often composed of TNT. Further, its manufacturing impurities include (a) 2,4-DNT, (b) 2,6-DNT, and (c) 1,3-dinitrobenzene (1,3-DNB). A thorough optimization of efficient SERS substrates and appropriate progress in signal collection and detection optics will make it possible to detect buried chemicals (*e.g.*, in sand). Machine learning/deep learning techniques augment the SERS data (wherever there are limitations).[305] A summary of the significant works on SERS-based sensing of explosives reported in recent years is presented in Table 1. In Fig. 8 shows a schematic summary of the SERS-based explosives sensing techniques, materials, and requirements for commercialization, including the future challenges and scope. There is also keen interest in developing novel SERS materials/substrates for detecting explosives.[333–338] For example, Kalasung *et al.* have developed effective Au/ZnO-based sensors to detect PETN.[339] Their sensors exhibited an optimal performance at $10^4$ g $mL^{-1}$ while the LOD was $10^{-7}$ g $mL^{-1}$ with an EF of $3.01 \times 10^6$. As discussed elsewhere, flexible SERS substrates are essential for various applications wherein the analyte available is too small and cannot be transported to the lab.[338] These substrates facilitate swabbing and collecting the trace analyte molecules from any uneven surface, and further, with the help of a portable Raman spectrometer, can be used to identify the molecule. With advancements in the preparation of novel, efficient, versatile SERS substrates and in the development of miniature spectrometers, explosive sensing is expected to become cost-effective and practical in the near future.

Table 1 A comprehensive summary of the recently reported works on SERS-based detection of trace explosives and chemical warfare simulants

| S. No. | Target molecules | SERS substrates | Preparation technique (s) | LOD | Ref. | Comments |
|---|---|---|---|---|---|---|
| 1 | RDX (1,3,5-trinitroperhydro-1,3,5-triazine) | Au NRs with Ag NPs | Chemical reduction | 0.39 mg $L^{-1}$ | 255 | RDX + HMX sensing in clay soil *via* UV-Visible and SERS |
| | | Triangular Au NPTs | Self-assembly of Au NPTs onto functionalized glass coverslip, followed by transferring it onto to a flexible adhesive substrate | 50 ppq | 261 | Detection of explosive residues from fingerprints left on solid surfaces |
| | | 2D-titanium nitride ($Ti_2NT_x$) (MXene) | Chemically synthesized and deposited on paper, silicon or glass | 1 μM | 256 | The performance of different substrates was compared. |
| | | Silver NCs | Polyol method | 1 nM | 268 | Enhancement factor (EF) $\sim 9.2 \times 10^{10}$ |
| | | AuAg film on glass | Sputtering | 40 pg | 271 | Distinction of explosive using PCA |
| | | Ag Nano dendrites (NDs) | Electroless etching process | 5 μM | 272 | $EF10^4$ |
| | | Ag NPs decorated-rGO substrate | rGO-modified Hummers' method; Ag NPs-*in situ* reduction | $10^{-12}$ M | 257 | The size of Ag NPs was around 20 nm and EF was $\sim 1.6 \times 10^9$ |
| | | Si micro squared arrays with AgAu alloy NPs | fs laser ablation | 1 μM | 274 | EF $\sim 10^4$ |
| | | Au nanogap | e-beam evaporation | 10 pM | 275 | Picomolar detection of TNT, RDX, and HMX |
| | | Ag–Au alloy NPs | ps laser ablation | 100 nM | 263 | Filter Paper loaded with NPs |
| | | Au-coated GaAs nano-ripple | fs laser ablation in liquid | 10 μM | 340 | 70 nm ripples |
| 2 | HMX (Cyclotetramethylene-tetranitramine) | TriangularAu NPTs | Self-assembly of Au NPTs onto functionalized glass coverslip, followed by transferring it onto to a flexible adhesive substrate | 0.61 mg $L^{-1}$ | 261 | Direct detection on a benchtop Raman system |
| | | 2D-titanium nitride (MXene) | Chemically synthesized and deposited on paper, silicon or glass | 1 μM | 256 | The performance of different substrates was compared. |
| | | Au NPs | Iterative hydroxylamine seeding method | $8.1 \times 10^{-6}$ M | 269 | ng sensitivity using a portable Raman spectrometer |
| | | Ag NPs decorated-rGO substrate | rGO-modified Hummers' method<br>Ag NPs: *In situ* chemical reduction | $10^{-12}$ M | 257 | 20 nm Ag NPs, EF $\sim 1.6 \times 10^9$ |
| | | Ag nanotubular arrays | Axicon-generated femtosecond Bessel beam ablation in air | 5 μM | 341 | TNT (50 nM), tetryl (50 nM), RDX (500 nM), superior RSD values, and enhancement factors of $\sim 10^6$ |
| 3 | PETN (Pentaerythritol tetranitrate) | 2D-titanium nitride (MXene) | Chemically synthesized and deposited on paper, silicon or glass | 1 μM | 256 | The performance of different substrates was compared. |
| | | Au nanogap | e-beam evaporation | 10 pM | 275 | Picomolar detection of TNT, RDX, HMX |
| | | Au NPs on quanrtz or glass fibers or polyurethane sponges | Iterative hydroxylamine seeding method | $1.5 \times 10^{-6}$ M | 269 | Detection of vapors using portable Raman spectrometer |
| | | AgAuCu | fs laser ablation | 500 μM | 276 | Laser-induced induced AgAuCu periodic surface structures |
| 4 | Fox-7 (1,1-diamino-2,2-dinitroethylene) | ZnO//Ag mesoporous nanosheetn on Si micropillars | Atomic layer deposition, chemical bath deposition, ion-sputtering | $10^{-9}$ M | 281 | Mesoporous<br>Nanosheets on a Si micropillar array |
| 5 | CL-20 (Hexanitrohexa-azaisowurtzitane) | Ag/ZnO nanostructures | Thermal oxidation | 10 μM | 282 | EF $\sim 10^4$ |
| | | Ag NPs | Laser ablation in liquid (LAL) | 5 μM | 277 | ~2 ps and ~40 fs, 800 nm; Axicon (base angle = 25°). LAL in distilled water with Bessel beam focusing |
| | | Cu NPs | Laser ablation in liquid (LAL) | 5 μM | 283 | ~2 ps and ~40 fs, 800 nm; axicon (base angle = 25°); pulse energy 25–400 μJ; LAL in acetone with Gaussian beam focusing |
| 6 | Ammonium nitrate (AN) | Ag NDs | Electroless etching process | 1 μM | 272 | EF$\sim 10^4$ |
| | | Ag NPs with Au NSTs | Ag NPs-ps laser ablation<br>Au NSTs-chemical reduction | 5 μM | 285 | Bessel beam-axicon lens (base angle of 10°) |
| | | Ag–Cu NPs | fs laser ablation | 5 μM | 287 | EFs ranging from $10^4$ to $10^7$ |
| | | Au decorated Ag NDs | Electroless etching process | 100 nM | 273 | Wafer-scale synthesis. Low-cost and high durability |
| | | Shell-wrapped core@shell Au@PdNPs | Pulsed laser ablation | 0.5 μM | 288 | Analysis of EFEF for different morphologies |
| 7 | TNT (2,4,6-Trinitrotoluene) | Ag sinusoidal nanograting | $SiO_2$ nanogratingn by two-beam interference (266 nm) followed by Ag evaporation | $10^{-5}$ M | 289 | 1-D SPP-supported Ag nanostructures |
| | | $TiO_2$ NRs with Au NPs | $TiO_2$ NRs: electron-beam evaporation with glancing-angle deposition | $10^{-7}$ M | 290 | Hybrid and recyclable substrates |

Table 1 (*continued*)

| S. No. | Target molecules | SERS substrates | Preparation technique (s) | LOD | Ref. | Comments |
|---|---|---|---|---|---|---|
| | | | Au NPs: deposition–precipitation | | | |
| | | Triangular Au NPTs | Self-assembled Au TNPTs on amine-functionalized glass, transferred to a flexible adhesive substrate by the stamping technique | 900 ppq | 261 | Direct detection on a benchtop device |
| | | Photonic crystal biosilica with Ag NPs | *In situ* growth | $10^{-10}$ M | 297 | Analyte delivered to the hotspot area using inkjet printing |
| | | Au nanogaps | Electron beam evaporation | 1 pM | 275 | pM detection of TNT, RDX, and HMX |
| | | Flexible PET nanocones with Au coating (30 nm) | Colloidal lithography and oxygen plasma etching | $10^{-13}$ M | 265 | Trace detection ($10^{-10}$ M) on cloth bag |
| | | Nanowrinkles@ micro (zigzag, coral, rectangular) patterned PDMS – Au film/Ag NPs | UV photolithography, oxygen plasma and stretching treatment – Au deposition by electron beam | $10^{-13}$ M | 266 | Trace detection ($10^{-9}$ M) on cloth surface |
| | | Au NPs | Chemical reduction | $1.1 \times 10^{-7}$ M | 269 | Au NPs on quartz fibers or polyurethane sponges to detect vapors using a handheld device |
| | | Pyramid AgFe NPs embedded rGO | rGO: Hummers' method<br>AgFe: chemical method | μM | 260 | TNT in an envelope, luggage, lake water, and clothing |
| | | MEA—modified Au NPs | Chemical methods | 21.47 pM | 301 | TNT in an envelope, luggage, lake water, and clothing |
| | | AuNR@Ag NCs on cellulose aerogels | Chemical methods | $8 \times 10^{-12}$ g $L^{-1}$ | 302 | *p*-ABT modified substrates to complex TNT *via* Meisenheimer complex formation |
| | | Ag nanoribbons | PS laser ablation | 25 nM | 342 | Cylindrical focusing |
| | | AuNPs@ polyimide heating chips | Liquid–liquid self-assembly; sandwich structure | $10^{-9}$ M | 317 | *In situ* collection and detection of TNT in complex environments soil, cloth, fruit |
| | | Digital microfluidic device with Ag NPs | Chip fabrication technique | 100 nM | 298 | Tested for real-world samples and proved good accuracy |
| 8 | DNT (2,4-Dinitrotoluene) | Polydopamine-Au nanowaxberry | Seed-mediated synthesis | 1 μM | 303 | DNT spiked in environmental water and methanol |
| | | AgAu NPs on filter paper | fs laser ablation | 1 μM | 267 | Optimization of the soaking time and studied the effects of NaCl concentration |
| | | Ag NCs | Polyol method | $10^{-15}$ M | 268 | Detected DNT vapor in a sealed container |
| | | Diatom photonic crystals and core–shell Au@$SiO_2$ NPs | Chemical methods | 10 ppb | 270 | DNT vapor using stagnant vapor and vapor flow chambers |
| | | Ag NPs/rGO hybrids | rGO: Hummers' method<br>Ag NPs: Chemical method | $10^{-12}$ M | 259 | Dual benefit of chemical and EM enhancement |
| | | Au NSs (linear and crossed pattern) | fs laser ablation in air | 3.6 pg $L^{-1}$ | 294 | Detection of DPA, DNT and PA with LODs 0.83 pg $L^{-1}$, 3.6 pg $L^{-1}$ and 2.3 pg $L^{-1}$ |
| 9 | Tetryl (2,4,6-trinitrophenyl-n methylnitramine) | Ag NPs | Chemical reduction | 17.2 ng $mL^{-1}$ | 304 | Detection *via* formation Janowsky complex with 3-mercapto-2-butanone |
| | | Laser-induced AgAuCu periodic nanostructures | fs laser ablation | 200 nM | 276 | Ladder-like NPs |
| | | Au NPs@Ag NDs | Electroless deposition | 100 nM | 305 | |
| | | Au-coated GaAs periodic surface structures<br>Au deposition and annealing | GaAs: fs laser ablation in air | $10^{-5}$ M | 343 | EFEF $\sim 10^4$ |
| 10 | Dipicolinic acid (Pyridine-2,6-dicarboxylic acid) | Au NSs (linear and crossed pattern) | fs laser ablation in air | 0.83 pg $L^{-1}$ | 294 | Detection of DPA, DNT and PA with LODs 0.83 pg $L^{-1}$, 3.6 pg $L^{-1}$ and 2.3 pg $L^{-1}$ |
| | | Au NP | Chemical reduction | 0.01 ppb | 295 | 30–100 nm NPs. Controllable aggregation upon addition of $Hg^{2+}$ ions and DPA |
| | | Au nanoclusters | Chemical reduction | 3.4 nM | 292 | Hybridization of $Tb^{3+}$ ion |
| | | Ag NPs doped PVDF | Suction filtration | 1 ppm | 293 | PVDF pretreated with various solvents and NaCl |
| | | Ag NPs with nitrogen and nitrogen–Sulphur with GO | GO: Hummers' method<br>Ag NPs: chemical methodmethod | 0.01 ppm | 258 | Nanomolar sensitivity |

Table 1 (*continued*)

| S. No. | Target molecules | SERS substrates | Preparation technique (s) | LOD | Ref. | Comments |
|---|---|---|---|---|---|---|
| | | Dielectric microspheres in PDMS film with Ag NPs | Modified photolithography | 0.1 μM | 291 | Proposed a new method called DSERS-based on dielectric materials |
| 11 | ANTA (5-amino, 3-nitro, -1*H*-1,2,4-nitrozole) | Au-coated laser-induced Si periodic surface structures | ps laser ablation | 100 nM | 278 | Focused airy pattern of the p-polarized laser |
| | | Ag plating on Si LINEPSS structures | fs laser ablation in acetone | 1 μM | 284 | SERS efficiency was improved by Ag/Au NP deposition on LINEPSS |
| 12 | NTO (3-nitro-1,2,4-triazol-5-one) | Mesoporous ZnOAg nanosheets on Si micropillar array | Atomic layer deposition, chemical bath deposition, ion-sputtering | $6 \times 10^{-12}$ M | 281 | SERS efficiency was improved by Ag/Au NPNP deposition on LINEPSS |
| | | AgAu NPs on filter paper | fs laser ablation | 10 μM | 267 | Detected TNT, NTO, FoX-7 ($10^{-8}$ M) in real-world samples, like river and tap water |
| | | Digital microfluidic device with Ag NPs | Chip fabrication technique | 10 nM | 298 | Optimization ofof the soaking time and studied the effects of NaCl concentration |
| | | Superhydrophobic Ag micro/nano-pillar array | Electrochemical deposition on structured Si | $10^{-13}$ M | 299 | Tested on real samples and proved good accuracy |
| 13 | 1-Nitropyrazole (NPZ) | Metal NSs | Laser ablation | fM | 280 | Different angles of incidence during laser ablation have been studied |
| 14 | Urea nitrate (UN) | Au NPs | Chemical reduction | $9.2 \times 10^{-4}$ M | 269 | Au NPs on quartz fibers or polyurethane sponges were used to detect vapors using a handheld spectrometer |
| 15 | Dimethyl methyl phosphonate (DMMP) | Cotton swab with Ag NPs | ATS—incorporated Ag NPsNPs later. Ag NPs: *in situ* chemical reduction ($NaBH_4$) | 1 g $L^{-1}$ | 314 | Flexible and reproducible |
| | | Citrate-stabilized Au NPs | Chemical reduction and self-assembly | 130 ppb | 310 | Gas phase detection |
| | | Core–shell Au@$ZrO_2$ NPs | Chemical reduction | 100 mg $kg^{-1}$ | 311 | Also detected methyl parathion and triazophos at 0.01 mg $kg^{-1}$. On orange peel, LOD of 0.5 and 0.1 mg $kg^{-1}$, respectively |
| | | Au micro/NSs bowl-like array | Electrodeposition | $10^{-3}$ mol $L^{-1}$ | 316 | Better signal at slower evaporation and stronger excitation power |
| | | Ag NPTs | Chemical reduction | 2.5 ppm V (14 mg $m^{-3}$) | 313 | Gas phase measurements using a portable Raman spectrometer |
| 16 | DIMP (Diisopropyl methylphosphonate) | Silver oxide | Electrochemical | 0.3 torr | 315 | Detection of DMMP vapor at 1.6 torr |
| 17 | VX (*O*-ethyl *S*-diisopropylaminomethyl methylphosphonothiolate), TABUN | Au-coated Si nanopillars | Lithography and reactive ion etching | ~13 and ~670 fmol | 312 | Flexible Au-decorated Si nanopillars and a handheld Raman system |
| | | Ag/Au-coated Si nanopillars | mask-less lithography process and electron beam evaporation | 0.4 μM for VX | 309 | Binding-specific SERS response decreases in the order: Tabun > VX > Cyclosarin |

LOD: limit of detection. LCD: lowest concentration detected. EF: enhancement factor. NP: nanoparticle. NPT: nanoplate. NC: nanocube. NR: nanorod. NS: nanosphere. NST: nanostar. ND: nanodendrite. LINEPSS: laser-induced NP-embedded periodic surface structures. PCA: principal component analysis. PVDF: Polyvinylidenefluoride. *p*-ABT: *p*-amino benzenethiol. ATS: N1-(3-trimethoxysilylpropyl) diethylenetriamine. MEA: Monoethanolamine.

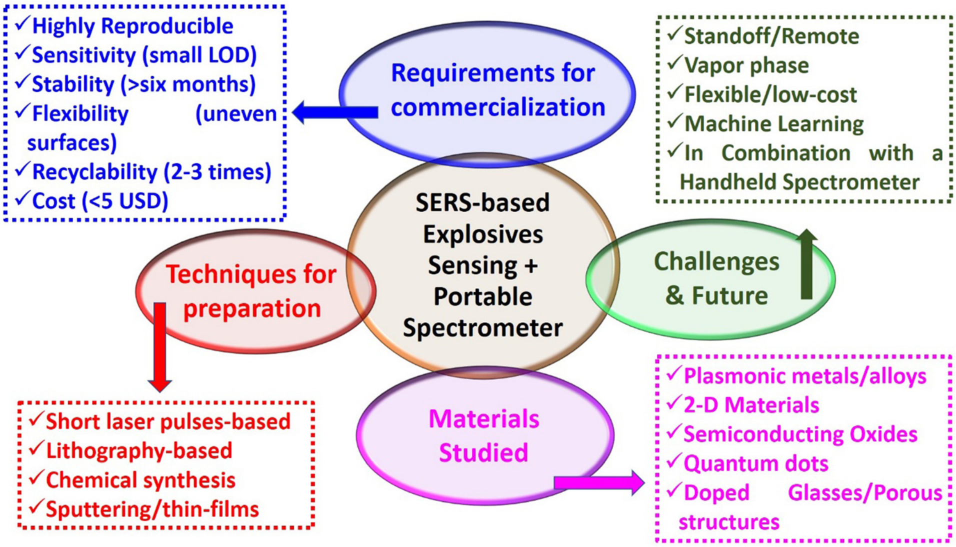
✓Highly Reproducible
✓Sensitivity (small LOD)
✓Stability (>six months)
✓Flexibility (uneven surfaces)
✓Recyclability (2-3 times)
✓Cost (<5 USD)
Requirements for commercialization
✓Standoff/Remote
✓Vapor phase
✓Flexible/low-cost
✓Machine Learning
✓In Combination with a Handheld Spectrometer
Techniques for preparation
SERS-based Explosives Sensing + Portable Spectrometer
Challenges & Future
✓Short laser pulses-based
✓Lithography-based
✓Chemical synthesis
✓Sputtering/thin-films
Materials Studied
✓Plasmonic metals/alloys
✓2-D Materials
✓Semiconducting Oxides
✓Quantum dots
✓Doped Glasses/Porous structures

Fig. 8 A schematic summary of the SERS-based explosives sensing techniques, materials, and requirements for commercialization, including the future challenges and scope.

**3.4.2. Ionic species.** The application of SERS in the direct detection of ionic species faces significant limitations, primarily due to their small Raman scattering cross-section or the absence of vibrational modes in atomic species. Despite the availability of alternative characterization techniques, such as absorption or emission spectroscopy for metal cations, which boast detection limits in the picomolar range, these methods often necessitate large sample amounts and are inherently destructive. In contrast, SERS spectroscopy offers a non-destructive approach that requires a small sample volume. Consequently, over the past few decades, numerous indirect SERS strategies have been developed to selectively detect and quantify various ionic species. The success of the detection of ionic species mostly depends on the specific characteristics of the ionic species, the metal nanostructures used, and the experimental conditions.

*3.4.2.1. Metallic cations.* Metallic cations, as atomic species, cannot be detected directly by SERS. However, different indirect SERS strategies have been developed for the selective and sensitive detection of metallic cationic species. Different strategies have been reported for cations such as Cd(II),[344,345] As(III),[346,347] Hg(II),[345,348–350] Pb(II),[350–352] Cu(II),[352] and Zn(II),[352] among others. One of the most common strategies involves inducing the aggregation of a colloidal dispersion of plasmonic nanoparticles through the presence of the target metal cation. This process begins with the functionalization of plasmonic nanoparticles, wherein they are initially coated with a Raman-active molecule displaying a specific affinity for the target cation *via* covalent or not covalent interactions. In the presence of the cation, the nanoparticles aggregate, forming hotspots that significantly enhance the SERS signal of the attached Raman-active molecule on the plasmonic surface (Fig. 9a).[347,353] This SERS signal enhancement is directly proportional to the concentration of the target cation, allowing for quantification. However, a key challenge lies in achieving high selectivity, necessitating the careful selection of an appropriate chelation system to avoid undesired interactions. Each system is tailored to a specific metal cation; for instance, Duan *et al.*[344] designed a self-aggregating gold nanoparticle system for the detection of Cd(II), a metal associated with conditions like cancer and cardiovascular diseases. The chelation of Cd(II) is initiated by atom transfer radical polymerization from the nanoparticle surface (SI-ATRP), resulting in immediate nanoparticle aggregation that produces an increase in the SERS signal of the nanoparticle probe. Importantly, this process is selective, as it does not occur in the presence of other cations.

Not all strategies for detecting metallic cation detection *via* SERS involve the aggregation of colloidal metal nanoparticles; some focus on solid plasmonic substrates functionalized with a DNA probe, which undergoes conformation changes in the presence of the target cation leading to a "turn-on/turn-off" SERS response. This approach has been extensively used for quantification of Hg(II). For instance, Chung *et al.*[356] employed a doubly labeled DNA, incorporating a thiol for binding to Au surface and a Raman-active molecule to provide the SERS signal at opposite ends. In the absence of Hg(II), no significant SERS signals are observed, as the Raman-active molecule remains distant from the Au surface. However, the presence of Hg(II) induced a conformational change of the DNA, causing the approximation of the Raman reporter to the surface, leading to the amplification of the SERS signals. Another strategic approach capitalizes on the strong affinity of certain cations for the plasmonic metal surface, as observed in the case of Hg(II) ions and gold. This high affinity prompts the displacement of a pre-assembled Raman-active molecule from the gold surface leading to a reduction in the SERS signal.[354] Moreover, higher concentrations of Hg(II) result in a more substantial replacement of the Raman-active molecule, leading to a further decrease in the SERS signal (Fig. 9b). It is important to note that this method is specifically applicable for identifying cations (or anions) with a pronounced affinity for the plasmonic surface.

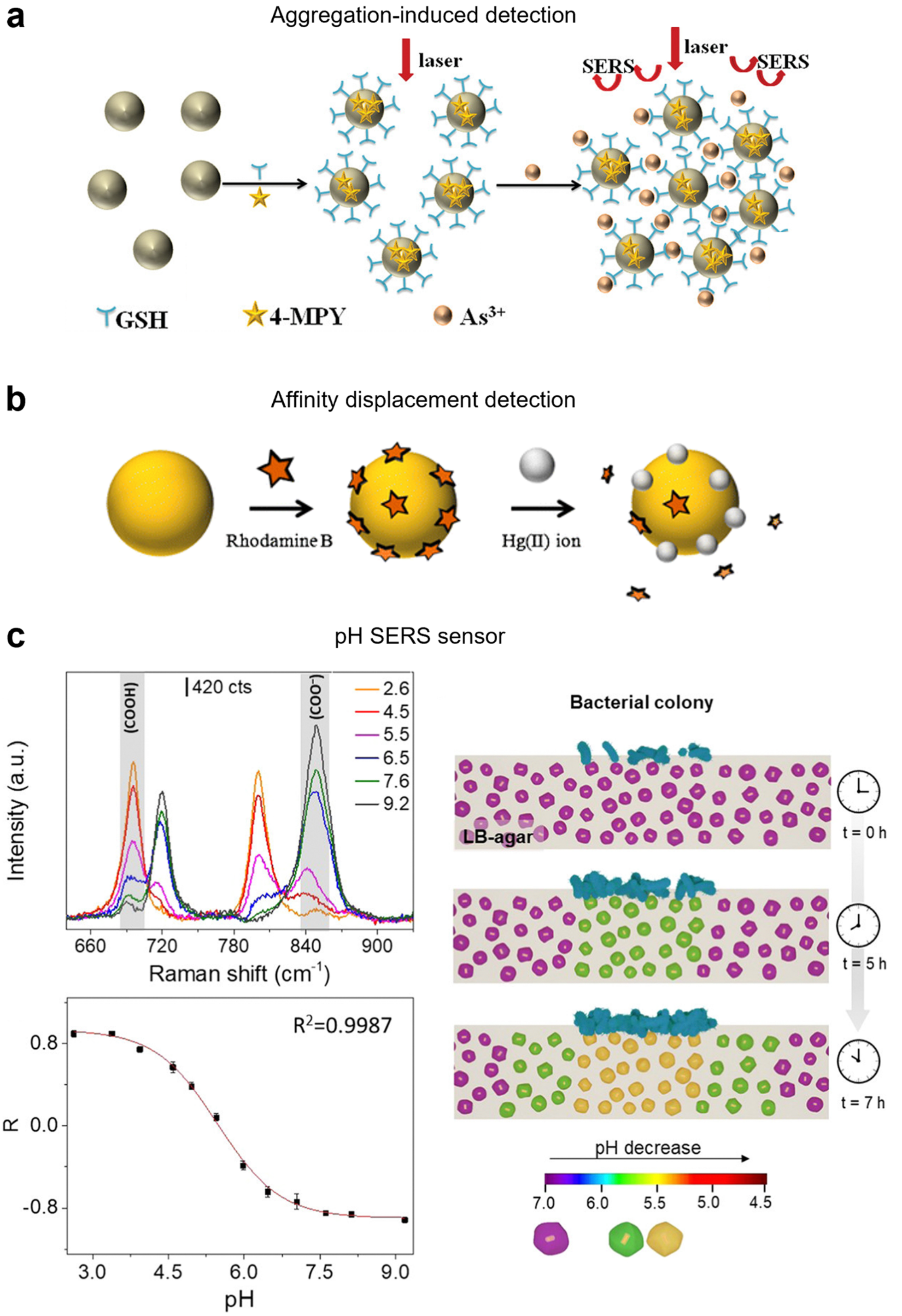
a
Aggregation-induced detection
laser
SERS
laser
SERS
GSH
4-MPY
As3+
b
Affinity displacement detection
Rhodamine B
Hg(II) ion
c
pH SERS sensor
420 cts
(COOH)
(COO-)
2.6
4.5
5.5
6.5
7.6
9.2
Intensity (a.u.)
660
720
780
840
900
Raman shift (cm-1)
R2=0.9987
0.8
0.0
-0.8
R
3.0
4.5
6.0
7.5
9.0
pH
Bacterial colony
LB-agar
t = 0 h
t = 5 h
t = 7 h
pH decrease
7.0
6.0
5.5
5.0
4.5

Fig. 9 Ionic SERS detection. (A) Schematic diagram of the detection of As(III) ion by the aggregation of nanoparticles in function of As(III) concentration. Reproduced from ref. 347 with permission from Elsevier Publication copyright 2020. (B) Schematic representation of the Hg(II) ion sensing mechanism based on the replacement of Rhodamine B molecules through the reduction of Hg(II) ions on the surface of gold nanoparticles. Reproduced from ref. 354 with permission from Springer publication, copyright 2009 (C) representative SERS spectra of 4-MBA at different pHs and experimental calibration curve or ratio $R = (A_{695} - A_{848})/(A_{695} + A_{848})$ as a function of pH. Reproduced from ref. 355 with permission from ACS publication, copyright 2021.

Regardless of the approach taken, the development of a strategy for simultaneous detection and quantification of various cations is a challenge. This challenge becomes particularly pronounced when the accurate quantification of each cation is required. To progress in this field, further exploration is essential, potentially involving the development of intricate plasmonic nanostructures. These nanostructures can integrate various chelation agents customized for each specific cation, resulting in the generation of distinct Raman responses as a function of the bound cation.

*3.4.2.2. Anions.* Similar to cations, atomic anions (such as halogens, $S^{2-}$, $N^{3-}$, *etc.*) cannot be directly detected by Raman. However, unlike cations, the direct or indirect detection of anions is deemed less significant, resulting in less exploration of their SERS detection. A notable exception lies with oxyanions ($SO_4^{2-}$, $ClO_4^-$, *etc.*) and other anions such as cyanide ($CN^-$) or thiocyanate ($SCN^-$) which possess moderate Raman cross-sections enabling their direct detection by SERS. Nevertheless, their limited affinity for plasmonic surfaces presents a challenge for direct detection. To overcome this hurdle, a common strategy involves functionalizing the plasmonic substrate to render it positively charged. This modification induces an electrostatic attraction, drawing the anions into close proximity with the SERS substrate, thus facilitating their detection. Du *et al.*[357] employed this strategy to successfully detect anions in water. They modified Ag-based SERS substrates with amino and amide groups to create a positively charged surface, enhancing the substrate's affinity for anions such as $SO4^{2-}$, $CN^-$, $SCN^-$, and $ClO_4^-$. As a result of this functionalization, the detection limits reached the ppb regime, showcasing the effectiveness of this approach in improving sensitivity for anion detection. It should be noted that while there are numerous approaches to detecting metallic cations, the methods for characterizing anions are comparatively fewer. This discrepancy likely arises from the lower perceived significance and demand for their detection and quantification.

*3.4.2.3. $H_3O^+/HO^-$ ions.* The quantification of the $H_3O^+/HO^-$ ions holds significant importance in biological systems due to the implications of pH. Understanding pH is paramount as its value profoundly influences the functionality of cells and organisms across myriad facets. In numerous applications, the necessity for straightforward, intuitive, sensitive, and stable pH detection, encompassing both acidic and basic characteristics inside and outside the cell, is indisputable. Moreover, SERS pH sensors offer the advantage of *in situ* real-time pH monitoring in a non-invasive and non-destructive manner. Halas *et al.* were the first to report the effect of the pH medium on the Raman signal of the 4-mercaptobenzoic acid (4-MBA) due to the partial ionization/deionization of the carboxylic group,[358] converting this Raman active molecule in a pH indicator that was used for the development of different pH sensors. However, while 4-MBA can accurately predict pH values within the range of 5.0 to 8.0 (Fig. 9C),[355] its limited coverage is insufficient for various applications. Consequently, alternative molecules with broader pH ranges have been explored. These include 3,5-dimercaptobenzoic acid, ranging from pH 4.0 to pH 8.0;[359] 4-mercaptopyridine, from pH 3.0 to pH 8.0;[360] 4-aminothiophenol, with a range of 3.0 to 9.0;[361] Alizarin Yellow R, covering pH 10.04 to 14.04;[362] among others. However, to date, no SERS pH sensor has been able to cover the entire pH range simultaneously, thus, further investigation is necessary to develop such a sensor.

The literature offers numerous examples of both extracellular and intracellular pH SERS sensors. For instance, De Marchi *et al.*[355] introduced a noteworthy extracellular pH SERS sensor consisting of a mesoporous plasmonic substrate (Au@Ag@m$SiO_2$ nanorattles functionalized with 4-MBA). This substrate allows for the diffusion of metabolites secreted by bacterial colonies, thereby inducing pH variations, which in turn enables the correlation between metabolite production and the corresponding phenotype discrimination. On a different note, Ren *et al.*[363] developed an intracellular pH SERS sensor based on Au NPs functionalized with 4-mercaptopyridine (4-MPy) as the probe molecule and Bovine serum albumin (BSA) to provide biocompatibility and stability. These NPs exhibited exceptional sensitivity from pH 4 to 9, biocompatibility, and stability. This innovative approach facilitates long-term dynamic monitoring of cellular processes and offers the potential for discriminating between normal and cancerous cells based on their pH distribution.

**3.4.3. Gaseous species.** In the XXI century, the key "4S"-sensor performance parameters: sensitivity (*i.e.* LOD), stability (*i.e.* drift, reversibility), speed (*i.e.* response/recovery time) and selectivity (*i.e.* no cross interferences to target response) have gained significant improvements. Nevertheless, the reliable detection of a specific component in a complex environment where other components may interfere remains a challenging task for "the state of the art" chemical microsensors. As Raman scattering analytical technique, SERS enables identification of target molecules in complex mixtures based on their unique molecular vibrational fingerprint in a nondestructive mode and multiplexed manner. Over the last decade, several SERS-based sensing studies have shown the capability for ultrasensitive detection of gaseous species representative of various fields of applications such as environmental pollution,[364,365] chemical threat protection,[366–368] personalized medicine and predictive health-care treatments,[369–371] and food safety screening.[372] The target molecules for these applications are mostly volatile organic compounds (VOCs) like aromatics, aldehydes, biogenic amines, toxic industrial chemicals (TICs) and chemical warfare agents (CWAs).

Detection, identification, and monitoring of ppb to few ppm of toxic and harmful gases in the environment is essential to address societal challenges; but is nonetheless challenging. This means, considering the low density of gases and the SERS surface selectivity, very few molecules per unit volume are available for detection. There are scarce examples of label-free SERS detection of gases, even at ppb level, by direct interaction with the bare metallic surface.[373–379] From a methodological point of view, the conventional approach uses rigid or flexible SERS substrates and gas sampling is performed directly from the environment. The experimental LOD and response time are mainly determined by the "sticking" probability of the target to the SERS substrate, highlighting the importance of proper surface functionalization and fluid-dynamics. The other important facing challenge is the small Raman cross section of the gaseous molecules of interest,[380] *i.e.* poor Raman scattering efficiency, up to 7 orders of magnitude lower than that of standard SERS probes. Thus, although in SERS the rational design of the metallic nanostructure is relevant, in the case of SERS-based gas sensing, the development of strategies for gas molecules confinement near the plasmonic surface is of paramount importance.[381,382]

Different approaches are being applied to bring the detection limits down to relevant levels for practical applications, including: analyte condensation by cooling the plasmonic material,[383] electrodynamic precipitation of targeted charged molecules,[384] the use of 3D matrices for constructing plasmonic nanostructures with efficient access to target analytes,[378,379,385–388] hybridization of noble metal-based SERS active substrates with semiconductors[369,389,390] for the synergetic coupling of EM and charge-transfer (CT) mechanisms, and surface functionalization. By far, functionalization of the metallic surface (see Fig. 10) is the strategy most widely attempted for enhancing the gas adsorption efficiency by means of: (i) capturing probes capable of non-covalent interactions with large Raman cross-section values for being used as reporters,[310,391–393] (ii) ultrathin layers of sensing materials capable for specific adsorption or eventually "*in situ*" reaction with the target molecules provoking a solid transformation,[394,395] (iii) 2D nanomaterials,[389,390] (iv) thin sheets of porous metal oxides[396–398] and (v) the extensively studied and reviewed metal–organic frameworks MOFs(mainly ZIF-8).[364,366,399–405] Special attention deserves the scarcely explored field of metal-oxide-wrapped plasmonic nanostructures. A SERS substrate based on CuO-coated (6 nm thick) Au-wrapped Si nanocone array was validated for the detection of 2-chloroethyl ethyl sulfide (CEES) in 10 min and the lowest detectable concentration was 10 ppbV.[395] The adsorption of CEES molecules on the CuO coating is attributed to the surface-hydroxyl-induced specific binding. Above all, metal-oxide-wrapped metal architecture offers unique opportunities for the development of dual-modal chemoresistive-SERS platforms.[397]

In addition to the preconcentration based SERS signal amplification, MOFs may also impair selectivity by molecular sieving effect, improve the stability of the metal and prevent the EM field decay along the radial direction.[402] Different strategies are described in the literature to unite MOFs with metal nanoparticles for gas detection.[406] The most extended is the encapsulation of individual metallic nanostructures into porous frameworks. As an example, a SERS platform based on a close-packed thin film of Au@Ag NRs individually encapsulated within a ZIF-8 framework has been demonstrated for the detection of chemical weapons in gas phase[366] (see Fig. 11a). Interestingly, the characteristic Raman peak of ZIF-8 at 685 $cm^{-1}$, was used as an internal standard for quantitative detection. The performance with a portable Raman instrumentation was validated for 2.5 ppm of DMMP in ambient air, and 76 ppb of CEES; with response times of 21 s and 54 s, respectively. The SERS substrate showed good stability and reusability by degassing at 200 °C. $H_2S$ detection by Au NBPs encapsulated in ZIF-8 occurred thanks to indirect detection.[401] Before introducing the gas, the peak corresponding to Au–Br (273 $cm^{-1}$) (cetyltrimethyl ammonium bromide is used as a soft template in the synthesis), is observed and after $H_2S$ exposure this peak decreases and at the same time Au–S peak (175 $cm^{-1}$) increases. The dynamic range for detection was 0.13 ppbV to 1300 ppmV. As proof-of-concept demonstration, this SERS substrate was applied to monitor the release of $H_2S$ from spoiled fish samples. Core–shell Ag NC@ZIF-8 nanostructures with cysteamine anchored on the silver surface have been used as SERS probes to build up the Array-SERS chip[407] for benzaldehydes detection (recognized as lung cancer biomarkers). The PDMS chip has a prism array patterned in the microfluidic channel to increase the sticking probability of the gaseous molecules and sensing interfaces and lower the LOD to 1 ppb. Through the specific Schiff reaction, a LOD of 10 ppb for aldehydes was achieved on gold super-particle functionalized with 4-ATP and coated with a thick shell of ZIF-8.[405] Here, MOF shells play an extra role: precluding big gaseous molecules present in complex VOC systems. In an attempt to accumulate more molecules in the proximity of the plasmonic surface for lowering LOD, hollow ZIF-8 wrapped in gold has been recently investigated.[408]

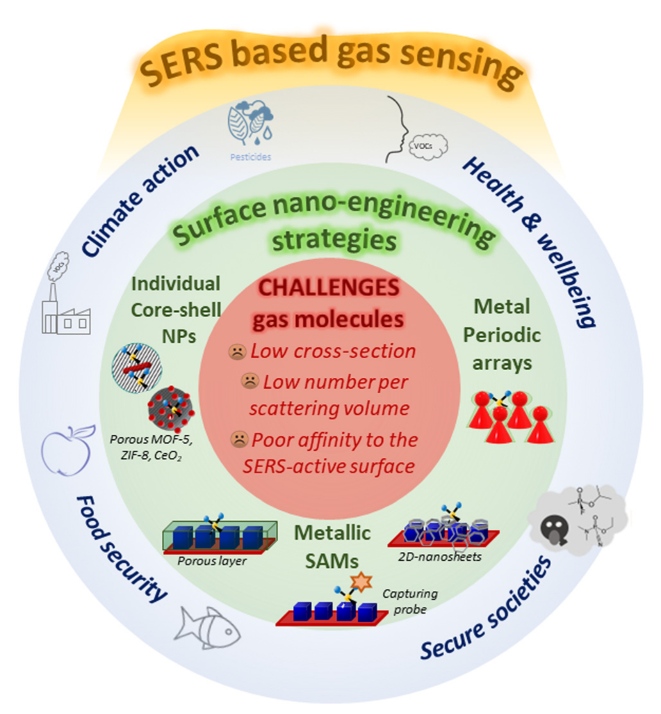

Fig. 10 Schematic illustration of SERS applications for gas sensing with focus on challenges and some of the surface nano-engineering strategies discussed in this section.

Although less investigated, the opposite configuration, coating of nano-porous particles with metallic nanoparticles also leads to plasmonic architectures with remarkable performance. As an illustrative example, the 2.5 ppm LOD of naked MIL-100 (Fe) crystals for toluene (attributed to π–π interactions and CT mechanism) decreased to 0.48 ppb level upon decoration with Au NPs due to hotspots formation.[370] Recently, the detection of DMMP down to the 100 ppb level has been demonstrated with MCM48-Au nanostructures,[398] comprising a spherical MCM48 mesoporous silica particle (1237 $m^2\ g^{-1}$) as core and a matrix of individual Au NPs randomly distributed on its outer surface (see Fig. 11b) The robust, reliable, and reusable SERS platform resulting from the integration of MCM48@Au nanostructured material in a microfluidic Si chip exhibits promising capabilities for on-field application.

The concept of harmful small gaseous molecules detection by ultrathin layer solid transformation enabled SERS was proposed by Bao *et al.*[394] (see Fig. 11c). They found the existence of an optimal thickness of the CuO wrapping layer and Au@CuO nanoparticles film in terms of LOD and response time. The

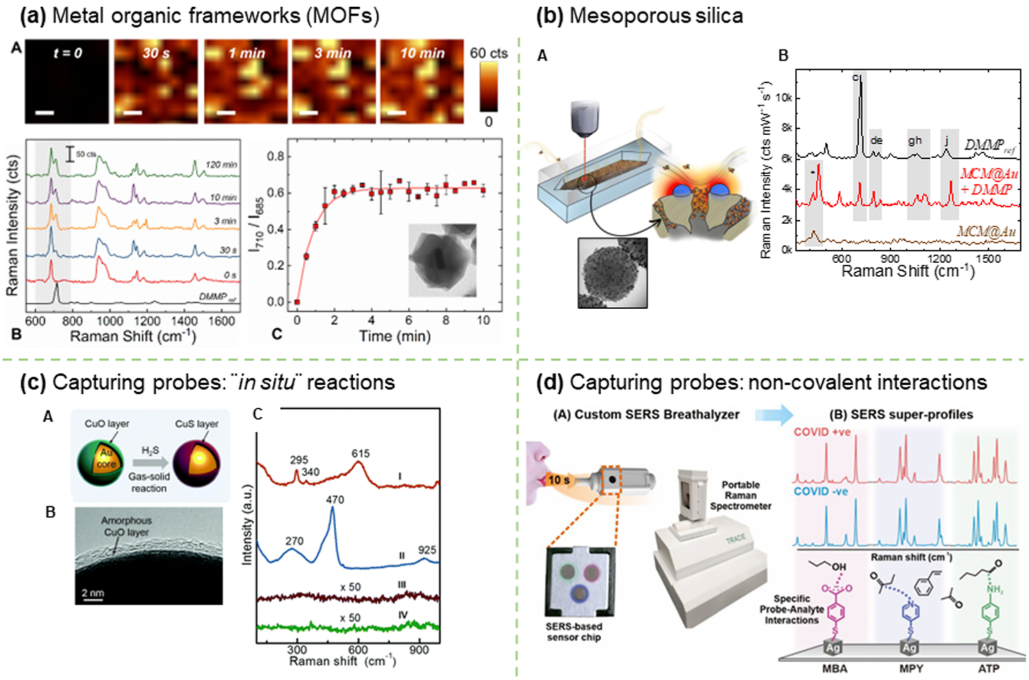

Fig. 11 Strategies for enhancing the gas adsorption efficiency. (a) Metal organic frameworks Reproduced from ref. 366 with permission from ACS publisher, copyright 2021 (A) time-resolved SERS detection of gaseous 2500 ppbV DMMP in $N_2$ using Au@Ag@ZIF-8 thin film as sensing platform: SERS intensity mappings; (B) average SERS spectra obtained from SERS mappings; and, (C) SERS intensity ratio $I_{710}/I_{685}$ between the intensity at 710 cm$^{-1}$ (DMMP) and the intensity at 685 cm$^{-1}$ (ZIF-8) as a function of exposure time. Insertion Au@Ag@ZIF-8 nanoparticle. (b) Mesoporous silica Reproduced from ref. 398 with permission from RSC publisher, copyright 2023 (A) plasmonic mesoporous nanoparticles (MCM@Au) allocated in the microfluidic SERS chip illustrating the preconcentration effect; (B) average SERS spectra of DMMP (2.5 ppmV) recorded on the MCM@Au compared to the Raman fingerprint of pure DMMP and blank MCM@Au. (c) Capturing probes: "*in situ*" reaction Reproduced from ref. 394 with permission RSC publisher, copyright 2020 (A) illustration of the interaction between the Au@CuO nanoparticle and $H_2S$; (B) HRTEM image of Au@CuO; and, (C) Raman spectra of the Au@CuO nanoparticles before (I) and after (II) exposure to $H_2S$ gas (100 ppb) for 10 min, and those corresponding to the Au NPs (III) and CuO NPs (IV) substrates after exposure. (d) Capturing probes: non-covalent interactions, reproduced from ref. 393 with permission from ACS publisher, copyright 2022 (A) Overview of the SERS-based strategy to identify COVID-positive individuals using their breath volatile organic compounds (BVOCs); (B) Representative SERS spectra of each molecular receptor (MBA, MPY, ATP) in the presence of COVID-positive and COVID-negative breath samples.

thickness of the layer has been demonstrated as a crucial parameter in SERS detection for other core–shell structures.[395–397] When exposed to $H_2S$, the CuO layer transforms to CuS with a characteristic Raman peak at 470 cm$^{-1}$. A dynamic range of 0.1 ppb to 1 ppm for $H_2S$ with RSD 8.5% with concentration-dependence pre-processing time (*i.e.* 25 s for 100 ppb of $H_2S$) is found. This versatile concept was extended to other gases, $SO_2$, $CS_2$, $CH_3SH$ and HCl by the addition of ultrathin Cu $(OH)_2$ and ZnO layers and the integration of the SERS substrate on a micro-electro-mechanical heating chip to induce those solid transformations that exhibit higher activation energy. The study of alternative substrates based on a thin CuO layer coated onto gold nanoshell films on a polystyrene sphere monolayer demonstrates the universality of the concept. The proposed strategy based on stable inorganic layers with higher Raman cross-section values is well-adapted to the typical excitation power of portable Raman instruments.

Ling and co-workers have been extensively working on array-based SERS platforms based on Ag nanocubes (AgNCs) with different surface functionalities to combine both chemical capture and physical molecular enrichment strategies. Firstly, MOF thin layers on top of multilayer ensemble of AgNCs[364] were studied due to beneficial EM field enhancement by short-range static dipolar coupling between metallic nanoparticles. Thanks to the preconcentration-based SERS signal amplification, an optimal ZIF-8 thickness of 146 nm was determined, and the resulting platform was successfully tested with polyaromatic hydrocarbons (PAHs) and VOCs. Recently, the same group reported a 91.7% accuracy for multiplex quantification of $SO_2$ and $NO_2$ within the typical composition of exhaust gases. In this case, AgNCs were functionalized with 4-mercaptopyridine and 4-aminophenyl disulfide[392] capturing probes. By introducing additional thiolated receptors, the AgNC SERS platform (32 AgNCs μm$^{-2}$) was successfully applied for flavor quantification in a machine-learning-driven "SERS taster", achieving up to 100% accuracy in an artificial wine matrix, containing 5 different flavors.[409] There are many diseases (diabetes, halitosis, cancer, pulmonary infections including COVID-19) that could be diagnosed by breath analysis, which is simply a non-invasive way of sampling. The same group[393] has developed a multi-probe AgNCs array capable of recording distinct SERS fingerprints after adsorption of exhaled VOCs (see Fig. 11d). Such platform has enabled to identify COVID-19 infected individuals in less than 5 min, achieving >95% sensitivity and specificity across 501 participants regardless of their displayed symptoms.

The simultaneous detection and quantification of 9 VOCs on a single microfluidic platform has been reported by Wang and co-workers.[390] This chip, based on her pioneering work,[407] is composed of a top PDMS layer with a microcolumn premixer and a bottom PDMS layer with 3 SERS detection areas. Each SERS detection unit is a honeycomb-type 3D hierarchical structure coated with core–shell–shell Au@Ag@Au bimetallic NCs, but is distinctively functionalized (nanosheets of $Ti_3C_2T_x$, 2,4-dinitrophenylhydrazine, functionalized $Ti_3C_2T_x$ layer, labelling with Rhodamine 6G). The so-called ''universal gas sensor'' was evaluated in two application scenarios, *i.e.* indoor pollution monitoring and exhaled breath analyses, showing a ppb level detection performance with a dynamic range of three orders of magnitude. In addition, it is quite noteworthy the robustness of the sensing platform, showing a relative standard deviation RSD of 8% in scanned areas of $100 \times 100\ \mu m^2$ besides an RSD of 9% among different chips.

SERS technology for gas detection is a relatively young field, but the last 5 years have seen substantial advances in surface nanoengineering to address the detection performance requirements for closing the gap with real-life applications. Universal concepts and array platforms combined with customized microfluidics chambers, machine learning and affordable handheld Raman equipment, rank SERS gas sensing as a real tool for a broad spectrum of applications with promising market shares. Nevertheless, there still technical aspects to solve, including the gas sampling procedures for on-site sensing,[410] the improvement of SERS instrumentation by means of easy plug-in for focusing on SERS substrates avoiding photothermal effects, the reusability of SERS substrates (assisted by UV light,[377] Raman laser line[411] or annealing[366,398,412]), an important issue for those that involve a certain complexity and significant cost. Future translations into practical workflows would clearly benefit from (i) the unification of optical and fluidic paths to build optofluidic SERS chips for highly effective detection, and (ii) the integration of less selective multiple transduction signals, thus serving to raise the first alarm before waking up the SERS platform.

### 3.4.4. Biomolecules

*3.4.4.1. Nucleic acid (DNA and RNA) biomarker sensing.* SERS has emerged as a powerful analytical technique for the detection of nucleic acids (poly-and oligonucleotides based on DNA and RNA) that can act as important biomarkers in diverse scenarios ranging from clinical diagnosis, bioterrorism, forensic cases, environmental analyses, and food safety.[75,413–418] One of the most established analytical tools for the detection of these markers is PCR and related molecular assays in variously modified forms, such as those involving the next generation sequencing.[75,413,414,419–421] However, the limitations in these methods, namely the prerequisite of specialized settings both in terms of infrastructure and expertise, turnaround time, cross-contamination among samples, and the need for amplification before detection, challenge their ability to be deployed for user-friendly and point-of-care (POC) applications. Thus, faster, and simpler alternative techniques that match the high sensitivity of molecular assays can be of great value for the on-demand sensing of nucleic acid biomarkers. SERS has shown promise in filling this gap by offering ultrahigh sensitivity with the potential to detect even single molecules through the careful design of SERS-active plasmonic nanostructures. Besides, several advantages associated with Raman-based sensing provide a strong justification and rationale for the recent upsurge in seen SERS-based sensors, especially in the context of DNA/RNA detection[422,423] These include the ability to use the Raman reporters (*i.e.*, a dye molecule with a specific Raman signal with narrow bands), the multiplexing ability (*i.e.*, detecting multiple targets simultaneously under a single laser excitation), the relative insensitivity of the Raman signal to environmental conditions (*e.g.*, variation in ambient humidity, oxygen levels, and temperatures), low sample volume requirements, and the ability to monitor Raman signal directly from the whole cells without requiring significant sample processing. Thus, this section aims to capture the recent progress made in the relevant field to date while discussing the challenges encountered during operation with the intent to highlight the prospects of plasmonic NPs for the detection of nucleic acids. The progress in this area is subdivided into two main strategies, including the direct (label-free) and indirect (labeled) detection approaches.

*3.4.4.2. Direct detection approaches.* In the direct approach, the generated Raman signal corresponds to the intrinsic fingerprints of nucleic acids that are brought in proximity to the EM fields enhanced by the plasmonic nanostructures, typically referred to as hotspots. In general, nucleic acids show four distinct Raman spectral regions corresponding to the (i) ring stretching bands at 500–820 $cm^{-1}$ from purines (adenine and guanine) and pyrimidines (cytosine, thymine and uracil); (ii) deoxyribose-linked phosphodiester vibrations at 820–1150 $cm^{-1}$ where symmetric stretching of phosphodioxy ($\nu PO_2^-$) gives rise to distinctive band at *ca.* 1089 $cm^{-1}$; (iii) in-plane ring variation of nucleobases at 1150–1620 $cm^{-1}$; and (iv) superimposition of carbonyl stretching modes at 1620–1720 $cm^{-1}$.[75] These intrinsic modes of nucleic acids are measured by obtaining the average SERS signal over several spots deposited on metallic surfaces (bulk SERS) or those arising from EM-field-activated few scattered locations (few/single-molecule SERS).

The direct SERS-based sensors are straightforward and convenient because of no requirement of fabricating and modifying the system with Raman reporters. However, the output signal highly depends on the effective adsorption and trapping of nucleic acids on hotspots in plasmonic NPs or SERS-active substrates. Therefore, reliable strategies that can enhance these binding events become an extremely important prerequisite for fabricating ultrasensitive and reproducible SERS sensors for the detection of nucleic acids.[424] The use of external linkers such as thiols in DNA that can spontaneously bond to plasmonic metal NPs and surfaces is one of the most broadly employed methods to enhance this binding.[425,426] Since the quality and reproducibility of the SERS signal can be influenced by the conformation (*e.g.*, secondary structures) within nucleic acid molecules and their packing density on the metal surface, a pre-treatment step of, thermal annealing is typically included. This allows nucleic acids to attain a linear confirmation prior to the adsorption on the NPs surface, thus facilitating binding events.[426] Although the reproducibility in the SERS output signal is observed to significantly improve with the use of thiolated DNA, the inherent drawbacks such as dependability of the process on DNA modification (thiolation) increases the cost and complexity of operation. Further, the possibility of non-specific binding of nucleobases on metal surfaces that lead to flattened configuration of nucleic acids on the NP surface rather than their placement in a standing-up configuration (despite the thermal annealing step) challenges optimum hybridization in the presence of the nucleic acid target.[427]

As an alternative strategy, non-specific physical adsorption of non-thiolated DNA on the metal NP surface *via* electrostatic interaction has been attempted.[426,427] This was initially reported with negatively charged Ag colloids and mixing of these NPs with DNA caused displacement of surface ions in NPs to facilitate DNA binding.[427] This was followed by the addition of magnesium sulfate ($MgSO_4$) to promote NP aggregation. The relatively low affinity of sulfate ions towards the Ag surface discouraged the displacement of DNA from Ag NPs even at high $MgSO_4$ concentrations. This allowed to produce a DNA sensor with a single base mismatch in a 24-mer short nucleotide sequence with a sensitivity of $10^{-6}$ M and a high signal-to-noise (S/N) ratio.[427] Subsequently, the same group attained an improved sensitivity ($10^{-9}$ M) and reproducibility to detect single-stranded (ssDNA) and double-stranded (dsDNA) using negatively charged Ag and Au colloids.[428] Further, since the calibration of sensor baseline is a hallmark for reliable target analyte quantification, efforts have been made to employ the signal from the phosphate backbone of DNA as an internal standard to calibrate absolute signal using iodide-modified Ag NPs and $MgSO_4$ in which iodide ions were proposed to function as a cleaning agent.[424]

Another important aspect of biomolecular detection is the ability to detect secondary structures, as these structures may play important functional roles in various biological processes. An aggregation-based method was described involving citrate-capped Ag NPs and aluminium ions (an aggregation agent) to distinguish the tetramolecular i-motifs (four-stranded DNA structure produced by cytosine-rich sequences) and G-quadruplexes (guanine-rich oligonucleotides) with high sensitivity.[429,430] The same group could also discriminate among the four nucleotide bases in DNA (A, T, C, and G) and specific structures of DNA (dsDNA, triple-stranded DNA, and G-quadruplex) with high sensitivity and reproducibility using core–shell Au@Ag particles as the enhancer of Raman signals and $Ca^{2+}$ ions as the aggregation agent.[431] Similarly, titanium ions (as an aggregation agent) and dichloromethane (as an interfacial agent) have been employed for the fabrication of a label-free SERS sensor for the detection of micro-RNAs (miRNA)[432] and DNA.[433]

It is reflected from the above examples that the use of different aggregation agents has remained a common underlying strategy when non-thiolated nucleic acids are employed to capture the target nucleic acid in direct SERS-based sensing strategies. Despite the progress made in aggregation-based direct SERS sensors, the addition of external aggregating agents leads to inconsistent aggregation since the trapping of the target nucleic acid in these aggregates relies on numerous interconnected experimental variables, including the concentration and the type of salt, mode and time of physical mixing, and the sequential order in which the reagents are added during the assay. To address such challenges, a microfluidic chip which provides control over the reagent movements and aggregation in the NPs was proposed.[434] The method could detect unlabeled polyadenosine and polycytosine RNA oligonucleotides selectively using nanolitre volume of the samples.

The aggregation agents-free and label-free sensors for DNA and miRNA have also been reported.[435–437] One such method involved the use of positively charged spermine-coated Ag NPs that acted as an "electrostatic glue" to adhere DNA on the NP surface. The adsorbed DNA promoted the clustering in NPs, thus trapping DNA on hotspots to deliver vibrant SERS signals. The distinctive difference in the signal with and without the target DNA served as the basis for the sensor which could detect DNA with nanograms per millilitre sensitivity.[435] The same group employed microfluidics to enhance sensitivity to picograms level[436] and achieved quantification of the base composition in ssDNA and dsDNA.[437] The key highlights of these studies are that these did not require pre-amplification and pre-treatment steps, while achieving good sensitivity with a minute amount of the sample.

Even though the above methods could distinguish either one or more nucleotides in the DNA sequences, the presence of the same four nucleotide bases on the target DNA still pose challenges with the identification of specific SERS signals from the target after its hybridization with the capture probe. To overcome this challenge, the adenine base in the capture probe DNA was substituted with 2-aminopurine and the adenine signal which was presented solely in the target DNA could be detected using SERS.[438] However, post-modification DNA showed tilted orientation and thus hindered the interaction of all adenine bases with the substrate, limiting the efficacy in SERS detection to less than 5 nm from the surface. To address this issue, peptide nucleic acid (PNA), an artificially generated DNA analogue that contains a pseudo-peptide polymer instead of the deoxyribose phosphate backbone in DNA was used as the capture probe on a glass slide.[439] The PNA molecules are uncharged in nature and consist of a flexible polyamide backbone and thus provide a faster hybridization rate and resistance to biological degradation. The hybridization of PNA with the target DNA results in a net negative charge which could facilitate the binding of silver ions to produce Ag NPs *in situ* through a chemical reaction between $AgNO_3$ and hydroquinone. This Ag enhancement effect was employed to produce a powerful SERS signal.[439]

Further, the use of amplification techniques which can amplify signal by altering the length of the nucleic acid fragments was also exploited to enhance the signals in direct SERS-based DNA and RNA sensing.[440] A recent study evinced the use of iodide-modified Ag NPs and magnetic beads with duplex-specific nuclease (DSN)-based signal amplification for the detection of miRNAs.[440] In this method, magnetic NPs with capture probes first hybridized with the target miRNA, followed by DSN-mediated cleavage in the formed DNA–RNA duplex that resulted in the release of miRNA to progress rehybridization with another probe. This step, subsequently followed by cyclic amplification released a higher number of nucleotide fragments from capture DNA to supernatant. The direct relationship between the total phosphate backbone (abundant nucleotide) in the supernatant with miRNA concentration was successfully utilized for the detection of miRNA-21 with a LOD of 42 aM. Furthermore, tip-enhanced Raman scattering (TERS) has also evolved as a promising tool for direct SERS-based DNA and RNA detection with superior performances and achieving single-molecule detection.[441]

*3.4.4.3. Indirect detection approaches.* Although the simplicity of experimental procedure for the direct SERS sensing is appealing, indistinguishable signals in the case of complex sample matrices, structural complexity of nucleic acid fragments, reliance on the surface chemistry of plasmonic nanostructures that modulate their affinity to nucleic acids, and the relatively low signal from the target molecules still pose challenges in the real-time applicability of the direct SERS methods.[413] To overcome such challenges, an indirect SERS-based strategy has been approached. The method typically involves the use of a Raman reporter as a label and measuring the signal corresponding to the distance between the Raman reporter and SERS-active surface as an indirect estimate of the targeted nucleic acid. The Raman reporter has been integrated in a variety of interesting approaches with a common criterion that the signal intensity of the Raman reporter should offer a direct relationship with the concentration of DNA/RNA of interest.

Sandwich-type construction is one of the broadly used approaches for indirect SERS sensors that uses capture DNA and reporter DNA probe with a Raman reporter. Both DNAs are partially complementary to different regions of the target DNA, which allows the creation of a capture-target-reporter sandwich-type structure post-hybridization. The use of this approach for the determination of six DNA targets, including the hepatitis A virus, Vall7 polyprotein gene, hepatitis B virus surface antigen gene, human immunodeficiency virus, Ebola virus, variola virus, and *Bacillus anthracis* protective antigen gene has been reported.[442] The study employed a chip in a microarray format on which the capture strand that was partially complementary to the target DNA was immobilized. The sensor also utilized Au NP nanoprobes modified with Raman reporter and oligonucleotide sequences that could specifically bind to the target DNA of interest. When the sample was exposed to the chip, the target DNA in the sample could hybridize with the capture probes on the chip, which was followed by the hybridization of Au NP nanoprobes using the overhanging region in the capture-target duplex. Washing steps post-hybridization eliminated the unbound nanoprobes and red colour (visible to the naked eye) was detected at high target concentration (pico to nanomolar). The use of Ag enhancement in which Ag NPs grew as a signal-enhancing layer on the surface of nanoprobes further improved the sensitivity (high attomolar and mid picomolar). Subsequently, the same group highlighted the application of a similar approach for multiple DNA detection in which chips were replaced with glass beads to provide a random-array approach for efficient hybridization kinetics, facile operation, and relatively lower production cost.[443] Besides Ag enhancement, the exploitation of numerous nanostructures with different EM enhancement factors has been reported for DNA and RNA sensing using this sandwich-type construction. This includes the use of silicon nanowires decorated with *in situ* grown Ag NP,[12] *in situ* Ag NP on silicon wafer,[444] Au particle-on-wire,[445] probe-tethered Ag NP,[446] Ag NP deposited silica-coated poly(styrene-*co*-acrylic acid) core,[447] and Au NP decorated graphene.[448]

In addition to the microarray format, modification of plasmonic NPs with the capture probes that are complementary to the target at various locations has also been reported for sandwich-type indirect SERS-based sensing of nucleic acids.[449,450] In such cases, in the presence of the target nucleic acid, capture probes hybridize with the target nucleic acid and create links between plasmonic NP. This gives rise to controlled plasmonic coupling in NPs (with and without nucleic acid target), and subsequent determination of the attached Raman reporter at different locations provides an indirect SERS response Further, the use of magnetic NPs in these systems has also seen to provide additional benefits to facilitate cleaning/separation (washing step) of the capture-target-reporter hybrids from the reaction mixture and concentrating the samples to achieve a strong SERS signal.[451–454]

Fabrication of a SERS-based lateral flow device (LFD) using this sandwich-type method has also been established for detecting DNA related to human immunodeficiency virus type 1 (HIV-1).[455] This development could overcome the relatively lower sensitivity in colorimetric LFDs and provided one step closer to practical real-time sensing of DNA using the SERS-based method. The device showed excellent sensitivity of 0.24 pg mL$^{-1}$, which was claimed to be at least 1000 times greater in comparison to the known colorimetric and fluorometric methods for HIV-1 detection. The same group evinced the multiplexing ability in LFDs by detecting two DNAs related to Kaposi's sarcoma and bacillary angiomatosis with superior sensitivities.[456] The intrinsic benefits from multiplexing, high sample throughput, low consumption of sample, and reduced cost per assay make the proposed SERS-based LFD a promising platform for the detection of diseases in its early stage. Different from a sandwich-type assay, the inherent differences in the affinity of ssDNA and dsDNA to metal NPs have also been exploited for indirect SERS-based DNA and RNA detection.[457] The underlying principle is similar to that exploited under direct SERS sensing[424] with an additional component of a Raman reporter attached to the probe DNA or the nanoparticle. Using similar concept, a PNA-based SERS sensor for DNA detection was also reported.[458,459]

As a further advancement, the integration of enzyme-free and enzyme-assisted nucleic acid amplification techniques with SERS has been attempted to improve the sensitivity for DNA and RNA detection.[459] In this case, sensitivity improvement is achieved *via* either signal (increased SERS signal by target recycling) or target (increased low amounts of target DNA to a detectable level) amplification. However, the intrinsic limitations of target amplification techniques in terms of potential contamination and non-specific amplification that require strict laboratory control and skilled labor, provide a strong rationale for the preferable use of signal amplification methods over target amplification. The widely employed nucleic acid amplification techniques include both enzyme-assisted and enzyme-free methods. The enzyme-assisted amplification methods include duplex-specific nuclease (DSN) in which a specific enzyme can degrade the dsDNA or DNA–RNA duplex over the ssDNA and double stranded-RNA; and rolling circle amplification (RCA) which is an isothermal polymerase chain reaction producing single-stranded repetitive DNA/RNA. Enzyme-free methods, on the other hand, include hybridization chain reaction (HCR) which is an isothermal and linear amplification method that works based on hybridization between DNA hairpins and interior stands; and catalytic hairpin assembly (CHA) which is a programmable DNA circuit utilizing partially complementary two DNA hairpins and one ssDNA.

The application of DSN-assisted amplification was reported using different SERS-active substrates and Raman reporters. Some representative examples include, Au NPs encapsulated within an AgAu shell,[460,461] Au NPs coated with Ag and magnetic NPs,[461] Ag-coated $Fe_3O_4$ NPs,[462] Ag-coated $Fe_3O_4$ and Ag-coated Au NPs,[463] stimuli-responsive DNA microcapsule with Raman dye,[464] and Raman reporter trapped in 3D hydrogels. Similarly, several reports have highlighted the application of RCA with SERS,[465] including Raman probes functionalized Au NPs,[466] probes functionalized Au NSs on glass slide and Au NRs,[467] and magnetic SERS substrate with Ag NP decorated core–shell Co@C.[468] Although the use of enzyme-assisted amplification methods has been able to achieve considerably greater sensitivity and wide linear range for detecting nucleic acids, the considerations of assay time, cost, thermostability of the employed enzyme and requirement of resource-rich settings may limit the applicability of these methods for real-time DNA and RNA sensing.

To circumvent those challenges, enzyme-free amplification techniques have been introduced and CHA is one of the commonly reported approaches with a range of Raman reporter-modified SERS-active substrates.[468] These include, Au nanodumbbells as core and Au NPs as satellite,[469] AuAg alloy NPs,[470] Ag-coated Au NPs,[471] hollow AgAu nanospheres,[472] Au nanocages,[473] Ag NP-decorated silicon wafer[474] and Au NPs.[475] Another enzyme-free signal amplification technique that is broadly employed is HCR, which has, for instance, used Raman probes functionalized bifunctional bio-barcode Au NPs,[476] DNA probes modified magnetic beads and Au NPs with Raman reporter,[476] and DNA-modified Ag NPs.[477] In contrast to signal amplification methods discussed above, target amplification techniques involving PCR have also been described for ultrasensitive DNA detection with an LOD of 11.8 aM.[478] Moreover, recent progress in the field has highlighted the prospects of coupling amplification-free methods such as clustered regularly interspaced short palindromic repeats (CRISPR) with SERS for the development of ultrasensitive DNA and RNA sensors.[479–481]

Although the use of SERS as a promising tool for the detection of DNA and RNA biomarkers has been able to accomplish superior sensitivity, some of the inherent challenges with SERS have hampered its applicability for real-time analysis. Reproducibility of the SERS signal perhaps remains the biggest hurdle since the amplitude of the Raman signal can vary substantially with the uneven and randomly distributed hotspots created by the plasmonic nanomaterials. These well-defined hotspots are otherwise critical to attaining a gigantic enhancement factor from a combination of EM and CT enhancement mechanisms. Thus, insufficient attention to standardizing protocols (*e.g.*, synthesis of NPs, the configuration of assembly on surfaces, use of excess chemicals, uncontrolled aggregation, and limited shelf-life of plasmonic crystals and substrates) can lead to vast variations and uncertainties in the generated Raman signals. To overcome these limitations, it is paramount to pay considerable attention to these variables and thus develop methodologies to fabricate robust, stable, and cost-effective Raman substrates within a high precision, reproducibility, is scalability framework. For example, a recent study designed Ag/black phosphorus nanocomposite that utilizes photoreduction to generate hotspots without the need of chemical reagents. This approach could evade background signal interference from the biological fingerprint and accurately detect single molecules with as low as $10^{-20}$ M sensitivity.[482] In addition, adopting large-scale standardized manufacturing processes, like those in the semiconductor industry, is crucial for producing stable and active SERS substrates with extremely high reproducibility. However, challenges lie ahead in combining colloidal synthesis approaches that are most suitable for producing SERS-active plasmonic NPs with microfabrication processes to produce reproducible surfaces and substrates. More recently, certain antistrophic colloidal NPs (*e.g.*, nanostars and nanorods),[483–485] nanoparticle dimers,[486] and self-assembled NPs[487,488] have seen progress towards uniform and even distribution of larger number of hotspots, which is crucial for greater reproducibility. On the other hand, use of a standard reference in which the signal remained constant relative to the employed signal probe has also been described recently to achieve enviable reproducibility in SERS-based miRNA sensing.[489,490] Another recent study reported the influence of the nanocrystal morphology for generating stable, reliable, and reproducible SERS signals using hierarchic Au NCs assembly assay.[491] The outcomes of this study evince the better suitability of precisely shaped NCs with the uniform EM field over the spherical NPs (curved interfaces) for stable and reproducible SERS signals. Similarly, the fabrication of SERS-active interior nanogap particles was also reported as a promising method to achieve stable, reliable, and reproducible SERS signal with ultrahigh sensitivity owing to uniformity and narrow distribution in enhancement factors in the as-synthesized nanostructures.[65,492–494] These studies suggest that alternative approaches for obtaining favorably stable substrates remain essential for reproducible SERS sensing.

Another challenge with the SERS-based biomolecular sensing is the background noise that stems during measurement of biological samples. The biological matrices, such as tissues, fluids, or cellular components may lead to scattering/fluorescence, while the amorphous carbon resulting from the burning of biomolecules upon laser excitation can generate a strong background signal and thus overshadow, distort, or mask the desired Raman signatures of the biomolecules of interest. To address this undesirable feature, the SERS community is also actively exploring strategies to enhance the signal-to-noise ratio, improve spectral resolution, and employ advanced data analysis algorithms to extract accurate and reliable information. In this context, combining SERS with artificial intelligence and deep machine learning approaches opens a new avenue for the analysis of SERS spectra. Various mathematical and statistical methods, including principal component analysis, discriminant analysis, cluster analysis, and sophisticated approaches such as decision trees, random forests, artificial neural networks (ANN), recurrent neural network (RNN), Bayesian learning, and support vector machines, can effectively extract the intricate characteristics of complex Raman spectra of biomolecules to deliver more accurate classification. These advanced analytical technologies have the potential to propel the practical applications of SERS to a new level. For example, compared to traditional linear spectral analysis methods, ANN can detect nonlinear dependencies, making them well-suited for complex biological samples lacking linear patterns. The use of such ANN models to train SERS spectra of DNA with an accuracy of over 85% in identifying DNA damage was demonstrated.[495] Similarly, the use of recurrent neural network (RNN) models to identify RNA was also described using DNA probes which can capture RNA from severe acute respiratory syndrome coronavirus 2 (SARS-CoV-2) using Ag NRs.[495] The RNN model demonstrated impressive prediction accuracies of 97.2% and 100% for positive and negative samples, respectively.[496]

Last but not least, the initial cost associated with the instrument and the requirement of skilled personnel to handle and service the instrument limits the use of this technique in resource-poor settings, irrespective of the progress witnessed in the field to date. To address this challenge several studies have evinced the fabrication of SERS-based point-of-care (POC) devices, a technology still in its infancy stage that requires a considerable amount of new research and development efforts.[455,456,471,473] Lastly, as the use of SERS is advancing towards *in vivo* applications,[497,498] the toxicity and stability of SERS probes need thorough evaluation and optimization for reliable *in situ* detection. In summary, addressing the current challenges with SERS-based detection of nucleic acids in terms of reproducibility, non-uniformity of hotspots, background interference, cost of operation, and potential toxicity and stability of probes are crucial for advancing the practical applications of this unique and promising diagnostics platform. Continued research and innovation in not only fabricating new SERS-active materials and substrates with consistent and reproducible SERS signals but also the development of novel strategies to detect DNA and RNA markers, perhaps by combining with innovations in other fields, could enable the widespread adoption of SERS as a mainstream spectroscopic technology in diverse fields, ranging from biomedical diagnostics to environmental monitoring and beyond (Fig. 12).

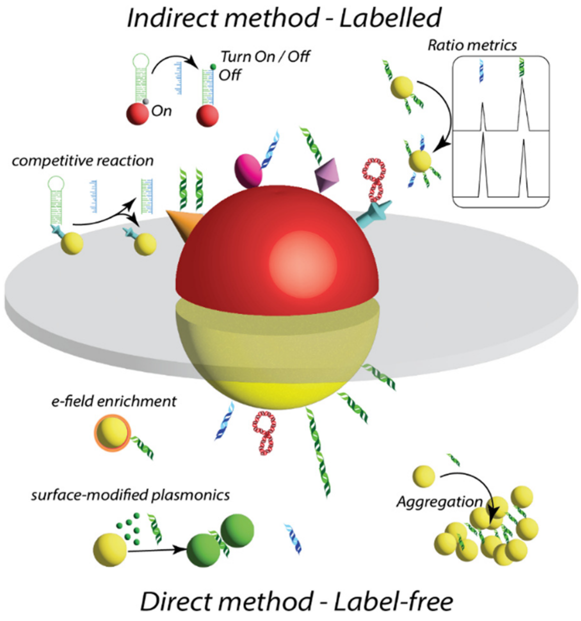

Fig. 12 A schematic representation of different SERS-based strategies deployed for detection of nucleic acid biomarkers, as classified under direct and indirect methods.

#### 3.4.4.4. *Protein sensing*

*3.4.4.4.1. In vivo protein detection and imaging.* The past two decades have witnessed a huge surge in the utility of SERS for clinically relevant molecular imaging *in vivo* and detection of protein biomarkers *ex vivo*. The ability of SERS to enable rapid, non-invasive real-time tracking *in vivo* is attributable to its high sensitivity, exceptional spatiotemporal resolution, and multiplexing owing to narrow spectral linewidths of Raman reporters.[499] These attributes of SERS are collectively controlled by the optical properties of the plasmonic NPs used,[200,500] the molecular characteristics of the Raman reporters used, the targeting ligands on the NP surface such as antibodies, peptides, and aptamers allowing specificity for a target protein,[501,502] and protective ligands such as PEG for stability.[503,504] Whereas early studies on SERS *in vivo* primarily focused on tracking one or two protein targets (Fig. 13),[505,506] recent work has leveraged multispectral palette with NPs to allow from 5-plex SERS imaging[507] to a library of 14 nanoprobes,[508] to 26-plex passively accumulated probes *in vivo.*[509] These examples demonstrate that with further signal optimization, SERS has the potential to propel clinically significant applications *in vivo*. However, a major hurdle in SERS that often limits its imaging potential is the tissue autofluorescence background and the overlap of Raman peaks of reporters in the fingerprint region with the native peaks of biological metabolites.[510] The tissue autofluorescence emerges from endogenous fluorophores such as collagen, elastin, nicotinamide adenine dinucleotide (NAD), and flavin adenine dinucleotide (FAD) among others.[511] Although using infrared excitations can reduce autofluorescence and self-absorption, it can significantly reduce Raman signal intensity due to the fourth power dependence of the Raman cross-section with excitation frequency. Moreover, the sensitivity of typical NIR detectors is also limited. Besides, the interference of background signals from other issue parts makes it challenging to quantify the real signals. Besides, the direct detection of proteins (without chromophores or functional groups that bind to metal surfaces) that have low Raman cross section and low affinity toward metal surfaces remains a

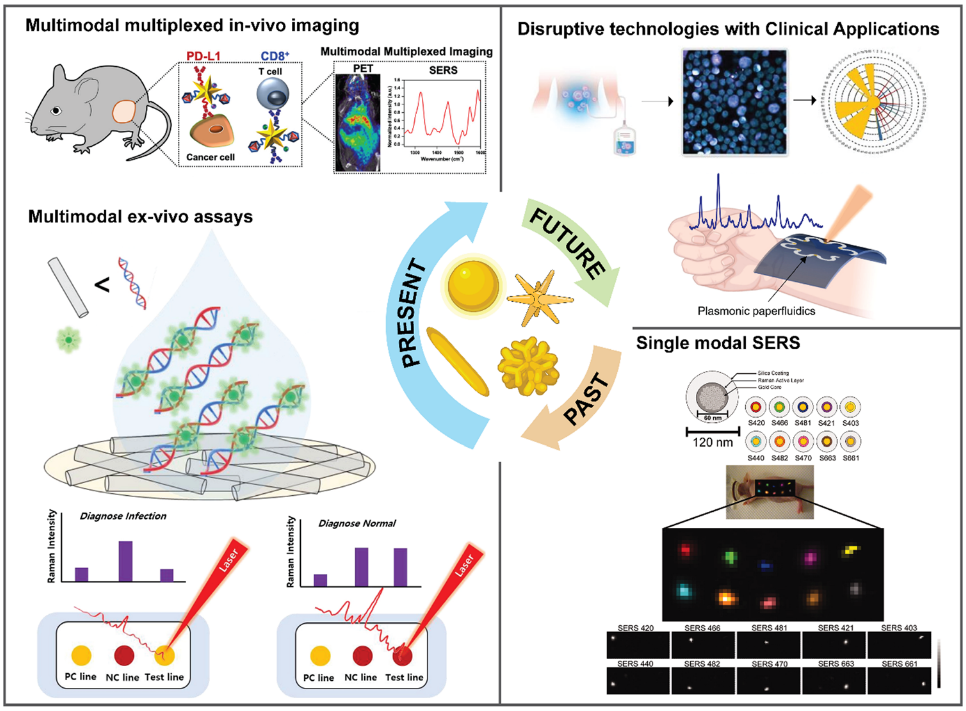
Multimodal multiplexed in-vivo imaging
PD-L1
CD8+
T cell
Cancer cell
Multimodal Multiplexed Imaging
PET
SERS
Disruptive technologies with Clinical Applications
Multimodal ex-vivo assays
PRESENT
FUTURE
PAST
Plasmonic paperfluidics
Single modal SERS
Silica Coating
Raman Active Layer
Gold Core
60 nm
120 nm
S420 S466 S481 S421 S403
S440 S482 S470 S663 S661
Diagnose Infection
Diagnose Normal
Raman Intensity
Laser
PC line NC line Test line
SERS 420 SERS 466 SERS 481 SERS 421 SERS 403
SERS 440 SERS 482 SERS 470 SERS 663 SERS 661

Fig. 13 Schematic representation of the past, present, and future of SERS. Single modal applications of SERS in the past transitioned to multimodal *in vivo* imaging in the present where SERS has been combined with clinical techniques such as PET (positron emission tomography) imaging, and *ex vivo* assays where SERS has been combined with clinically established PCR. In the future we expect SERS will enable disruptive technologies with real time measurement of clinical samples, and wearable devices for rapid screening.

major hurdle. To surmount these challenges, multiple approaches have been implemented including the synthesis of bioorthogonal reporters with peaks in the biological Raman silent region (1740–2800 cm$^{-1}$) which have minimal overlap with biological metabolites.[512] Such Raman reporters have shown excellent targeted multiplexed detection allowing background-free high contrast in a *c. Elegans in vivo* model.[513]

In addition to synthesis approaches, improvement in SERS signal *in vivo* has also resulted from advanced Raman setups that reduce biological noise during data collection. Spatially offset Raman scattering (SORS) is such an approach where the signal from the scattered photons is collected by offsetting the point of the light source from the point of the photon collection.[514] This lateral shift allows the collection of signals from the scattered photons originating from deeper in the tissues despite interfering substrates such as bones. Leveraging this approach, Raman spectra have been obtained at high resolution through 7 mm of thick skull tissue that enabled higher signal-to-noise than conventional Raman spectroscopy techniques.[515] Another advanced Raman setup used shifted-excitation Raman difference spectroscopy (SERDS) for *in vivo* imaging where the laser source allows two slightly shifted emission lines similar to the bandwidth of the Raman peaks being studied.[516] The spectral data resulting from these emission lines differ in wavenumbers but with negligible change in signal from the background. Therefore, with SERDS the Raman data has minimal interference from the tissue autofluorescence background, and this setup has enabled researchers to pursue highly precise intraoperative imaging with a handheld Raman device.

Whereas SERS *in vivo* has largely focused on the use of nanoparticles conjugated with Raman reporters, tracking the Raman signal of intrinsic metabolites has also enabled innovations in intradermal glucose detection *in situ* with microneedle array-based sensors.[517] In this unique study, diabetes was induced with streptozotocin in mice fed with a high-fat diet, and the microneedles coated with Ag nanoparticles were gently inserted on mouse skin to measure glucose levels in the subcutaneous interstitial fluid. SERS data was collected through each needle tip of the microneedle arrays with a handheld scanner, and the glucose measured was on par with levels measured with conventional glucometers. Unlike traditional methods to monitor glucose where diabetic patients use finger-stick devices, which is painful and inconvenient, this study demonstrates a clinically significant application of SERS in a point-of-care setting where minimally invasive microneedle arrays allow a painless procedure for glucose tracking with no bleeding. The clinical relevance of SERS has also been enhanced by combining it with clinical imaging modalities to leverage the strengths of SERS while overcoming its limitations in whole-body and depth-resolved imaging.[518] The ability to integrate SERS with other imaging techniques is driven by the innovative design of nanoparticles labeled with Raman reporters and other molecules and ligands. Such multifunctional NPs should also maintain their overall biocompatibility, stability, and functionality of each component on the NPs.[519,520] Multimodal imaging has the potential to not only enable highly precise biomarker tracking *in vivo*, but also allow margin assessment before, during, and after surgical procedures.

In this effort, magnetic resonance imaging (MRI) and SERS have been combined with Prussian blue-coated Au NPs where Prussian blue played a dual role-the iron ions allowed MRI contrast and cyanide bridges allowed bioorthogonal SERS signal in the biological Raman silent region.[517] By targeting the CD44 receptors with hyaluronic acid ligands, these nanoparticles showed homing in the tumor periphery. In a more ambitious approach, multifunctional NPs were synthesized by Shi *et al.* that integrated SERS, MRI, and computed tomography (CT) imaging and dual therapeutics including drug delivery and photothermal therapy.[521] The authors designed gold core-silica shell gap-enhanced NPs that they decorated with gadolinium to allow MRI contrast and Raman reporters and achieved receptor targeting *via* folate molecules. They also loaded ibrutinib, which is a small-molecule oral drug used for treating lymphomas. These "all-in-one" NPs enabled preoperative tumor imaging with MR/CT and intraoperative accuracy with SERS while also allowing highly effective multivalent treatment. In addition to MRI, positron emission tomography (PET) imaging is also a mainstay in the clinic facilitating deep tissue whole-body imaging. Single-channel PET with a single radiotracer has been effective when combined with SERS active NPs allowing preoperative planning, intraoperative resection of the lymphatic tissue, and postoperative margin confirmation.[520] However, multiplexing cannot be achieved with PET; therefore, integration of SERS in a single functional NP is beneficial for tracking multiple proteins *in vivo*. In a work by Bardhan and co-workers,[522] the authors showed that PET-CT-SERS active multimodal NSTs enable simultaneous detection of multiple immunomarkers *in vivo* combining the merits of all imaging modalities. In their approach, two sets of Au NSTs were synthesized, each conjugated to a different Raman reporter with minimal spectral overlap to target $CD8^+$ (cluster of differentiation 8) T cells and PD-L1 (programmed cell death ligand 1) expressing cancer cells *in vivo*. Nanostars were also conjugated with anti CD8 or anti PD-L1 antibodies and $^{64}Cu$ radiotracer was chelated *via* DOTA (dodecane tetraacetic acid). The NSTs tracked the two immunomarkers *in vivo* as well as provided early response to antiPD-L1 + antiCD137 checkpoint blockade immunotherapies in both treatment-responsive and treatment-resistant melanoma tumors. There are now several clinical trials ongoing where multiple imaging modalities have been integrated for diagnostics (*e.g.*, trial # NCT02790853). This suggests that SERS combined with a clinical technique enabled by biocompatible NPs may transition this technology "*from bench to bedside*" for clinical diagnosis (Fig. 13).[523]

#### 3.4.4.4.2. *Ex vivo protein detection.*

In addition to *in vivo* imaging, SERS has also enabled highly precise detection of proteins *ex vivo* with femtomolar detection limits (Fig. 13).[524] SERS-based *ex vivo* assays are quantitative, allow multiplexing of >30 biomolecules, and are comparatively low cost than fluorescence-based assays.[525] In such *ex vivo* assays, the type of the metal NPs used (Ag, Au, and Al) and the type of the targeting moiety conjugated on the NPs (antibodies, peptides, DNA *etc.*) govern the sensitivity, specificity, stability, and overall shelf-life of the nanoprobes used for detection.[195,526] Whereas sandwich immunoassays have been the most prevalent in *ex vivo* SERS sensors,[527] recent innovations in lateral flow assays (LFAs),[528] porous architectures,[529] and microfluidics[530] demonstrate the promise of these technologies for ultimate use as POC devices for at-home use. Here we will discuss a few examples of *ex vivo* SERS assays and conclude this section with commercialization of SERS substrates.

In a unique approach by Chen *et al.*, nanoporous anodic aluminum oxide (AAO) was developed as a vertical flow sensing unit, and bimetallic core–shell Au@Ag nanotags encoded with Raman reporters as the labeling unit.[531] Through this approach the authors detected multiple inflammatory biomarkers including, procalcitonin, interleukin-6, serum amyloid A, and C reactive protein in patient samples by functionalizing the bimetallic NPs with four distinct Raman reporters and antibodies specific to these proteins. The high surface area to volume ratio and the nanoscale confinement within the AAO pores aided with the highly effective SERS nanoprobes allowed femtomolar LOD of 7.53, 4.72, 48.3, and 53.4 fg $mL^{-1}$ for the four biomarkers, respectively. In another multiplexing study, Bardhan and co-workers reported a novel sensor portable, reusable, accurate diagnostics with nanostar antennas (PRADA) for detecting biomarkers of cardiac disorders including cardiac troponin 1 (cTn1) and neuropeptide Y (NPY) in cardiac patient serum samples.[532] PRADA is a rendition of a sandwich immunoassay with Au NSTs functionalized with targeting peptides and Raman tags as the detection unit, and magnetic microbeads conjugated with polyclonal antibodies as the capture units. Through this unique architecture, PRADA achieved a LOD of 5.5 pg $ml^{-1}$ of cTnI and 120 pg $ml^{-1}$ for NPY demonstrating that small peptides can achieve detection sensitivities on par with antibodies while enabling high stability of the nanoprobes. PRADA was reusable where the magnetic microbead bottom probes could be removed with a magnet allowing regeneration of the sensor chip for ~14 cycles making PRADA amenable to affordable sensing at remote sites. In addition to antibodies and peptides, aptamers conjugated NPs are also excellent in selectively detecting proteins allowing to expand SERS assays to neurological diseases. In this effort, a self-assembled conjugate of Raman tag-encoded poly-adenine (poly-A) block oligonucleotides was anchored on Au NPs and coated with targeting aptamers.[533] When the protein of interest is bound to the aptamers, it induces aggregation of Au NPs increasing the plasmonic coupling effect and leading to hotspots. These functionalized Au NPs enabled multiplexed detection of Aβ1-42 and Tau proteins, which are biomarkers of Alzheimer's disease enabling LOD of 0.00042 pM for Aβ1-42 and 0.037 nM for Tau proteins, respectively. In addition to the traditional SERS sensor architectures, microfluidic devices have expanded the capabilities of SERS *ex vivo* assays achieving rapid and ultrasensitive detection attributable to the spatial confinement of nanoprobes and better mixing of nanoprobes with the analytes of interest. For example, Wang *et al.* designed an extracellular vesicle phenotype analyzer chip (EPAC),[534] "nano" mixing enhanced microchip that allowed the authors to track low-abundance tumor-specific extracellular vesicles (EVs) in biological fluids. Multiplexing was achieved by labeling the EVs Au NPs and Raman reporters to detect receptor tyrosine-protein kinase, melanoma cell adhesion molecule, low-affinity nerve growth factor receptor, and melanoma chondroitin sulfate proteoglycan with high sensitivity and specificity. In another study, Tian and co-workers developed a futuristic design (Fig. 13) of a flexible and wearable paper-based microfluidics for quantitative detection of uric acid (UA) in sweat at physiological concentrations.[535] The authors used chromatography paper with uniformly distributed Au nanorods to fabricate the plasmonic paper-based microfluidic biochip. The nanorods contributed to high SERS signal and ultrasensitive detection of UA in sweat. The authors also showed that microfluidic biochips are highly flexible and can be stretched and twisted withstanding stress and strain. They also demonstrated that the flexible biochips can be conformally laminated on a human subject and with the utility of a portable Raman spectrometer, rapid and accurate data collection is possible.

These examples show that SERS has progressed rapidly since its advent and has emerged as a mature technology with many commercial sources of SERS substrates that are now available.[201,536,537] A recent study compared the efficacy of 7 different commercial SERS substrates in the detection of cocaine in oral biofluids from healthy donors.[536] The substrates were purchased from Diagnostic a SERS, JASMAT Optics Corp, Silmeco Aps, FLEW Solutions, Quark Photonics, and Metrohm Australia. The authors found that only one of these substrates excelled in reaching a 1 ng $\mathrm{mL^{-1}}$ LOD for cocaine in buffered solutions, and 10 ng $\mathrm{mL^{-1}}$ in human samples. The authors attributed the superior performance of these substrates to their design where silicon pillars were used as the substrate backing and Ag as the active metal. The performance of the substrate was controlled as the pillars leaned towards each other giving rise to clusters as the solvent evaporated. The nanogap (25–40 nm) created between the tips of the pillars within the clusters enabled intense SERS hotspot and high Raman signal. In a similar study, three different commercial SERS substrates including RAM-SERS-SP from Ocean Optics, QSERS from Nanova Inc., and Hamamatsu from Hamamatsu Photonics were compared with 4-mercaptobenzoic acid (MBA) as a model probe molecule.[537] The authors used two different excitation wavelengths (633 and 785 nm) and calculated the LOD and limit of quantification (LOQ) between 1–10 μM with a range of use of only one or two orders of magnitude. The best performing substrate for MBA was Hamamatsu at the 633 nm excitation wavelength. These comparative studies are highly informative in (i) demonstrating the potential and limitations of current commercial SERS substrates, (ii) motivating researchers who have designed custom SERS platforms with exceptional sensitivities to move their technology "from bench to market", and (iii) inspiring new technological innovations that go beyond the well-established protein targets to sensing unconventional biomolecules in rare diseases that have not been previously probed.

*3.4.4.4.3. Cell detection.* In recent years SERS strategies to aid in cell detection, analysis, phenotyping or functionality studies have been increasingly used. SERS has been extensively used for the detection of single or multiple cells in cell culture media, plasma, serum, tissues, or even body fluids.[538] Lately, particular attention has been given to the detection of circulating tumour cells (CTCs) in different cancer types with SERS.[538–541] Ding and co-workers have also reported on a dual strategy combining SERS and fluorescence for the detection of circulating tumor cells (CTCs).[542] In this work they used Au nanoflowers onto indium tin oxide (ITO) surfaces, which were functionalized with aptamers able to capture CTCs. Simultaneously, Au NSTs were used as probes having an anti-EpCAM to improve the selectivity of the strategy. After the retention of the CTCs, then by using a complementary aptamer sequence to that of the retention, the originally captured CTCs were released into the medium to perform the dual SERS-fluorescence detection. Remarkably, they could detect down to 5 and 10 cells $\mathrm{mL^{-1}}$ with SERS and fluorescence respectively, ensuring linearity up to 200 cells $\mathrm{mL^{-1}}$. Another example using SERS tags by Oliveira *et al.* showed that by combining SERS tags paired with membrane protein recognition antibodies and microfluidic platforms, it is possible to perform a multiplex analysis of the surface protein expression at the single cell level.[543] For this, they used Au NSTs codified with different Raman reporters, which were subsequently coated with a silica layer and later functionalized with the target antibodies EpCAM, Vimentin, and CD45. Interestingly, by having the individual cells contained within droplets, it is possible to map the surface of those cells in terms of the intensity of the SERS tags, which directly report the presence or absence of the specific proteins on top of the SERS tags. Unlike fluorescence in which a binary reply on whether a protein is present or not, by using these SERS tags it is possible to analyze the distribution of the protein expression along the cell membrane (Fig. 14).

The use of label-free methods for cell analysis using SERS offers advantages such as simplicity, lower costs and time savings, and with the advent of data analytics its potential is boosted with respect to codified SERS strategies, which were most pursued in the past decade.[544–546] For example, Agnieszka Kamińska *et al.* in which they used a membrane containing plasmonic nanoparticles to capture and analyze CTCs.[547] Unlike the previous works presented, in this case they present a label-free analysis of cancer cells (leucocytes, HeLa, and PC3 cells). A tailor-made membrane was used for both the capture of cells and their subsequent analysis. A combination of eletrospinning of polymer fibers followed by physical vapor deposition of AuAg alloy was the chosen strategy. After the acquisition of reference SERS spectra of the three cell lines, the authors show the successful classification of cell types by using PCA achieving an accuracy of 95% in 2D PCA to 98% in 3D PCA.

Besides the detection of whole cells, it is worth mentioning that SERS has proven to be quite successful in the development of the detection strategies for cell related intra-,[548,549] and extracellular metabolites,[550,551] extracellular vesicles (EVs),[552,553] cell lysates,[554] cells within tissues[555] or cell imaging.[556,557] For example, the work by Masson and co-workers described the monitoring of metabolic events of cells using SERS.[558] In this work, in which the report a sensitivity down to the single molecule level, they used a set

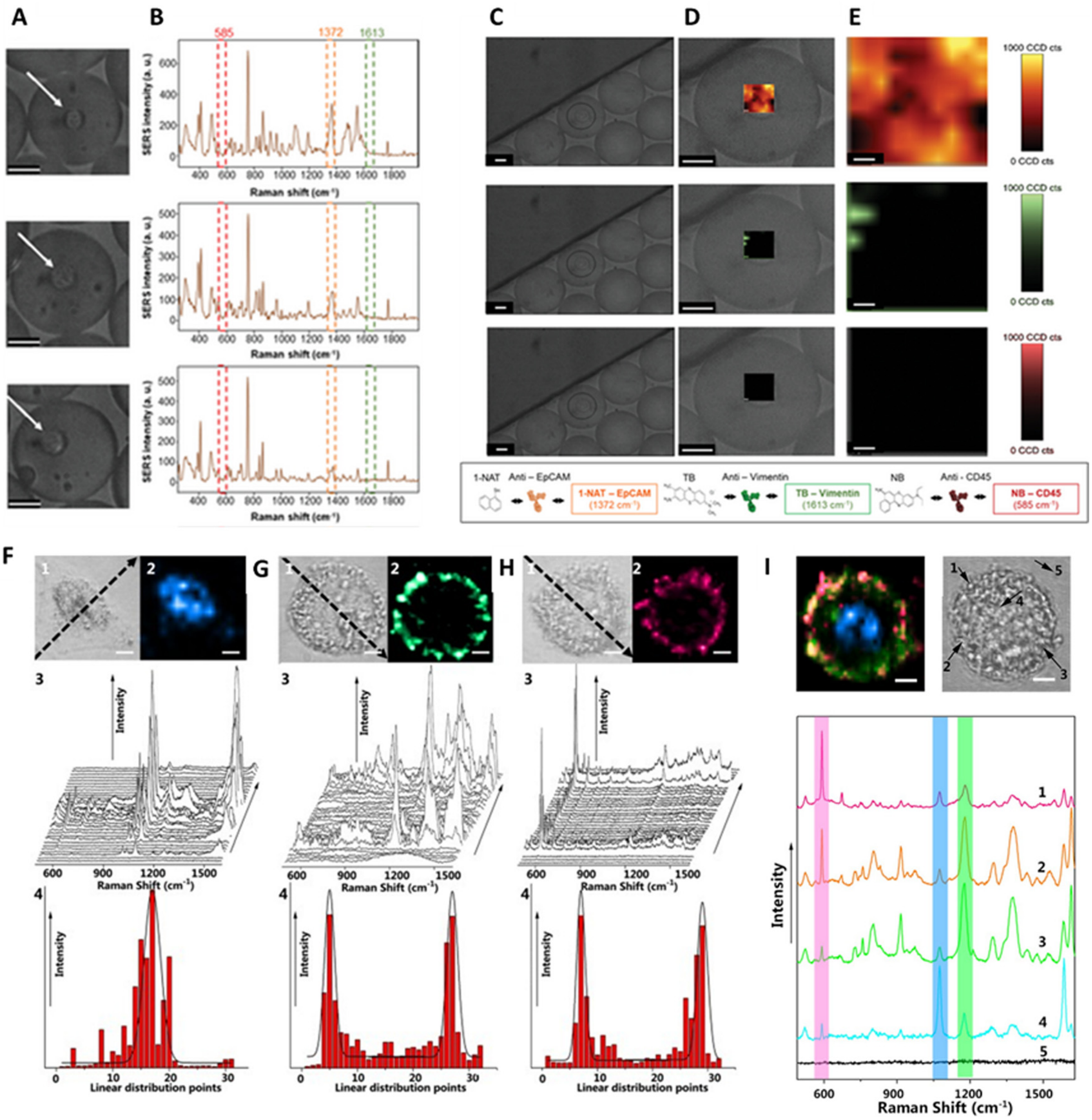

Fig. 14 (A) Three bright-field images of three different cell-containing microdroplets; (B) SERS spectra after measurements in each cell; (C)–(E) multiplex phenotypic characterization of MDA-MB-435 cells using three different SERS tags; (C) bright-field of an MDA-MB-435S cell labeled with Au NSs@RaR encapsulated in a microdroplet; (D) high magnification image and overlay of SERS mapping on top of a single cell; (E) respective SERS intensity maps for each RaR, and corresponding intensity colour scale (scale bar 3 μm). Inset: Pairing of RaRs with specific antibodies for recognition of cell membrane receptors. Reproduced from ref. 538 with permission from Wiley-VCH GmbH publisher, copyright 2021 (F)–(H) SERS imaging of a HeLa cell treated with MBA-coated Au NPs (F), CV-coated Au NPs (G), and CVa-coated Au NPs (H); (F1–CH1) Bright-field images and (F2-G2) SERS images corresponding to the detected HeLa cell. (F3–G3) SERS spectra were obtained from different positions within the cell *via* point-by-point detection. The histogram displays the Raman intensity at 1078 $cm^{-1}$ (MBA-coated, A4), 1175 $cm^{-1}$ (CV-coated, B4) and 595 $cm^{-1}$ (CVa-coated, C4) obtained from the spectra in (A3–C3) along the dotted line in (F1–H1) (scale bar ≡ 4 μm); (I) Multi-targeting SERS imaging of a HeLa cell treated with CVa-coated, CV-coated and MBA-coated AuNPs; (I) left: overlap of SERS images of CVa-coated Au NPs (red), CV-coated Au NPs (green) and MBA-coated Au NPs (blue); right: bright-field image of the investigated HeLa cell; bottom: SERS spectra obtained from different positions in the cell (marked in bright-field cell image above by arrows (scale bar ≡ 4 μm)). Reproduced from ref. 544 with permission from Nature publisher, Copyright 2016.

of borosilicate nanopipettes decorated with Au NPs as plasmonic sensor. The metabolites detected were the common suspects such as pyruvate, lactate, ATP, and urea simultaneously. In this approach, the detection was done by placing the SERS sensor at varying distances of living cells and after the application of a lysis process to boost cell secretion. In this way, the authors were able to monitor metabolite gradients and mixtures that could be related to disease stages.

As shown, a broad range of SERS applied to cell detection in different fashions is available in the literature. However, it is needed to consider the chosen SERS strategy taking into account the clinical need for a specific use case. As an example, in most cases for cancer diagnosis and monitoring, therapy guidance and clinical utility are key for the uptake of novel technologies. As such, guided therapy is based either on protein expression or on specific mutations. In this scenario, cell identification alone would not be sufficient to offer clinical utility, and the use of SERS tags to identify specific mutations, proteins or biomarkers would offer the relevant clinical information. However, some diseases can be diagnosed based on the presence/absence of aberrant cells, in which label-free approaches for rare cell detection could make a huge difference in clinical practice. Finally, with the advent of advanced data analytics, heavy SERS analytical data can be now interpreted and deconvoluted with much more efficiency and robustness, which should be exploited by the community to finally bring SERS to hospitals as diagnostic and clinically useful tools.[559]

*3.4.4.4.4. Bacteria and virus sensing.* Specific bacteria or viruses can cause infectious diseases with a significant impact on human health. For example, sepsis is a severe and life-threatening disease caused by bacteria or bacterial toxins in the bloodstream, triggering a severe inflammatory response.[560] The respiratory disease SARS-CoV-2 has ravaged the world for the past four years, causing the rapid spread of the infectious disease and resulting in hundreds of millions of infected individuals worldwide, leading to the loss of lives of many elderly people.[561,562] Therefore, the accurate and fast diagnosis and prevention of the spread of these infections are crucial. Reverse transcription-polymerase chain reaction (RT-PCR) is a widely used standard diagnostic method that extracts, amplifies, and detects RNA or DNA. However, it has limitations in detection time and requires experts who can effectively utilize it.[563,564] The LFA strip, which extracts protein biomarkers instead of RNA/DNA and provides quick on-the-spot diagnosis, has been commercially successful in diagnosing SARS-CoV-2. However, the sensitivity is low, leading to a high false-negative diagnostic rate for early infected or asymptomatic infected individuals.[565,566] Consequently, there is a need for a new high-sensitivity detection method that can significantly improve diagnostic sensitivity and address the problem of infection spread due to false-negative diagnoses.

SERS detection method has been recognized as a new diagnostic technique that can overcome the sensitivity limits of existing biomedical detection techniques in terms of absorbance, fluorescence, and chemiluminescence.[567,568] In addition, SERS-LFA or SERS-ELISA technology, which combines SERS detection with an immunoassay platform, has been developed, which may overcome the sensitivity limit of immunoassays. The novel SERS-LFA diagnostic system was developed to diagnose infectious diseases caused by bacteria or viruses, such as *Orientia tsutsugamushi* (*O. tsutsugamushi*), a Gram-negative intracellular bacterium, or SARS-CoV-2 on site.[569] Fig. 15a shows a conceptual diagram of the system, which consists of a SERS-LFA strip, a portable Raman reader that can measure Raman signals of the test and control lines of the strip, and a lysis buffer used to extract the target protein (nucleocapsid protein) from clinical samples. The sample preparation process for the quantitative analysis of SARS-CoV-2 is similar to that of a commercial LFA strip, for which the result is interpreted as positive or negative by the eye.[570] First, the clinical sample is placed in a running buffer, including a lysis

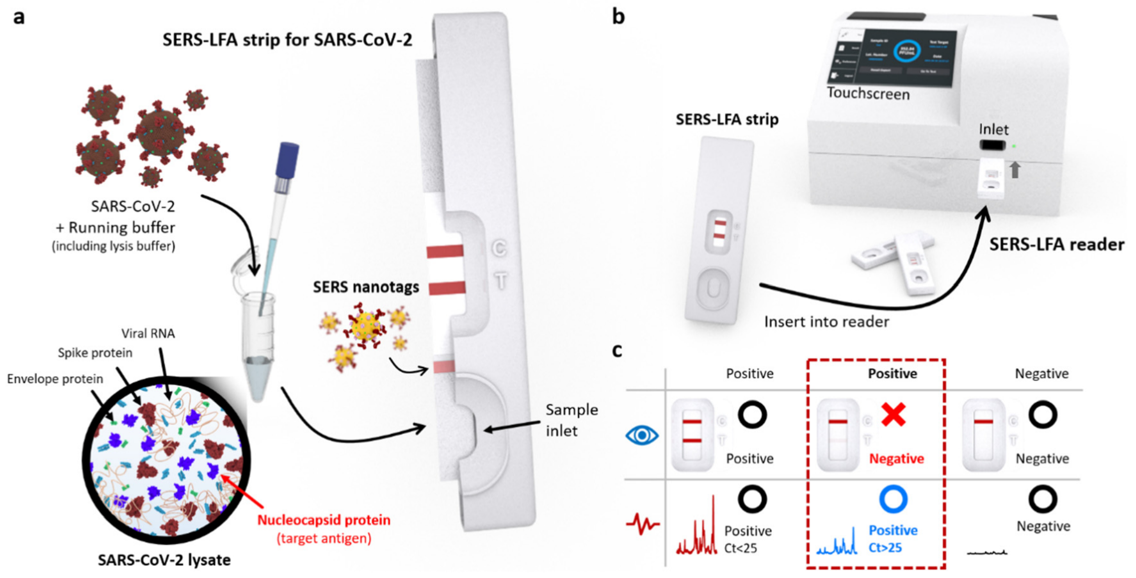

Fig. 15 Illustration of the SERS-LFA system for on-site diagnosis of SARS-CoV-2. (a) Schematic of the SERS-LFA strip for SARS-CoV-2 antigen testing. SARS-CoV-2 is added to the running buffer, including a lysis buffer to lyse the virus. After mixing the SARS-CoV-2 with the running buffer, the solution is loaded into the inlet of the SERS-LFA strip. When this SARS-CoV-2 lysate reaches the conjugate pad, the target NC proteins and NC antibody-conjugated SERS nanotags form immunocomplexes through antibody–antigen interactions. The running buffer, including the NC protein-SERS nanotag complexes, moves towards the test and control lines. (b) After the running buffer reaches the absorption pad through the test and control lines, the SERS-LFA strip is inserted into the portable Raman reader. (c) Advantage of the SERS-LFA system over the commercial LFA strip. Both LFA and SERS-LFA show a negative result for SARS-CoV-2-negative patients. Both methods are positive for clinical samples with a high virus concentration (Ct $<$ 25 in RT-PCR). The LFA strip usually shows a false-negative result for clinical samples with a relatively low virus concentration (25 $<$ Ct in RT-PCR); however, the SERS-LFA system shows a true-positive result owing to its high sensitivity, Reproduced from ref. 570 with permission from ACS publisher, Copyright 2022.

buffer solution to lyse the virus. Then, the target protein is extracted and loaded into the inlet of the SERS-LFA strip along with the running buffer. This solution moves to the conjugate pad by capillary force and binds to antibody-conjugated SERS nanotags through antigen–antibody binding when the target protein is present. These target protein-SERS nanotag complexes continue to flow in the direction of the absorbent pad and are accumulated by combining with the antibodies immobilized on the test line. The SERS nanotags that did not bind to the antigen accumulate on the control line through antibody-antibody interactions. When the target protein is absent, the SERS nanotags do not bind to the test line and only bind to the control line through antibody-antibody interactions. Test and control lines that combine with SERS nanotags show a red color due to the surface plasmon effects of Au NPs, like commercial colorimetric LFA strips. However, due to the low sensitivity of these colorimetric LFA strips, it is difficult to detect the SARS-CoV-2 virus below 350 plaque-forming units (PFU) mL$^{-1}$, resulting in false-negative diagnoses.

A portable Raman-LFA strip reader has been developed to solve sensitivity issues. Fig. 15b shows a schematic diagram of the SERS-LFA strip reader. A 632.8 nm diode laser serves as the light source, and the laser beam is focused through an objective lens on the test and control lines of the LFA strip. The laser beam is moved in 200 μm intervals in the $x$ and $y$ axes using a laser scanning module to obtain a reproducible Raman signal, and Raman mapping signals for 39 pixels for both test and control lines are obtained and averaged. For quantitative analysis, the target protein concentration is determined based on the Raman intensity ratio obtained for the test and control lines, which would indicate a positive or negative result. Fig. 15c compares the sensitivity of the on-site SERS-LFA system using a portable Raman strip reader with that of a commercial colorimetric LFA strip. Based on the cycle threshold (Ct) value of RT-PCR, when the concentration of the virus is very high (Ct < 25), both LFA and SERS-LFA would show a positive result, and both methods would show a negative result for non-infected samples. However, the false-negative diagnostic rate is expected to be significantly reduced when using the SERS-LFA system for early infected patients with a low virus concentration or asymptomatic infected patients (Ct > 25). After testing 54 clinical samples in the range of 0 < Ct < 35, a commercial LFA strip showed a sensitivity of approximately 35% for 31 clinical samples with 25 < Ct < 35. On the other hand, the sensitivity of the SERS-LFA system was 93%. Therefore, the SERS-LFA system could markedly improve the false-negative diagnostic rate by significantly increasing the diagnostic sensitivity for patients with a low concentration of the SARS-CoV-2 virus.[570]

ELISA techniques are widely used instead of LFA strips to perform protein assays in the laboratory. For SERS-ELISA, Au NPs are often used as SERS nanotags; however, signal enhancement is limited due to the lack of hotspots between particles in the nanogap. A 96-well plate coated with Au has been commercialized for nano-plasmonic immunoassay to induce hotspots between Au NPs and substrate surfaces. However, such a plate is expensive, and it is not easy to control hotspots accurately during the assay process. To address this problem, $SiO_2$-coated core–satellite (CS) Au@Au SERS nanotags have been developed by assembling 32 nm and around 75 nm Au NPs.[571] Multiple hotspots could be formed within individual CS NPs due to the abundance of nanogaps formed between the Au NP core and Au NPs satellite, resulting in greatly amplified EM signals. In addition, the stability of SERS nanotags could be improved by encapsulating $SiO_2$ on the CS surface, improving antibody immobilization and assay effectiveness. Immunoassays were performed using SARS-CoV-2 lysates at the same concentration to evaluate the plasmonic coupling characteristics and stability of CS@$SiO_2$ SERS nanotags. In comparison with conventional ELISA based on absorption/fluorescence detection methods or SERS-ELISA using Au NPs, the sensitivity and reproducibility of SERS-ELISA using CS@$SiO_2$ SERS nanotags were significantly improved. Fig. 16 shows a schematic of SERS-ELISA using CS@$SiO_2$ SERS nanotags. A 384-well plate was used in SERS-ELISA instead of the 96-well plate typically used in conventional ELISA to analyze as many clinical samples as possible in a high-throughput manner. In comparison with the 96-well plate, the 384-well plate could lower the assay cost by reducing the amount of expensive capture and detection antibodies required for the assay because the sample volume in each well is reduced from 400 μL to 130 μL. Additionally, the amount of target antigens can be quantified by measuring the Raman signal of SERS nanotags directly bound to them without an additional enzymatic reaction to induce a color change with a secondary antibody, which is required in conventional absorbance-based ELISA. This straightforward approach is advantageous for applying the SERS-ELISA technique to biomedical analysis (Fig. 16c). Fig. 16d shows the results of assays with SARS-CoV-2 lysates using three different SERS nanotags: CS@$SiO_2$, silica-encapsulated hollow Au NP (HAuNP@$SiO_2$), and silica-encapsulated AuNP (AuNP@$SiO_2$). As expected, HAuNP@$SiO_2$ and AuNP@$SiO_2$ demonstrated poor sensitivity due to limited EM enhancement at the individual particle level. On the other hand, multiple hotspots could be created within one unit using CS@$SiO_2$ SERS nanotags, resulting in significantly increased sensitivity. Therefore, the SERS-based assay platform may be a next-generation *in vitro* diagnostic technology that can overcome the sensitivity limits of existing on-site diagnostic methods for infectious diseases.

### 3.5. SERS for monitoring reaction progress and intermediates

It is critical to analyze the intermediates of a reaction to understand their mechanisms. Traditionally, IR, NMR, or other spectroscopy techniques have been used to probe the reaction progress and intermediates. In the last decade, SERS has emerged as an alternative and noninvasive method to monitor reaction progress by *in situ* analysis of reaction products and intermediates because of the ability to provide molecular-level information about the chemical composition of molecules.[572] It has been used to study a wide range of chemical reactions, including catalytic reactions, electrochemical reactions, and photochemical reactions because it provides important

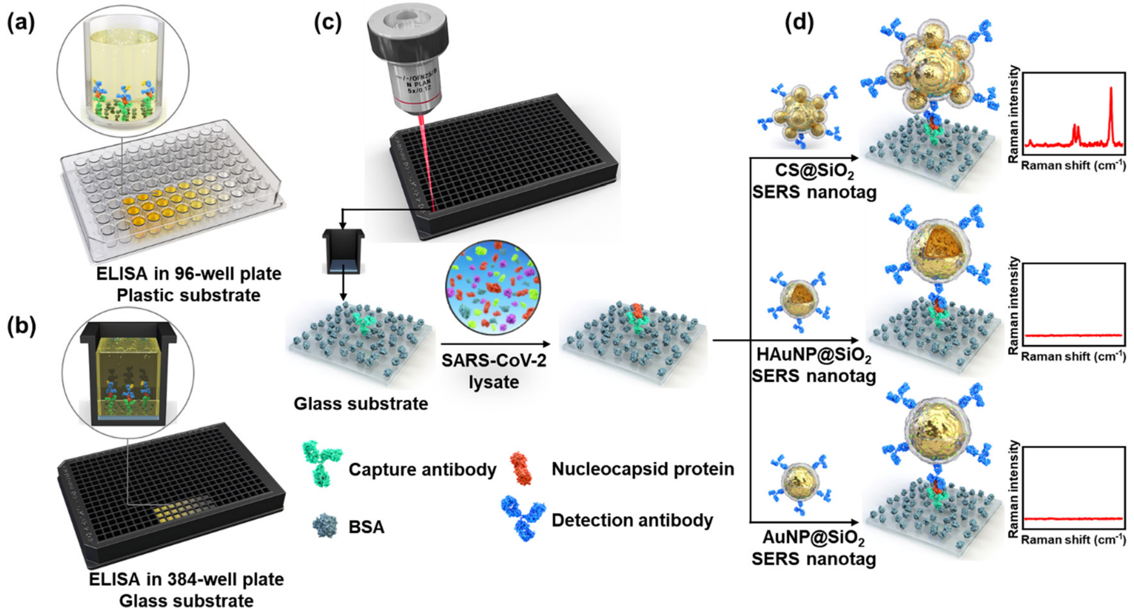

Fig. 16 Schematic illustration of the SERS-ELISA method using CS@$SiO_2$ ($SiO_2$-coated core–satellite Au@Au NPs) SERS nanotags. Conventional ELISA using (a) a 96-well plastic plate and (b) a 384-well glass plate. (c) SERS-ELISA of SARS-CoV-2 in a 384-well glass plate using SERS nanotags. (d) Evaluation of SERS-ELISA for detecting SARS-CoV-2 using CS@$SiO_2$ (top), HAuNP@$SiO_2$ (middle), and AuNP@$SiO_2$ (bottom) SERS nanotags. Reproduced from ref. 571 with permission from Elsevier publisher, Copyright 2023.

insights into the reaction mechanism and kinetics, and the nature of the reaction intermediates (Fig. 17). In this section, we will discuss the research progress on studying chemical transformation by SERS probing of reactants and products.

### 3.5.1. Study of reaction progress by SERS.

SERS can be used to monitor the content of reactants and products in real-time, providing information about the kinetics of the reaction. It can also be used to study the effect of the reaction conditions, such as temperature, pressure, and pH, on the reaction progress by monitoring the peaks related to reactants, products, and intermediates. One of the most studied examples of catalytic reactions is the reduction of *p*-nitrophenol (*p*-NP) into *p*-aminophenol by sodium borohydride in the presence of plasmonic NC catalysts. This reaction follows pseudo-first-order kinetics, and it is easy to follow its progress by UV-vis absorption spectroscopy and SERS due to the high cross-section of the reactants and the products. In this context, Zheng *et al.* employed SERS to monitor the reduction of *p*-NP on filter paper loaded with Au NPs.[574] As shown in Fig. 17b, the intensity of the SERS signal of *p*-NP (peaks at 1343 and 1571 $cm^{-1}$) decreased with time, while the intensity of the SERS signal of *p*-aminophenol (1593 $cm^{-1}$), which corresponds to the final product, increased with time. In the final spectra (green), there are no *p*-NP peaks, only the peaks that correspond to *p*-aminophenol present, indicating the completion of the reaction. Similarly, SERS has also been used to study the kinetics of reactions with biomedical relevance. In this regard, Taladriz-Blanco *et al.* demonstrated the use of bimetallic AuAg NPs coupled to carbon nanotubes (CNT@AgAu) as catalysts to trigger the release of nitric oxide (NO) from aromatic nitrosothiols (RSNOs) at physiological pH.[575] The RSNO bond was immediately cleaved due to the high affinity of gold for thiols, liberating NO and aromatic thiol. In this case, the nitrosothiols are bound to gold and release NO, and the process can be monitored by SERS using aromatic thiols as spectroscopic labels. The ring breathing mode of the thiol (1072 $cm^{-1}$) was used as a label to monitor the first-order NO-releasing process. Moreover, the authors showed that by tuning the gold amount in bimetallic nanoparticles, the rate of NO generation can be controlled.

Besides, SERS has also been employed to study the reaction progress of photochemical reactions. For instance, one of the most important photochemical reactions is the reduction of $CO_2$ into other organic species, which is critical to reducing greenhouse gases. Probing such a catalytic process and knowing intermediates could help to design better catalytic systems. With this aim, Devasia *et al.* have used SERS to determine a large number of C–C species formed by the photocatalyst reduction of $CO_2$ in the presence of a plasmonic structure.[576] Likewise, Kumari *et al.* studied the reaction progress of the photocatalytic reduction of $CO_2$ on a plasmonic nanoparticle by SERS.[577] They also found the formation of intermediate species, whose concentration increased at the early stage of the reaction and then decreased in later states, suggesting that these species were the intermediates in the reaction, thanks to the high specificity and sensitivity of SERS.

### 3.5.2. Identification and characterization of reaction intermediates by SERS.

Another of the greatest features of the SERS technique is its ability to provide molecular-level information about the chemical composition of the molecules attached or close to the plasmonic NP's surfaces. This makes SERS an excellent tool for identifying and characterizing reaction intermediates in chemical reactions when these intermediates are stable at least for the minimum time required to measure.

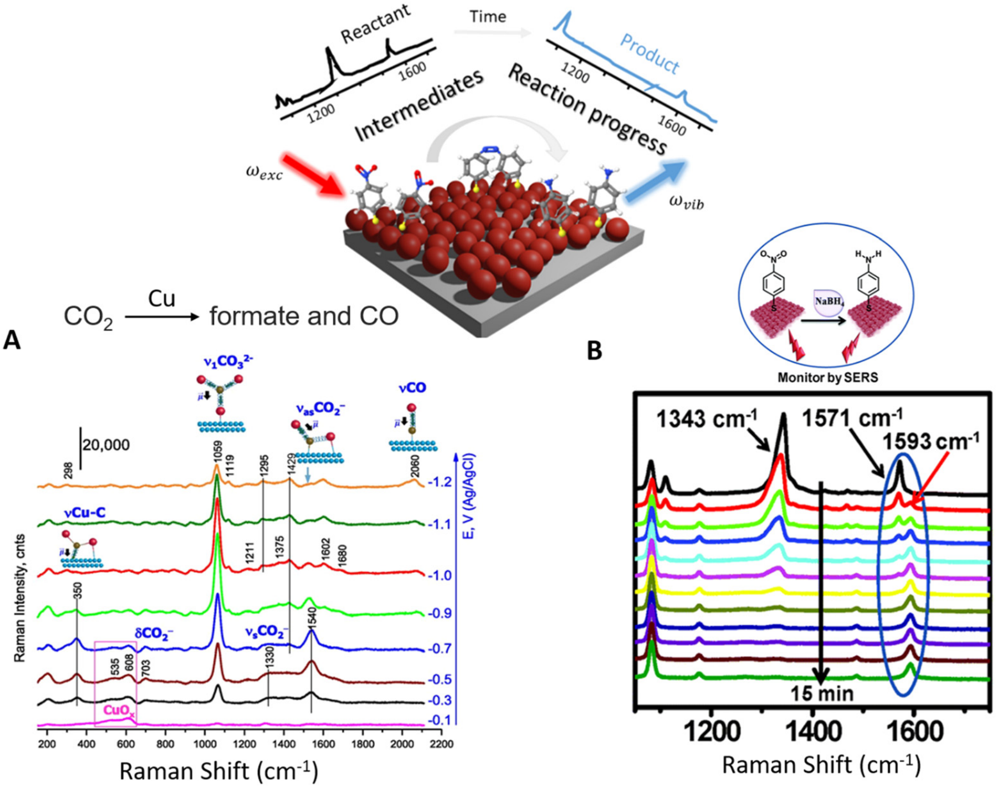

Fig. 17 Schematic illustration of probing reaction progress and intermediates by SERS by collecting inelastic light scattering by molecules adsorbed on a metallic surface. (a) SERS spectra of intermediates of the transformation of $CO_2$ into formate and CO on a Cu surface Reproduced from ref. 573 with permission from PNAS, Copyright 2018. (b) Time-dependent SERS spectra of the conversion of *p*-NP conversion into *p*-aminophenol. The reaction can be probed by the disappearance of *p*-NP bands and the evolution of peaks of the product (*p*-aminothiophenol) with time. Reproduced from ref. 574 with permission from RSC publisher, Copyright 2015.

Several studies have used SERS to identify and characterize reaction intermediates in catalytic reactions. Due to the intrinsic nature of SERS, it allows us to follow the formation of new components with different vibrational bands. For instance, the catalytic hydrogenation of *p*-NP can be considered a two-step consecutive reaction, either *via* the formation of an azo compound or *via* the formation of the hydroxylamine intermediate.[578] Normally, the formation of any of these intermediates and their kinetic are difficult to follow due to the reaction being too fast to observe *via* SERS. However, by reducing the amount of sodium borohydride, the reaction can be slowed down and then it is possible to observe the formation of the 4,4′-dimercaptoazobenzene, the intermediate in the reduction of *p*-NP.[579,580] Regarding this, Xie *et al.* have performed a SERS study of the reduction of *p*-NP in a microfluidic system. They were able to detect the intermediate by SERS when the laser is switched on, and the *p*-NP when the laser is off.[581] This technique has also been used to identify and characterize reaction intermediates in photochemical reduction reactions. For instance, Chernyshova *et al.* have resolved the discrepancy in the first step of $CO_2$ reduction into fuels in aqueous electrolytes (Fig. 18a).[573] They observed, through SERS, the formation of a carboxylate anion coordinated to the surface through the C–O bonds. The small changes in the vibrational states of different molecular species (CO, $CO_3^{2-}$ and $CO_2^{-}$) have been distinguished by SERS, as shown in Fig. 18a. The plasmonic NPs used, either for as catalysts or to induce SERS signals, can also provide electrons to the molecules absorbed on their surfaces upon photoexcitation, as shown in Fig. 17a and b.[582] The hot-electron transfer to nearby molecules (*p*-ATP) can trigger chemical transformations, which can be probed by SERS. As shown in Fig. 18c and d, the relative SERS intensity of DMAB to *p*-ATP linearly increases with the increase of excitation laser power, suggesting the hot-electron-driven chemical transformation.[582]

Similarly, SERS has also been used to study the reaction intermediates in oxygen reduction reactions on a platinum surface.[583] It was found that the type of intermediates depends on the pH or the crystalline structure of the surface. In this case, at high pH, only one intermediate was observed independent of the Pt crystalline structure. When the oxygen reduction reaction was performed at normal conditions, the intermediate $HO_2^*$ was adsorbed on the Pt (111) surface, while the Pt (110) and Pt (100) surfaces preferentially adsorb the intermediate HO*. In conclusion, SERS has evolved as a powerful analytical technique that can provide molecular-level information about the transformations and reaction kinetics. However, it is only limited to specific reactions where the analytes physically or chemically adsorb on plasmonic substrates. More studies are needed in the future to fully exploit the power of SERS in understanding reaction mechanisms.

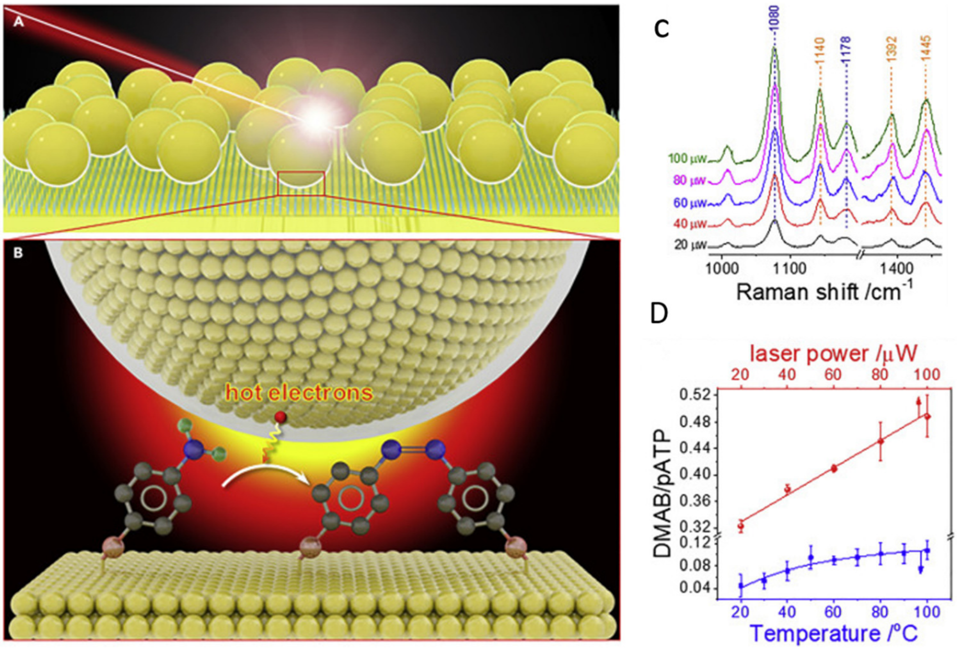

Fig. 18 (a) Scheme of *in situ* SERS study on the interfacial hot electron transfer in the photocatalytic conversion of *p*-aminothiophenol (*p*-ATP) to dimercaptoazobenzene (DMAB). (b) SERS spectra of the conversion of *p*-ATP catalyzed by Au NPs at different laser power excitations. (c) The relative intensity of DMAB to *p*-ATP bands with different incident laser powers. The figure is adapted from ref. 582 with permission from Springer, Copyright 2020.

### 3.6. Tip-enhanced Raman scattering

As a powerful analytical technique, SERS can demonstrate detection sensitivity at the molecular scale under the plasmon enhancement effect. It can provide rich molecular structure information to analyze chemical composition and structure accurately.[85,195,584] However, the enhancement effect of the SERS signal depends on the experimental conditions and the nanostructure of the sample surface, which is not stable enough in practical applications. Second, background interference significantly affects SERS signals, especially those from fluorescence and scattering, reducing the detection sensitivity of target substances.[198] In addition, fabricating and controlling high-quality SERS-enhanced substrates remains challenging, especially for large-scale fabrication and practical applications. Tip-enhanced Raman scattering (TERS) is based on scanning electron/atomic force microscopy, which can achieve high-sensitivity Raman signal detection and perform high-precision morphology characterization of detection targets in real-time and realize detection at the single-molecule scale. SERS and TERS utilize the plasmon enhancement effect to enhance the Raman scattering signal. SERS focuses on nanostructured surfaces local EM field enhancement effect, while TERS achieves higher resolution and more sensitive analysis through the local enhancement effect of nanotip probes. TERS uses the local enhancement effect of tip probes (such as metal needle tips) to focus the enhanced electric field to the nanometer scale to achieve high-resolution Raman images and spectral information acquisition of samples.[72,585–587] Compared with SERS, TERS has higher spatial resolution and sensitivity requirements, so it has a wide range of applications in nanomaterial characterization, surface catalysis, and biological analysis. TERS is an enhanced Raman technique based on metal tip probes, generally consisting of a tip (such as a metal tip) and a Raman spectrometer shown in Fig. 19a.

The initial development of TERS can be traced back to the early 1990s due to advances in atomic force microscopy (AFM).[592] At that time, researchers began to try to use the tip to achieve high spatial resolution Raman spectroscopy measurements on samples. Initial studies focused on using the local electric field enhancement effect at the metal tip to enhance the intensity of the Raman signal. Deckert *et al.* found in 2000 that the Raman scattering signals of brilliant cresyl blue (BCB) molecules and $C_{60}$ molecules could be enhanced in the nanometer range using the AFM-TERS system in an atmospheric environment, as shown in Fig. 19b.[588] The spatial resolution of the sample is limited only by the size and shape of the apex of the metal tip and does not require special sample preparation. Moreover, the Raman signal enhancement uniformity at any sample position is excellent, so the quantitative measurement of the SERS spectrum can be performed. In addition, when the tip of the AFM-TERS system scans the surface of the sample, the morphology characterization results of the sample can be obtained simultaneously and correspond to the spectral data. Comparing the Raman signal when the metal tip is close to and away from the sample, it can be shown that the essence of the enhancement is due to the local EM field accumulated at the apex of the metal tip, which amplifies the Raman signal of nearby molecules. Moreover, using this method, the laser wavelength can be adjusted to precisely match the corresponding plasmon frequency to achieve Raman signal enhancement of a single molecule. For the TERS

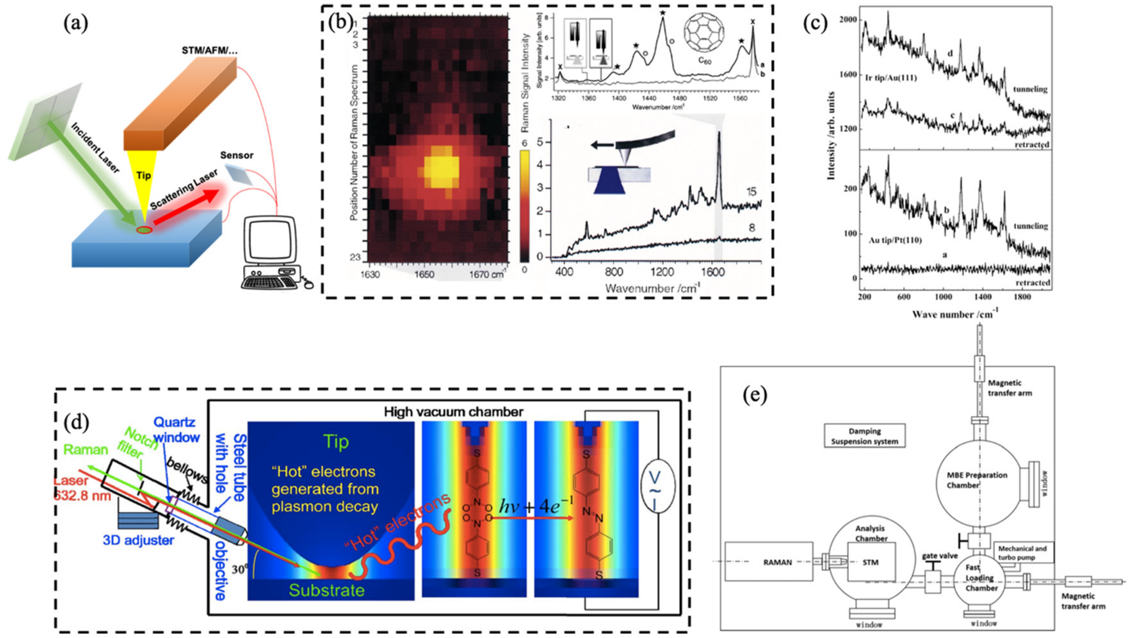
(a)
STM/AFM/...
Incident Laser
Tip
Sensor
Scattering Laser
(b)
Position Number of Raman Spectrum
Raman Signal Intensity
C60
Wavenumber /cm-1
(c)
Ir tip/Au(111)
tunneling
retracted
Au tip/Pt(110)
Intensity /arb. units
Wave number /cm-1
(d)
Raman
Notch filter
Quartz window
Laser 632.8 nm
bellows
3D adjuster
Steel tube with hole
objective
High vacuum chamber
Tip
"Hot" electrons generated from plasmon decay
"Hot" electrons
Substrate
hν + 4e-1
(e)
Magnetic transfer arm
Damping Suspension system
MBE Preparation Chamber
Analysis Chamber
RAMAN
STM
gate valve
Fast Loading Chamber
Mechanical and turbo pump
window

Fig. 19 (a) Schematic diagram of the TERS system. (b) TERS spectra of C60 and BCB samples and mapping of BCB, Reproduced from ref. 588 with permission from Elesvier publisher, Copyright 2000 (c) TERS and RRS of $CN^{-1}$. Top panel: Ir tip/Au (111), bottom panel: Au tip/Pt (110) Reproduced from ref. 589 with permission from American Physical Society publisher, Copyright 2004 (d) Schematic and physical mechanism of HV-TERS, Reproduced from ref. 590 with permission from Nature publisher, Copyright 2012 (e) HV-TERS system structure (including analysis chamber, fast loading chamber, and molecular beam epitaxy chamber), Reproduced from ref. 591 with permission from AIP publisher, Copyright 2016.

structure, the metal tip and substrate are the cores of the whole detection system. Choosing different materials to prepare metal tips and substrates with various shapes will also affect the detected Raman signal. Pettinger *et al.* used Ir and Au as other metal tip materials. They used Au (111) and Pt (110) single crystal surfaces as scanning tunneling microscopy (STM)-TERS substrates, respectively, to study the Raman signal enhancement effect of malachite $CN^-$.[589] As shown in Fig. 19c, the enhancement effect of the Ir tip on the $CN^-$ molecules on the Au (111) substrate is close to $4 \times 10^5$, and when the tip is far away, the resonance Raman scattering (RRS) on the Au (111) is also apparent. But for the Au tip and Pt (110) substrate, the TERS signal of the $CN^-$ molecule is gradually enhanced when the Au tip is close. However, when the Au tip moved away slowly, no RRS signal was found on the surface of the Pt (110) substrate. On the one hand, the interaction between Au and $CN^-$ molecules will make the Au substrate and $CN^-$ molecules form a stable coordination bond, while the adsorption of $CN^-$ molecules on the Pt surface is weak. On the other hand, the Ir tip has a higher local electric field enhancement effect than the Pt substrate, which can enhance the Raman scattering signal intensity of $CN^-$ molecules. However, the local electric field enhancement effect between the Au tip and the Pt substrate is weak.

Despite that, various gas molecules existing in the atmospheric environment may interact with the sample surface and interfere with the acquisition and analysis of Raman signals. In the atmospheric environment, the electrostatic effect on the sample surface will cause its charge distribution to change, thereby interfering with the Raman signal. Fortunately, these unfavorable factors can be perfectly solved in the high vacuum (HV)-TERS system, but the insufficient optical collection efficiency is a huge hindrance to designing HV-TERS systems. As shown in (Fig. 19d) Sun *et al.* designed an HV-TERS system based on STM equipment to meet the requirements of optical collection efficiency and used it to research the reduction reaction of 4-nitrobenzenethiol (4-NBT) to dimercaptoazobenzene (DMAB) catalyzed by local hot-electron induction.[590] The plasmon intensity can control the chemical reactions in the high vacuum environment, while the local EM field intensity at the tip can be controlled by the incident laser intensity, tunneling current and bias voltage in the HV-TERS system. The high vacuum environment not only solves the problems in the measurement process, but also avoids the interference of molecules in the atmospheric environment on the Raman signal, and also prevents the interaction between the atmospheric environment and the sample, so that the monitoring of catalytic reactions and reduction reactions can be realized. The completion of this work provides a new way to realize efficient HV-TERS system, chemical catalysis and molecular synthesis. After that, Sun *et al.* further optimized the HV-TERS system. As shown in Fig. 19e, they placed the sample preparation, transfer, spectral measurement, and imaging in a high vacuum environment of $10^{-7}$ Pa, which can ensure the cleanliness of the sample and avoid material interference.[591] This study enables the analysis of the nature of plasmon-driven reactions on metal surfaces in a pure environment.

After completing the design and practicality of the HV-TERS system, how to complete the imaging and detection of TERS spectra at the single-molecule spatial resolution scale has become a new direction for researchers. Fig. 20a shows that based on the spectral matching between plasmon resonance and molecular vibrational electronic transitions, Hou *et al.* have realized Raman spectral imaging with a spatial resolution below 1 nm and can resolve the internal structure and surface configuration of a single molecule. They exploited the extremely strong plasmon resonance effect between the Ag tip and the substrate to realize the detection of the single-molecule TERS spectrum of meso-tetrakis(3,5-di-*tert*-butylphenyl)porphyrin ($H_2$TBPP) and study its dependence on the molecular orientation. The TERS mapping of $H_2$TBPP single molecule on Ag (111) substrate was also completed. This work advances the detection and imaging technology of the HV-TERS system at the single-molecule scale with spatial resolution. Wu *et al.* designed a high-performance TERS structure based on the low-temperature HV-TERS system combined with the molecular beam epitaxy (MBE) system.[593] In Fig. 20b, it can not only realize the preparation of 2D materials, but also complete *in situ* STM imaging and TERS detection. In an ultra-low temperature environment, the HV-STM-TERS system can achieve an enhancement factor of $10^9$ and a spatial resolution of 0.5 nm for 2D silicene. If the TERS structure is combined with a femtosecond laser system, it is possible to realize femtosecond excitation TERS on a time-resolved scale. In previous work, they also used this system to identify different vibrational properties of silicene phases in different bending directions of Si–Si bonds. The local vibration signatures of silicene defects and edge positions can also be successfully identified.[594] In TERS studies, the monitoring of catalytic reactions at time resolution enables the detection and recording of fast vibrations and dynamic changes in the sample. Molecular dynamics on nanosecond and sub-nanosecond time scales can be captured. Weckhuysen *et al.* used the TERS system to study time-resolved tip-enhanced Raman spectroscopy to monitor catalytic reactions at the nanoscale, which is shown in Fig. 20c.[595] A silver tip to enhance the Raman signal and act as a catalyst is placed near the surface of the Au substrate with *p*-nitrothiophenol (*p*NPT). A 532 nm laser was used to induce the photocatalytic reduction process at the apex of the tip, and a 633 nm laser was used to monitor the conversion process during the reaction. This research, based on the high spatial resolution of TERS, shows great promise for studying time-resolved molecular dynamics processes on individual catalytic particles, especially for heterogeneous catalysis.

The surface plasmon is a collective oscillation mode at the interface of a metal surface and a medium, resulting from the interaction of free electrons with an optical field. Excitons are quasiparticles in solids, bound states formed by Coulomb interactions between electrons and holes. When an LSPR is coupled to an exciton, the plexciton is produced, which has both LSPR and exciton characteristics. It leads to the rearrangement of their energy level structure, the energy exchange between photons and electron–hole pairs, and coupling together to form new excited states. The field localization makes plexciton have a strong localized EM field enhancement effect in the nanoscale range,

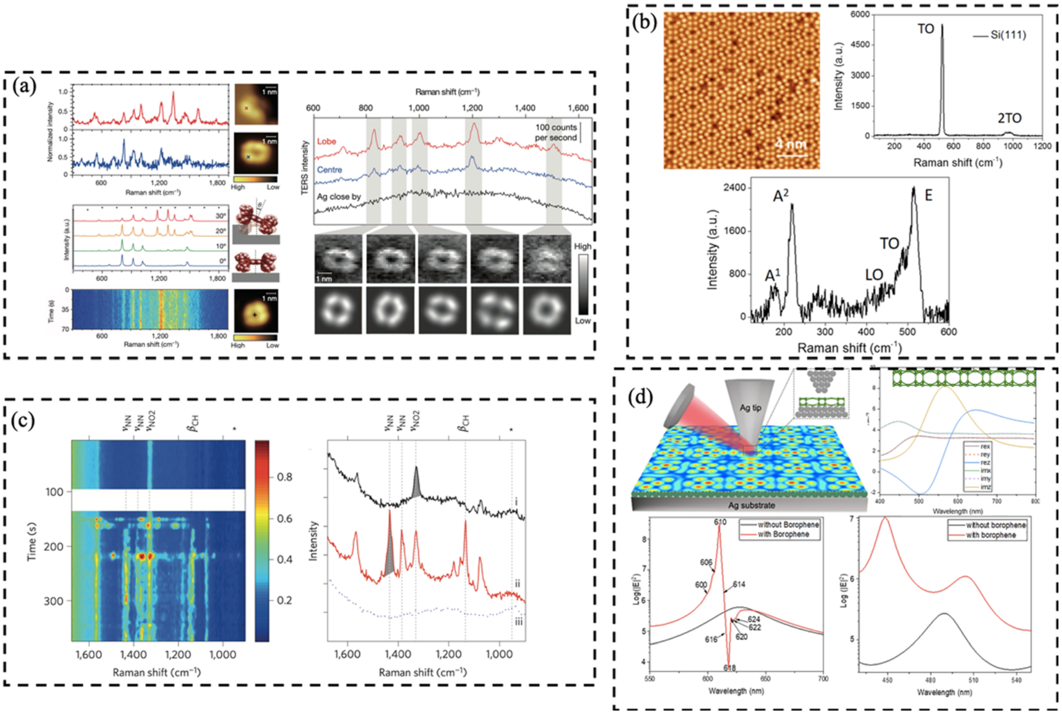

Fig. 20 (a) Single-molecule TERS spectra and their dependency on molecular orientations, and TERS mapping of a single $H_2$TBPP molecule on Ag (111), Reproduced from ref. 596 with permission from Nature publishing group, Copyright 2013 (b) STM image of the Si (111) and *in situ* normal Raman spectrum of the Si (111) surface/coexisting phases, Reproduced from ref. 593 with permission from Elsevier publisher, Copyright 2018 (c) time-dependent TERS measurement before and after reaction, Reproduced from ref. 595 with permission from Elsevier publisher, Copyright 2012 (d) TERS-BL borophene system and plexciton traits, Reproduced from ref. 597 with permission from AIP publisher, Copyright 2023.

which will enhance the absorption and scattering of light. Based on the characteristics of plexciton, Sun *et al.* constructed the TERS-BL borophene system with the Ag tip and the Ag substrate surface double-layer borophene, as shown in Fig. 20d.[597] The negative real part of BL borophene in the strong coupling region indicates that it has the plasmonic properties of metals, leading to the Rabi splitting of plexcitons. The Fanoresonant propagating plexcitons appear in weakly coupled regions. The plasmonic properties of TERS and BL borophene around 488 nm originate from the coupled plasmon–exciton interaction, resulting in two plexciton peaks. This research demonstrates that plexciton-selectively enhanced spectroscopy is possible for the TERS-BL borophene system based on the plasmon–exciton coupling effect. Meanwhile, it provides a new idea for the future use of the TERS system in the study of the corners of 2D materials. Both SERS and TERS are enhanced Raman scattering techniques, which have critical applications in molecular-level characterization and analysis. SERS utilizes the localized EM field on the surface of metal nanostructures to enhance the Raman signal, while TERS further enhances the Raman signal by forming a nanoscale localized EM field between the metal tip and the sample. Therefore, TERS can be seen as an extension and improvement of SERS, achieving higher spatial/time resolution and sensitivity.

### 3.7. SERS data analysis

In-depth analysis of the inherently complex SERS data often holds the key to elucidating the wealth of chemical information that is embedded within.[246,598–600] In recent decades, the progressive shift from traditional manual visual inspections of acquired SERS spectra to state-of-the-art chemometric and machine learning (ML) approaches has unlocked numerous potential applications of SERS-based nanosensors in the biomedical, environmental, and food industries.[601–604] Fundamentally, these exciting achievements leverage advancements in both SERS-based sensing technologies as well as ML-driven data processing to accomplish breakthroughs in analyte identification and quantification. However, such success is heavily dependent on the ability to judiciously translate subtle differences present within high-dimensional SERS data into unbiased analyte identification and quantification outcomes through robust visualization or predictive models.

The inherent complexity of SERS data stems from the representation of its fingerprint region as thousands of individual wavenumber-to-intensity values, depending on the spectral resolution. For chemometric and ML analysis, such a large number of input features can complicate the problem unnecessarily as (1) the algorithms struggle to find a generalizable function that describes the observations, (2) the signal-to-noise ratio may be lowered as a result of uninformative data, leading to model overfitting.[605] Hence, a common and intuitive approach is to decompose SERS data with dimensionality reduction algorithms. Some ubiquitous examples include linear methods such as PCA, linear discriminant analysis (LDA), and singular value decomposition (SVD), as well as nonlinear methods such as isometric mapping (Isomap), t-distributed stochastic neighbor embedding (t-SNE) and uniform manifold approximation and projection (UMAP) (Fig. 21a).[606,607] In this section, we will briefly discuss some applications using PCA, t-SNE and UMAP.

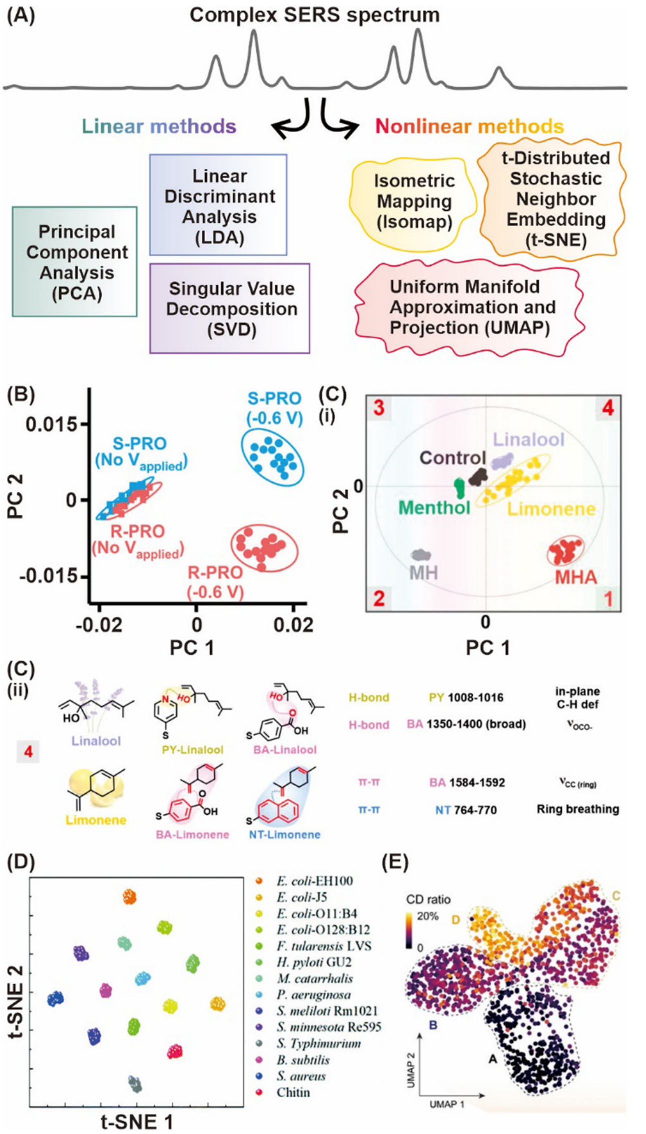

Fig. 21 Dimensionality reduction algorithms decompose and visualize high dimensional SERS data based on their most significant variations. (A) Scheme describing common dimensionality reduction techniques. (B) PCA score plot of *R*- and *S*-propranolol (PRO) based on their naphthyl vibrational modes with and without an applied voltage. Reproduced from ref. 608 with permission from ACS publisher, Copyright 2021. (C) (i) PCA score plot showing the relative flavor data cluster separation using the SERS taster strategy. (ii) Correlating PCA scores in terms of the relative flavor data cluster positions with its loadings, elucidating key receptor–flavor interactions and their corresponding vibrational peak assignment. Reproduced from ref. 409 with permission from ACS publisher, Copyright 2021. (D) t-SNE plot of the 256-feature space projected onto a 2D map extracted by the modified 1D convolutional neural network model (RamanNet). Reproduced from ref. 609 with permission from RSC publisher, Copyright 2022. (E) UMAP representation of phenotypic responses based on the whole Raman fingerprint region of all individual cells under ampicillin treatment where each point is a measurement of a single cell. Reproduced from ref. 610 with permission from Wiley-VCH GmbH publisher Copyright 2023.

As a stand-alone technique, PCA is a simple unsupervised clustering algorithm that allows automated, objective, and concurrent comparison of numerous SERS spectra based on their most significant variations. For example, Leong *et al.*

utilized PCA to distinguish the propranolol enantiomeric pair accurately highlighting visible differences in their naphthyl vibrational modes with electrochemical SERS (EC-SERS) sensing on nanoporous Au bowls (Fig. 21b).[608] Even if the spectral differences appear subtle, the ability to interpret PCA scores through their component loadings enables retrospective correlations to attribute key vibrational modes. This can be seen in Leong *et al.*'s work, in which detailed analyses of the PCA loadings plot revealed crucial receptor-flavor compound SERS interactions arising from each receptor, which contributed to the distinct score clusters of five different flavor compounds (Fig. 21c).[409]

Apart from functioning as a stand-alone technique, PCA can also act as a preliminary decomposition step that is easily integrated into customized workflows. This is highly desirable to avoid classifier oversampling of SERS data, where the number of features often easily outnumbers the number of samples.[611,612] In Safir *et al.*, PCA was utilized to reduce a 508 wavenumber SERS spectrum to 24 principal components accounting for 90% of the overall variance captured.[613] Subsequent input to a random forest classifier enabled $\geq$87% classification accuracy across acoustic bioprinted droplets containing Au NRs mixed with three single-cell-line and three bacteria mixtures. Despite gaining widespread popularity, one of the most critical drawbacks of PCA being a linear dimensionality reduction technique has become increasingly evident, especially for tasks where a nonlinear relationship between key components is expected. This motivated the venture towards nonlinear techniques such as t-SNE and UMAP, which are capable of preserving much of the local structure while also revealing global structure as clusters at various scales in high-dimensional SERS data.[614,615] Briefly, t-SNE is primarily a visualization technique that evaluates pair-wise similarities and models them in a low-dimensional (2D/3D) scatter plot. For instance, a t-SNE plot was employed to illustrate maximal cluster separations attained with 256 features extracted by a modified convolutional neural network (CNN) (Fig. 21d).[609] The high distinctiveness is a result of clear SERS spectral differences of 11 bacterial endotoxins acquired using an Ag NR array.

In contrast, UMAP is a generalizable dimensionality reduction technique like PCA, based upon the well-established manifold approximation theory. Moreover, UMAP offers comparable visualization quality to t-SNE, albeit being a relatively new technique. Yang *et al.* exemplified the capability of UMAP in revealing four bacterial subpopulations with distinct phenotypic responses to increased antibiotic stress during resistance evolution through 1250 single-cell SERS spectra.[610] Importantly, these algorithms are built upon robust mathematical frameworks and are applicable for large datasets with complex underlying correlations, making them invaluable to numerous applications in SERS and beyond.

Besides trying to reduce the complexity of SERS data, it is also imperative to pick up even the most minute spectral variance to accurately predict the type and amount of an analyte present. To date, a whole suite of algorithms including but not limited to regression-based algorithms like partial least-squares (PLS), support vector machines (SVM), tree-based frameworks like random forest (RF) and neural networks like CNN exist for this purpose. In general, they traverse different routes to reach the same goal – that is to establish a universal set of mathematical functions to describe the observed relationship between SERS variations and assigned data classes. When adeptly deployed, these powerful algorithms can swiftly highlight subtle spectral variances almost invisible to the naked eye and provide new chemical insights that may otherwise be overlooked. This is apparent in Nguyen *et al.*, where the use of SVM to construct calibration curves was instrumental in enabling multiplex trace quantification of small gaseous molecular targets (sulfur and nitrogen dioxides) (Fig. 22a).[392] They justified that a ring complexation strategy involving two SERS-based molecular receptors was crucial to induce key SERS spectral variances, which in turn allowed the SVM model to achieve a 91.7% quantification accuracy. Similarly, Shin *et al.* employed a CNN model to attain a diagnostic sensitivity of 90.2% and specificity of 94.4% for six types of early-stage cancers (lung, breast, colon, liver, pancreas, and stomach) by analyzing the SERS profiles of exosomes (Fig. 22b).[616] Importantly, they found that the first convolutional layer was particularly influential in elucidating the complex exosomal Raman fingerprints contributed by numerous protein constituents.

It is also interesting to note that, while seemingly contradictory, deliberate amplification of SERS data dimensionality

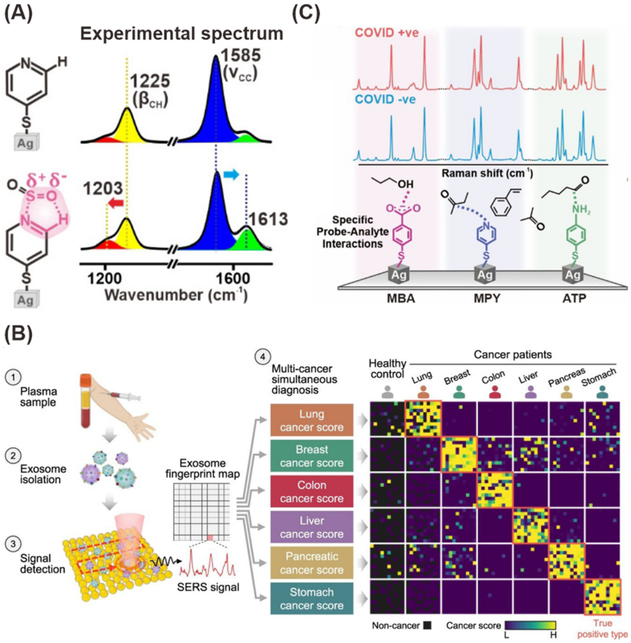

Fig. 22 ML-driven classification and regression models constructed based on subtle SERS spectral differences. (A) Formation of a five-membered ring complex with sulfur dioxide inducing spectral variations that are visually subtle. Reproduced from ref. 392 with permission from Wiley-VCH GmbH publisher, Copyright 2024. (B) Obtaining exosome SERS fingerprints from plasma samples of patients with six different types of cancer. The CNN model outputs predictions about cancer presence and tissue of origin. Reproduced from ref. 616 with permission from Springer Nature publisher, Copyright 2023. (C) Combining three receptor SERS spectra as a "SERS super-profile" to discriminate the breath profiles of COVID-positive and healthy individuals. Reproduced from ref. 393 with permission from ACS publisher, Copyright 2022.

has been proven as a sound strategy specifically for molecular receptor-based SERS sensing. This is because hosting a series of nonspecific noncovalent interactions can effectively probe different facets of target analytes and provide meaningful information about complex sample matrices.[617] This concept was highlighted by Leong *et al.*, where the combination of spectral information arising from three molecular receptors allowed ≥ 95% sensitivity and specificity in the SERS-based distinction of healthy breath volatile organic compound (BVOC) profiles and individuals infected with coronavirus disease 2019 (COVID-19) (Fig. 22c).[393] Such diverse strategic choices demonstrate the immense potential and versatility of ML algorithms in providing tailored solutions when analyzing complex SERS data.

While sophisticated algorithms can deliver unprecedented results, it is pertinent to ensure that a constructed predictive model is interpretable and remains grounded in strong scientific principles. In fact, the loss in model interpretability often results in the "black box" phenomena or the generation of grossly overfit models that crumble when exposed to unseen data. To avoid this pitfall, a straightforward approach is to extract feature importance and corroborate important features to known Raman vibrational modes, thereby deducing molecular-level insights. For algorithms that do not possess inherent interpretability, framework-agnostic methods such as local interpretable model-agnostic explanations (LIME), Shapley additive explanations (SHAP), and contrastive explanation method (CEM) aim to provide a generalized and comprehensive set of feature rankings.[618–620] Alternatively, Živanović *et al.* evaluated specialized approaches like the minimal depth variable selection (MD) and surrogate minimal depth (SMD) technique in ranking important SERS bands found with a RF model.[621] These bands elucidated the presence of cholesterol amongst sphingomyelin and other lipid entities in the analysis of lipid accumulation in lysozymes after treatment with three antidepressants. Naturally, such understanding will also guide downstream feature selection and engineering protocols which can convert wavenumber-based data into more chemically meaningful representations such as peak positions and intensities.

Overall, we have provided a concise overview of the application of state-of-the-art artificial intelligence-driven ML algorithms in SERS data analytics, including dimensionality reduction and visualization algorithms, classification and regression predictive modeling and interpretability techniques. Notably, this overview precludes other expansive topics such as feature selection and engineering as well as data augmentation methods which should be considered of equivalent importance to those covered. Nonetheless, the inherently challenging nature of high-dimensional SERS data presents an interesting conundrum that is likely to motivate further explorations and fuel more exciting discoveries.

# 4. Surface-enhanced fluorescence (SEF) plasmonic sensors

Various techniques, such as multiple-fluorophore labels,[622] rolling circle amplification,[623,624] and photonic crystal enhancement,[625] have been explored to improve the signal-to-noise ratio of fluorescence-based sensing and imaging techniques. Despite the improved sensitivity, these technologies are not widely adopted in biomedical research or clinical settings. This is because most of these technologies require significant modifications to the existing practices, such as additional steps that significantly prolong the assay time, specialized and expensive read-out systems, non-traditional data processing and analysis, or the use of temperature-sensitive reagents, which usually require tightly controlled transport and storage conditions. Yet another attractive approach for fluorescence enhancement is metal- or plasmon-enhanced fluorescence. Enhancement in the emission of fluorophores in close vicinity to plasmonic nanostructures is attributed to the enhanced EM field at the surface of the plasmonic nanostructures and a decrease in the fluorescence lifetime due to the coupling between excited fluorophores and surface plasmons of the nanostructures.[626–635]

Plasmon-enhanced fluorescence (PEF) biosensors harness the large enhancement of fluorescence near metal nanostructures to enhance the sensitivity of various bioassays. Depending on the integration strategy between the plasmonic nanostructures and the bioassay, PEF biosensors can be broadly categorized into three types: (i) In the first method, PEF biosensors involve metal nanostructures adsorbed or grown on rigid substrates such as glass, silicon, and plastics. This configuration fixes the plasmonic nanostructures to enhance the emission from molecular fluorophores typically used as labels in bioassays. (ii) In the second method, PEF biosensors use an "add-on" plasmonic nanostructure/surface that can be applied to completed fluoroimmunoassays. This method relaxes the reliance on plasmonically-active substrate and makes the PEF biosensor platform more versatile. (iii) Finally, PEF biosensors use ultrabright fluorescent nanolabels that directly replace conventional fluorophores. This strategy integrates the plasmonic nanostructure and the fluorophore into a single nanoscale label for maximal sensitivity, ease-of-use, and ultimate versatility of PEF-based biosensors. Below we briefly describe these methods by highlighting a few specific examples.

## 4.1. Plasmonically active substrates for enhancing the sensitivity of bioassays

There have been numerous reports that harness plasmonic nanostructures adsorbed on a surface to amplify the fluorescence signals from a bioassay implemented on the surface.[636–640] Among the wide variety of metal nanostructures explored for PEF biosensors, gold nanoisland films known as plasmonic gold chips (pGOLD) have gained extensive attention, pioneered by Dai's group.[629] Fabricated through a gold seeding process followed by the growth of winding and elongated gold islands across the surface, pGOLD substrates contain abundant nanogaps on the order of 10 nm between adjacent islands (Fig. 23a). These hotspot-rich films effectively couple incident light to generate greatly amplified NIR fluorescence, enhancing detection sensitivity up to 100-fold,[630] Owing to the substantial fluorescence enhancement, high reproducibility, and small

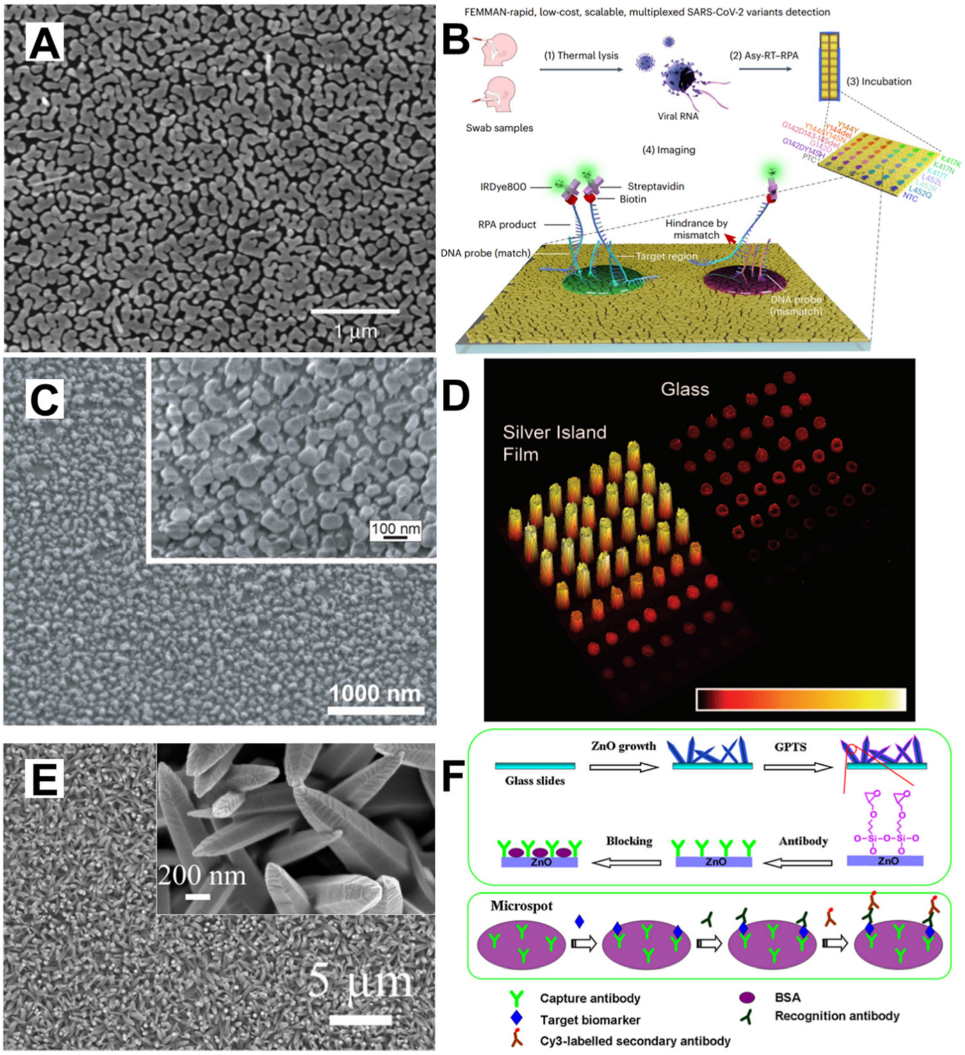
A
1 µm
B
FEMMAN-rapid, low-cost, scalable, multiplexed SARS-CoV-2 variants detection
Swab samples
(1) Thermal lysis
Viral RNA
(2) Asy-RT-RPA
(3) Incubation
(4) Imaging
IRDye800
Streptavidin
Biotin
RPA product
Hindrance by mismatch
DNA probe (match)
Target region
DNA probe (mismatch)
Y144Y
Y144del
Y144SY145N
G142D143-145del
G142D
G142DY145H
PTC
K417K
K417N
K417T
L452L
L452R
L452Q
NTC
C
100 nm
1000 nm
D
Glass
Silver Island Film
E
200 nm
5 µm
F
Glass slides
ZnO growth
GPTS
Antibody
Blocking
ZnO
Microspot
Capture antibody
Target biomarker
Cy3-labelled secondary antibody
BSA
Recognition antibody

Fig. 23 (A) SEM image showing the plasmonically-active gold nanoisland film, Reproduced from ref. 630 with permission from Nature publishing group, Copyright 2014 (B) Schematic of the FEMMAN workflow. SARS-CoV-2 related DNA probe targeting different variants' sites, a terminal biotin-labelled DNA probe as positive control and a DNA probe unrelated to SARS-CoV-2 as negative control are arrayed on the plasmonic gold substrate, Reproduced from ref. 641 with permission from Nature publishing group, Copyright 2023 (C) SEM image of SIF shows the heterogeneity of the particles' shapes and sizes. The inset is a higher magnification of the SIF, Reproduced from ref. 642, 643 with permission from Elsevier publisher, Copyright 2006 and 2011 (D) Fluorescence image of labeled oligonucleotide targets hybridized to MEF and glass DNA arrays, Reproduced from ref. 642 with permission from Oxford University Press publisher, Copyright 2006 (E) SEM images of ZnO nanorods grown on glass Reproduced from ref. 643 with permission from Elsevier publishing, Copyright 2011 (F) Schematic of the fabrication of ZnO-based antibody microarray, Reproduced from ref. 643 with permission from Elsevier publisher, Copyright 2011.

sample volumes, pGOLD assays have demonstrated immense potential for various bioassays and have been widely adopted across diverse diagnostic settings over the past decade. One implementation in lung cancer profiling utilized multiplexed pGOLD microarrays to simultaneously measure clinically relevant protein biomarkers carcinoembryonic antigen (CEA), Cyfra21-1, and neuron-specific enolase (NSE) in patient blood, achieving much higher sensitivity and specificity over standard bead-based immunoassays.[632] More recently, by integrating with portable automated microfluidics, Zhang's group employed pGOLD chips as substrates for a platform termed FEMMAN (Fig. 23b) to perform rapid single nucleotide-level discrimination among 12 SARS-CoV-2 variants directly from patient samples, with performance rivaling tedious genome sequencing.[641] DNA probes complementary to sequences unique to each viral lineage were immobilized on the plasmonically-active gold nanoislands for this nucleic acid-based assay. Patient RNA samples underwent an asymmetric amplification step in which 5' biotinylated amplicons were generated, enabling specific capture at perfectly matched DNA probes to generate plasmon-enhanced fluorescence signal. Only 1 viral RNA copy was required without extraction or purification, with 98.8% sensitivity and 100% specificity metrics that showed 97.6% agreement with gold standard genome testing.

Beyond gold nanoislands, other nanostructure architectures, including silver island films (SIFs) developed by Lakowicz's group[644] and zinc oxide nanorod substrates created by

Li's group,[643] have also enabled highly sensitive plasmon-enhanced fluorescence biosensing. Lakowicz's lab pioneered the concept of SIFs (Fig. 23c), comprised of silver island films grown at controlled rates on glass substrates using vapor deposition techniques. By immobilizing rabbit IgG on SIFs and capturing fluorescently labeled anti-rabbit IgG antibodies, they systematically studied the dependence of PEF on emission wavelength. Their results revealed more efficient fluorescence enhancement in the near-infrared (NIR) wavelengths compared to the visible wavelengths. In a follow-on work, they demonstrated up to a 28-fold increase in fluorescence signal for DNA microarrays by leveraging near-infrared Cy5 dye and SIFs, highlighting the potential to significantly improve nucleic acid detection sensitivity using far-red fluorophores[642] (Fig. 23d). SIFs were also shown to provide 10–15× amplification for sandwich immunoassays detecting cardiac biomarker myoglobin, lowering detection limits below 50 ng mL$^{-1}$ concentrations and underscoring the broader applicability to enhance the sensitivity of surface-based bioassays.[645] Beyond metal films, Li's group introduced zinc oxide nanorod substrates (Fig. 23e) as an alternative PEF transducer architecture. By growing aligned zinc oxide nanorod arrays, precise sub-wavelength spacing between nanorods yielded exceptional optical properties that could be harnessed for surface plasmon-coupled fluorescence enhancement[646,647] (Fig. 23f). Using this platform for cancer biomarker microarrays, they demonstrated detection sensitivity improvements down to 1 pg mL$^{-1}$ for protein biomarkers such as carcinoembryonic antigen (CEA) and α-fetoprotein (AFP) in serum.[643] Collectively, these examples highlight the versatility of nanostructure-enabled PEF for ultrasensitive bioanalysis across various assay formats beyond gold nanoisland films.

As described above, various plasmonic substrates such as periodic gold arrays[648,649] and metal nano-islands[629–632] have been shown to result in a large fluorescence enhancement. Although these plasmonic surfaces are highly attractive, their application in routine biomedical research and clinical settings has been limited. The limited application of plasmon-enhanced fluoroimmunoassays in research and clinical settings is due to: (i) stringent requirement for the fluoroimmunoassay to be implemented on pre-fabricated substrates, typically a rigid glass slide deposited with metal nanostructures, instead of standard or sometimes irreplaceable bioanalytical platforms (*e.g.*, 96-well plates and nitrocellulose membranes), which significantly limits the broad applicability of the technique; More importantly, the requirement of special substrates limits cross-platform and cross-laboratory consistency and seamless integration with widely employed bioanalytical procedures, which represents a major bottleneck of conventional plasmon-enhanced fluorescence techniques; (ii) non-traditional bioconjugation procedures, complex interaction between biomolecules and the metal nanostructures, and poor stability of biomolecules (*e.g.*, antibodies) immobilized on metal surfaces not only complicate the assay procedures but also impose further technical challenges in their widespread application;[650] and (iii) fluorescence quenching due to non-radiative energy transfer, which is difficult to control when the immunoassay is performed on a metal surface. Thus, it is imperative to address these challenges to propel the plasmon-enhanced fluorescence techniques to real-world applications.

Overcoming these limitations, add-on plasmonic architectures that can be interfaced with completed bioassays provide a more flexible and easy-to-implement route for integrating PEF. An illustrative example of successfully transitioning to an add-on PEF biosensor is the plasmonic nanogap cavity assay developed by Mikkelsen and Chilkoti's groups.[651] They fabricated the base platform by grafting a polymer brush coating of poly(oligo-(ethylene glycol) methyl ether methacrylate) (POEGMA) chains onto a gold film-sputtered glass surface, which enabled inkjet printing of both capture antibodies and fluorescently-labeled detection antibodies (with Alexa Fluor 647 dye) as microarray spots. Two spot types were printed on the POEGMA layer – "stable" spots containing surface-immobilized capture antibodies, and "soluble" spots where detection antibodies were mixed with an excipient that dissolved upon sample addition to facilitate antibody release. After completing the immunoassay, Ag NCs were appended above each printed spot using a poly(allylamine hydrochloride)(PAH) intermediate layer or conjugating the NCs to a secondary antibody. This formed nanogap cavities with a plasmonic metal–dielectric–metal geometry structured to amplify fluorescence emission. They termed the resulting architecture the plasmonically enhanced D4 (PED4; D4 stands for Dispense, Dissolve, Diffuse, Detect) assay (Fig. 24a). Using cardiac biomarker B-type natriuretic peptide (BNP) as a model analyte, optimization of POEGMA brush thickness and NC parameters enabled ∼150-fold fluorescence enhancement along with 14-fold improvement in detection limits compared to standard assays (Fig. 24b). The combination of the versatile D4 assay format[652] with the add-on nanostructure PEF amplifier imparts both excellent sensitivity and field-deployable ease-of-use relevant for point-of-care applications.

Among other prominent efforts to develop add-on plasmonic amplifiers, Singamaneni's group has introduced a flexible "plasmonic patch". Their key innovation involves adsorbing tunable plasmonic nanostructures onto an elastomeric polymer film to create a conformal nanoplasmonic interface[653,654] (Fig. 24c). When interfaced with completed fluoroimmunoassays in microwell plates or microarrays, this plasmonic patch can provide up to 100-fold fluorescence enhancement. Critically, the LSPR wavelength of the embedded nanostructures can be tuned to match the absorption/emission profile of the fluorescent reporter for maximal amplification.[654] Moreover, they systematically investigated the distance-dependent fluorescence enhancement to determine optimal spacer layer thickness. Assays for two key renal health indicators were evaluated to demonstrate the broad applicability across diverse protein biomarkers: kidney injury molecule-1 (KIM1) and neutrophil gelatinase-associated lipocalin (NGAL). Both biomarker immunoassays were performed using standard ELISA protocols, substituting streptavidin-fluorophore conjugates for streptavidin-horseradish peroxidase (HRP). By interfacing the completed assay with an LSPR-matched plasmonic patch, fluorescence intensity increased 36-fold, and detection limits improved 280-fold for KIM1 (Fig. 24d). Similarly, NGAL fluorescence boosted 103-fold while detection limits enhanced 100-fold. Furthermore, the plasmonic patch successfully enabled

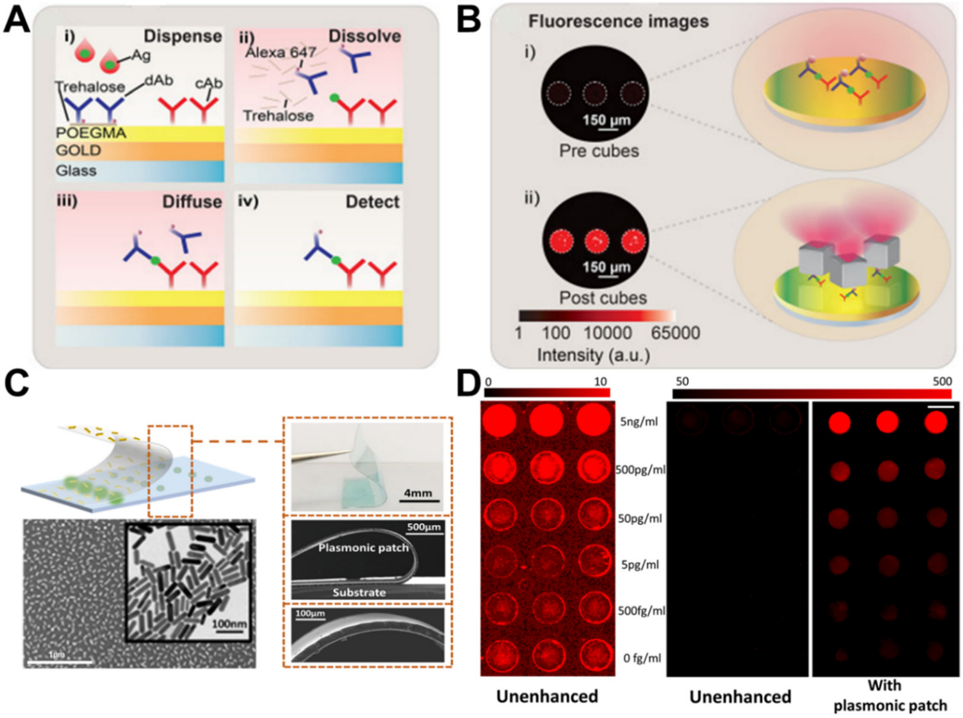

Fig. 24 (A) Schematic of workflow for D4 assay, Reproduced from ref. 651 with permission from the American Chemical Society, Copyright 2020 (B) comparison of fluorescence images for PED4 assay pre and post cubes addition, Reproduced from ref. 651 with permission from the American Chemical Society, Copyright 2020 (C) representative visual photo and SEM images of plasmonic patch. TEM images of nanorods used to modify the plasmonic patch, Reproduced from ref. 653 with permission from Nature publishing group, Copyright 2018 (D) fluorescence scanning images of fluorobioassay performed with and without the enhancement of plasmonic patch, Reproduced from ref. 653 with permission from Nature publishing group, Copyright 2018.

quantification of biomarker concentrations in patient samples that were undetectable without signal amplification. This highlights the versatility of the add-on nanostructure approach to harness plasmon-enhanced fluorescence for ultrasensitive clinically viable assays.

### 4.2. Ultrabright fluorescent nanolabels based on PEF

Building on their plasmonic patch concept, Singamaneni's group continued advancing integrations of plasmonic nanostructures with bioassays to harness sensitivity gains from PEF. By realizing optimized plasmonic nanostructure structures conjugated to fluorescent reporters, they developed exceptionally bright nanolabels, termed "plasmonic-fluors" (PFs), that are nearly 7000-fold brighter than their corresponding molecular fluorophores[655] (Fig. 25a). Streptavidin modification enables the PFs to substitute for streptavidin-fluorophore or streptavidin-HRP conjugates in common assay formats like FLISA and ELISA, providing built-in signal amplification tailored to each biomarker system (Fig. 25b). Using the model cytokine IL-6, they demonstrated plasmon-enhanced fluorescence-linked immunosorbent assay termed p-FLISA that lowered detection limits 1440-fold *versus* standard FLISA and 189-fold below conventional ELISA, highlighting the ultrasensitive quantification (Fig. 25c). Moreover, all previously demonstrated PEF biosensors have relied on modifying the conventional substrates or assay procedures, constraining the real-world utility. The nanolabel architecture of the PFs liberates plasmonic signal enhancement for integration into diverse analytical formats, including competitive and sandwich immunoassays,[656–658] CRISPR-based RNA detection,[659] serological assays,[660] flow cytometry,[655] microneedle-based non-invasive sampling,[661] LFA,[662] and measurements of live cell protein secretion.[663–665] In one demonstration, by integrating PFs into lateral flow immunoassays (p-LFAs) (Fig. 25d), detection sensitivity improved 1785-fold over conventional colorimetric LFAs (Fig. 25e) and 30-fold over standard clinical lab tests such as ELISA. Additionally, p-LFA successfully identified 34 out 35 positive COVID patient samples based on SARS-CoV-2 antigen levels, significantly outperforming colorimetric LFA. Coupled with a portable fluorescence scanner, the versatile plasmonic-fluor nanoparticle labels provide a broadly applicable solution to harness PEF for point-of-care testing applications spanning nucleic acids, antigens, and other biomarkers.

In a recent work, Tian's lab has demonstrated a buoyant biosensor that enabled multiplexed, *in situ* detection and quantification of attomolar cytokine concentrations in cell culture media with 15 min temporal resolution,[666] Plasmonic-fluors combined with digital counting further enhanced the detection limit to 14 ag mL$^{-1}$ for IL-6, preserving viable macrophages while quantifying dynamically secreted cytokines.[667] The facile sensor demonstrates strong promise for quantifying the temporal protein biomarker concentration changes in biological systems without perturbation. Plasmonic-fluors have also been

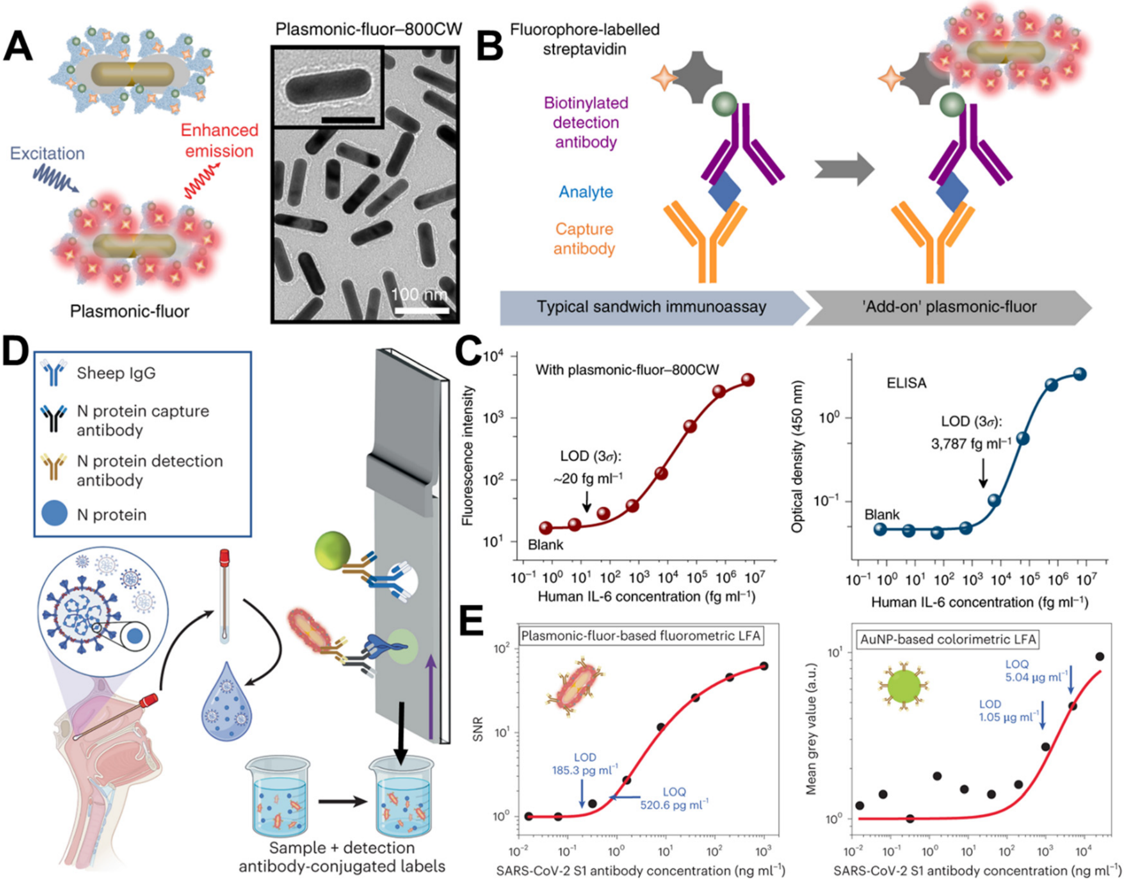

Fig. 25 (A) Schematic and TEM image of plasmonic-fluor structure, Reproduced from ref. 655 with permission from Nature publishing group, Copyright 2020 (B) schematic of workflow for plasmonic-fluor enhanced fluorobioassay, Reproduced from ref. 655 with permission from Nature publishing group, Copyright 2020 (C) comparison of ELISA and p-FLISA regarding the performance of human IL-6 detection Reproduced from ref. 655 with permission from Nature publishing group, Copyright 2020 (D) Schematic of construct and workflow of p-LFA in detection of SARS-CoV-2 N protein, Reproduced from ref. 662 with permission from Nature publishing group, Copyright 2023 (E) comparison of Au NP-based colorimetric and plasmonic-fluor-based fluorometric LFA performance of N protein detection, Reproduced from ref. 662 with permission from Nature publishing group, Copyright 2023.

employed as ultrabright nanolabels for probing the interaction of charge-controlled nanostructures with neurons and for demonstrating plasmon-enhanced expansion microscopy.[668,669] The emission from PFs was further amplified by coupling with resonant modes of a photonic crystal.[670] Cunningham and co-workers demonstrated the synergistic coupling of plasmonic and photonic modes to significantly boost the emission from plasmonic-fluors. Optimal match of the resonant modes of a plasmonic fluor and a photonic crystal resulted in a 52-fold improvement in signal intensity. This enhanced emission was employed to achieve an ultrasensitive digital immunoassay on photonic crystal surface.

Overall, PEF has been extensively explored in the past two decades as a powerful tool to boost the sensitivity of various fluorescence-based bioanalytical techniques. Tremendous progress has been made in the last five years in overcoming the challenges associated with translation of these technologies to routine real-world use. We can expect a widespread use of these technologies in the near future based on the extensive commercialization interest in these technologies.

## 5. Localized surface plasmon resonance (LSPR) sensing

### 5.1. Fundamentals of LSPR sensing

As mentioned before, metal NPs support LSPR which are responsible for an intense EM field enhancement very close to their surfaces.[671–673] Optically, these plasmonic NPs exhibit wavelength light absorption and scattering which is largely dependent on the NP dimensions, geometry, chemical nature, interparticle interactions, and the surrounding medium refractive index (RI).[674–677] The latter is the reason why they have been extensively used for sensing applications, and by precisely tuning the former parameters it is possible to maximize their high refractive index sensitivities (RIS).[678] For spheroidal NPs Mie–Gans theory can directly deduce the RIS for a NP with a given aspect-ratio (AR) as follows.:[678,679]

$$\mathrm{RIS}(\mathrm{nm/RIU}) = \frac{\lambda_{\mathrm{p}}^{2}}{n}\sqrt{\varepsilon_{\infty} + \left(\frac{1}{L} - 1\right)n^{2}} \qquad (9)$$

where $\lambda_p$ is the particle plasma frequency, $\varepsilon_\infty$ is the high-frequency contribution to dielectric permittivity of the NP, $L$ is the depolarization, $n$ is the medium RI and RIU the refractive index unit. Therefore, a direct relationship between the sensing performance of the NPs can be traced to their geometry and material properties. A consequence of higher RIS is the gradual shift towards higher wavelengths.[680–682] This advancement offers numerous potential applications, particularly in the NIR wavelength range, where optical fibers exhibit lower transmission losses,[683,684] paving the way to remote sensing applications using NPs on optical fiber platforms. Furthermore, the usage of optical fibers for plasmonic sensing applications has led to the development of sensing tips and overall cost-effective setups.[685] Furthermore, higher RIS contributes to the development of superior chemical and biochemical sensors, as the presence of analytes on the NP surface modifies the effective surrounding RI, refractive index, resulting in stronger optical responses.[686]

In the context of plasmonic sensors, in general, NPs exhibit smaller RIS compared to their thin film counterparts.[685,687] Nevertheless, their usage can be advantageous in certain scenarios due to the absence of phase-matching conditions, which significantly reduces the costs associated with the interrogation setup.[688] Moreover, the distribution and uniformity of NPs immobilization, particularly in the case of colloidal NPs, can be more easily achieved, especially when dealing with complex optical platforms where physical vapor deposition techniques may be challenging or impractical, as with micro-structured optical fibers.[689,690] Also, plasmonic sensors based on colloidal NPs present far greater scalability potential and lower-cost setups for synthesis and immobilization, two crucial factors for the widespread implementation of any sensing technology. In the next sections, the interaction between NPs and optical platforms is explored, with particular interest in the use of optical fibers, recent trends in NP arrangement for enhanced RIS, and finally, providing an outlook on the development of optical fiber-NP systems for improved sensors.

### 5.2. Optical platform and sensor configurations

The linear light dispersion of plasmonic NPs contrasts with the strong light dispersion observed in thin film-based SPR. However, when NPs are near or in contact with substrates, strong polarizability effects emerge, causing their optical response to be significantly influenced by the NP-substrate distance, as well as the substrate material itself.[673,685,691] This is caused by the EM-field enhancement being partly buried in the substrate (Fig. 26a), as so the effective RI around the NP gets modified, causing wavelength shifts and intensity extinction variations (Fig. 26b).[692] Also, this presents relevant consequences regarding their RIS, where the RIS gets diminished by the immobilization over a dielectric substrate, when compared to the same particles in colloidal solution (Fig. 26c).[691] However, a different trend is observed when the substrate material gets replaced by a metal. This optical response has been explored in recent years, showing that strong redshifts can be observed without significant band widening (Fig. 26d).[693] The presence of the metal layer acts as a charge mirror, effectively mimicking the presence of another NP in its vicinity. Thus, by changing the dielectric spacer length, it is possible to tune the strength of the plasmon hybridization (Fig. 26e). Further tuning can be achieved by changing the thickness of the metal layer,[694] or substrate materials, as the case of $TiO_2$.[695] Also, modifying the NP geometry, *e.g.* using nanorods, can produce even stronger optical variations with interesting results, as higher order plasmonic modes respond differently to polarization changes (Fig. 26f).[695,696] These later configurations are commonly known as nanoparticle on film (NPoF) structures and can behave as light waveguiding structures, composing a metal–insulator–metal (MIM) configuration, where the metallic top layer is replaced by the NPs (Fig. 26g).[697] Recently, this kind of structure has received a lot of attention and even other nanostructures have been explored. Nevertheless, for sensing purposes the main tuning parameter still lies within the nanocavity. This is based on the principle of achieving a large effective RI in the spacing layer with the decrease of its dimensions. Thus, the ability to decrease this spacing will greatly impact the structure performance (Fig. 26g). However, despite the recent progress observed with these MIM wave-guiding structures, the EM-field shows strong confinement between the NP and thin film layer, which is not ideal for sensing purposes, as the field enhancement should extend towards the surrounding medium. Accordingly, to increase the sensing performance of these structures, this issue should be addressed. Nevertheless, several high RIS were reported using these NPoF configurations, as shown in Table 2. To the moment, the highest reported RIS was presented by Xia *et al.*, where an experimental RIS of 15 747 and 25 642 nm $RIU^{-1}$ for Au NS and Au NR, respectively, was attained on a photonic crystal fiber (PCF) coated with an Au thin film.[698]

Other waveguiding structures have also been proposed, showing better prospects for effective implementation of high-performance NP-based plasmonic structures. Namely, the insulator–metal–insulator (IMI) waveguide scheme (Fig. 26h). In this case, randomly assembled NPs over a glass substrate are seen as an effective RI layer between the substrate and the external medium. This metal layer can be modeled using effective medium theories such as Bruggeman or the Maxwell-Garnett effective index approximations,[706] and it will present high effective indices enabling it to guide light. The light will be highly compressed according to $\lambda_{\text{eff}} = \lambda/n_{\text{eff}}$. Consequently, as the $n_{\text{eff}}$ increases, the more efficient waveguiding becomes, which can be done by increasing the NP density. In addition, a stronger field in the meta-layer will lead to a stronger interaction with the surrounding medium, causing an increase in RIS (See right panel of Fig. 26h).[701] As this is a waveguiding mechanism light dispersion is expected, so it will become dependent on the wave-vector of the excitation light, causing a dependence on the angle of incidence.

As the light illumination conditions can determine the sensing system performance, it is relevant to explore not only the optical behavior of NPs under colloidal suspension but also when immobilized over planar substrates or optical fibers and discuss the benefits of either situation. First, using the NPs in colloidal solutions allows for the simpler usage of all, as it can

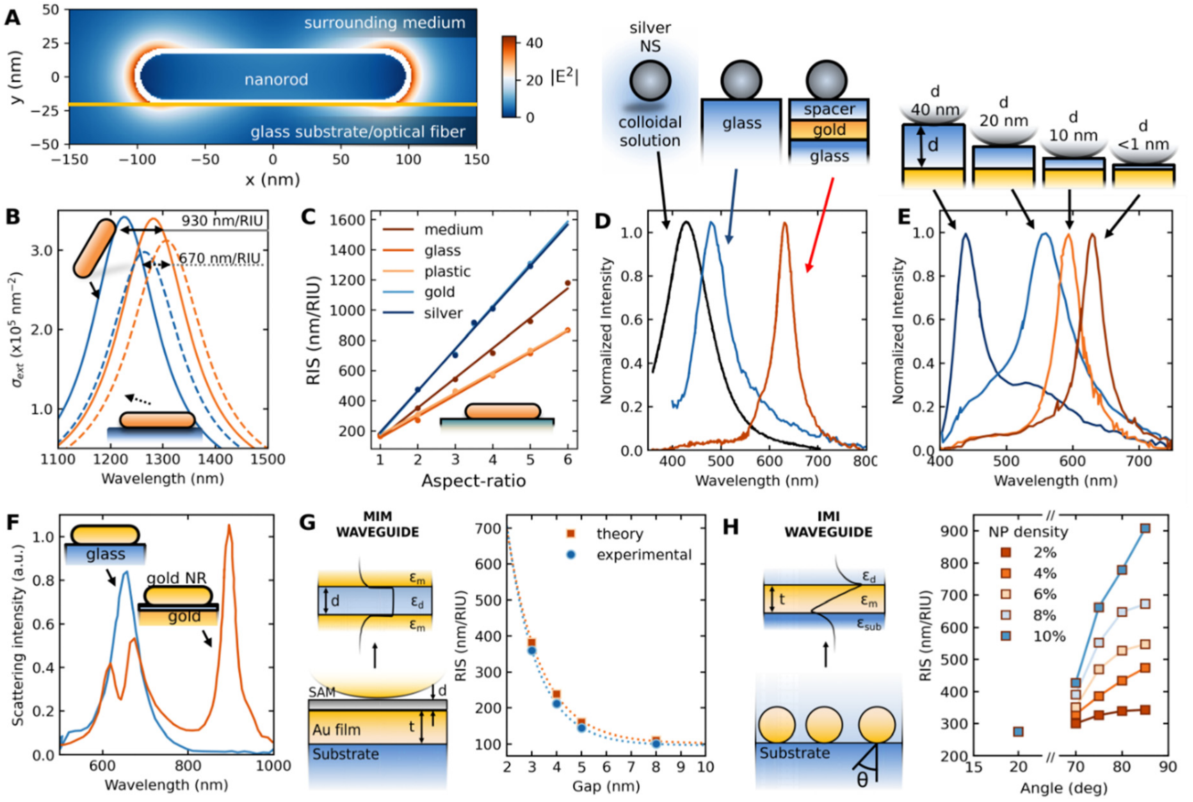

Fig. 26 (A) Near field simulation of an Ag nanorod (NR) immobilized on a glass substrate using boundary elements method at the peak of the longitudinal mode LSPR band reproduced from ref. 692 with permission from Optica publisher, Copyright 2010 (B) spectra comparison upon change in the medium RI for an Ag nanorod immobilized on a glass substrate and on colloidal suspension. (C) Impact of the substrate material on the RI sensitivity (RIS). (D) Spectra of an Ag nanosphere (NS) on colloidal solution, over a glass substrate and at proximity (<1 nm) to an Au thin film layer. Reproduced from ref. 693 with permission from ACS publisher, Copyright 2010 (E) impact on the optical behavior on the changing of the spacer thickness, showing a strong red shift with decreased spacing. Reproduced from ref. 693 with permission from ACS publisher, Copyright 2010 (F) Au NR immobilized over an Au thin film and over a glass substrate, showing the appearance of higher order modes due to plasmon hybridization. Reproduced from ref. 699 with permission from ACS publishing, Copyright 2018 (G) metal–insulator–metal (MIM) waveguide structure composed of an Au thin film and Au NS along the RIS dependency on gap length. Reproduced from ref. 697 with permission ACS publisher Copyright 2021 and RIS results Reproduced from ref. 700 with permission from RSC publisher, Copyright 2022 (H) insulator–metal–insulator (IMI) waveguide structure representation, along the RIS dependence on launching angle. Reproduced from ref. 701 with permission from ACS publisher, Copyright 2011.

Table 2 List of reports of NPoF configurations with high refractive index sensitivity (RIS)

| Optical platform | RIS (nm RIU$^{-1}$) | Ref. |
|---|---|---|
| Photonic crystal fiber with Au thin film and Au NSs | 15 747 | 698 |
| Photonic crystal fiber with Au thin film and Au NRs | 25 642 | 698 |
| Side polished multimode fiber with Au thin film and Au NSs | 3074 | 702 |
| Multimode fiber tip coated with Au thin film and carboxylated multi-walled carbon nanotubes | 2524 | 703 |
| Multimode fiber tip coated with Au thin film and carboxylated multi-walled carbon nanotubes, and Pt NPs | 5923 | 703 |
| Multimode fiber coated with $SnO_2$ thin layer and 50 nm $SnO_2$ NPs | 5334 | 704 |
| Multimode fiber coated with 9 PSS-$SnO_2$ bilayers and 50 nm $SnO_2$ NPs | 4704 | 704 |
| Photonic crystal fiber section between two MMF with Au film and Au NRs | 3915 | 705 |

just be placed inside a lab bench spectrometer and measure the extinction coefficient. Nevertheless, it was seen that by placing them on a substrate, they can enhance the NPs RIS. In this situation, to control excitation conditions, a more complex optical setup such as the Kretschmann or Otto configuration is required, allowing for precise wavevector conditions control. However, the costs associated with these setups can rapidly increase and require a sampling system or microfluidic channel to transport the analyte into contact with the immobilized NPs. Another option is the use of optical fibers, as they allow for easy multiplexing, long-range sensing, potentially lower costs, and material choice, as well as a broad choice of sensing configurations such as sensing tips.[707–710]

Among the multitude of optical fiber sensing configurations available the most common are based on exposing the fiber core and immobilizing the NPs on that section, by side polishing, cladding removal on MMF, or bending a fiber to such a small curvature radius that causes an evanescent field to interact with the immobilized NPs.[689,708,711–715] Another approach is structural modification *via* grating inscription to partially redirect the light to the fiber cladding allowing for evanescent interaction with the NPs, as in the case of the long-period fiber gratings (LPFG) or multi-single-multimode (SMS) fiber configuration (Fig. 27a).[716,717] When NPs are assembled on optical fibers, the reports on RIS don't match with the ones of the same kind of NPs immobilized on glass slides, indicating that not only polarizability effects are of concern (Fig. 27b). Effectively, several reports show RIS higher than 1000 nm RIU$^{-1}$ for simple gold nanospheres (NS) when immobilized over optical fiber, contrasting to the case of glass slides and colloidal solutions. To the best of the author's knowledge, the highest reported RIS with gold NSs are 2016, 350, and 180 nm RIU$^{-1}$ on optical fibers, glass slides, and colloidal dispersion, respectively.[718,719] The large discrepancies observed between the optical fiber and the other two can be attributed more to the light excitation conditions than the material specificities. To the moment no consensus exists to explain the observations, whereas some authors as Otte *et al.*,[701] consider that the higher sensitivities are related to wave-guiding phenomena, while others attribute to the creation of hotspots due to interparticle-coupling or lossy-mode resonances.[718,720] The same trend was observed on other NP shapes and materials.[721–738] Focusing on a better performant spheroidal NP shape than NS, *i.e.*, Au NRs, by comparing their performance on different optical platforms (Fig. 27c), it is possible to see that fibers show the better overall performance with a RIS/Aspect-Ratio of 304 nm/RIU/Aspect-Ratio, contrasting to a ratio of 113 and 33 nm/RIU/Aspect-Ratio for the NRs on glass slides and colloidal solutions, respectively. Thus, suggesting that better performance can be accomplished with the conjunction of higher AR NRs and optical fibers. To the best of the authors knowledge there is no RIS data reported for NRs with AR larger than 5 on optical fibers. Thus, causing a low $R^2$ value in the linear regression analysis. Nevertheless, as the NR synthesis protocols become more mature, resulting in higher yields, NP monodispersity, and larger AR, it is expected that more focus will be given to such high AR NRs – optical fiber plasmonic sensor configurations.

The recent advancements in synthesis methods have led to increased yields, enhanced NP monodispersity, improved colloidal stability, and enhanced biocompatibility.[749] Consequently, the widespread implementation of sensing applications utilizing plasmonic NPs may be on the horizon. Recent trends of NPs-based plasmonic sensors were found to rely on optical fibers as the optical platform. As well, NPs stacking and even immobilization over or in between metallic thin films have been proven to unravel new paths towards unprecedented RIS and overall optical performance.[711,750–754] Enhanced chemical and biochemical sensing applications have been recently reported, showing the feasibility of high-performance NP-based plasmonic sensing. In the future, more works in NIR wavelengths with NPs and optical fibers are expected, which can greatly advance the field and produce even higher RIS and overall chemical/biochemical sensors.

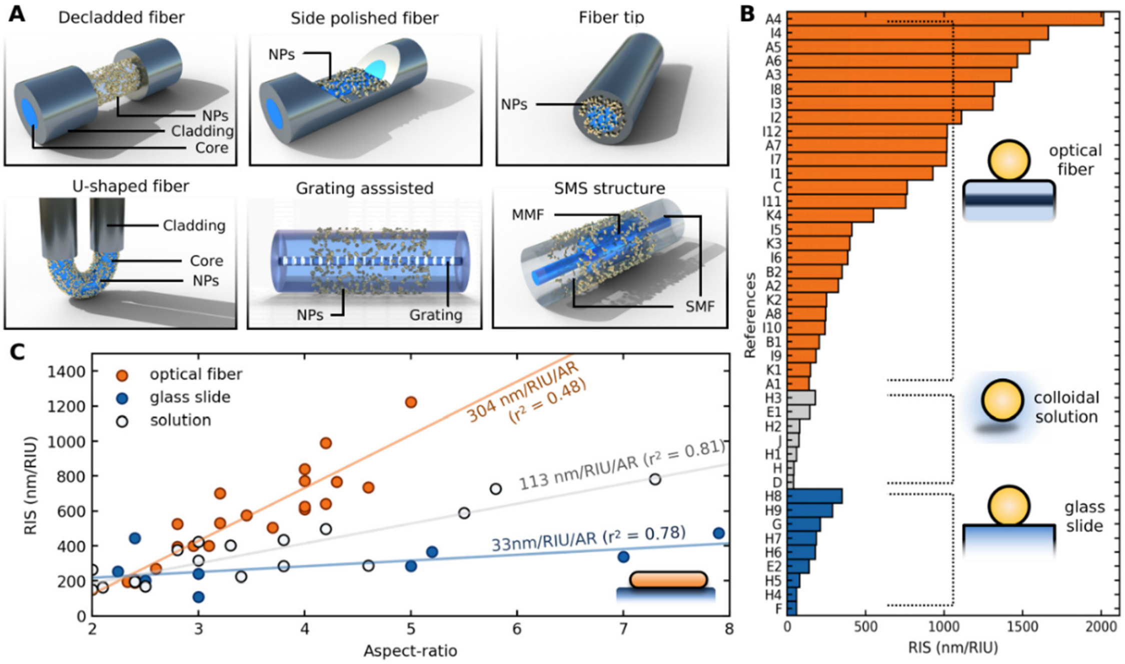

Fig. 27 (A) Typical nanoparticle-based plasmonic optical fiber sensor configurations (B) Refractive index sensitivity (RIS) comparison between Au nanospheres (NSs) immobilized on optical fiber sensor configurations, glass slides, or in colloidal solutions. The data labels correspond to the following works: A1-A8;[718] B1,B2;[739] C;[716] D;[736] E1,E2;[734] F;[740] G;[741] H;[742] H1-H9;[719] I1-I12;[720] J;[743] (C) RIS for gold nanorods (NRs) comparison for the same two optical platforms and on colloidal solution. Data were reproduced from ref. 678, 724, 732, 736, 738, 740, 742, 744–748 with permission from ACS publication, Springer New York publisher, ACS publication Elsevier publisher, MDPI publisher, Copyright 2007, 2022, 2016, 2008, 2022, 2007, 2009, 2021, 2018 respectively.

### 5.3. Colorimetric sensing

**5.3.1. Substrate-based colorimetric sensing.** The trichromatic perception by humans (blue, green, and red light) led to the development of tristimulus representation of colors which describes the relative amounts of blue, green, and red channels of a given color perception.[755] Thus, a typical color can be represented in a 3-dimensional linear color space, including RGB (red-green-blue), CIE XYZ, or HSV (hue-saturation-value) currently used in standardized color descriptions. In colorimetric sensors based on plasmonic nanoparticles, the detection of an analyte (small molecules) or environmental factors (refractive index, temperature, humidity, strain) can be quantified based on the change in color by tracking the variation of one or more of the three dimensions in given color space. For example, the change of the $x$ and $y$ chromaticity dimensions can be deduced from the arithmetical difference between the initial and final cartesian pairs, $\Delta(x, y) = (x_2-x_1, y_2-y_1)$ to yield color difference ($\Delta E$) (Fig. 28, center).[756]

Traditionally, colorimetric plasmonic sensing has emerged from the LSPR spectral sensors, where the plasmon modes in the visible spectral range shift by the alteration of the refractive index (RI) of the surrounding medium. The initial attempt to transition from spectral to colorimetric sensing was limited to a qualitative readout, *e.g.*, the presence or absence of an analyte. Over the past few years, the advancement in the design and fabrication of dynamic plasmonic systems enabled the implementation of standardized mathematical descriptions for color change due to RI variation. King *et al.*[757] designed a 2D Fanoresonant plasmonic system consisting of a centered Al disk with N number of satellite planar Al nanodisks (Fig. 28a-i) that scattered light in the visible spectral range allowing apparent vibrant color (pure saturated). The authors introduced a Figure of Merit (FOM), $|\Delta\text{Hue}/\Delta n|$, a measure to quantify the change of hue in the polar coordinate of the CIE lightness-chroma-hue color space (CIE LCHab). The value of FOM correlated linearly with RI in the range from 1 to 1.6, achieving the Δhue as large as 216°. In a similar approach, Reinhard *et al.*[758] designed a RI sensor comprising Au NPs (18–115 nm) attached to a solid substrate to detect sucrose solutions (Fig. 28a-ii). The authors found the hue was the most sensitive color parameter among 15 other parameters tested (*e.g.*, hue, r, g, and b chromaticities). Through the ratio $\Delta y$/RIU, where $y$ is the color parameter and RIU is the change of RI, the value of Δhue equal to 0.07 (or 26.5°) was obtained for $1.33 < \text{RI} < 1.42$ (RIU = 0.09), exceeding by nearly 6-fold the sensitivity of the

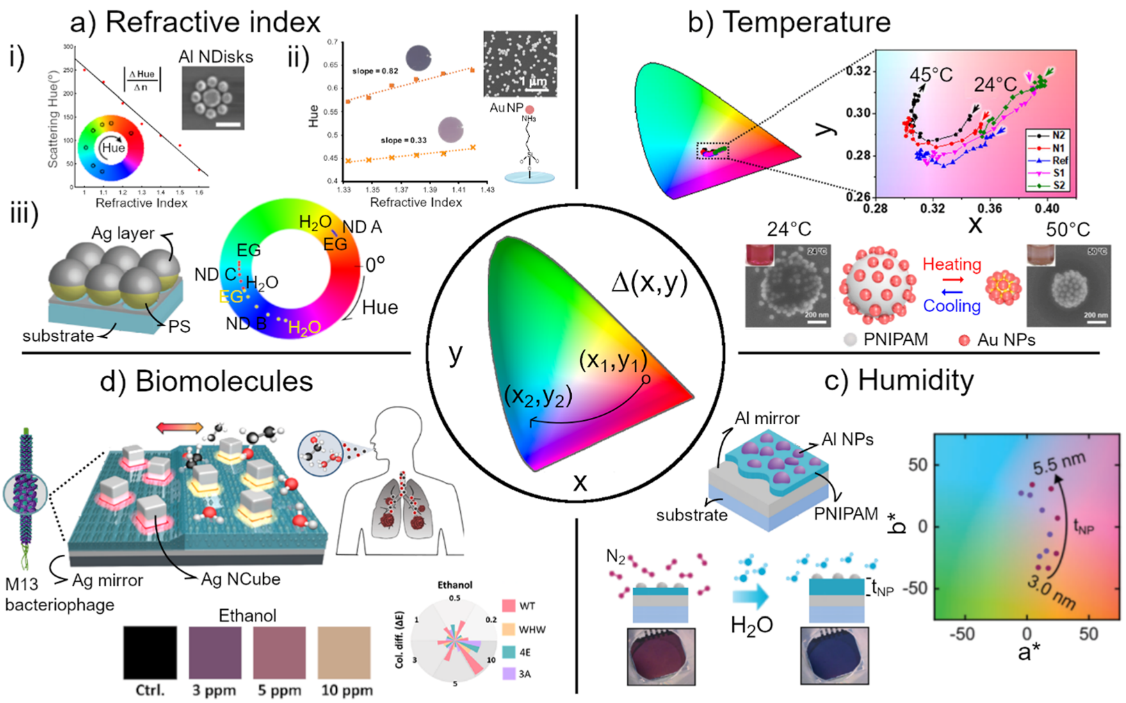
a) Refractive index
i)
Al NDisks
|ΔHue/Δn|
Scattering Hue(°)
Hue
Refractive Index
ii)
slope = 0.82
slope = 0.33
Hue
Au NP
NH2
1 μm
Refractive Index
iii)
Ag layer
substrate
PS
H2O
ND A
EG
EG
ND C
H2O
EG
0°
Hue
ND B
H2O
b) Temperature
y
45°C
24°C
N2
N1
Ref
S1
S2
x
24°C
50°C
Heating
Cooling
PNIPAM
Au NPs
Δ(x,y)
y
(x1,y1)
(x2,y2)
x
d) Biomolecules
M13 bacteriophage
Ag mirror
Ag NCube
Ethanol
Ctrl.
3 ppm
5 ppm
10 ppm
Ethanol
Col. diff. (ΔE)
WT
WHW
4E
3A
c) Humidity
Al mirror
Al NPs
substrate
PNIPAM
N2
H2O
tNP
5.5 nm
3.0 nm
tNP
b*
a*
50
0
-50
-50
0
50

Fig. 28 Colorimetric sensing based on plasmonic nanoparticles categorized according to the type of analyte. (A) Refractive index sensors: (i) measurement of the RI change (1 < $n$ > 1.6) through the shift of the change of hue of Al nanodisk array substrates. (ii) Lineal hue changes of a substrate comprising gold nanoparticles because of sucrose concentrations from reflectance and transmission images. (iii) Variation of hue of Ag nanodome arrays by changing the surrounding medium from water to ethylene glycol. (B) Colorimetric measure of temperature by the plasmon coupling of Au-coated pNIPAM microgels at different salt additives, where the color change is monitored through the chromaticity coordinates $x$ and $y$. (C) Humidity sensor measured by Al NPs on Al mirror with pNIPAM as a spacer in which the color change is monitored in the CIE L*a*b* space. (D) Biosensor of volatile organic compounds detected by using Ag NCs on Ag mirror with a bacteriophage spacer as a transducer. Color difference ($\Delta E$) is quantified for a wide range of ethanol concentrations. (a-i) and (a-ii) Reprinted from ref. 757, 758 with permission from ACS publisher, Copyright 2015, 2020. (a-iii) Reprinted from ref. 759 with permission from Wiley-VCH Verlag GmbH & Co. KGaA publisher, Copyright 2020 (b) Reprinted from ref. 760 with permission from Springer publisher, Copyright 2018. (c) Adapted with permission from the Authors of ref. 761. (d) Reprinted from ref. 762 with permission from ACS publisher, Copyright 2022.

r chromaticity. The authors concluded that the sensitivity to RI increases with the particle size and that a larger color difference is achieved in transmission rather than reflection. In a more recent publication, Toma *et al.*[759] designed a RI sensor consisting of polystyrene bead monolayers (200–300 nm) coated with Ag thin films to form Ag nanodomes whose surface colors were optimized by changing the size of the polystyrene beads (Fig. 28a-iii). The sensitivity was evaluated through the hue parameter for water and ethylene glycol at different volume ratios and three Ag nano-dome diameters. In the best-performing architecture, Δhue of 59.6° for a RIU = 0.1 was obtained. The authors demonstrated that the resolution of the colorimetric detection ($5.0 \times 10^{-5}$ RIU) was higher than spectral detection ($10^{-4}$ RIU).

With the integration of plasmonic nanostructures alongside other advanced materials, colorimetric sensors have expanded beyond detecting changes in RI. Choe *et al.*[760] have developed plasmonic colorimetric patches to sense temperature. The authors used Au-coated poly (*N*-isopropyl acrylamide) (pNIPAM) microgels embedded within a hydrogel matrix (Fig. 28b). The pNIPAM exhibits lower critical solution temperature (LCST) at 32 °C. Below LCST, the microgel particles gain volume, increasing the separation of Au NPs, hence the color transition from blue to red. Above LCST, the pNIPAM chains collapse, reducing the specific volume of microgels and thus turning red to blue due to plasmon coupling. To correlate the color change and temperature, the authors employed the RGB color space and varied the transition temperature by adding different salts to the hydrogel films in which the Au NPs pNIPAM microgels were incorporated: N1-0.2 M NaCl, N2-0.1 M NaCl, S1-1 mM SDS, S2-2 mM SDS, and control-no additives. The authors found that the red component exhibits high sensitivity for S1, $\Delta R_{S1} = -33$, and S2, $\Delta R_{S2} = -61$, in temperature ranges of 29–33 °C and 33–40 °C, respectively. Interestingly, the authors achieved a temperature resolution of 0.2 °C, allowing precise monitoring of temperature variations on various substrates. By exploiting the concept of particles on the mirror, Cencillo-Abad *et al.*[761] have developed a humidity sensor using Al NPs (3 nm to 5.5 nm) on Al mirror (Fig. 28c). These nanoparticles were separated by a pNIPAM layer of 35.5 nm at relative humidity (RH) of 50% (at 20 °C). At low RH levels, the desorption of water caused shrinkage of the pNIPAM layer, resulting in the optical coupling of NPs with mirror, in consequence, an enhancement of the red component of the reflected light. At high RH levels, the pNIPAM layer expanded, reducing the coupling and enhancing the blue component in the reflected light. The color of the sensor switched from magenta to blue that could be tracked with the change of the component a* and b* of the CIE L*a*b* color space (L*-lightness-, a*-red to violet-, and b*-yellow to blue-coordinates, Fig. 28c). The device effectively transformed changes in relative humidity into observable color changes.

Recent advancements in biotechnology enabled the fabrication of biological constructs of synthetic and natural origin that can serve as biomarkers or signal transducers in colorimetric sensing involving plasmonic nanoparticles. Nguyen *et al.*[762] have employed genetically engineered bacteriophage as a spacer between Ag NCs and silver film (gap plasmonic color film, GPCF) to detect volatile organic compounds (VOCs) as biomarkers of lung cancer (Fig. 28d). The bacteriophage layer worked as an actuator, adjusting the gap in response to the concentration of VOC. The researchers selected over 43 VOC biomarkers and tested the biosensor's performance with five gases: acetone, ethanol, isopropyl alcohol, diethyl ether, and hexane. The analyte changed the gap and thus the color difference (Fig. 28d shows the $\Delta E$ for ethanol). The GPCF-based biosensor demonstrated exceptional selectivity, and ease of fabrication, making it a promising platform for developing novel diagnostic devices. The colorimetric sensing of biomolecules was proposed by Sanromán-Iglesias *et al.*,[763] where aggregating DNA-coated Au nanoparticles were used as an optical signal transduction to detect bacterial nucleases – a biomarker of *Salmonella* spp. In the presence of nucleases, the aggregation of nanoparticles was inhibited (red color) due to enzymatic cleavage of double-stranded probe sequences (positive readout). Without nucleases, the nanoparticles were allowed to aggregate (red-to-blue color transition, negative readout) due to the selective binding of complementary DNA strands. Through naked-eye inspection, the method detected living bacteria down to 1 CFU mL$^{-1}$ in naturally contaminated food samples. Unlike substrate-based plasmonic sensors, colorimetric detection based on nanoparticle aggregation suffers from a poor quantitative description of color change. This is because many geometrical parameters (mutual particle orientation or interparticle-gap) condition the reproducibility of color difference. Recently, Montaño-Priede *et al.*[764] have evaluated the effect of geometrical descriptors (particle shape and size, number of particles per cluster, and interparticle distance) on the resulting change in Hue during the aggregation of gold nanoparticles. Through the comparison of experimental and theoretical data, the authors found that gold decahedra with an edge length of 30 nm outperform other shapes, showing $\Delta H$ = 72% ($\Delta H$ = ΔHue/max(ΔHue)). The proposed methodology for calculating hue values and associated FOM $\Delta H$ provided new universal and quantitative tools to monitor color transitions during the aggregation of nanoparticles induced by any molecule.

To close, plasmonic colorimetric sensing offers a quantitative measure of color change in the presence of biomolecules and environmental stressors. This type of sensor is expected to experience substantial improvements in forthcoming years. The main driving force is the progress in bottom-up fabrication that allows for obtaining structural diversity, reproducibility, and switchable optical outcome that can be quantified through standardized color spaces (RGB, CIE XYZ, or HSV). Further integration of active plasmonic sensors into substrates obtained by the top-down approach will offer portability, cost-effectiveness, and suitability for point-of-care applications by reducing the need for expensive, specialized instruments. Still, the performance of a plasmonic colorimetric sensor depends on the selection of suitable color space, requiring a trial-and-error approach. Thus, further standardization of the current methods is needed to ultimately render high-performance and hyperchromatic sensing.[765]

#### 5.3.2. Colloidal colorimetric sensing.

Plasmonic NPs have been widely used in colorimetric sensing due to their unique optical properties.[766,767] Because of the LSPR, plasmonic NPs possess strong extinction and multicolorimetric signal readouts.[633,768] For example, gold nanoparticles with 13 nm diameter possess a high extinction coefficient of $2.7 \times 10^8\ M^{-1}\ cm^{-1}$ at ∼520 nm, which is three to five orders of magnitude higher than those of organic dyes.[633] The LSPR wavelengths span a wide range from visible to NIR regions of the light spectrum. The intensities and wavelengths of LSPR spectra are sensitive to the size, shape, composition, and aggregation of the plasmonic NPs, and the changes in the refractive index of their surrounding environment. These form the basis for the mechanism of colorimetric plasmonic biosensors. Owing to their simplicity and low cost, colloidal NP-based colorimetric sensors have been developed for a wide range of analytes, including ions, proteins, DNA, and bacteria, at low concentrations.[769,770] The target-dependent color changes can be easily visualized, allowing for qualitative or semi-quantitative detection with the naked eye. Based on the mechanism of colorimetric response, colloidal plasmonic colorimetric sensors can be divided into three categories: growth-based, etching-based, and plasmonic coupling-based.[770,771] The most common mechanism in colloidal colorimetric sensors is nanoparticle aggregation induced strong plasmonic coupling and dramatic color changes. However, the aggregation is sensitive to many factors, including pH, temperature, ionic strength, and charged molecules.[772,773] The NP surface chemistry plays a very important role in precise control over the aggregation state, which affects the reliability and reproducibility of color changes. Growth and etching-based colorimetric sensors can be implemented in solution and on substrates, which offer improved stability and reproducibility.

In this section, we will highlight some examples to illustrate these mechanisms. Growth-based plasmonic sensors have been developed to detect various analytes, including metabolites,[774] DNA,[775] enzymes,[775] protein biomarkers,[776] bacteria,[777] and viruses.[778] The growth of plasmonic nanoparticles can be modulated by enzymes. Common precursors include $Au^{3+}$ and $Ag^{+}$ for gold and silver nanostructure growth. For example, a plasmonic ELISA based on Au NP growth modulated by enzymatic decomposition of a reducing agent was reported by the Stevens group.[776] Following a standard ELISA procedure, the reducing agent, hydrogen peroxide ($H_2O_2$), and gold ion precursor solution were introduced sequentially (Fig. 29a). In the presence of targets, the enzymes linked to detection antibodies consume $H_2O_2$, slow down the gold reduction in 2-(*N*-morpholino)ethanesulphonic acid (MES) buffer and yield aggregated gold nanoparticles, which result in blue color solution. In the absence of targets, the high concentration of $H_2O_2$ leads to a fast reduction and the Au NPs are not aggregated, which yields red color solution. A distinguishable blue to red color transition happens in a narrow $H_2O_2$ concentration range between 100 and 120 μM. The method enabled the detection of prostate specific antigen (PSA) and human immunodeficiency virus HIV-1 capsid antigen p24 in whole serum at an ultralow concentration of $1\times 10^{-18}$ g mL$^{-1}$. Detecting p24 at such a low concentrations using a standard ELISA format without the need for expensive nucleic acid-based tests could offer a robust alternative for diagnosing HIV infection through naked-eye observation. Based on a similar approach, Huang *et al.* reported naked-eye detection of Gram-negative *Escherichia coli* (*E. coli*) and *Klebsiella pneumoniae* (*K. pn*) in urine samples.[777] These bacteria produce catalase that decomposes $H_2O_2$, which modulates the growth of Au NPs to yield different colors. This approach takes 85–100 minutes from sample collection to analysis and provides a limit of detection of ∼$10^6$ CFU mL$^{-1}$. Many enzymes, such as glucose oxidase,[774] tyrosinase,[779] and alkaline phosphatase,[778] can catalyze the decomposition of substrates into reducing agents which induce nanoparticle growth. A simple example is an enzymatic glucose sensor, in which $H_2O_2$ was generated in the presence of glucose and oxygen.[774] The glucose concentration is proportional to the amount of $H_2O_2$ produced to modulate the NP growth. The same growth mechanism can also expand to the detection of enzyme[775] and reducing agent[780] targets. In addition to self-nucleation, Au and Ag growth can occur on many predefined nanostructures, such as Au NSs,[774] Au NRs,[780] Au NBPs,[778] and Au NSTs.[775]

Etching-based colorimetric sensing involves the etching of predefined NPs by the targets or the intermediates produced following the presence of targets. The predefined NCs include Au NSs,[784] Au NRs,[781] triangular Ag NPts,[785] Au NBPs,[786] and Ag-coated Au NSs.[787] The etching-based colorimetric sensors have been reported to detect various targets, including metal ions,[784] anions,[788] metabolites,[785] DNA,[789] proteins,[781] and exosomes.[790] The presence of various ions, such as $Cl^-$, $Br^-$, and $CN^-$, can reduce the redox potential of gold and silver and induce the etching under certain conditions.[787,788,791] This can be used to detect these ions in the presence of oxidizing agents, including oxygen,[787] hydrogen peroxide,[792] and nitric acid.[791] Similarly, targets with oxidizing ability, such as $NO_2^-$, $Cu^{2+}$, and $Cr^{6+}$, can be detected after the redox potential of Au and Ag decreases.[788,793,794] The formation of Pb–Au alloys can accelerate the etching of gold nanospheres in the presence of 2-mercaptoethanol and thiosulfate ($S_2O_3^{2-}$), which was used to detect $Pb^{2+}$.[784] Enzymatic reactions that produce $H_2O_2$ to etch triangular Ag NPts[785] or Au NRs[795] can be used to detect glucose. The $H_2O_2$ produced in ELISA can be used to detect DNA based on color changes in the etched silver triangular nanoplates.[789] Another universal way was based on the $TMB^{2+}$ produced in the HRP-3,3′,5,5′-tetramethylbenzidine (TMB) ELISA, which etches gold nanorods to yield vivid color responses (Fig. 29b).[781] $TMB^{2+}$ shortened Au NRs in the presence of cetyltrimethyl ammonium bromide (CTAB) within 90 seconds. This led to a blue shift of LSPR peak and a colorful transition from brown (Au NRs) to pink (Au NSs). The colorless solution indicates the thorough oxidization of Au NRs into $AuBr_2^-$ and the yellow color at even higher $TMB^{2+}$ concentrations is due to excess $TMB^{2+}$. The multichromatic response allows for semi-quantitative detection of carcinoembryonic antigen and PSA with naked eyes with low LODs at ∼2.5 ng mL$^{-1}$ and ∼75 pg mL$^{-1}$, respectively. The approach can be adapted to other biomarkers with such a simple add-on step, which changes a monochromic response from the traditional colorimetric assay to a multicolor display.

In plasmonic-coupling-based colorimetric sensors, analytes can modulate aggregation or dispersion of plasmonic NPs, generating a colorimetric response. The reported plasmonic NPs include Au NSs,[796] Au NRs,[797] AuAg nanoshells,[782] and

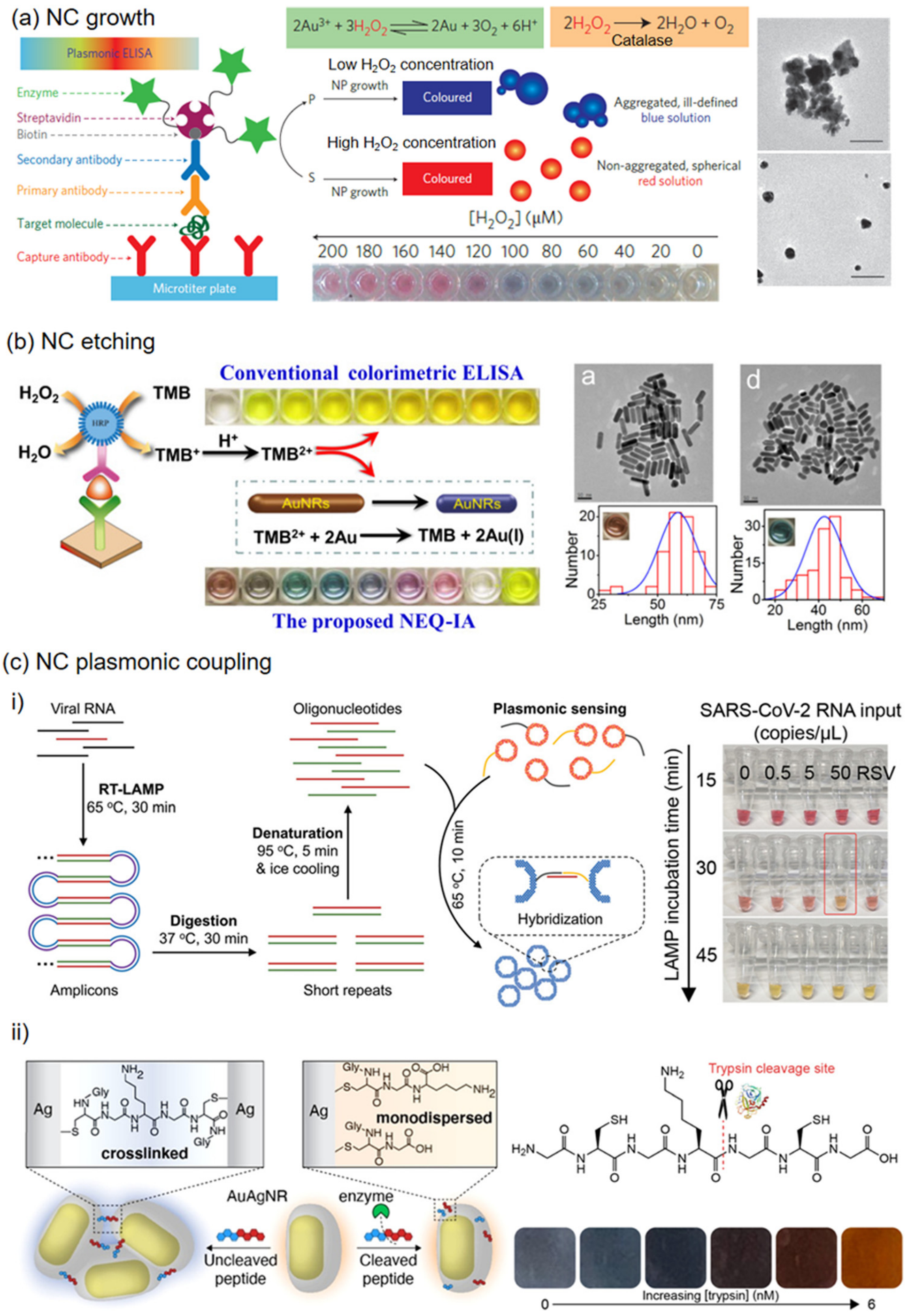
(a) NC growth
Plasmonic ELISA
Enzyme
Streptavidin
Biotin
Secondary antibody
Primary antibody
Target molecule
Capture antibody
Microtiter plate
2Au3+ + 3H2O2 ⇌ 2Au + 3O2 + 6H+
2H2O2 → 2H2O + O2
Catalase
Low H2O2 concentration
NP growth
Coloured
Aggregated, ill-defined blue solution
High H2O2 concentration
Coloured
NP growth
Non-aggregated, spherical red solution
P
S
[H2O2] (μM)
200 180 160 140 120 100 80 60 40 20 0
(b) NC etching
H2O2
TMB
H2O
TMB+
H+
TMB2+
HRP
Conventional colorimetric ELISA
AuNRs
AuNRs
TMB2+ + 2Au → TMB + 2Au(I)
The proposed NEQ-IA
a
d
Number
Length (nm)
20
10
0
25
50
75
30
15
0
20
40
60
(c) NC plasmonic coupling
i)
Viral RNA
RT-LAMP
65 °C, 30 min
Amplicons
Digestion
37 °C, 30 min
Short repeats
Denaturation
95 °C, 5 min
& ice cooling
Oligonucleotides
65 °C, 10 min
Plasmonic sensing
Hybridization
SARS-CoV-2 RNA input (copies/μL)
0 0.5 5 50 RSV
LAMP incubation time (min)
15
30
45
ii)
Ag
crosslinked
Ag
monodispersed
NH2
Gly
HN
NH
S
Gly-NH
OH
NH2
Trypsin cleavage site
H2N
SH
SH
OH
AuAgNR
enzyme
Uncleaved peptide
Cleaved peptide
Increasing [trypsin] (nM)
0
6

Fig. 29 Colloidal NP-based colorimetric sensing examples categorized according to signal generation mechanisms. (A) NP growth: ultrasensitive detection of prostate specific antigen and HIV-1 capsid antigen p24 based on the growth of gold NPs band reproduced with permission from ref. 776 Copyright Nature publisher (B) NP etching: multichromatic semiquantitative immunoassay enabled by $TMB^{2+}$etched Au NRs band reproduced from ref. 781 with permission from Elsevier publisher, Copyright 2017 (C) NC plasmonic coupling: (i) specific and sensitive detection of SARS-CoV-2 RNA through the agglomeration of gold-silver alloy nanoshells involving loop-mediated isothermal amplification reproduced from ref. 782 with permission from Wiley-VCH publisher, Copyright 2022 (ii) Trypsin detection by modulating the aggregation of Ag-coated Au NRs reproduced from ref. 783 with permission from ACS publisher, Copyright 2022.

Ag-coated Au NRs.[783] The plasmonic-coupling-based colorimeter sensors have been reported to detect various targets, including metal ions,[798] proteins,[796] DNA,[799] bacteria,[800] and viruses. A common approach is to modulate the weak interaction between high-affinity ligand-modified nanoparticles. For example, an HRP-mediated, iodide-catalyzed cascade reaction was reported to control the oxidation of cysteine to cystine and the following dispersion/aggregation of Au NPs for the detection of proteins.[796] An enzyme-free colorimetric sensor was based on the release of cysteine from liposomes and subsequent aggregations of Au NPs.[800] This approach enabled the visual detection of single-digit bacteria and target antibodies at an attomolar concentration. Plasmonic NPs can be functionalized with an aptamer, DNAzyme, or probe DNA, which changes color after complementary DNA is added to initiate DNA hybridization and NP aggregation.[799,801] Ye *et al.* demonstrated specific and sensitive naked-eye detection of SARS-CoV-2 RNA with a low limit of detection at 10 copies per reaction and a ~75-min assay time (Fig. 29c, i).[782] The RNA was reverse transcribed and amplified with loop-mediated isothermal amplification. The amplicons were then prepared into short repeats in oligonucleotides. For colorimetric readout, the oligonucleotide-functionalized AuAg alloy nanoshells were introduced, and a color change from red to yellow was induced by the agglomeration of the plasmonic nanoshells *via* DNA hybridization within 10 min at 65 °C. The AuAg nanoshells as plasmonic sensors show 4 times stronger extinction and 20 times lower limit of detection compared to gold counterparts. Creyer *et al.* constructed a colorimetric assay using core–shell AuAg NPs for trypsin detection.[783] In this application, the authors investigated three types of nanostructures, including Ag-coated Au NRs with orange slice shape, Au-coated Ag NSs with spherical shape, and Ag-coated Au NRs with nanocuboid shape. Cysteine-containing peptides (Gly-Cys-Gly-Lys-Gly-Cys-Gly) were used to mediate the aggregation of NPs, producing a color response from orange to blueish grey (Fig. 29c, ii). In the presence of trypsin, the crosslinker is cleaved, and the aggregation of the NPs is attenuated. Among the three nanostructures, the orange slice-like Ag-coated Au NRs showed the strongest colorimetric response and provided a low LOD of trypsin at ~0.5 nM.

Plasmonic colorimetric sensors have the potential to detect a wide range of analytes, including ions, metabolites, proteins, bacteria, and viruses, at point-of-care and resource-limited settings. Colloidal colorimetric sensors rely on chemically synthesized Au and Ag NPs, which are low-cost and easy to scale up compared to lithography-fabricated plasmonic NPs on substrates. To further reduce material cost, plasmonic NPs made of other materials, such as copper, aluminum, and magnesium, can be considered.[802] Surface functionalization plays an important role in achieving the desired sensitivity, specificity, and stability of colorimetric sensors. The growth-based and etching-based colorimetric sensors offer better stability and reproducibility than the plasmonic coupling-based approach. Further improvement can be realized by immobilizing nanomaterials on low-cost substrates, such as paper and foam, which enables highly uniform nanostructure immobilization and easy integration with a microfluidic platform.[803–811] The strategy to enable multiplexed detection with a small volume of samples is useful for many applications, such as disease diagnosis and health monitoring.[811–813] The specificity of colorimetric sensors needs vigorous testing against potential interferents, considering the complexity of real samples in targeted applications. To achieve specificity, many sensors utilize antibodies and enzymes, which have limited stability at room temperature and under harsh environmental conditions. Stable biorecognition elements, such as molecular imprinted polymers and aptamers, can be utilized to address this challenge.[814–816] Alternatively, preservation materials, such as glycerol, organosiloxane, silk, and metal–organic framework, can be deployed to enhance biomolecule stability and prolong sensor shelf life.[666,817–819] Among these, the best-performing materials require removal to make biomolecules accessible for specific interaction with targets, which complicates the implementation in colorimetric sensor operation. There is still a need to develop superior materials to provide robust preservation capability, which can be easily implemented in high throughput and low cost. Another challenge is to detect analytes by differentiating the changes in color wavelength and intensity with the naked eye. A promising solution is to use a smartphone camera, which is widely available, with image-processing algorithms to achieve robust detection and quantification of targeted analytes.

### 5.4. Lateral flow assays (LFAs)

LFAs are another type of plasmonic NP-based sensor whose response is also based on colorimetry.[820–822] LFAs are paper-based biosensors in which the sample flows by capillarity, dragging with it the nanoparticles to the areas where the recognition takes place, the test and control lines (TL, CL). In fact, these types of biosensors are an evolution of paper chromatography[823] and the technology behind well-known products as the pregnancy test. LFAs are ideal for point-of-care (POC) testing,[74] where the patient is located, either in the hospital (diagnostics), at home (it grants the patient a plus of privacy) or even in the field (environmental sensing). The qualities that make LFAs so suitable for POC are their portability, easiness of use (no special training is required, and any person can use them) and the fact that they are completely battery and equipment-free. In addition, LFAs are very affordable and sustainable, since the main component is, as we said, paper (cellulose and nitrocellulose). The common design of a LFA is a paper-strip composed of 4 different pads,[824,825] as illustrated in Fig. 30. A sample pad is generally composed of cotton fiber (cellulose), although other materials such as polyester, polypropylene and glass fiber can be also employed, and it is where the sample is dropped (Fig. 30a).

A sample pad is normally pre-treated with salts, which will act as buffer for all the reactions across the strip, and other compounds such as surfactants, that may contribute the fluidic or releasing the sample (*e.g.* by breaking a viral capsid). The sample will then flow to the conjugate pad (Fig. 30b), commonly made of glass fiber, polyester, or polypropylene, although hybrid materials have been emerging during the last years (*e.g.* Fusion 5).[826] In the conjugate pad there is a nanoconjugate (NP conjugated with a bioreceptor, *e.g.* an antibody or a DNA strain, that specifically recognizes the target analyte) dry stored that will be rehydrated and dragged by the flow. The nanoconjugate captures the target analyte, if present in the sample, and flow together throught the detection pad. The detection pad is made of nitrocellulose on a plastic support. The two parameters of this material that are key for the assay are: the pore size of the paper, which will control the flow speed (being s/4 cm a common flow unit given by nitrocellulose

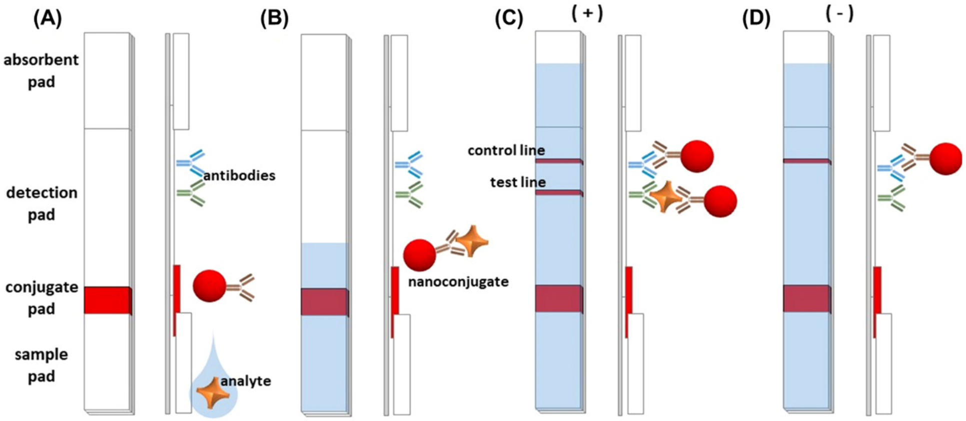

Fig. 30 Illustration of a LFA and its working principle. (A) Components of a LFA paper strip (front and side views). (B) Sample flowing across the paper strip. (C) Positive response, nanoconjugate reaches TL and CL. (D) Negative response, in absence of the analyte, only CL is visible. Reprinted from ref. 822 with permission from **https://www.sensor100.com/Sens_Tech_Dir/lateral-flow/**, copyright 2023.

manufacturers), and the affinity for the proteins (related to the amount of nitro groups on the nitrocellulose structure) which can be tuned by pre-treating the material with surfactants or proteins. In the detection pad there are the TL and CL are in the detection pad (Fig. 30c). When color is visible in the TL the response is positive (the analyte is present on the sample). TL consists of a bioreceptor able to capture the analyte, which at the same time is attached to the nanoconjugate, thus in a positive sample a "sandwich" recognition takes place (TL bioreceptor – analyte – nanoconjugate bioreceptor – nanomaterial). CL indicates if the assay is working properly. Thus, CL presents a printed bioreceptor that targets the bioreceptor of the nanoconjugate. The absence of CL may indicate a failure in the assay therefore considering the result null. If the sample is negative (Fig. 30d) there will be no recognition on TL and thus only CL will be visible. The methodology described follows the "standard" or "direct" LFA mechanism, however, other systems employ "competitive" or "indirect" strategies, not discussed within this review, which are less reported but useful for cases in which the analyte is too small and the "sandwich" recognition may not work due steric hindrances between the bioreceptors.[820]

LFAs can be employed for the recognition of different types of analytes, from proteins and hormones,[827] to allergens in food,[828] or dust,[829] bacteria,[830] DNA,[831] extracellular vesicles,[832] and even heavy metals;[833] practically any type of analyte as long as there is a bioreceptor able to carry on the recognition. Actually, LFAs can be used for multiplexing, detecting several analytes at the time by placing several TL on the strip, or a dots array instead.[834,835]

**5.4.1 Signal enhancement on LFAs using nanomaterials.** Thanks to the plasmonic properties of nanomaterials, the response on LFAs can be quantified by relating the colour intensity of the TL with the concentration of analyte in the sample. This signal value can be measured by simply using a smartphone[836] or by using commercially available SPR readers specially designed for LFAs.[837] Among the different nanomaterials, Au NPs stand as the most commonly used nanomaterial in LFAs[827–835] due to its strong red colour, easy synthetic procedure (Turkevich method)[838] and biocompatibility with bioreceptors (*e.g.* antibodies or DNA).[839–841]

There exist several strategies that can be carried out using nanomaterials to enhance the colorimetric signal,[842,843] such as increasing the ratio of nanoparticles per unit of analyte (which can be done by combining nanoparticles together to increase the plasmonic intensiry,[844,845] or by reducing the number of bioreceptors on the surface of non-spheroidal nanoparticles,[846] so each nanoparticle captures a minimum amount of target analyte units), exploring novel nanomaterials with stronger plasmonic response (*e.g.* C dots[847] or $IrO_2$ NPs[848]) and even fluorescent properties,[849] using nanomaterials to modify the paper substrate properties,[850,851] relying on secondary reactions to enhance the colorimetric signal (*e.g.* nanozymes: mimicking enzymatic reactions using NPs),[852,853] modifying paper architecture (altering the flow across the strip)[854,855] or seeking for novel sensing techniques, as thermochromism.[856] Some selected examples are explained below with more detail.

NP clusters (nanoclusters) exhibit higher sensitivity levels than single particles on LFAs,[848] however working with them can be hard since they easily tend to aggregate. Oh *et al.* synthetized colour-preserved Au NPs clusters stable against aggregation for LFAs.[857] In their work, they compared different clusters selecting those of 40 nm diameter Au NPs, in which the particles remained stably separated with a gap around 15 nm thanks to streptavidin and biotinylated antibodies (Fig. 31a). Their LFA exhibited a LoD of 0.038 ng $mL^{-1}$ for the SARS-CoV-2 nucleocapsid protein; this is around 4000 times lower than a non-enhanced LFA for a model protein (*e.g.* human IgG).[850] It must be noted that authors may use different methods to calculate LOD values, so the comparison between systems is not always "precise". We recommend calculating the LOD from the equation of the calibrate, *e.g.* $f(x) = a + b{\cdot}\log(x)$, considering as "$f(x)$" the value of blank plus 3.3 times its standard deviation and then isolating from the equation the concentration parameter "$x$" as the LoD value.[858]

Graphene has the property to quench (turn-off) the fluorescence of several nanomaterials (*e.g.* nanoclusters[860] and quantum dots,[861] QDs), and this property can be also applied inside the LFAs.[859] Morales-Narváez *et al.*[861] and Hassan *et al.*[859] took

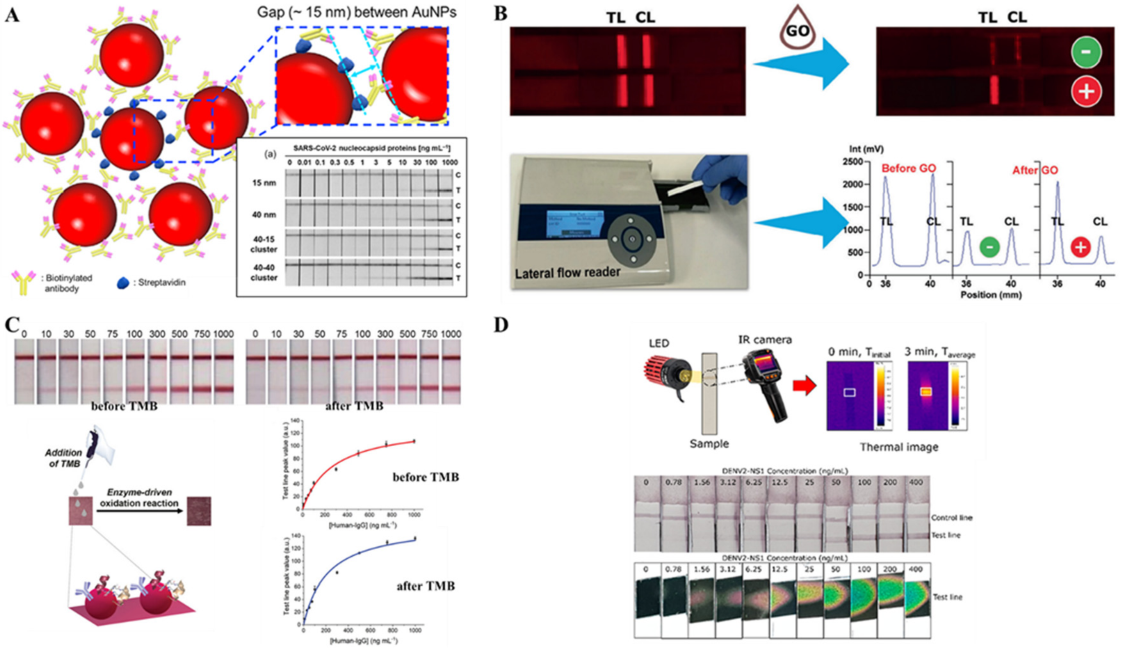

Fig. 31 (A) Streptavidin-stabilized Au NPs nanoclusters for LFAs. Reproduced from ref. 857 with permission from Elsevier, copyright 2022 (B) Fluorescent response observed on QDs-based LFAs in which the signal is quenched by graphene. Reproduced from ref. 859 with permission from Elsevier publisher, Copyright 2019. (C) Enzymatic reaction using an artificial enzyme to enhance LFAs response. Reproduced from ref. 852 with permission from Wiley-VCH publisher, Copyright 2023 (D) Au NPs being heated on a LFAs and thermochromically measured. Reproduced from ref. 856 with permission from RSC publisher, Copyright 2023.

advantage of this effect and designed a system very different from conventional LFAs: they immobilized QDs on TL and CL. QDs were conjugated to the antibodies recognizing the target (the bacterium *Escherichia coli* in both cases), and bare QDs were immobilized in CL. After the bacteria has been added to the strip, the graphene solution is dropped and quenches the fluorescence of QDs, except if bacteria are there (in the TL) since it generates a gap between QDs and graphene, impeding their quenching. Thus, if the sample is negative, all the fluorescence, both TL and CL, are quenched. If the sample is positive, after adding graphene only the TL should be visible (Fig. 31b). The response can be quantified with a table fluorescence reader,[862] reaching a LOD as low as $10^5$ CFU mL$^{-1}$, only 100 times greater than commercial ELISA kits.[863]

As previously mentioned, another way to enhance the signal on LFAs is by carrying out enzymatic colorimetric reactions on the nanomaterials, which may act as nanozymes.[853] However, in the work of Renzi *et al.* they immobilized an artificial metalloenzyme (a.k.a. mimochrome) called "FeMC6*a" on Au NPs,[852] claiming its advantages over nanozymes. In the assays, nanozymes may lead to some irreproducibility issues due to little variations in NPs shape and size can provoke variations in the catalytic reactions. Instead, metalloenzyme behaviour imitates the molecular level behaviour of enzymes, being able to replicate native enzyme functions with greater reproducibility.[864] So, in the work of Renzi *et al.*, FeMC6*a was immobilized on Au NPs and, after running the assay as a standard LFA, a substrate (3,3′,5,5′-tetramethylbenzidine, TMB) was added to the strip that, when oxidized by the metalloenzyme, increased the colour intensity of the TL (Fig. 31c). With this method the LOD of the assay was decreased from 36.4 to 8.2 ng mL$^{-1}$.

As a last example, Trakoolwilaiwan *et al.* explored different nanomaterials for their application in thermochromic LFAs, as a new signal quantification method.[856] It must be highlighted that the orientation of plasmonic NPs has a great impact on the ability to be heated, since the closer the particles can be, the greater the heat transmission. Then, as they found, spherical Au NPs exhibited greater response when heated by LED light and measured by an IR camera (Fig. 31d), compared to other structures such as NRs, which difficult the contact among the nanomaterials. They observed that the working range of their LFAs did not differ too much from conventional optical LFAs. However, the sensitivity of the assay (the capacity to discern between close values, *i.e.* the slope of the calibration plot) was greater, allowing a better quantification. Thermal measurements on LFAs have reported up to an 8-fold increase in the sensitivity of the assays.[865]

**5.4.2 Prospects of LFAs.** There is a lot to explore regarding the known and new properties of plasmonic nanoparticles and their application on LFAs. As we have explained, nanomaterials exhibit a great potential to enhance the signal on these types of sensors. We strongly believe that the future of LFAs will move to seek more precise quantification, and for that purpose, new methods for translating the signal (besides the naked eye) will emerge. Apart from plasmonic methods, electrochemical-based techniques[820,842,843,866] (not discussed within the topic of this review) are of great potential and could help to improve the quantification when using nanomaterials in the assay.

However, the integration of electrodes on a paper substrate is not an easy task.[867] Also, electrokinetic methods (*e.g.* electrophoresis) may add extra advantages to the performance (*e.g.* matrix washing, interfering species removal, *etc.*).[868,869] The bioreceptors employed on future LFAs will change as well, from classical immunoassays (*i.e.* antibodies) to molecular biosensing (*i.e.* DNA and derivate probes, such as aptamers),[870,871] not only because of the robustness and inexpensiveness of these probes but also because of the possibility of integrating DNA amplification techniques inside the LFA protocol.[872] For example, the isothermal amplification method based on recombinase polymerase amplification (RPA) has been already widely reported on LFAs.[873–875] In any of these cases, the use of smartphones as a tool to interpret the response is feasible. Smartphones have the potential as "partners" of LFAs, not only to record the result, but to explain the test procedure, provide electrical supply to the test (if necessary), or share the response with a clinician or specialist, among many other possibilities.[836]

# 6. Chiroptical sensing

Chirality is a universal phenomenon observed at various length scales ranging from small molecules, NPs, and large structures.[876,877] Of special interest has been the chiral signatures in amino acid units, which are the building blocks of proteins. Protein chirality can further extend to complex structural units which in turn has resulted in the induction of optical activity into other biomolecular systems such as DNA and RNA. Due to the rich abundance of optically active species in living systems, the development of sensing platforms dependent on chiroptical spectroscopy can be a powerful tool for the detection of biologically relevant molecules.[878] Realizing these facts, different research groups have focused their attention towards the development of chiroptical sensors that are relevant to the detection of various diseases and biomarkers.[879,880]

Among different classes of biosensors that rely on chiroptical spectroscopy, the ones based on chiral plasmonic nanomaterials, owing to their ability to focus light onto nanoscale dimensions,[881,882] have emerged as promising candidates for applications in the field of biomedical research.[883,884] Most sensors rely on circular dichroism (CD) which measures the differential absorption of left- and right-circularly polarized light. In this regard, plasmonic nanostructures, due to their large absorption and scattering cross sections, can generate intense CD signals. Recent advances in synthetic protocols have offered versatile avenues for the fabrication of a wide range of nanomaterials.[885] Efforts in this direction have resulted in the fabrication of chiral nanostructures with enhanced sensing capabilities.[884] Detection limits as low as attomolar and zeptomolar concentrations have been achieved rendering this class of sensors extremely relevant in the field of forensic science, drug industry, and biomedical applications, areas that demand very high sensitivities.[879,880] Moreover, these nanomaterials generate chiral plasmonic signals in the visible and NIR regions of the EM spectrum, a spectral range that is clear from the interference of biomolecule and solvent signals.

The interaction of plasmonic NPs with chiral analytes can generate plasmonic CD signals that can be used as a biosensing platform. Depending on the nature of interactions and the mechanism of chiral induction, plasmonic chirality for biosensing applications can be broadly divided into two classes; (i) assembly of achiral NPs on the chiral templates leading to the generation of coupled plasmonic CD signals[137,886–891] and (ii) generation of induced plasmonic CD through the interaction of chiral molecules with the plasmonic field of achiral NPs.[892–898] The following section will discuss a few examples wherein plasmonic CD signals generated through these two approaches are used for sensing of biologically relevant analytes.

## 6.1. Template-assisted NP assemblies

Plasmonic NPs, due to their unique LSPR properties that enable the trapping of light into nano-dimensions, experience larger chiroptical responses compared to their molecular counterparts. However, self-assembly of these NPs into chiral geometries, results in plasmonic coupling between adjacent NPs leading to intense chiroptical responses that aid sensing of the analytes at extremely low concentrations.[137,880] One of the common techniques to fabricate chiral-shaped nanostructures and their assemblies is electron-beam lithography. However, the technique is limited by scalability and high cost, and hence we will focus our discussion on the various solution-processed bottom-up approaches developed for the synthesis of chiral NP assemblies. DNA, RNA, peptides, proteins, and other biomolecular assemblies act as robust templates for the assembly of NPs, and some of the relevant examples are discussed in the following section.[137,886–890]

Initial studies on the generation of plasmonic chirality relied on the use DNA and peptides, even though the objective then was not on the biosensing.[886,887] Thomas and co-workers, in one of the initial reports, used self-assembled peptides to obtain mirror image plasmonic CD signals from Au NPs attached to opposite isomers of the peptide surface.[887] Since then, there has a large number of reports on generation and tuning of plasmonic chirality using a variety of templates. Recent efforts in this direction have focused on finding applications for nanohybrid systems, with biosensing is at the forefront of all of these endeavors. Liz-Marzan and co-workers utilized the assembly of NRs on the protein fibrils formed from α-synuclein for the detection of Parkinson's disease (Fig. 32a).[137] The chiral nature of the fibrils facilitated helical assembly of NRs which in turn generated plasmonic CD signals in the visible and NIR region (Fig. 32b). Fibrillation of protein being a hallmark of neurodegenerative diseases, the chiral plasmonic signals could be used for the detection of Parkinson's disease. Kuang and co-workers developed a DNA-based detection platform for the sensing of mycotoxin, namely, ochratoxin A (OTA).[888] Chiral satellite superstructures synthesized using core–shell Ag@Au NPs (functionalized with OTA aptamers) and Au NSs (functionalized with complementary sequence of OTA aptamers) exhibiting intense negative CD signal at 530 nm was employed as the plasmonic platform. Upon addition of OTA, the superstructures disassembled leading to a gradual reduction in the CD signals as a function of OTA concentration. The linear fit could

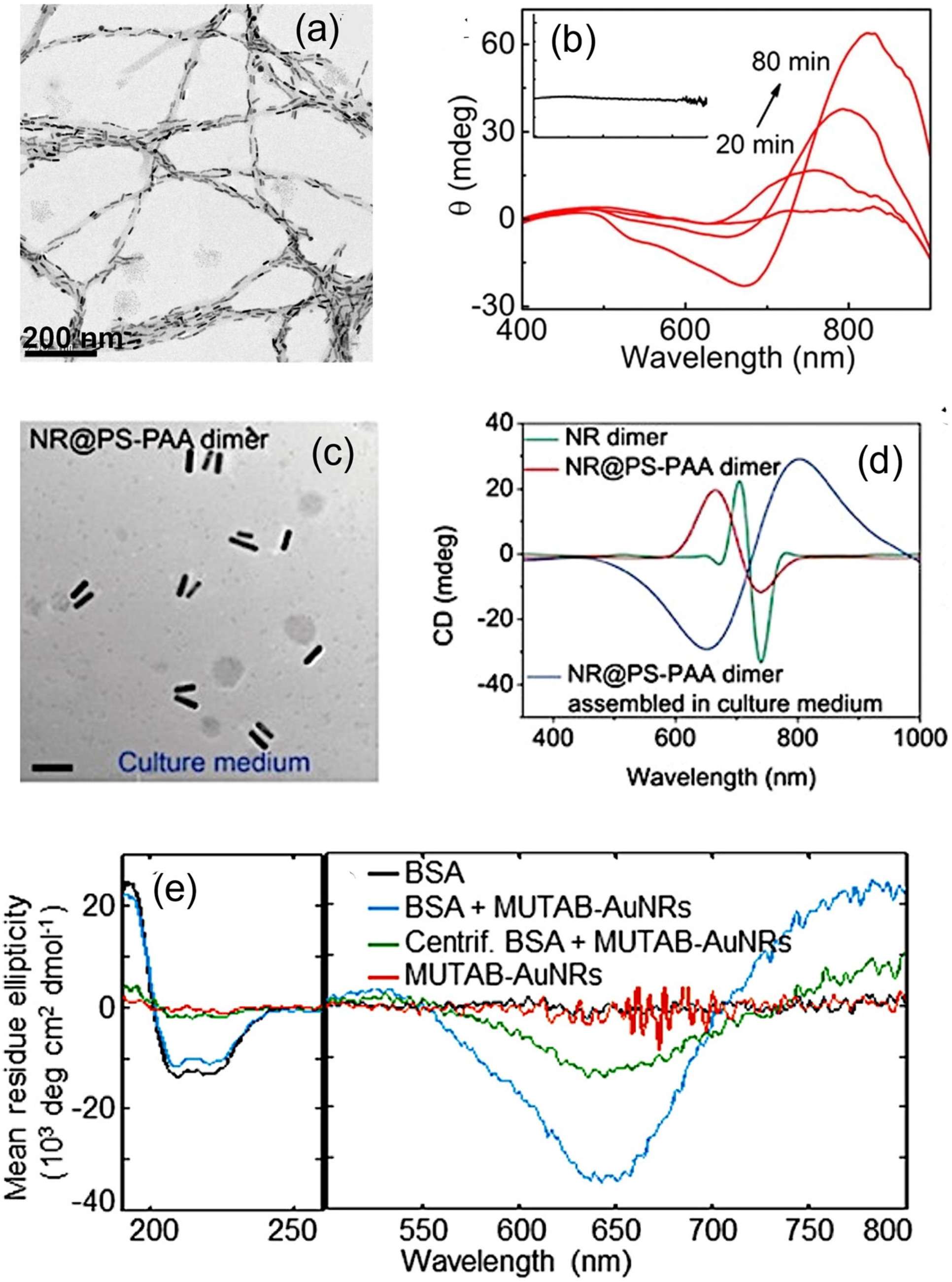

Fig. 32 Detection of Parkinson's disease. (A) TEM image depicting the assembly of Au NRs on protein fibrils and (B) the corresponding CD spectra showing an enhancement as the assembly progresses. Spectra in the inset shows no CD for NRs in the native protein sample. Reproduced from ref. 137 with permission from PANAS publisher, Copyright 2018. (c,d) Detection of miRNA. (C) TEM image of NRs encapsulated by PS-PAA in culture medium (scale bar = 100 nm). (D) CD spectra side-by-side assembled dimers of bare Au NRs (green trace) and NRs encapsulated by PS-PAA in PBS buffer (red trace) and culture medium in the presence of 100 pM of synthetic microRNA-21 (right). Reproduced from ref. 890 with permission from Wiley publisher, Copyright 2018 (E) Unfolding of BSA upon adsorption to MUTAB-AuNRs. CD spectra of BSA (black trace), MUTAB-AuNRs alone (red trace), BSA/MUTAB-AuNRs (blue trace), centrifuged BSA/MUTAB-AuNRs (green trace) Reproduced from ref. 891 with permission from ACS publisher, Copyright 2016.

be used for the qualitative and quantitative detection of OTA. In different approach, Liedl and co-workers used DNA origami template to generate switchable plasmonic chirality that could detect specific RNA at picomolar concentrations.[889]

Xu and co-workers used the side-by-side assembly of Au NRs for the detection of microRNA (miRNA). DNA functionalized Au NR dimers were further stabilized with poly (styrene-*b*-acrylic acid) (PS-PAA) for intracellular stability and biocompatibility.[890] miRNA driven side-by-side self-assembly of the PS-PAA-coated Au NRs in living cells generated distinct plasmonic CD signals that helped the *in vivo* detection of miRNA in picomolar concentrations (Fig. 32c and d). BSA detection through the aggregation of mercaptoundecyltrimethylammonium bromide (MUTAB)-coated Au NRs was demonstrated by Link and co-workers.[891] Adsorption of BSA on the NP surface led to the unfolding of the protein. Subsequent interactions between the unfolded proteins drive the NP aggregation resulting in plasmonic CD signals (Fig. 32e). Au NR aggregation at nanomolar concentrations of BSA facilitates the use of plasmonic platforms for biosensing applications. Kotov and co-workers studied the cell internalization of NPs using plasmonic CD signals from assembled NR dimers.[892] DNA-bridged chiral NP dimers upon introduction to mammalian cell media showed a variation in the magnitude and sign of CD signal for NPs internalized in the cell. The CD reversal was attributed to the spontaneous twisting motion around the DNA bridge due to changes in the electrostatic repulsion between NP in a dimer during the transmembrane transport. There are several reports on similar NP assemblies being used for applications such as drug screening, and detection of other biologically relevant analytes. The enhancement in signal intensity during the assembly process makes this approach an attractive tool for the highly sensitive detection of analytes.

### 6.2 Induced plasmonic chirality as a biosensing tool

Another approach for the generation of plasmonic CD signals is through the Coulombic interaction between a chiral molecule and an achiral NP. While there are different classifications to such an effect, we restrict our discussions to the plasmon-coupled circular dichroism phenomenon which deals with the chiral induction into nanoantenna by a chiral molecule through dipolar or multipolar interactions. Govorov *et al.* framed detailed theoretical formulations for these effects and attributed the origin of plasmonic chirality to different mechanisms such as far-field EM coupling, near-field interactions, and orbital hybridization.[893] The initial investigations in this direction were carried out by Naik and co-workers who created optically active Au NPs through their interaction with random coil and α-helix peptides as chiral analytes.[894] The peptide–Au NP interactions produced plasmonic CD at the LSPR of Au NPs. Later, the same effect was widely used for the generation of plasmonic CD signals in achiral NPs that were coupled with a wide variety of chiral molecules, such as DNA, peptides, proteins, and dye molecules.

Markovich and co-workers used a chiral molecule riboflavin to induce chiral plasmonic signals into Au islands deposited on a glass slide.[895] While the Au islands coated with the achiral polymer, poly (methyl methacrylate) (PMMA), did not exhibit any CD signals, riboflavin-embedded PMMA when coated onto the Au islands showed CD peaks in the plasmonic region (Fig. 33a). They could further demonstrate the distance dependence of the same effect by coating an achiral polyelectrolyte spacer between the Au island and the chiral layer. Enhanced plasmonic CD signal in achiral core–shell Au@Ag NCs was achieved through DNA attachment by Gang and co-workers.[899] The greater sensitivity was attributed to the lower plasmon loss and stronger LSPR enhancement of Ag compared to Au in the visible region of the spectrum. There have been several attempts to obtain higher sensitivity by modifying the composition as well as the morphological features of the synthesized nanostructures. Attempts in this direction have led to a unique phenomenon termed as hotspot enhanced plasmonic chirality.

The theoretical formulations for hotspot-enhanced plasmonic chirality were first provided by Zhang and Govorov on Ag nanosphere dimer with varying gap space.[896] Later, Liedl and co-workers experimentally verified this effect on Au NP dimers assembled using DNA-origami.[897] They could observe orders of magnitude CD enhancement which could be attributed to the high field created at the hotspots of NPs (Fig. 33b). Recently, Severoni *et al.* demonstrated the hotspot-driven chiral enhancement in linearly assembled Au NRs wherein chiral bile salt derivative was used as the linker (Fig. 33c).[898] This peculiar effect has the potential to develop into an efficient platform reaching up to single-molecule detection. However, the major challenge is to precisely position the analytes at the plasmonic hotspots. In short, it can be summarized that the advancement in the field of NP synthesis has boosted the potential of chiral plasmonic detection platforms to a great extent. However, a lot needs to be explored in understanding the analyte structural/conformational changes and their interaction with the NPs at the molecular level. Further experimental and theoretical investigations can help understand these fundamental effects better. Future challenges also lie in demonstration in *in vivo* experiments and transitioning the detection tool for application in the market.

## 7. Outlook

Plasmonic NP-based sensors have emerged as formidable tools across a diverse array of applications. Even before a comprehensive understanding of their colorimetric properties, these NPs were used as colorimetric sensors, gradually evolving into practical applications such as LFIAsLFIAs, now commonplace in-home diagnostics. Subsequent comprehension of the principles governing their colorimetric behavior, coupled with advancements in SPR technologies, opened new vistas for plasmonic sensors. However, the discovery of SERS catalyzed an exponential surge in the development of new plasmonic nanoparticle sensors.

Despite the significant advantages offered by surface-enhanced characterization techniques, including theirtheir non-invasive nature, real-time monitoring capabilities, and multiplexing potential, theirtheir adoption outside academia has been relatively limited, failing to transition seamlessly into industrial settings. Numerous studies showcasee the exceptional detection limits and selectivity of plasmonic NP-basedbased sensors across various applications, yet translating this technology into practical use faces several hurdles.

Foremost among these challenges is the development of commercial plasmonic NP-based sensors sensors that meet industrial requirements: reproducibility, stability, and cost-effectiveness. Recent strides in this area have been promising, with notable progress achieved in fabricating nanostructures withwith excellent quality and tailored morphologies. In some instances, these advancements have led to the creation of nanostructures with smaller, more precisely engineered 2D

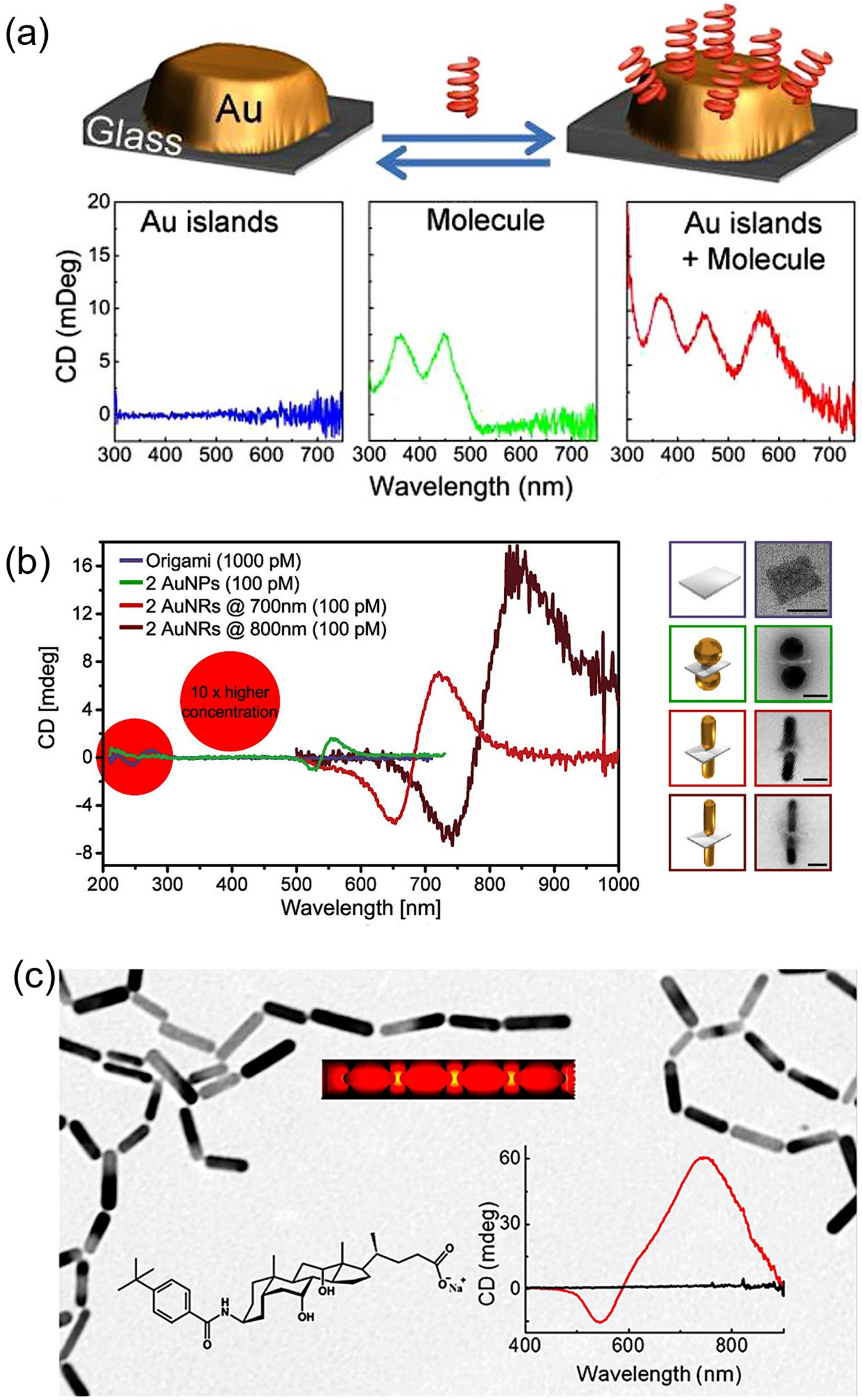

Fig. 33 (A) Induced chirality in Au islands. CD spectra of bare Au islands (blue trace), riboflavin molecule (green trace), and Au Island with riboflavin embedded in PMMA (red trace). Reproduced from ref. 895 with permission from ACS publisher, Copyright 2013. (B) Hotspot-enhanced CD in DNA origami-assembled Au NP dimers. Compared to the bare DNA origami template (purple), 30-fold and 300-fold amplified CD is observed for Au NP dimers (green trace) and Au NR dimers (red and brown traces). Scale bars = 40 nm. Reproduced from ref. 897 with permission from ACS publisher, Copyright 2018 (C) Hotspot enhanced CD induction in linearly assembled Au NRs. Bile salt derivative acts as the linker for the linear assembly of NRs Reproduced from ref. 898 with permission from ACS publisher, Copyright 2020.

and 3D nanogaps. Such innovative fabrication strategies and techniques have facilitated the rapid, cost-effective, and reproducible large-scale production of substrates and nanotags exhibiting robust signal responses, suitable for both general-purpose and target-specific sensing applications. However, further investigation is needed in areas such as the development of flexible plasmonic nanoparticle substrates that facilitate on-site analyte collection and transportation for later characterization, as well as their integration into small devices or even wearable devices. Another necessary improvement is finding a way to reuse the plasmonic substrates without a loss in efficiency. Significant advances have been made by applying UV light or plasma etching, but further investigation is required.

For plasmonic SERS sensors, a significant obstacle lies in the interpretation of SERS spectra. Despite theirtheir immense potential, the complex and intricate nature of SERS spectra often poses challenges in accurately deciphering and extracting meaningful information. The inherent variability in spectra associated with substrate fabrication arisesarises from factors such as nanoparticle size, shape, composition, and hotspot distribution, as well as the influence of the surrounding environment, complicatinging spectral analysis. Furthermore, the presence of spectral features originating from multiple analytes,contaminants, or plasmonic NP ligands further exacerbates the issue, confounding the identification and quantification of target molecules. Addressing these challenges requires innovative approaches, and one promising avenue is the integration of artificial intelligence or machine learning protocols. Machine learning algorithms offer a powerful means to navigate the complexity of SERS spectra, enabling the extraction of valuable insights and facilitating the identification of relevant spectral features. By leveraging advanced data processing techniques, machine learning algorithms can discern subtle patterns within spectra, discriminate between different analytes, and mitigate the effects of spectral variability. Moreover, machine learning models can adapt and improve over time, refining their predictive capabilities and enhancing the accuracy of spectral interpretation. Integrating machine learning protocols into SERS-based sensing platforms holds immense potential for enhancing analytical performance and expanding the scope of applications. By harnessing the complementary strengths of machine learning and SERS spectroscopy, researchers can unlock new opportunities for sensitive, selective, and reliable detection across diverse fields, ranging from biomedical diagnostics to environmental monitoring and beyond. Moreover, the synergistic combination of these technologies paves the way for developingdeveloping autonomous sensing systems capable of real-time, on-site analysis, thereby revolutionizing traditional analytical workflows and empowering users with actionable insights in various settings.

On the other hand, SEF applications also benefit from the implementation of machine learning algorithms to filter background noise and autofluorescence as well as to separate overlapping spectral features from the fluorophores and the metallic nanostructures, leading to clearer and more accurate fluorescence signals. However, the major limitation in this case is controlling the interaction between plasmonic nanoparticles and fluorophores to overcome the quenching effect. Controlling the distance between the fluorophore and the metal surface requires precise control and still needs further investigation.

Plasmonic colorimetric sensors require NP surface functionalization to achieve the desired sensitivity, specificity, and stability. Their major limitation is specificity since, considering the complexity of real samples in targeted applications, they can suffer from potential interferents. To avoid this limitation, many sensors utilize antibodies and enzymes, which have limited stability at room temperature and under harsh environmental conditions. However, this challenge continues to need addressing through new and more complex functionalization options. In the particular case of LFA, apart from finding new possible functionalizations for the plasmonic NPs, it is necessary to search for new bioreceptors such as DNA aptamers that could allow the integration of DNA amplification techniques into the LFA protocol. Also, another key parameter for the future improvement of LFAs is the employment of more precise quantification techniques besides the naked eye, such as the combination with SERS spectroscopy.

Chiral plasmonic detection platforms are a relatively new characterization technique that still requires further exploration to understand the analyte structural/conformational changes and their interaction with the NPs at the molecular level. Further experimental and theoretical investigations can help understand these fundamental effects better. In general, one major area for future development is the integration of plasmonic NP-based sensors with modern digital and communication technologies. Combining plasmonic sensors with smartphones, portable devices, and Internet of Things (IoT) platforms could enable real-time, remote, and user-friendly diagnostics. For example, the integration of LFA sensors with smartphones will allow the recording of the test result, guaranteeing its correct interpretation, and even sharing the response with a clinician or specialist if necessary. This integration requires advancements in miniaturization and the development of robust, cost-effective, and easy-to-use sensor kits.

In conclusion, plasmonic NP-based sensors have a bright future with the potential to revolutionize various fields, including medical diagnostics, environmental monitoring, and security. By addressing the current challenges and leveraging technological advancements, these sensors can become indispensable tools for real-time, highly sensitive, and specific detection of a wide range of analytes.

## Author contributions:

K. K., L. P., and I. P. S. initiated and coordinated the review. L. P. and I. P. S. edited the manuscript. The manuscript was written through the contributions of all authors. L. P. contributed to the introduction; X. X. and J. W. contributed in different type of plasmonic metal nano crystal; L. P. contributed to the Methods of plasmonic sensing; R. A. A. contributed to the Basics of SERS; T. L. contributed to the Single molecule SERS; K. K. and D. R.

contributed to the SESR Sensing platforms; V. R. S., S. S. B. M., and R. B., contributed to the Chemical Sensing Medium; L. G. C. and D. G. L. contributed to the Ionic Species sensing; M. L., R. M., and M. P. P. contributed to the Gas Sensing; P. W., S. M. and V. B., contributed to the SERS-based Nucleic acid detection; B. R., and S. K., contributed to the SERS Protein detection; S. A. C. contributed to the SESR cell Detection; Y. J., Q. Y., and J. C., contributed to the SERS-based bacterial/viral sensors; P. H., and S. G.-G, contributed to the Sensing Reaction progress and intermediates; Y. C., and M. S., contributed to the SERS + Other technologies; S. S., Y. L., and Y. L. contributed to the Surface enhanced fluorescence based plasmonic sensors; X. Y. L., contributed to the SERS Data Analysis; P. S. S., P. L. C., and J. M. M. A., contributed to the LSPR; J. L. M. P., and M. G., contributed to the colorimetric sensing; H. G., and L. T., contributed to the colloidal colorimetric sensing; D. Q. G., and A. M., contributed to the LFAs; J. K., and S. M., contributed to the Chiroptical; J. P. J and I. P. S., contributed to the Outlook. All authors read the manuscript and have approved the final version of the manuscript.

## Data availability

No primary research results, software or code have been included and no new data were generated or analysed as part of this review.

## Conflicts of interest

The authors declare the following competing financial interest(s): Srikanth Singamaneni is an inventor on a pending patent related to plasmonic-fluor technology, and the technology has been licensed by the Office of Technology Management at Washington University in St. Louis to Auragent Bioscience LLC. He is a co-founder/shareholder of Auragent Bioscience LLC. He along with Washington University, may have financial gain through Auragent Bioscience, LLC through this licensing agreement.

## Acknowledgements

Krishna Kant acknowledge European Union's Horizon 2020 research and innovation program under the Marie Sklodowska-Curie grant agreement no. 894227. Lara González-Cabaleiro acknowledge Xunta de Galicia for a predoctoral scholarship (Programa de axudas á etapa predoutoral da Consellería de Cultura, Educación e Universidades da Xunta de Galicia, reference number: 2022/294). Heng Guo and Limei Tian acknowledge the funding from the National Science Foundation (Grant No: 1648451), and the National Institutes of Health (Grant No: R21EB029064 and R35 GM147568). Ramon A. Alvarez-Puebla acknowledges support by the projects PID2020-120306RB-I00 (funded by MCIN/AEI/10.13039/501100011033), PDC2021-121787-I00 (funded by MCIN/AEI/10.13039/501100011033 and European Union Next Generation EU/PRTR), 2020SGR00166 (funded by Generalitat de Cataluña) and 2021PFR-URV-B2-02 (funded by Universitat Rovira i Virgili). Maria P. Pina acknowledges support from: the European Union's Horizon 2020 research and innovation program under grant agreements No. 883390 (H2020-SU-SECU-2019 SERSing Project), No. 823895 (H2020-MSCA-RISE-2018 SENSOFT), AEI Spain (PID2019-108660RB-I00). Marta Lafuente, thanks Ministerio de Universidades (Spain) and Next Generation EU for the postdoctoral grant "Margarita Salas". Rizia Bardhana and Siddhant Kothadiya acknowledge support from the National Institutes of Health (NIH) award R01EB029756-01A1 and congressionally directed medical research program (CDMRP) award W81XWH-20-1-0620. Jaebum Choo thanks the financial support from the National Research Foundation of Korea (Grant numbers 2020R1A5A1018052 and RS-2024-00352256). Daniel Quesada-González and Arben Merkoçi acknowledge that the ICN2 is funded by the CERCA programme/Generalitat de Catalunya. The ICN2 is supported by the Severo Ochoa Centres of Excellence programme, Grant CEX2021-001214-S, funded by MCIN/AEI/10.13039.501100011033 and Grant PID2021-124795NB-I00 funded by MICIU/AEI/10.13039/501100011033 and by "ERDF/EU" and Departament de Recerca i Universitats of Generalitat de Catalunya for the grant 2021 SGR 01464. Sergio Gómez-Graña acknowledges support by the projects PID2020-117371RA-I00, TED 2021-131628A-I00 and CNS2022-135531 funded by MCIN/AEI/10.13039/501100011033. Soma Venugopal Raoexpresses thanks to Defence Research and Development Organization, India, for the financial support received through ACRHEM [#ERIP/ER/1501138/M/01/319/D(R&D)] and the financial support from the Institute of Eminence (IoE) [ref. No. UOH/IOE/RC1/RC1-20-016]. The IoE project was awarded to the University of Hyderabad by the Ministry of Education, Government of India, per the MHRD notification F11/9/2019-U3(A). Sara Abalde-Cela acknowledges supported by the 3DSecret project, funded by the EU under the program HORIZON-EIC-2022-PATHFINDEROPEN-01-01 (ga 101099066) and by the UK Research and Innovation (UKRI) under the UK government's Horizon Europe funding guarantee (ga 10063360). José Luis Montaño-Priede acknowledges the financial support received from the IKUR Strategy under the collaboration agreement between the Ikerbasque Foundation and Materials Physics Center on behalf of the Department of Education of the Basque Government. Marek Grzelczak acknowledges financial support from EITB Maratoia. Srikanth Singamaneni acknowledges National Science Foundation (CBET-2316285, CBET-2224610) and National Institutes of Health (R21AI178217). L. P. acknowledges support from the Spanish Ministerio de Ciencia e Innovación through Ramón y Cajal grant (grant no. RYC2018-026103-I), the Spanish State Research Agency (grant no. PID2020-117371RA-I00 and TED2021-131628A-I00), and a grant from the Xunta de Galicia (grant no. ED431F2021/05). The authors acknowledge the Universidad de Vigo/CSIUG for open access funding. Jorge Pérez-Juste and Isabel Pastoriza-Santos acknowledge support from MICIU/AEI/10.13039/501100011033 and ERDF/EU (Grant Number: PID2022-138724NB-I00) and the European Innovation Council (Horizon 2020 Project Number: 965018—BIOCELLPHE).

# References

1 C. R. Lowe, *Trends Biotechnol.*, 1984, **2**, 59–65.
2 S. M. Borisov and O. S. Wolfbeis, *Chem. Rev.*, 2008, **108**, 423–461.
3 N. J. Ronkainen, H. B. Halsall and W. R. Heineman, *Chem. Soc. Rev.*, 2010, **39**, 1747.
4 L. Su, W. Jia, C. Hou and Y. Lei, *Biosens. Bioelectron.*, 2011, **26**, 1788–1799.
5 S. Balbinot, A. M. Srivastav, J. Vidic, I. Abdulhalim and M. Manzano, *Trends Food Sci. Technol.*, 2021, **111**, 128–140.
6 J. R. Mejía-Salazar and O. N. Oliveira, *Chem. Rev.*, 2018, **118**, 10617–10625.
7 M. Ahmed, M. O. Mavukkandy, A. Giwa, M. Elektorowicz, E. Katsou, O. Khelifi, V. Naddeo and S. W. Hasan, *npj Clean Water*, 2022, **5**, 12.
8 B. Brunekreef and S. T. Holgate, *Lancet*, 2002, **360**, 1233–1242.
9 J. Homola, *Chem. Rev.*, 2008, **108**, 462–493.
10 K. M. Mayer and J. H. Hafner, *Chem. Rev.*, 2011, **111**, 3828–3857.
11 O. Tokel, F. Inci and U. Demirci, *Chem. Rev.*, 2014, **114**, 5728–5752.
12 L. Song, J. Chen, B. B. Xu and Y. Huang, *ACS Nano*, 2021, **15**, 18822–18847.
13 J. Langer, D. Jimenez de Aberasturi, J. Aizpurua, R. A. Alvarez-Puebla, B. Auguié, J. J. Baumberg, G. C. Bazan, S. E. J. Bell, A. Boisen, A. G. Brolo, J. Choo, D. Cialla-May, V. Deckert, L. Fabris, K. Faulds, F. J. García de Abajo, R. Goodacre, D. Graham, A. J. Haes, C. L. Haynes, C. Huck, T. Itoh, M. Käll, J. Kneipp, N. A. Kotov, H. Kuang, E. C. Le Ru, H. K. Lee, J.-F. Li, X. Y. Ling, S. A. Maier, T. Mayerhöfer, M. Moskovits, K. Murakoshi, J.-M. Nam, S. Nie, Y. Ozaki, I. Pastoriza-Santos, J. Perez-Juste, J. Popp, A. Pucci, S. Reich, B. Ren, G. C. Schatz, T. Shegai, S. Schlücker, L.-L. Tay, K. G. Thomas, Z.-Q. Tian, R. P. Van Duyne, T. Vo-Dinh, Y. Wang, K. A. Willets, C. Xu, H. Xu, Y. Xu, Y. S. Yamamoto, B. Zhao and L. M. Liz-Marzán, *ACS Nano*, 2020, **14**, 28–117.
14 L. Polavarapu and L. M. Liz-Marzán, *Phys. Chem. Chem. Phys.*, 2013, **15**, 5288.
15 L. Polavarapu, J. Pérez-Juste, Q.-H. Xu and L. M. Liz-Marzán, *J. Mater. Chem. C*, 2014, **2**, 7460.
16 A. M. Shrivastav, U. Cvelbar and I. Abdulhalim, *Commun. Biol.*, 2021, **4**, 70.
17 R. Rahad, A. K. M. Rakib, M. A. Haque, S. S. Sharar and R. H. Sagor, *Results Phys.*, 2023, **49**, 106478.
18 T. Liyanage, B. Alharbi, L. Quan, A. Esquela-Kerscher and G. Slaughter, *ACS Omega*, 2022, **7**, 2411–2418.
19 F. Jafrasteh, A. Farmani and J. Mohamadi, *Sci. Rep.*, 2023, **13**, 15349.
20 M. Beheshti Asl, J. Karamdel, M. Khoshbaten and A. Rostami, *Opt. Continuum*, 2022, **1**, 2043.
21 L. Wang, *Sensors*, 2017, **17**, 1572.
22 I. Chirisa, T. Mutambisi, M. Chivenge, E. Mabaso, A. R. Matamanda and R. Ncube, *Geochem. J.*, 2022, **87**, 815–828.
23 B. Giri, S. Pandey, R. Shrestha, K. Pokharel, F. S. Ligler and B. B. Neupane, *Anal. Bioanal. Chem.*, 2021, **413**, 35–48.
24 D. Ndwandwe and C. S. Wiysonge, *Curr. Opin. Immunol.*, 2021, **71**, 111–116.
25 N. W. Schluger, D. Kinney, T. J. Harkin and W. N. Rom, *Chest*, 1994, **105**, 1116–1121.
26 P. Hornbeck, *Curr. Protoc. Immunol.*, 2015, **110**, 2.1.1–2.1.23.
27 A. Francisco-Cruz, E. R. Parra, M. T. Tetzlaff and I. I. Wistuba, *Biomarkers Immunother., Cancer: Methods Protoc.*, 2020, 467–495.
28 S. D. Richardson, *Anal. Chem.*, 2009, **81**, 4645–4677.
29 X. Huang, Y. Zhu and E. Kianfar, *J. Mater. Res. Technol.*, 2021, **12**, 1649–1672.
30 A. Chamorro-Garcia and A. Merkoçi, *Nanobiomedicine*, 2016, **3**, 184954351666357.
31 A. K. Yadav, N. Basavegowda, S. Shirin, S. Raju, R. Sekar, P. Somu, U. T. Uthappa and G. Abdi, *Mol. Biotechnol.*, 2024, DOI: 10.1007/s12033-024-01157-y.
32 T. S. Dhahi, A. K. Y. Dafhalla, S. A. Saad, D. M. I. Zayan, A. E. T. Ahmed, M. E. Elobaid, T. Adam and S. C. B. Gopinath, *Biotechnol. Appl. Biochem.*, 2024, **71**, 429–445.
33 F. Achi, A. M. Attar and A. A. Lahcen, *TrAC, Trends Anal. Chem.*, 2024, **170**, 117423.
34 E. Priyadarshini and N. Pradhan, *Sens. Actuators, B*, 2017, **238**, 888–902.
35 K. Saha, S. S. Agasti, C. Kim, X. Li and V. M. Rotello, *Chem. Rev.*, 2012, **112**, 2739–2779.
36 J. R. Mejía-Salazar and O. N. Oliveira, *Chem. Rev.*, 2018, **118**, 10617–10625.
37 J. Zhao, X. Zhang, C. R. Yonzon, A. J. Haes and R. P. Van Duyne, *Nanomedicine*, 2006, **1**, 219–228.
38 E. Petryayeva and U. J. Krull, *Anal. Chim. Acta*, 2011, **706**, 8–24.
39 K. A. Willets and R. P. Van Duyne, *Annu. Rev. Phys. Chem.*, 2007, **58**, 267–297.
40 L. M. Liz-Marzán, *Langmuir*, 2006, **22**, 32–41.
41 N. Zhou, V. López-Puente, Q. Wang, L. Polavarapu, I. Pastoriza-Santos and Q.-H. Xu, *RSC Adv.*, 2015, **5**, 29076–29097.
42 X. Lu, M. Rycenga, S. E. Skrabalak, B. Wiley and Y. Xia, *Annu. Rev. Phys. Chem.*, 2009, **60**, 167–192.
43 C. M. Cobley, S. E. Skrabalak, D. J. Campbell and Y. Xia, *Plasmonics*, 2009, **4**, 171–179.
44 Y. Xia and N. J. Halas, *MRS Bull.*, 2005, **30**, 338–348.
45 M. Rycenga, C. M. Cobley, J. Zeng, W. Li, C. H. Moran, Q. Zhang, D. Qin and Y. Xia, *Chem. Rev.*, 2011, **111**, 3669–3712.
46 J. Kimling, M. Maier, B. Okenve, V. Kotaidis, H. Ballot and A. Plech, *J. Phys. Chem. B*, 2006, **110**, 15700–15707.
47 J. Turkevich, *Gold Bull.*, 1985, **18**, 86–91.
48 N. R. Jana, L. Gearheart and C. J. Murphy, *Chem. Commun.*, 2001, 617–618.
49 B. Nikoobakht and M. A. El-Sayed, *Chem. Mater.*, 2003, **15**, 1957–1962.
50 Y. Sun and Y. Xia, *Science*, 2002, **298**, 2176–2179.
51 J. E. Millstone, S. J. Hurst, G. S. Métraux, J. I. Cutler and C. A. Mirkin, *Small*, 2009, **5**, 646–664.
52 L. R. Hirsch, A. M. Gobin, A. R. Lowery, F. Tam, R. A. Drezek, N. J. Halas and J. L. West, *Ann. Biomed. Eng.*, 2006, **34**, 15–22.

53 A. Guerrero-Martínez, S. Barbosa, I. Pastoriza-Santos and L. M. Liz-Marzán, *Curr. Opin. Colloid Interface Sci.*, 2011, **16**, 118–127.

54 I. B. Becerril-Castro, I. Calderon, N. Pazos-Perez, L. Guerrini, F. Schulz, N. Feliu, I. Chakraborty, V. Giannini, W. J. Parak and R. A. Alvarez-Puebla, *Analysis Sensing*, 2022, **2**, e202200005.

55 Y. Luo, C. Chi, M. Jiang, R. Li, S. Zu, Y. Li and Z. Fang, *Adv. Opt. Mater.*, 2017, **5**(16), 1700040.

56 V. K. Valev, J. J. Baumberg, C. Sibilia and T. Verbiest, *Adv. Mater.*, 2013, **25**, 2517–2534.

57 J. Dostálek and W. Knoll, *Biointerphases*, 2008, **3**, FD12–FD22.

58 M. Cottat, N. Thioune, A.-M. Gabudean, N. Lidgi-Guigui, M. Focsan, S. Astilean and M. Lamy de la Chapelle, *Plasmonics*, 2013, **8**, 699–704.

59 C. A. Mirkin, R. L. Letsinger, R. C. Mucic and J. J. Storhoff, *Nature*, 1996, **382**, 607–609.

60 A. P. Alivisatos, K. P. Johnsson, X. Peng, T. E. Wilson, C. J. Loweth, M. P. Bruchez and P. G. Schultz, *Nature*, 1996, **382**, 609–611.

61 L. Polavarapu, J. Pérez-Juste, Q.-H. Xu and L. M. Liz-Marzán, *J. Mater. Chem. C*, 2014, **2**, 7460.

62 M. Moskovits, *Rev. Mod. Phys.*, 1985, **57**, 783–826.

63 M. Moskovits, *Rev. Mod. Phys.*, 1985, **57**, 783–826.

64 R. Pilot, R. Signorini, C. Durante, L. Orian, M. Bhamidipati and L. Fabris, *Biosensors*, 2019, **9**, 57.

65 D.-K. Lim, K.-S. Jeon, H. M. Kim, J.-M. Nam and Y. D. Suh, *Nat. Mater.*, 2010, **9**, 60–67.

66 A. B. Zrimsek, N. Chiang, M. Mattei, S. Zaleski, M. O. McAnally, C. T. Chapman, A.-I. Henry, G. C. Schatz and R. P. Van Duyne, *Chem. Rev.*, 2017, **117**, 7583–7613.

67 P. Zhan, T. Wen, Z. Wang, Y. He, J. Shi, T. Wang, X. Liu, G. Lu and B. Ding, *Angew. Chem., Int. Ed.*, 2018, **57**, 2846–2850.

68 S. Nie and S. R. Emory, *Science*, 1997, **275**, 1102–1106.

69 R. Gupta, P. Gupta, S. Wang, A. Melnykov, Q. Jiang, A. Seth, Z. Wang, J. J. Morrissey, I. George, S. Gandra, P. Sinha, G. A. Storch, B. A. Parikh, G. M. Genin and S. Singamaneni, *Nat. Biomed. Eng.*, 2023, **7**, 1556–1570.

70 M. Fan, G. F. S. Andrade and A. G. Brolo, *Anal. Chim. Acta*, 2020, **1097**, 1–29.

71 Y. Yuan, N. Panwar, S. H. K. Yap, Q. Wu, S. Zeng, J. Xu, S. C. Tjin, J. Song, J. Qu and K.-T. Yong, *Coord. Chem. Rev.*, 2017, **337**, 1–33.

72 T. Itoh, M. Procházka, Z.-C. Dong, W. Ji, Y. S. Yamamoto, Y. Zhang and Y. Ozaki, *Chem. Rev.*, 2023, **123**, 1552–1634.

73 H. K. Lee, Y. H. Lee, C. S. L. Koh, G. C. Phan-Quang, X. Han, C. L. Lay, H. Y. F. Sim, Y.-C. Kao, Q. An and X. Y. Ling, *Chem. Soc. Rev.*, 2019, **48**, 731–756.

74 D. Quesada-González and A. Merkoçi, *Chem. Soc. Rev.*, 2018, **47**, 4697–4709.

75 E. Garcia-Rico, R. A. Alvarez-Puebla and L. Guerrini, *Chem. Soc. Rev.*, 2018, **47**, 4909–4923.

76 A. I. Pérez-Jiménez, D. Lyu, Z. Lu, G. Liu and B. Ren, *Chem. Sci.*, 2020, **11**, 4563–4577.

77 X. X. Han, R. S. Rodriguez, C. L. Haynes, Y. Ozaki and B. Zhao, *Nat. Rev. Methods Primers*, 2022, **1**, 87.

78 M. Fleischmann, P. J. Hendra and A. J. McQuillan, *Chem. Phys. Lett.*, 1974, **26**, 163–166.

79 M. G. Albrecht and J. A. Creighton, *J. Am. Chem. Soc.*, 1977, **99**, 5215–5217.

80 D. L. Jeanmaire and R. P. Van Duyne, *J. Electroanal. Chem. Interfacial Electrochem.*, 1977, **84**, 1–20.

81 M. Moskovits and B. D. Piorek, *J. Raman Spectrosc.*, 2021, **52**, 279–284.

82 B. Sharma, R. R. Frontiera, A.-I. Henry, E. Ringe and R. P. Van Duyne, *Mater. Today*, 2012, **15**, 16–25.

83 R. A. Álvarez-Puebla, *J. Phys. Chem. Lett.*, 2012, **3**, 857–866.

84 K. Kneipp, Y. Wang, H. Kneipp, L. T. Perelman, I. Itzkan, R. R. Dasari and M. S. Feld, *Phys. Rev. Lett.*, 1997, **78**, 1667–1670.

85 K. Kneipp, Y. Wang, H. Kneipp, L. T. Perelman, I. Itzkan, R. R. Dasari and M. S. Feld, *Phys. Rev. Lett.*, 1997, **78**, 1667–1670.

86 A. Otto, I. Mrozek, H. Grabhorn and W. Akemann, *J. Phys.: Condens. Matter*, 1992, **4**, 1143–1212.

87 C. Liang, J. Luan, Z. Wang, Q. Jiang, R. Gupta, S. Cao, K.-K. Liu, J. J. Morrissey, E. D. Kharasch, R. R. Naik and S. Singamaneni, *ACS Appl. Mater. Interfaces*, 2021, **13**, 11414–11423.

88 R. Goodrum and H. Li, *Biotechnol. J.*, 2024, **19**, 2300519.

89 A. Sultangaziyev and R. Bukasov, *Sens Biosensing Res*, 2020, **30**, 100382.

90 M. Bauch, K. Toma, M. Toma, Q. Zhang and J. Dostalek, *Plasmonics*, 2014, **9**, 781–799.

91 C. D. Geddes and J. R. Lakowicz, *J. Fluoresc.*, 2002, **12**, 121–129.

92 J. R. Lakowicz, *Plasmonics*, 2006, **1**, 5–33.

93 K. Aslan, I. Gryczynski, J. Malicka, E. Matveeva, J. R. Lakowicz and C. D. Geddes, *Curr. Opin. Biotechnol*, 2005, **16**, 55–62.

94 J. R. Lakowicz, *Anal. Biochem.*, 2005, **337**, 171–194.

95 A. Seth, Y. Liu, R. Gupta, Z. Wang, E. Mittal, S. Kolla, P. Rathi, P. Gupta, B. A. Parikh, G. M. Genin, S. Gandra, G. A. Storch, J. A. Philips, I. A. George and S. Singamaneni, *Nano Lett.*, 2024, **24**, 229–237.

96 J. R. Lakowicz, *Anal. Biochem.*, 2005, **337**, 171–194.

97 K. Aslan, I. Gryczynski, J. Malicka, E. Matveeva, J. R. Lakowicz and C. D. Geddes, *Curr. Opin. Biotechnol*, 2005, **16**, 55–62.

98 C. D. Geddes and J. R. Lakowicz, *J. Fluoresc.*, 2002, **12**, 121–129.

99 J. R. Lakowicz, *Plasmonics*, 2006, **1**, 5–33.

100 D. Gontero, A. V. Veglia and A. G. Bracamonte, *Photochem. Photobiol. Sci.*, 2020, **19**, 1168–1188.

101 S. M. Fothergill, C. Joyce and F. Xie, *Nanoscale*, 2018, **10**, 20914–20929.

102 M. Zheng, Y. Li, L. Zhang, C. Li, M. Liu and H. Tang, *Anal. Methods*, 2024, **16**, 3099–3108.

103 J.-H. Choi and J.-W. Choi, *Nano Lett.*, 2020, **20**, 7100–7107.

104 Y. Jeong, Y.-M. Kook, K. Lee and W.-G. Koh, *Biosens. Bioelectron.*, 2018, **111**, 102–116.

105 C. Joyce, S. M. Fothergill and F. Xie, *Mater. Today Adv.*, 2020, **7**, 100073.

106 W. P. Hall, S. N. Ngatia and R. P. Van Duyne, *J. Phys. Chem. C*, 2011, **115**, 1410–1414.

107 M. P. Raphael, J. A. Christodoulides, S. P. Mulvaney, M. M. Miller, J. P. Long and J. M. Byers, *Anal. Chem.*, 2012, **84**, 1367–1373.

108 B. Sepúlveda, P. C. Angelomé, L. M. Lechuga and L. M. Liz-Marzán, *Nano Today*, 2009, **4**, 244–251.

109 S. Unser, I. Bruzas, J. He and L. Sagle, *Sensors*, 2015, **15**, 15684–15716.

110 A. Vestri, M. Rippa, V. Marchesano, D. Sagnelli, G. Margheri, J. Zhou and L. Petti, *J. Mater. Chem. B*, 2021, **9**, 9153–9161.

111 R. Wang, L. Schirmer, T. Wieduwilt, R. Förster, M. A. Schmidt, U. Freudenberg, C. Werner, A. Fery and C. Rossner, *Langmuir*, 2022, **38**, 12325–12332.

112 S. Qian, Y. Cui, Z. Cai and L. Li, *Biosens. Bioelectron.: X*, 2022, **11**, 100173.

113 B. Liu, J. Zhuang and G. Wei, *Environ. Sci.: Nano*, 2020, **7**, 2195–2213.

114 H. Aldewachi, T. Chalati, M. N. Woodroofe, N. Bricklebank, B. Sharrack and P. Gardiner, *Nanoscale*, 2018, **10**, 18–33.

115 V. X. T. Zhao, T. I. Wong, X. T. Zheng, Y. N. Tan and X. Zhou, *Mater. Sci. Energy Technol.*, 2020, **3**, 237–249.

116 X. Huang and M. A. El-Sayed, *J. Adv. Res.*, 2010, **1**, 13–28.

117 M. Song, D. Wang, S. Peana, S. Choudhury, P. Nyga, Z. A. Kudyshev, H. Yu, A. Boltasseva, V. M. Shalaev and A. V. Kildishev, *Appl. Phys. Rev.*, 2019, **6**(4), 41308.

118 J.-S. Lee, P. A. Ulmann, M. S. Han and C. A. Mirkin, *Nano Lett.*, 2008, **8**, 529–533.

119 R. Kanjanawarut and X. Su, *Anal. Chem.*, 2009, **81**, 6122–6129.

120 M. H. Jazayeri, T. Aghaie, A. Avan, A. Vatankhah and M. R. S. Ghaffari, *Sens. Biosens. Res.*, 2018, **20**, 1–8.

121 E. Celikbas, E. Guler Celik and S. Timur, *Anal. Chem.*, 2018, **90**, 12325–12333.

122 X. Xue, F. Wang and X. Liu, *J. Am. Chem. Soc.*, 2008, **130**, 3244–3245.

123 J. Du, L. Jiang, Q. Shao, X. Liu, R. S. Marks, J. Ma and X. Chen, *Small*, 2013, **9**, 1467–1481.

124 R. Cao, B. Li, Y. Zhang and Z. Zhang, *Chem. Commun.*, 2011, **47**, 12301.

125 B. Li, X. Li, Y. Dong, B. Wang, D. Li, Y. Shi and Y. Wu, *Anal. Chem.*, 2017, **89**, 10639–10643.

126 X. Xie, W. Xu and X. Liu, *Acc. Chem. Res.*, 2012, **45**, 1511–1520.

127 F. Zhang and J. Liu, *Anal. Sens.*, 2021, **1**, 30–43.

128 S. Mason, *Trends Pharmacol. Sci.*, 1986, **7**, 20–23.

129 F. Wang, X. Yue, Q. Ding, H. Lin, C. Xu and S. Li, *Nanoscale*, 2023, **15**, 2541–2552.

130 N. H. Cho, H. Kim, J. W. Kim, Y.-C. Lim, R. M. Kim, Y. H. Lee and K. T. Nam, *Chemistry*, 2024, **10**, 1052–1070.

131 W. Ma, L. Xu, A. F. de Moura, X. Wu, H. Kuang, C. Xu and N. A. Kotov, *Chem. Rev.*, 2017, **117**, 8041–8093.

132 H.-E. Lee, H.-Y. Ahn, J. Mun, Y. Y. Lee, M. Kim, N. H. Cho, K. Chang, W. S. Kim, J. Rho and K. T. Nam, *Nature*, 2018, **556**, 360–365.

133 L. Zhang, Y. Chen, J. Zheng, G. R. Lewis, X. Xia, E. Ringe, W. Zhang and J. Wang, *Angew. Chem., Int. Ed.*, 2023, **135**(52), e202312615.

134 G. González-Rubio, J. Mosquera, V. Kumar, A. Pedrazo-Tardajos, P. Llombart, D. M. Solís, I. Lobato, E. G. Noya, A. Guerrero-Martínez, J. M. Taboada, F. Obelleiro, L. G. MacDowell, S. Bals and L. M. Liz-Marzán, *Science*, 2020, **368**, 1472–1477.

135 D. Vila-Liarte, N. A. Kotov and L. M. Liz-Marzán, *Chem. Sci.*, 2022, **13**, 595–610.

136 C. Song, M. G. Blaber, G. Zhao, P. Zhang, H. C. Fry, G. C. Schatz and N. L. Rosi, *Nano Lett.*, 2013, **13**, 3256–3261.

137 J. Kumar, H. Eraña, E. López-Martínez, N. Claes, V. F. Martín, D. M. Solís, S. Bals, A. L. Cortajarena, J. Castilla and L. M. Liz-Marzán, *Proc. Natl. Acad. Sci. U. S. A.*, 2018, **115**, 3225–3230.

138 X. Wu, L. Xu, L. Liu, W. Ma, H. Yin, H. Kuang, L. Wang, C. Xu and N. A. Kotov, *J. Am. Chem. Soc.*, 2013, **135**, 18629–18636.

139 Y. Xia, K. D. Gilroy, H. Peng and X. Xia, *Angew. Chem., Int. Ed.*, 2017, **56**, 60–95.

140 Y. Xia, Y. Xiong, B. Lim and S. E. Skrabalak, *Angew. Chem., Int. Ed.*, 2009, **48**, 60–103.

141 E. Carbó-Argibay and B. Rodríguez-González, *Isr. J. Chem.*, 2016, **56**, 214–226.

142 N. G. Bastús, J. Comenge and V. Puntes, *Langmuir*, 2011, **27**, 11098–11105.

143 Y.-N. Wang, W.-T. Wei, C.-W. Yang and M. H. Huang, *Langmuir*, 2013, **29**, 10491–10497.

144 F. Qin, T. Zhao, R. Jiang, N. Jiang, Q. Ruan, J. Wang, L. Sun, C. Yan and H. Lin, *Adv. Opt. Mater.*, 2016, **4**, 76–85.

145 J. Zheng, X. Cheng, H. Zhang, X. Bai, R. Ai, L. Shao and J. Wang, *Chem. Rev.*, 2021, **121**, 13342–13453.

146 Q. Ruan, L. Shao, Y. Shu, J. Wang and H. Wu, *Adv. Opt. Mater.*, 2014, **2**, 65–73.

147 Y. Zheng, X. Zhong, Z. Li and Y. Xia, *Part. Part. Syst. Charact.*, 2014, **31**, 266–273.

148 F. Zhou, Z.-Y. Li, Y. Liu and Y. Xia, *J. Phys. Chem. C*, 2008, **112**, 20233–20240.

149 S. Mazzucco, N. Geuquet, J. Ye, O. Stéphan, W. Van Roy, P. Van Dorpe, L. Henrard and M. Kociak, *Nano Lett.*, 2012, **12**, 1288–1294.

150 L. Zhang, Y. Zhang, J. Ahn, X. Wang and D. Qin, *Chem. Mater.*, 2019, **31**, 1057–1065.

151 L. Scarabelli, A. Sánchez-Iglesias, J. Pérez-Juste and L. M. Liz-Marzán, *J. Phys. Chem. Lett.*, 2015, **6**, 4270–4279.

152 X. Zhuo, X. Zhu, Q. Li, Z. Yang and J. Wang, *ACS Nano*, 2015, **9**, 7523–7535.

153 J.-H. Lee, K. J. Gibson, G. Chen and Y. Weizmann, *Nat. Commun.*, 2015, **6**, 7571.

154 S. Atta, M. Beetz and L. Fabris, *Nanoscale*, 2019, **11**, 2946–2958.

155 X. Cui, F. Qin, Q. Ruan, X. Zhuo and J. Wang, *Adv. Funct. Mater.*, 2018, **28**, 1705516.

156 S. Yoo, S. Go, J. Son, J. Kim, S. Lee, M. Haddadnezhad, H. Hilal, J.-M. Kim, J.-M. Nam and S. Park, *J. Am. Chem. Soc.*, 2021, **143**, 15113–15119.

157 Q. Li, X. Zhuo, S. Li, Q. Ruan, Q. Xu and J. Wang, *Adv. Opt. Mater.*, 2015, **3**, 801–812.

158 X. Kou, S. Zhang, C.-K. Tsung, M. H. Yeung, Q. Shi, G. D. Stucky, L. Sun, J. Wang and C. Yan, *J. Phys. Chem. B*, 2006, **110**, 16377–16383.

159 X. Zhuo, H. K. Yip, X. Cui, J. Wang and H.-Q. Lin, *Light: Sci. Appl.*, 2019, **8**, 39.

160 S. Li, R. Ai, K. K. Chui, Y. Fang, Y. Lai, X. Zhuo, L. Shao, J. Wang and H.-Q. Lin, *Nano Lett.*, 2023, **23**, 4183–4190.

161 J. Lee, P. Lee, H. Lee, D. Lee, S. S. Lee and S. H. Ko, *Nanoscale*, 2012, **4**, 6408.

162 T. H. Chow, N. Li, X. Bai, X. Zhuo, L. Shao and J. Wang, *Acc. Chem. Res.*, 2019, **52**, 2136–2146.

163 H. Chen, L. Shao, T. Ming, Z. Sun, C. Zhao, B. Yang and J. Wang, *Small*, 2010, **6**, 2272–2280.

164 X. Yang, Y. Liu, S. H. Lam, J. Wang, S. Wen, C. Yam, L. Shao and J. Wang, *Nano Lett.*, 2021, **21**, 8205–8212.

165 L. Peng, H. Chan, P. Choo, T. W. Odom, S. K. R. S. Sankaranarayanan and X. Ma, *Nano Lett.*, 2020, **20**, 5866–5872.

166 X. Cui, Y. Lai, R. Ai, H. Wang, L. Shao, H. Chen, W. Zhang and J. Wang, *Adv. Opt. Mater.*, 2020, **8**, 2001173.

167 H. Huang, H. Wang, S. Li, J. Jiang, Y. Liu, M. Cai, L. Shao, H. Chen and J. Wang, *ACS Nano*, 2022, **16**, 14874–14884.

168 S. Schlücker, *Angew. Chem., Int. Ed.*, 2014, **53**, 4756–4795.

169 M. Moskovits, *J. Chem. Phys.*, 1978, **69**, 4159–4161.

170 D. Pines and D. Bohm, *Phys. Rev.*, 1952, **85**, 338–353.

171 J. A. Creighton, C. G. Blatchford and M. G. Albrecht, *J. Chem. Soc., Faraday Trans. 2*, 1979, **75**, 790.

172 J. Billmann, G. Kovacs and A. Otto, *Surf. Sci.*, 1980, **92**, 153–173.

173 J. A. Creighton, *Surf. Sci.*, 1983, **124**, 209–219.

174 M. Moskovits and J. S. Suh, *J. Phys. Chem.*, 1984, **88**, 5526–5530.

175 H. Metiu, *Prog. Surf. Sci.*, 1984, **17**, 153–320.

176 M. Kerker, *Acc. Chem. Res.*, 1984, **17**, 271–277.

177 A. Wokaun, *Mol. Phys.*, 1985, **56**, 1–33.

178 M. Kerker, (No Title).

179 G. C. Schatz and R. P. Van Duyne, in *Handbook of Vibrational Spectroscopy*, ed. P. R. Griffiths, Wiley, 2001.

180 P. Etchegoin, L. F. Cohen, H. Hartigan, R. J. C. Brown, M. J. T. Milton and J. C. Gallop, *J. Chem. Phys.*, 2003, **119**, 5281–5289.

181 R. Aroca, *Surface-Enhanced Vibrational Spectroscopy*, Wiley, 2006.

182 C. F. Bohren and D. R. Huffman, *Absorption and Scattering of Light by Small Particles*, Wiley, 1998.

183 M. Kerker, *Science*, 1969, 666.

184 K. L. Kelly, E. Coronado, L. L. Zhao and G. C. Schatz, *J. Phys. Chem. B*, 2003, **107**, 668–677.

185 R. Alvarez-Puebla, L. M. Liz-Marzán and F. J. García de Abajo, *J. Phys. Chem. Lett.*, 2010, **1**, 2428–2434.

186 L. Rodríguez-Lorenzo, R. A. Álvarez-Puebla, I. Pastoriza-Santos, S. Mazzucco, O. Stéphan, M. Kociak, L. M. Liz-Marzán and F. J. García de Abajo, *J. Am. Chem. Soc.*, 2009, **131**, 4616–4618.

187 E. Hao and G. C. Schatz, *J. Chem. Phys.*, 2004, **120**, 357–366.

188 A. Kudelski and J. Bukowska, *Surf. Sci.*, 1996, **368**, 396–400.

189 K. Kneipp, H. Kneipp, V. B. Kartha, R. Manoharan, G. Deinum, I. Itzkan, R. R. Dasari and M. S. Feld, *Phys. Rev. E*, 1998, **57**, R6281–R6284.

190 E. Pazos, M. Garcia-Algar, C. Penas, M. Nazarenus, A. Torruella, N. Pazos-Perez, L. Guerrini, M. E. Vázquez, E. Garcia-Rico, J. L. Mascareñas and R. A. Alvarez-Puebla, *J. Am. Chem. Soc.*, 2016, **138**, 14206–14209.

191 K. Ataka, T. Yotsuyanagi and M. Osawa, *J. Phys. Chem.*, 1996, **100**, 10664–10672.

192 D. L. Allara and R. G. Nuzzo, *Langmuir*, 1985, **1**, 52–66.

193 *Handbook of Vibrational Spectroscopy*, ed. J. M. Chalmers and P. R. Griffiths, Wiley, 2001.

194 S. Fornasaro, F. Alsamad, M. Baia, L. A. E. Batista de Carvalho, C. Beleites, H. J. Byrne, A. Chiadò, M. Chis, M. Chisanga, A. Daniel, J. Dybas, G. Eppe, G. Falgayrac, K. Faulds, H. Gebavi, F. Giorgis, R. Goodacre, D. Graham, P. La Manna, S. Laing, L. Litti, F. M. Lyng, K. Malek, C. Malherbe, M. P. M. Marques, M. Meneghetti, E. Mitri, V. Mohaček-Grošev, C. Morasso, H. Muhamadali, P. Musto, C. Novara, M. Pannico, G. Penel, O. Piot, T. Rindzevicius, E. A. Rusu, M. S. Schmidt, V. Sergo, G. D. Sockalingum, V. Untereiner, R. Vanna, E. Wiercigroch and A. Bonifacio, *Anal. Chem.*, 2020, **92**, 4053–4064.

195 B. Sharma, R. R. Frontiera, A.-I. Henry, E. Ringe and R. P. Van Duyne, *Mater. Today*, 2012, **15**, 16–25.

196 C. E. Ott and L. E. Arroyo, *WIREs Forensic Sci.*, 2023, **5**, e1483.

197 W. R. Premasiri, Y. Chen, J. Fore, A. Brodeur and L. D. Ziegler, *Frontiers and Advances in Molecular Spectroscopy*, Elsevier, 2018, pp. 327–367.

198 L. Jiang, M. M. Hassan, S. Ali, H. Li, R. Sheng and Q. Chen, *Trends Food Sci. Technol.*, 2021, **112**, 225–240.

199 Podagatlapalli Gopala Krishna, Hamad Syed and V. R. Soma, *J. Phys. Chem. C*, 2015, **119**, 16972–16983.

200 H. Liu, X. Gao, C. Xu and D. Liu, *Theranostics*, 2022, **12**, 1870–1903.

201 Y. Liu, Y. Zhang, M. Tardivel, M. Lequeux, X. Chen, W. Liu, J. Huang, H. Tian, Q. Liu, G. Huang, R. Gillibert, M. L. de la Chapelle and W. Fu, *Plasmonics*, 2020, **15**, 743–752.

202 M. Richard-Lacroix and V. Deckert, *Light: Sci. Appl.*, 2020, **9**, 35.

203 L. A. Lane, X. Qian and S. Nie, *Chem. Rev.*, 2015, **115**, 10489–10529.

204 Y. Wang, B. Yan and L. Chen, *Chem. Rev.*, 2013, **113**, 1391–1428.

205 Z. Tao, W. Zhao, S. Wang, B. Zhao, R. Hua, J. Qin and Z. Xu, *Nanotechnol. Precis. Eng.*, 2021, **4**(4), 043004.

206 Y. Wu, Y. Jiang, X. Zheng, S. Jia, Z. Zhu, B. Ren and H. Ma, *R. Soc. Open Sci.*, 2018, **5**, 172034.

207 L. Petti, R. Capasso, M. Rippa, M. Pannico, P. La Manna, G. Peluso, A. Calarco, E. Bobeico and P. Musto, *Vib. Spectrosc.*, 2016, **82**, 22–30.

208 M. Li, J. Lu, J. Qi, F. Zhao, J. Zeng, J. C.-C. Yu and W.-C. Shih, *J. Biomed. Opt.*, 2014, **19**, 050501.

209 S. Yan, H. Tang, J. Sun, C. Zhu, Q. Pan, B. Chen and G. Meng, *Adv. Opt. Mater.*, 2024, **12**, 2302010.

210 A. Pandya, J. C. Kumaradas and A. Douplik, in *Novel Biophotonics Techniques and Applications V*, ed. A. Amelink and S. K. Nadkarni, SPIE, 2019, vol. Part F142-ECBO, pp. 5.

211 C. Hamon and L. M. Liz-Marzán, *J. Colloid Interface Sci.*, 2018, **512**, 834–843.

212 A. Marques, B. Veigas, A. Araújo, B. Pagará, P. V. Baptista, H. Águas, R. Martins and E. Fortunato, *Sci. Rep.*, 2019, **9**, 17922.

213 J. Choi, J. Lee and J. H. Jung, *Biosens. Bioelectron.*, 2020, **169**, 112611.

214 H. Pu, W. Xiao and D.-W. Sun, *Trends Food Sci. Technol.*, 2017, **70**, 114–126.

215 B. L. Scott and K. T. Carron, *Anal. Chem.*, 2012, **84**, 8448–8451.

216 J. P. Camden, J. A. Dieringer, J. Zhao and R. P. Van Duyne, *Acc. Chem. Res.*, 2008, **41**, 1653–1661.

217 P. L. Stiles, J. A. Dieringer, N. C. Shah and R. P. Van Duyne, *Annu. Rev. Anal. Chem.*, 2008, **1**, 601–626.

218 E. C. Le Ru and P. G. Etchegoin, *Chem. Phys. Lett.*, 2006, **423**, 63–66.

219 E. J. Blackie, E. C. Le Ru and P. G. Etchegoin, *J. Am. Chem. Soc.*, 2009, **131**, 14466–14472.

220 J. A. Dieringer, R. B. Lettan, K. A. Scheidt and R. P. Van Duyne, *J. Am. Chem. Soc.*, 2007, **129**, 16249–16256.

221 D.-K. Lim, K.-S. Jeon, H. M. Kim, J.-M. Nam and Y. D. Suh, *Nat. Mater.*, 2010, **9**, 60–67.

222 J. H. Yoon, F. Selbach, L. Langolf and S. Schlücker, *Small*, 2018, **14**, 1870018.

223 J. H. Yoon, F. Selbach, L. Schumacher, J. Jose and S. Schlücker, *ACS Photonics*, 2019, **6**, 642–648.

224 H. Cha, J. H. Yoon and S. Yoon, *ACS Nano*, 2014, **8**, 8554–8563.

225 J.-H. Lee, J.-M. Nam, K.-S. Jeon, D.-K. Lim, H. Kim, S. Kwon, H. Lee and Y. D. Suh, *ACS Nano*, 2012, **6**, 9574–9584.

226 P. W. K. Rothemund, *Nature*, 2006, **440**, 297–302.

227 W. Fang, S. Jia, J. Chao, L. Wang, X. Duan, H. Liu, Q. Li, X. Zuo, L. Wang, L. Wang, N. Liu and C. Fan, *Sci. Adv.*, 2019, **5**, eaau4506.

228 J. Prinz, B. Schreiber, L. Olejko, J. Oertel, J. Rackwitz, A. Keller and I. Bald, *J. Phys. Chem. Lett.*, 2013, **4**, 4140–4145.

229 V. V. Thacker, L. O. Herrmann, D. O. Sigle, T. Zhang, T. Liedl, J. J. Baumberg and U. F. Keyser, *Nat. Commun.*, 2014, **5**, 3448.

230 P. Kühler, E.-M. Roller, R. Schreiber, T. Liedl, T. Lohmüller and J. Feldmann, *Nano Lett.*, 2014, **14**, 2914–2919.

231 M. Pilo-Pais, A. Watson, S. Demers, T. H. LaBean and G. Finkelstein, *Nano Lett.*, 2014, **14**, 2099–2104.

232 K. Tapio, A. Mostafa, Y. Kanehira, A. Suma, A. Dutta and I. Bald, *ACS Nano*, 2021, **15**, 7065–7077.

233 S. Simoncelli, E.-M. Roller, P. Urban, R. Schreiber, A. J. Turberfield, T. Liedl and T. Lohmüller, *ACS Nano*, 2016, **10**, 9809–9815.

234 A. Otto, *J. Raman Spectrosc.*, 2002, **33**, 593–598.

235 J. Szczerbiński, L. Gyr, J. Kaeslin and R. Zenobi, *Nano Lett.*, 2018, **18**, 6740–6749.

236 C. Heck, Y. Kanehira, J. Kneipp and I. Bald, *Molecules*, 2019, 24.

237 E. J. Bjerneld, F. Svedberg, P. Johansson and M. Käll, *J. Phys. Chem. A*, 2004, **108**, 4187–4193.

238 P. Senthil Kumar, I. Pastoriza-Santos, B. Rodríguez-González, F. Javier García de Abajo and L. M. Liz-Marzán, *Nanotechnology*, 2008, **19**, 15606.

239 Y. Kanehira, K. Tapio, G. Wegner, S. Kogikoski Jr., S. Rüstig, C. Prietzel, K. Busch and I. Bald, *ACS Nano*, 2023, **17**, 21227–21239.

240 S. Tanwar, V. Kaur, G. Kaur and T. Sen, *J. Phys. Chem. Lett.*, 2021, **12**, 8141–8150.

241 C. Heck, Y. Kanehira, J. Kneipp and I. Bald, *Angew. Chem., Int. Ed.*, 2018, **57**, 7444–7447.

242 F. Schuknecht, K. Kołątaj, M. Steinberger, T. Liedl and T. Lohmueller, *Nat. Commun.*, 2023, **14**, 7192.

243 F. Schuknecht, K. Kołątaj, M. Steinberger, T. Liedl and T. Lohmueller, *Nat. Commun.*, 2023, **14**, 7192.

244 M. Sharma, C. Kaur, P. Singhmar, S. Rai and T. Sen, *Nanoscale*, 2024, **16**, 15128–15140.

245 L. M. Wassermann, M. Scheckenbach, A. V. Baptist, V. Glembockyte and A. Heuer-Jungemann, *Adv. Mater.*, 2023, **35**, 2212024.

246 F. Lussier, V. Thibault, B. Charron, G. Q. Wallace and J.-F. Masson, *TrAC, Trends Anal. Chem.*, 2020, **124**, 115796.

247 A. B. Zrimsek, N. Chiang, M. Mattei, S. Zaleski, M. O. McAnally, C. T. Chapman, A.-I. Henry, G. C. Schatz and R. P. Van Duyne, *Chem. Rev.*, 2017, **117**, 7583–7613.

248 J.-A. Huang, M. Z. Mousavi, Y. Zhao, A. Hubarevich, F. Omeis, G. Giovannini, M. Schütte, D. Garoli and F. De Angelis, *Nat. Commun.*, 2019, **10**, 5321.

249 Y. Qiu, C. Kuang, X. Liu and L. Tang, *Sensors*, 2022, **22**, 4889.

250 Z. Zhang, S. Sheng, R. Wang and M. Sun, *Anal. Chem.*, 2016, **88**, 9328–9346.

251 J. Zhou, P.-L. Zhou, Q. Shen, S. A. Ahmed, X.-T. Pan, H.-L. Liu, X.-L. Ding, J. Li, K. Wang and X.-H. Xia, *Anal. Chem.*, 2021, **93**, 11679–11685.

252 S. Jiang, Y. Zhang, R. Zhang, C. Hu, M. Liao, Y. Luo, J. Yang, Z. Dong and J. G. Hou, *Nat. Nanotechnol.*, 2015, **10**, 865–869.

253 Z. Liu, S.-Y. Ding, Z.-B. Chen, X. Wang, J.-H. Tian, J. R. Anema, X.-S. Zhou, D.-Y. Wu, B.-W. Mao, X. Xu, B. Ren and Z.-Q. Tian, *Nat. Commun.*, 2011, **2**, 305.

254 J. Qi, J. Zeng, F. Zhao, S. H. Lin, B. Raja, U. Strych, R. C. Willson and W.-C. Shih, *Nanoscale*, 2014, **6**, 8521–8526.

255 B. Guven, M. Eryilmaz, A. Üzer, I. H. Boyaci, U. Tamer and R. Apak, *RSC Adv.*, 2017, **7**, 37039–37047.

256 B. Soundiraraju and B. K. George, *ACS Nano*, 2017, **11**, 8892–8900.

257 P. Garg, Bharti, R. K. Soni and R. Raman, *J. Mater. Sci.: Mater. Electron.*, 2020, **31**, 1094–1104.

258 N. Singh, T. K. Naqvi, P. Awasthi, A. M. Siddiqui, A. K. Srivastava and P. K. Dwivedi, *Sens Actuators, A*, 2022, **347**, 113915.

259 T. K. Naqvi, M. Sree Satya Bharati, A. K. Srivastava, M. M. Kulkarni, A. M. Siddiqui, S. V. Rao and P. K. Dwivedi, *ACS Omega*, 2019, **4**, 17691–17701.

260 V. R. Kahkhaie, M. H. Yousefi, S. M. R. Darbani and A. Mobashery, *Photonics Nanostruct. Fundam. Appl.*, 2020, **41**, 100801.

261 T. Liyanage, A. Rael, S. Shaffer, S. Zaidi, J. V. Goodpaster and R. Sardar, *Analyst*, 2018, **143**, 2012–2022.

262 C. Wang, B. Liu and X. Dou, *Sens. Actuators, B*, 2016, **231**, 357–364.

263 C. Byram, J. Rathod, S. S. B. Moram, A. Mangababu and V. R. Soma, *Nanomaterials*, 2022, **12**, 2150.

264 W. Fan, S. Yang, Y. Zhang, B. Huang, Z. Gong, D. Wang and M. Fan, *ACS Sens.*, 2020, **5**, 3599–3606.

265 R. Gao, X. Song, C. Zhan, C. Weng, S. Cheng, K. Guo, N. Ma, H. Chang, Z. Guo, L.-B. Luo and L. Yu, *Sens. Actuators, B*, 2020, **314**, 128081.

266 R. Gao, H. Qian, C. Weng, X. Wang, C. Xie, K. Guo, S. Zhang, S. Xuan, Z. Guo and L.-B. Luo, *Sens. Actuators, B*, 2020, **321**, 128543.

267 S. S. B. Moram, C. Byram, S. N. Shibu, B. M. Chilukamarri and V. R. Soma, *ACS Omega*, 2018, **3**, 8190–8201.

268 S. Ben-Jaber, W. J. Peveler, R. Quesada-Cabrera, C. W. O. Sol, I. Papakonstantinou and I. P. Parkin, *Nanoscale*, 2017, **9**, 16459–16466.

269 V. Heleg-Shabtai, A. Zaltsman, M. Sharon, H. Sharabi, I. Nir, D. Marder, G. Cohen, I. Ron and A. Pevzner, *RSC Adv.*, 2021, **11**, 26029–26036.

270 K. J. Squire, K. Sivashanmugan, B. Zhang, J. Kraai, G. Rorrer and A. X. Wang, *ACS Appl. Nano Mater.*, 2020, **3**, 1656–1665.

271 A.-M. Dowgiallo, A. Branham and D. Guenther, *Spectroscopyonline*, 2017, **32**, 8–17.

272 V. S. Vendamani, S. V. S. N. Rao, A. P. Pathak and V. R. Soma, *RSC Adv.*, 2020, **10**, 44747–44755.

273 V. S. Vendamani, R. Beeram, M. M. Neethish, S. V. S. N. Rao and S. V. Rao, *iScience*, 2023, **25**, 104849.

274 S. S. B. Moram, A. K. Shaik, C. Byram, S. Hamad and V. R. Soma, *Anal. Chim. Acta*, 2020, **1101**, 157–168.

275 S. Adhikari, E. K. Ampadu, M. Kim, D. Noh, E. Oh and D. Lee, *Sensors*, 2021, **21**, 5567.

276 D. Banerjee, M. Akkanaboina, R. K. Kanaka and V. R. Soma, *Appl. Surf. Sci.*, 2023, **616**, 156561.

277 G. K. Podagatlapalli, S. Hamad, M. A. Mohiddon and S. V. Rao, *Laser Phys. Lett.*, 2015, **12**, 36003.

278 R. K. Avasarala, T. Jena, S. K. Balivada, C. Angani, H. Syed, V. R. Soma and G. K. Podagatlapalli, *Results Opt.*, 2021, **5**, 100153.

279 C. Byram, S. S. B. Moram and V. R. Soma, *Analyst*, 2019, **144**, 2327–2336.

280 S. V. Rao, G. K. Podagatlapalli and S. Hamad, *International Conference on Fibre Optics and Photonics*, 2016, Th4D.2.

281 X. He, Y. Liu, Y. Liu, S. Cui, W. Liu and Z. Li, *CrystEngComm*, 2020, **22**, 776–785.

282 U. P. Shaik, S. Hamad, M. Ahamad Mohiddon, V. R. Soma and M. Ghanashyam Krishna, *J. Appl. Phys.*, 2016, **119**, 093013.

283 H. Syed, G. Krishna Podagatlapalli, M. A. Mohiddon and V. Rao Soma, *Adv. Mater. Lett.*, 2015, **6**, 1073–1080.

284 S. Hamad, S. S. Bharati Moram, B. Yendeti, G. K. Podagatlapalli, S. V. S. Nageswara Rao, A. P. Pathak, M. A. Mohiddon and V. R. Soma, *ACS Omega*, 2018, **3**, 18420–18432.

285 J. Rathod, C. Byram, R. K. Kanaka, M. Sree Satya Bharati, D. Banerjee, M. Akkanaboina and V. R. Soma, *ACS Omega*, 2022, **7**, 15969–15981.

286 S. S. B. Moram, C. Byram and V. R. Soma, *RSC Adv.*, 2023, **13**, 2620–2630.

287 M. S. S. Bharati, B. Chandu and S. V. Rao, *RSC Adv.*, 2019, **9**, 1517–1525.

288 A. K. Verma and R. K. Soni, *Opt. Laser Technol.*, 2023, **163**, 109429.

289 C. Xiao, Z. Chen, M. Qin, D. Zhang and L. Fan, *Photonic Sens.*, 2018, **8**, 278–288.

290 B. Samransuksamer, M. Horprathum, T. Jutarosaga, A. Kopwitthaya, S. Limwichean, N. Nuntawong, C. Chananonnawathorn, V. Patthanasettakul, P. Muthitamongkol and A. Treetong, *Sens. Actuators, B*, 2018, **277**, 102–113.

291 M. Ge, W. Zhao, Y. Han, H. Gai and C. Zong, *Front. Chem.*, 2023, **11**, 1–9.

292 N. Bi, Y.-H. Zhang, M.-H. Hu, J. Xu, W. Song, J. Gou, Y.-X. Li and L. Jia, *Spectrochim. Acta, Part A*, 2023, **284**, 121777.

293 C. Chin, C. Chen, X. Chen, H. Yen, H. Hsien, J. Young and Y. Chen, *Sens. Actuators, B*, 2021, **347**, 130614.

294 T. K. Naqvi, A. Bajpai, M. S. S. Bharati, M. M. Kulkarni, A. M. Siddiqui, V. R. Soma and P. K. Dwivedi, *J. Hazard. Mater.*, 2021, **407**, 124353.

295 X.-R. Bai, Y. Zeng, X.-D. Zhou, X.-H. Wang, A.-G. Shen and J.-M. Hu, *Anal. Chem.*, 2017, **89**, 10335–10342.

296 N. Singh, A. M. Shrivastav, N. Vashistha and I. Abdulhalim, *Sens. Actuators, B*, 2023, **374**, 132813.

297 X. Kong, Y. Xi, P. Le Duff, X. Chong, E. Li, F. Ren, G. L. Rorrer and A. X. Wang, *Biosens. Bioelectron.*, 2017, **88**, 63–70.

298 W. Liu, Z. Wang, Z. Liu, J. Chen, L. Shi, L. Huang, Y. Liu, S. Cui and X. He, *ACS Sens.*, 2023, **8**, 1733–1741.

299 X. He, Y. Liu, X. Xue, J. Liu, Y. Liu and Z. Li, *J. Mater. Chem. C*, 2017, **5**, 12384–12392.

300 Y. Shi, W. Wang and J. Zhan, *Nano Res.*, 2016, **9**, 2487–2497.

301 D. Lin, R. Dong, P. Li, S. Li, M. Ge, Y. Zhang, L. Yang and W. Xu, *Talanta*, 2020, **218**, 121157.

302 J. Wu, Y. Feng, L. Zhang and W. Wu, *Carbohydr. Polym.*, 2020, **248**, 116766.

303 D. Chen, X. Zhu, J. Huang, G. Wang, Y. Zhao, F. Chen, J. Wei, Z. Song and Y. Zhao, *Anal. Chem.*, 2018, **90**, 9048–9054.

304 K. Milligan, N. C. Shand, D. Graham and K. Faulds, *Anal. Chem.*, 2020, **92**, 3253–3261.

305 R. Beeram, V. S. Vendamani and V. R. Soma, *Spectrochim. Acta, Part A*, 2023, **289**, 122218.

306 R. Beeram, D. Banerjee, L. M. Narlagiri and V. R. Soma, *Anal. Methods*, 2022, **14**, 1788–1796.

307 R. Beeram and V. R. Soma, *Opt. Mater.*, 2023, **137**, 113615.

308 F. Wan, Q. Liu, W.-P. Kong, Z.-Y. Luo, S.-F. Gao, Y.-Y. Wang and W.-G. Chen, *IEEE Sens. J.*, 2023, **23**, 6849–6856.

309 L. Juhlin, T. Mikaelsson, A. Hakonen, M. S. Schmidt, T. Rindzevicius, A. Boisen, M. Käll and P. O. Andersson, *Talanta*, 2020, **211**, 120721.

310 M. Lafuente, I. Pellejero, V. Sebastián, M. A. Urbiztondo, R. Mallada, M. P. Pina and J. Santamaría, *Sens. Actuators, B*, 2018, **267**, 457–466.

311 T. Li, B. Wen, Y. Zhang, L. Zhang and J. Li, *J. Raman Spectrosc.*, 2022, **53**, 1386–1393.

312 A. Hakonen, T. Rindzevicius, M. S. Schmidt, P. O. Andersson, L. Juhlin, M. Svedendahl, A. Boisen and M. Käll, *Nanoscale*, 2016, **8**, 1305–1308.

313 M. Lafuente, D. Sanz, M. Urbiztondo, J. Santamaría, M. P. Pina and R. Mallada, *J. Hazard. Mater.*, 2020, **384**, 121279.

314 W.-C. Huang and H.-R. Chen, *Molecules*, 2023, **28**, 520.

315 N. Taranenko, J. Alarie, D. L. Stokes and T. Vo-Dinh, *J. Raman Spectrosc.*, 1996, **27**, 379–384.

316 J. Wang, G. Duan, G. Liu, Y. Li, Z. Chen, L. Xu and W. Cai, *J. Hazard. Mater.*, 2016, **303**, 94–100.

317 Z. Wang, Y. Dai, X. Zhou, Z. Liu, W. Liu, L. Huang, M. Yuan, S. Cui and X. He, *Talanta*, 2023, **258**, 124460.

318 J. Wu, L. Zhang, F. Huang, X. Ji, H. Dai and W. Wu, *J. Hazard. Mater.*, 2020, **387**, 121714.

319 D. J. Klapec, G. Czarnopys and J. Pannuto, *Forensic Sci. Int.*, 2023, **6**, 100298.

320 K. C. To, S. Ben-Jaber and I. P. Parkin, *ACS Nano*, 2020, **14**, 10804–10833.

321 F. Zapata, M. López-López and C. García-Ruiz, *Appl. Spectrosc. Rev.*, 2016, **51**, 227–262.

322 S. Botti, S. Almaviva, L. Cantarini, A. Palucci, A. Puiu and A. Rufoloni, *J. Raman Spectrosc.*, 2013, **44**, 463–468.

323 A. P. Lister, W. J. Sellors, C. R. Howle and S. Mahajan, *Anal. Chem.*, 2020, **93**, 417–429.

324 A. W. Fountain III, S. D. Christesen, R. P. Moon, J. A. Guicheteau and E. D. Emmons, *Appl. Spectrosc.*, 2014, **68**, 795–811.

325 C. Byram, M. Sree Satya Bharati, B. Dipanjan, B. Reshma, R. Jagannath and S. Venugopal Rao, *J. Opt.*, 2023, **25**, 043001.

326 R. Beeram, K. R. Vepa and V. R. Soma, *Biosensors*, 2023, **13**, 328.

327 S. Adhikari, D. Noh, M. Kim, D. Ahn, Y. Jang, E. Oh and D. Lee, *Spectrochim. Acta, Part A*, 2024, 123996.

328 S. Adhikari, D. Noh, M. Kim, D. Ahn, Y. Jang, E. Oh and D. Lee, Available at SSRN 4258144.

329 V. Heleg-Shabtai, H. Sharabi, A. Zaltsman, I. Ron and A. Pevzner, *Analyst*, 2020, **145**, 6334–6341.

330 G. C. Phan-Quang, H. K. Lee, H. W. Teng, C. S. L. Koh, B. Q. Yim, E. K. M. Tan, W. L. Tok, I. Y. Phang and X. Y. Ling, *Angew. Chem., Int. Ed.*, 2018, **57**, 5792–5796.

331 X. Zhang, K. Zhang, H. von Bredow, C. Metting, G. Atanasoff, R. M. Briber and O. Rabin, *Front. Phys.*, 2022, **9**, 752943.

332 Y. Huang, W. Liu, Z. Gong, W. Wu, M. Fan, D. Wang and A. G. Brolo, *ACS Sens.*, 2020, **5**, 2933–2939.

333 K. R. Kumar, D. Banerjee, A. Mangababu, R. S. P. Goud, A. P. Pathak, V. R. Soma and S. V. S. N. Rao, *J. Phys. D: Appl. Phys.*, 2022, **55**, 405103.

334 D. Wang, Z. Gong, M. Tang, W. Fan, B. Huang and M. Fan, *Anal. Methods*, 2022, **14**, 3798–3801.

335 D. Banerjee, M. Akkanaboina, S. Ghosh and V. R. Soma, *Materials*, 2022, **15**, 4155.

336 G. A. Khan, Ö. Demirtaş, A. K. Demir, Ö. Aytekin, A. Bek, A. S. Bhatti and W. Ahmed, *Colloids Surf., A*, 2021, **619**, 126542.

337 A. K. Verma and R. K. Soni, *Opt. Mater.*, 2023, **139**, 113820.

338 M. S. S. Bharati and V. R. Soma, *Opto-Electron. Adv.*, 2021, **4**, 210048.

339 S. Kalasung, K. Aiempanakit, I. Chatnuntawech, N. Limsuwan, K. Lertborworn, V. Patthanasettakul, M. Horprathum, N. Nuntawong and P. Eiamchai, *Sens Actuators, B*, 2022, **366**, 131986.

340 M. Akkanaboina, D. Banerjee, K. R. Kumar, R. S. P. Goud, V. R. Soma and S. V. S. N. Rao, *Opt. Lett.*, 2023, **48**, 5539–5542.

341 D. Banerjee, M. Akkanaboina, R. K. Kanaka, B. Ghose and V. R. Soma, *J. Phys. Chem. C*, 2024, **128**, 4655–4665.

342 H. Marrapu, R. Avasarala, V. R. Soma, S. K. Balivada and G. K. Podagatlapalli, *RSC Adv.*, 2020, **10**, 41217–41228.

343 M. Akkanaboina, D. Banerjee, K. R. Kumar, R. S. P. Goud, V. R. Soma and S. V. S. N. Rao, *Surf. Interfaces*, 2023, **36**, 102563.

344 J. Yin, T. Wu, J. Song, Q. Zhang, S. Liu, R. Xu and H. Duan, *Chem. Mater.*, 2011, **23**, 4756–4764.

345 V. M. Zamarion, R. A. Timm, K. Araki and H. E. Toma, *Inorg. Chem.*, 2008, **47**, 2934–2936.

346 J. Li, L. Chen, T. Lou and Y. Wang, *ACS Appl. Mater. Interfaces*, 2011, **3**, 3936–3941.

347 J. Li, B. Zheng, Z. Zheng, Y. Li and J. Wang, *Sens. Actuators Rep.*, 2020, **2**(1), 100013.

348 X. Ding, L. Kong, J. Wang, F. Fang, D. Li and J. Liu, *ACS Appl. Mater. Interfaces*, 2013, **5**, 7072–7078.

349 C. Song, B. Yang, Y. Yang and L. Wang, *Sci. China: Chem.*, 2016, **59**, 16–29.

350 Q. Zou, X. Li, T. Xue, J. Zheng and Q. Su, *Talanta*, 2019, **195**, 497–505.

351 Y. Wang and J. Irudayaraj, *Chem. Commun.*, 2011, **47**, 4394–4396.

352 Y. X. Yuan, L. Ling, X. Y. Wang, M. Wang, R. A. Gu and J. L. Yao, *J. Raman Spectrosc.*, 2007, **38**, 1280–1287.

353 L. Polavarapu, J. Pérez-Juste, Q. H. Xu and L. M. Liz-Marzán, *J. Mater. Chem. C*, 2014, **2**, 7460–7476.

354 G. Wang, C. Lim, L. Chen, H. Chon, J. Choo, J. Hong and A. J. deMello, *Anal. Bioanal. Chem.*, 2009, **394**, 1827–1832.

355 S. De Marchi, D. García-Lojo, G. Bodelón, J. Pérez-Juste and I. Pastoriza-Santos, *ACS Appl. Mater. Interfaces*, 2021, **13**, 61587–61597.

356 D. Han, S. Y. Lim, B. J. Kim, L. Piao and T. D. Chung, *Chem. Commun.*, 2010, **46**, 5587.

357 S. Tan, M. Erol, S. Sukhishvili and H. Du, *Langmuir*, 2008, **24**, 4765–4771.

358 S. W. Bishnoi, C. J. Rozell, C. S. Levin, M. K. Gheith, B. R. Johnson, D. H. Johnson and N. J. Halas, *Nano Lett.*, 2006, **6**, 1687–1692.

359 L. S. Lawson, J. W. Chan and T. Huser, *Nanoscale*, 2014, **6**, 7971–7980.

360 L. Bi, Y. Wang, Y. Yang, Y. Li, S. Mo, Q. Zheng and L. Chen, *ACS Appl. Mater. Interfaces*, 2018, **10**, 15381–15387.

361 K. V. Kong, U. S. Dinish, W. K. O. Lau and M. Olivo, *Biosens. Bioelectron.*, 2014, **54**, 135–140.

362 B. Liu, Y. Huang, W. Zheng, D. Wang and M. Fan, *Anal. Methods*, 2022, **14**, 1856–1861.

363 X. S. Zheng, P. Hu, Y. Cui, C. Zong, J. M. Feng, X. Wang and B. Ren, *Anal. Chem.*, 2014, **86**, 12250–12257.

364 C. S. L. Koh, H. K. Lee, X. Han, H. Y. F. Sim and X. Y. Ling, *Chem. Commun.*, 2018, **54**, 2546–2549.

365 J. Prakash, P. R. de Oliveira, H. C. Swart, M. Rumyantseva, M. Packirisamy, B. C. Janegitz and X. Li, *Sens. Diagn.*, 2022, **1**, 1143–1164.

366 M. Lafuente, S. De Marchi, M. Urbiztondo, I. Pastoriza-Santos, I. Pérez-Juste, J. Santamaría, R. Mallada and M. Pina, *ACS Sens.*, 2021, **6**, 2241–2251.

367 M. Lafuente, D. Sanz, M. Urbiztondo, J. Santamaría, M. P. Pina and R. Mallada, *J. Hazard. Mater.*, 2020, **384**, 121279.

368 A. Hakonen, P. O. Andersson, M. Stenbæk Schmidt, T. Rindzevicius and M. Käll, *Anal. Chim. Acta*, 2015, **893**, 1–13.

369 Y. Chen, Y. Zhang, F. Pan, J. Liu, K. Wang, C. Zhang, S. Cheng, L. Lu, W. Zhang, Z. Zhang, X. Zhi, Q. Zhang, G. Alfranca, J. M. de la Fuente, D. Chen and D. Cui, *ACS Nano*, 2016, **10**, 8169–8179.

370 J. Fu, Z. Zhong, D. Xie, Y. Guo, D. Kong, Z. Zhao, Z. Zhao and M. Li, *Angew. Chem., Int. Ed.*, 2020, **59**, 20489–20498.

371 X. Qiao, B. Su, C. Liu, Q. Song, D. Luo, G. Mo and T. Wang, *Adv. Mater.*, 2018, **30**, 1–8.

372 K. Chang, Y. Zhao, M. Wang, Z. Xu, L. Zhu, L. Xu and Q. Wang, *Chem. Eng. J.*, 2023, **459**, 141539.

373 N. Taranenko, J.-P. Alarie, D. L. Stokes and T. Vo-Dinh, *J. Raman Spectrosc.*, 1996, **27**, 379–384.

374 D. A. Stuart, K. B. Biggs and R. P. Van Duyne, *Analyst*, 2006, **131**, 568.

375 R. K. Lauridsen, P. B. Skou, T. Rindzevicius, K. Wu, S. Molin, S. B. Engelsen, K. G. Nielsen, H. K. Johansen and A. Boisen, *Anal. Methods*, 2017, **9**, 5757–5762.

376 C. L. Wong, U. S. Dinish, M. S. Schmidt and M. Olivo, *Anal. Chim. Acta*, 2014, **844**, 54–60.

377 X. He, H. Wang, Z. Li, D. Chen, J. Liu and Q. Zhang, *Nanoscale*, 2015, **7**, 8619–8626.

378 S. Kim, D.-H. Kim and S.-G. Park, *Analyst*, 2018, **143**, 3006–3010.

379 S. Kim, H. S. Jung, D.-H. Kim, S.-H. Kim and S.-G. Park, *Analyst*, 2019, **144**, 7162–7167.

380 S. D. Christesen, *Appl. Spectrosc.*, 1988, **42**, 318–321.

381 Y. Liu, M. Kim, S. H. Cho and Y. S. Jung, *Nano Today*, 2021, **37**, 101063.

382 V. M. Szlag, R. S. Rodriguez, J. He, N. Hudson-Smith, H. Kang, N. Le, T. M. Reineke and C. L. Haynes, *ACS Appl. Mater. Interfaces*, 2018, **10**, 31825–31844.

383 M. Oh, R. De and S. Yim, *J. Raman Spectrosc.*, 2018, **49**, 800–809.

384 E.-C. Lin, J. Fang, S.-C. Park, F. W. Johnson and H. O. Jacobs, *Nat. Commun.*, 2013, **4**, 1636.

385 M. Lafuente, E. Berenschot, R. Tiggelaar, R. Mallada, N. Tas and M. Pina, *Micromachines*, 2018, **9**, 60.

386 A. Chauvin, M. Lafuente, J. Y. Mevellec, R. Mallada, B. Humbert, M. P. Pina, P.-Y. Tessier and A. El Mel, *Nanoscale*, 2020, **12**, 12602–12612.

387 K. J. Squire, K. Sivashanmugan, B. Zhang, J. Kraai, G. Rorrer and A. X. Wang, *ACS Appl. Nano Mater.*, 2020, **3**, 1656–1665.

388 K. Huang, S. Gong, L. Zhang, H. Zhang, S. Li, G. Ye and F. Huang, *Chem. Commun.*, 2021, **57**, 2144–2147.

389 K. Yang, K. Zhu, Y. Wang, Z. Qian, Y. Zhang, Z. Yang, Z. Wang, L. Wu, S. Zong and Y. Cui, *ACS Nano*, 2021, **15**, 12996–13006.

390 K. Yang, C. Zhang, K. Zhu, Z. Qian, Z. Yang, L. Wu, S. Zong, Y. Cui and Z. Wang, *ACS Nano*, 2022, **16**, 19335–19345.

391 M. Mueller, M. Tebbe, D. V. Andreeva, M. Karg, R. A. Alvarez Puebla, N. Pazos Perez and A. Fery, *Langmuir*, 2012, **28**, 9168–9173.

392 L. B. T. Nguyen, Y. X. Leong, C. S. L. Koh, S. X. Leong, S. K. Boong, H. Y. F. Sim, G. C. Phan-Quang, I. Y. Phang and X. Y. Ling, *Angew. Chem.*, 2022, **61**(33), e202207447.

393 S. X. Leong, Y. X. Leong, E. X. Tan, H. Y. F. Sim, C. S. L. Koh, Y. H. Lee, C. Chong, L. S. Ng, J. R. T. Chen, D. W. C. Pang, L. B. T. Nguyen, S. K. Boong, X. Han, Y.-C. Kao, Y. H. Chua, G. C. Phan-Quang, I. Y. Phang, H. K. Lee, M. Y. Abdad, N. S. Tan and X. Y. Ling, *ACS Nano*, 2022, **16**, 2629–2639.

394 H. Bao, H. Zhang, H. Fu, L. Zhou, P. Zhang, Y. Li and W. Cai, *Nanoscale Horiz.*, 2020, **5**, 739–746.

395 W. Xu, H. Bao, H. Zhang, H. Fu, Q. Zhao, Y. Li and W. Cai, *J. Hazard. Mater.*, 2021, **420**, 126668.

396 Z. Zhao, H. Bao, Q. Zhao, H. Fu, L. Zhou, H. Zhang, Y. Li and W. Cai, *ACS Appl. Mater. Interfaces*, 2022, **14**, 47999–48010.

397 H. Bao, Y. Guo, T. Zhang, H. Fu, S. Zhu, L. Zhou, H. Zhang, Y. Li and W. Cai, *Adv. Mater. Interfaces*, 2022, **9**, 1–10.

398 M. Lafuente, F. Almazan, E. Bernad, I. Florea, R. Arenal, M. A. Urbiztondo, R. Mallada and M. P. Pina, *Lab Chip*, 2023, 3160.

399 L. He, Y. Liu, J. Liu, Y. Xiong, J. Zheng, Y. Liu and Z. Tang, *Angew. Chem., Int. Ed.*, 2013, **52**, 3741–3745.

400 L. E. Kreno, N. G. Greeneltch, O. K. Farha, J. T. Hupp and R. P. Van Duyne, *Analyst*, 2014, **139**, 4073.

401 J. Chen, L. Guo, L. Chen, B. Qiu, G. Hong and Z. Lin, *ACS Sens.*, 2020, **5**, 3964–3970.

402 C. Huang, A. Li, X. Chen and T. Wang, *Small*, 2020, **16**, 1–17.

403 T. Zorlu, M. A. Correa-Duarte and R. A. Alvarez-Puebla, *J. Chem. Phys.*, 2023, **158**, 171001.

404 G. C. Phan-Quang, N. Yang, H. K. Lee, H. Y. F. Sim, C. S. L. Koh, Y.-C. Kao, Z. C. Wong, E. K. M. Tan, Y.-E. Miao, W. Fan, T. Liu, I. Y. Phang and X. Y. Ling, *ACS Nano*, 2019, **13**, 12090–12099.

405 X. Qiao, B. Su, C. Liu, Q. Song, D. Luo, G. Mo and T. Wang, *Adv. Mater.*, 2018, **30**, 1–8.

406 Q.-Q. Chen, R.-N. Hou, Y.-Z. Zhu, X.-T. Wang, H. Zhang, Y.-J. Zhang, L. Zhang, Z.-Q. Tian and J.-F. Li, *Anal. Chem.*, 2021, **93**, 7188–7195.

407 K. Yang, S. Zong, Y. Zhang, Z. Qian, Y. Liu, K. Zhu, L. Li, N. Li, Z. Wang and Y. Cui, *ACS Appl. Mater. Interfaces*, 2020, **12**, 1395–1403.

408 A. Li, X. Qiao, K. Liu, W. Bai and T. Wang, *Adv. Funct. Mater.*, 2022, **32**, 1–7.

409 Y. X. Leong, Y. H. Lee, C. S. L. Koh, G. C. Phan-Quang, X. Han, I. Y. Phang and X. Y. Ling, *Nano Lett.*, 2021, **21**, 2642–2649.

410 K. Nemciauskas, L. Traksele, A. Salaseviciene and V. Snitka, *Microelectron. Eng.*, 2020, **225**, 111282.
411 J. Plou, M. Charconnet, I. García, J. Calvo and L. M. Liz-Marzán, *ACS Nano*, 2021, **15**, 8984–8995.
412 L. Ma, H. Wu, Y. Huang, S. Zou, J. Li and Z. Zhang, *ACS Appl. Mater. Interfaces*, 2016, **8**, 27162–27168.
413 E. Pyrak, J. Krajczewski, A. Kowalik, A. Kudelski and A. Jaworska, *Molecules*, 2019, **24**, 4423.
414 C. Chen, W. Liu, S. Tian and T. Hong, *Sensors*, 2019, **19**, 1712.
415 T. K. Sharma, R. Ramanathan, R. Rakwal, G. K. Agrawal and V. Bansal, *Proteomics*, 2015, **15**, 1680–1692.
416 G. K. Agrawal, A. M. Timperio, L. Zolla, V. Bansal, R. Shukla and R. Rakwal, *J. Proteomics*, 2013, **93**, 74–92.
417 D. J. Sarkar, B. K. Behera, P. K. Parida, V. K. Aralappanavar, S. Mondal, J. Dei, B. K. Das, S. Mukherjee, S. Pal, P. Weerathunge, R. Ramanathan and V. Bansal, *Biosens. Bioelectron.*, 2023, **219**, 114771.
418 F. Arshad, M. Deliorman, P. Sukumar, M. A. Qasaimeh, J. S. Olarve, G. N. Santos, V. Bansal and M. U. Ahmed, *Trends Food Sci. Technol.*, 2023, **136**, 145–158.
419 E. Pyrak, A. Kowalczyk, J. L. Weyher, A. M. Nowicka and A. Kudelski, *Spectrochim. Acta, Part A*, 2023, **295**, 122606.
420 A. Szaniawska and A. Kudelski, *Front. Chem.*, 2021, **9**, 664134.
421 B. K. Behera, B. Dehury, A. K. Rout, B. Patra, N. Mantri, H. J. Chakraborty, D. J. Sarkar, N. K. Kaushik, V. Bansal, I. Singh, B. K. Das, A. R. Rao and A. Rai, *Gen. Rep.*, 2021, **25**, 101372.
422 X. Wei, S. Su, Y. Guo, X. Jiang, Y. Zhong, Y. Su, C. Fan, S. Lee and Y. He, *Small*, 2013, **9**, 2493–2499.
423 Y. He, S. Su, T. Xu, Y. Zhong, J. A. Zapien, J. Li, C. Fan and S.-T. Lee, *Nano Today*, 2011, **6**, 122–130.
424 L.-J. Xu, Z.-C. Lei, J. Li, C. Zong, C. J. Yang and B. Ren, *J. Am. Chem. Soc.*, 2015, **137**, 5149–5154.
425 E. Papadopoulou and S. E. J. Bell, *Chem. Commun.*, 2011, **47**, 10966.
426 A. Barhoumi, D. Zhang, F. Tam and N. J. Halas, *J. Am. Chem. Soc.*, 2008, **130**, 5523–5529.
427 E. Papadopoulou and S. E. J. Bell, *Angew. Chem., Int. Ed.*, 2011, **50**, 9058–9061.
428 E. Papadopoulou and S. E. J. Bell, *Chem. – Eur. J.*, 2012, **18**, 5394–5400.
429 Y. Li, X. Han, Y. Yan, Y. Cao, X. Xiang, S. Wang, B. Zhao and X. Guo, *Anal. Chem.*, 2018, **90**, 2996–3000.
430 Y. Li, X. Han, S. Zhou, Y. Yan, X. Xiang, B. Zhao and X. Guo, *J. Phys. Chem. Lett.*, 2018, **9**, 3245–3252.
431 T. Zhang, X. Quan, N. Cao, Z. Zhang and Y. Li, *Nanomaterials*, 2022, **12**, 3119.
432 D. Li, L. Xia, Q. Zhou, L. Wang, D. Chen, X. Gao and Y. Li, *Anal. Chem.*, 2020, **92**, 12769–12773.
433 Y. Li, T. Gao, G. Xu, X. Xiang, B. Zhao, X. X. Han and X. Guo, *Anal. Chem.*, 2019, **91**, 7980–7984.
434 E. Prado, A. Colin, L. Servant and S. Lecomte, *J. Phys. Chem. C*, 2014, **118**, 13965–13971.
435 L. Guerrini, Ž. Krpetić, D. van Lierop, R. A. Alvarez-Puebla and D. Graham, *Angew. Chem., Int. Ed.*, 2015, **54**, 1144–1148.
436 J. Morla-Folch, H. Xie, P. Gisbert-Quilis, S. G. Pedro, N. Pazos-Perez, R. A. Alvarez-Puebla and L. Guerrini, *Angew. Chem., Int. Ed.*, 2015, **54**, 13650–13654.
437 J. Morla-Folch, R. A. Alvarez-Puebla and L. Guerrini, *J. Phys. Chem. Lett.*, 2016, **7**, 3037–3041.
438 A. Barhoumi and N. J. Halas, *J. Am. Chem. Soc.*, 2010, **132**, 12792–12793.
439 Y. Qian, T. Fan, Y. Yao, X. Shi, X. Liao, F. Zhou and F. Gao, *Sens. Actuators, B*, 2018, **254**, 483–489.
440 Y. Yao, H. Zhang, T. Tian, Y. Liu, R. Zhu, J. Ji and B. Liu, *Talanta*, 2021, **235**, 122728.
441 E. Bailo and V. Deckert, *Angew. Chem., Int. Ed.*, 2008, **47**, 1658–1661.
442 Y. C. Cao, R. Jin and C. A. Mirkin, *Science*, 2002, **297**, 1536–1540.
443 R. Jin, Y. C. Cao, C. S. Thaxton and C. A. Mirkin, *Small*, 2006, **2**, 375–380.
444 Z. Y. Jiang, X. X. Jiang, S. Su, X. P. Wei, S. T. Lee and Y. He, *Appl. Phys. Lett.*, 2012, **100**(20), 203104.
445 T. Kang, S. M. Yoo, I. Yoon, S. Y. Lee and B. Kim, *Nano Lett.*, 2010, **10**, 1189–1193.
446 G. Braun, S. J. Lee, M. Dante, T.-Q. Nguyen, M. Moskovits and N. Reich, *J. Am. Chem. Soc.*, 2007, **129**, 6378–6379.
447 J.-M. Li, C. Wei, W.-F. Ma, Q. An, J. Guo, J. Hu and C.-C. Wang, *J. Mater. Chem.*, 2012, **22**, 12100.
448 S. He, K.-K. Liu, S. Su, J. Yan, X. Mao, D. Wang, Y. He, L.-J. Li, S. Song and C. Fan, *Anal. Chem.*, 2012, **84**, 4622–4627.
449 D. Graham, D. G. Thompson, W. E. Smith and K. Faulds, *Nat. Nanotechnol.*, 2008, **3**, 548–551.
450 X. Qian, X. Zhou and S. Nie, *J. Am. Chem. Soc.*, 2008, **130**, 14934–14935.
451 T. Donnelly, W. E. Smith, K. Faulds and D. Graham, *Chem. Commun.*, 2014, **50**, 12907–12910.
452 J.-M. Li, W.-F. Ma, L.-J. You, J. Guo, J. Hu and C.-C. Wang, *Langmuir*, 2013, **29**, 6147–6155.
453 H. Zhang, M. H. Harpster, W. C. Wilson and P. A. Johnson, *Langmuir*, 2012, **28**, 4030–4037.
454 H. Zhang, M. H. Harpster, H. J. Park, P. A. Johnson and W. C. Wilson, *Anal. Chem.*, 2011, **83**, 254–260.
455 X. Fu, Z. Cheng, J. Yu, P. Choo, L. Chen and J. Choo, *Biosens. Bioelectron.*, 2016, **78**, 530–537.
456 X. Wang, N. Choi, Z. Cheng, J. Ko, L. Chen and J. Choo, *Anal. Chem.*, 2017, **89**, 1163–1169.
457 A. MacAskill, D. Crawford, D. Graham and K. Faulds, *Anal. Chem.*, 2009, **81**, 8134–8140.
458 L. Fabris, M. Dante, G. Braun, S. J. Lee, N. O. Reich, M. Moskovits, T.-Q. Nguyen and G. C. Bazan, *J. Am. Chem. Soc.*, 2007, **129**, 6086–6087.
459 C. Yuan, J. Fang, M. L. de la Chapelle, Y. Zhang, X. Zeng, G. Huang, X. Yang and W. Fu, *TrAC, Trends Anal. Chem.*, 2021, **143**, 116401.
460 D. Ma, C. Huang, J. Zheng, J. Tang, J. Li, J. Yang and R. Yang, *Biosens. Bioelectron.*, 2018, **101**, 167–173.
461 W. Xu, A. Zhao, F. Zuo, R. Khan, H. M. J. Hussain and J. Chang, *Microchim. Acta*, 2020, **187**, 384.
462 Y. Pang, C. Wang, J. Wang, Z. Sun, R. Xiao and S. Wang, *Biosens. Bioelectron.*, 2016, **79**, 574–580.

463 Y. Pang, C. Wang, L. Lu, C. Wang, Z. Sun and R. Xiao, *Biosens. Bioelectron.*, 2019, **130**, 204–213.

464 X. Yang, S. Wang, Y. Wang, Y. He, Y. Chai and R. Yuan, *ACS Appl. Mater. Interfaces*, 2018, **10**, 12491–12496.

465 Y. He, X. Yang, R. Yuan and Y. Chai, *Anal. Chem.*, 2017, **89**, 8538–8544.

466 J. Hu and C. Zhang, *Anal. Chem.*, 2010, **82**, 8991–8997.

467 B. Guven, I. H. Boyaci, U. Tamer, E. Acar-Soykut and U. Dogan, *Talanta*, 2015, **136**, 68–74.

468 Y. He, X. Yang, R. Yuan and Y. Chai, *Anal. Chem.*, 2017, **89**, 2866–2872.

469 C. Liu, C. Chen, S. Li, H. Dong, W. Dai, T. Xu, Y. Liu, F. Yang and X. Zhang, *Anal. Chem.*, 2018, **90**, 10591–10599.

470 Y. Si, L. Xu, T. Deng, J. Zheng and J. Li, *ACS Sens.*, 2020, **5**, 4009–4016.

471 W. Wang, Y. Li, A. Nie, G.-C. Fan and H. Han, *Analyst*, 2021, **146**, 848–854.

472 Y. Sun and T. Li, *Anal. Chem.*, 2018, **90**, 11614–11621.

473 Y. Mao, Y. Sun, J. Xue, W. Lu and X. Cao, *Anal. Chim. Acta*, 2021, **1178**, 338800.

474 J. Chen, Y. Wu, C. Fu, H. Cao, X. Tan, W. Shi and Z. Wu, *Biosens. Bioelectron.*, 2019, **143**, 111619.

475 J. Zhang, X. Miao, C. Song, N. Chen, J. Xiong, H. Gan, J. Ni, Y. Zhu, K. Cheng and L. Wang, *Biosens. Bioelectron.*, 2022, **212**, 114379.

476 S. Ye, Y. Wu, X. Zhai and B. Tang, *Anal. Chem.*, 2015, **87**, 8242–8249.

477 F. Gao, J. Lei and H. Ju, *Anal. Chem.*, 2013, **85**, 11788–11793.

478 Y. Zhao, L. Liu, H. Kuang, L. Wang and C. Xu, *RSC Adv.*, 2014, **4**, 56052–56056.

479 B. Yin, Q. Zhang, X. Xia, C. Li, W. K. H. Ho, J. Yan, Y. Huang, H. Wu, P. Wang, C. Yi, J. Hao, J. Wang, H. Chen, S. H. D. Wong and M. Yang, *Theranostics*, 2022, **12**, 5914–5930.

480 Y. Pang, Q. Li, C. Wang, S. Zhen, Z. Sun and R. Xiao, *Chem. Eng. J.*, 2022, **429**, 132109.

481 J. Liang, P. Teng, W. Xiao, G. He, Q. Song, Y. Zhang, B. Peng, G. Li, L. Hu, D. Cao and Y. Tang, *J. Nanobiotechnology*, 2021, **19**, 273.

482 C. Lin, S. Liang, Y. Peng, L. Long, Y. Li, Z. Huang, N. V. Long, X. Luo, J. Liu, Z. Li and Y. Yang, *Nanomicro Lett.*, 2022, **14**, 75.

483 P. Senthil Kumar, I. Pastoriza-Santos, B. Rodríguez-González, F. Javier García de Abajo and L. M. Liz-Marzán, *Nanotechnology*, 2008, **19**, 015606.

484 A. Guerrero-Martínez, S. Barbosa, I. Pastoriza-Santos and L. M. Liz-Marzán, *Curr. Opin. Colloid Interface Sci.*, 2011, **16**, 118–127.

485 R. A. Alvarez-Puebla, A. Agarwal, P. Manna, B. P. Khanal, P. Aldeanueva-Potel, E. Carbó-Argibay, N. Pazos-Pérez, L. Vigderman, E. R. Zubarev, N. A. Kotov and L. M. Liz-Marzán, *Proc. Natl. Acad. Sci.*, 2011, **108**, 8157–8161.

486 P. Kusch, S. Mastel, N. S. Mueller, N. Morquillas Azpiazu, S. Heeg, R. Gorbachev, F. Schedin, U. Hübner, J. I. Pascual, S. Reich and R. Hillenbrand, *Nano Lett.*, 2017, **17**, 2667–2673.

487 Y. Xu, M. P. Konrad, W. W. Y. Lee, Z. Ye and S. E. J. Bell, *Nano Lett.*, 2016, **16**, 5255–5260.

488 M. P. Konrad, A. P. Doherty and S. E. J. Bell, *Anal. Chem.*, 2013, **85**, 6783–6789.

489 Y. He, X. Yang, R. Yuan and Y. Chai, *J. Mater. Chem. B*, 2019, **7**, 2643–2647.

490 A. Woo, K. Lim, B. H. Cho, H. S. Jung and M. Lee, *Anal. Sci. Ad.*, 2021, **2**, 397–407.

491 M. Kim, S. M. Ko, C. Lee, J. Son, J. Kim, J.-M. Kim and J.-M. Nam, *Anal. Chem.*, 2019, **91**, 10467–10476.

492 D.-K. Lim, K.-S. Jeon, J.-H. Hwang, H. Kim, S. Kwon, Y. D. Suh and J.-M. Nam, *Nat. Nanotechnol.*, 2011, **6**, 452–460.

493 J.-E. Shim, Y. J. Kim, J.-H. Choe, T. G. Lee and E.-A. You, *ACS Appl. Mater. Interfaces*, 2022, **14**, 38459–38470.

494 M. Kim, S. M. Ko, J.-M. Kim, J. Son, C. Lee, W.-K. Rhim and J.-M. Nam, *ACS Cent. Sci.*, 2018, **4**, 277–287.

495 O. Guselnikova, A. Trelin, A. Skvortsova, P. Ulbrich, P. Postnikov, A. Pershina, D. Sykora, V. Svorcik and O. Lyutakov, *Biosens. Bioelectron.*, 2019, **145**, 111718.

496 Y. Yang, H. Li, L. Jones, J. Murray, J. Haverstick, H. K. Naikare, Y.-Y. C. Mosley, R. A. Tripp, B. Ai and Y. Zhao, *ACS Sens.*, 2023, **8**, 297–307.

497 M. Prochazka, *Surface-Enhanced Raman Spectroscopy: Bioanalytical, Biomolecular and Medical Applications*, Springer International Publishing, Cham, 2016, pp. 149–211.

498 Y. Wu, M. R. K. Ali, K. Chen, N. Fang and M. A. El-Sayed, *Nano Today*, 2019, **24**, 120–140.

499 S. E. J. Bell, G. Charron, E. Cortés, J. Kneipp, M. L. de la Chapelle, J. Langer, M. Procházka, V. Tran and S. Schlücker, *Angew. Chem., Int. Ed.*, 2020, **59**, 5454–5462.

500 Y. Zhang, H. Hong, D. V. Myklejord and W. Cai, *Small*, 2011, **7**, 3261–3269.

501 Y. Li, Z. Wang, X. Mu, A. Ma and S. Guo, *Biotechnol. Adv.*, 2017, **35**, 168–177.

502 R. M. Crist, S. S. K. Dasa, C. H. Liu, J. D. Clogston, M. A. Dobrovolskaia and S. T. Stern, *WIREs Nanomed. Nanobiotechnol.*, 2021, **13**, e1665.

503 B. Andreiuk, F. Nicolson, L. M. Clark, S. R. Panikkanvalappil, M. Rashidian, S. Harmsen and M. F. Kircher, *Nanotheranostics*, 2022, **6**, 10–30.

504 B. Tim, M. Rojewska and K. Prochaska, *Int. J. Mol. Sci.*, 2022, **23**, 12822.

505 Y.-C. Ou, J. A. Webb, C. M. O'Brien, I. J. Pence, E. C. Lin, E. P. Paul, D. Cole, S.-H. Ou, M. Lapierre-Landry, R. C. DeLapp, E. S. Lippmann, A. Mahadevan-Jansen and R. Bardhan, *Nanoscale*, 2018, **10**, 13092–13105.

506 C. L. Zavaleta, B. R. Smith, I. Walton, W. Doering, G. Davis, B. Shojaei, M. J. Natan and S. S. Gambhir, *Proc. Natl. Acad. Sci.*, 2009, **106**, 13511–13516.

507 J. H. Yu, I. Steinberg, R. M. Davis, A. V. Malkovskiy, A. Zlitni, R. K. Radzyminski, K. O. Jung, D. T. Chung, L. D. Curet, A. L. D'Souza, E. Chang, J. Rosenberg, J. Campbell, H. Frostig, S. Park, G. Pratx, C. Levin and S. S. Gambhir, *ACS Nano*, 2021, **15**, 19956–19969.

508 S. Bock, Y.-S. Choi, M. Kim, Y. Yun, X.-H. Pham, J. Kim, B. Seong, W. Kim, A. Jo, K.-M. Ham, S. G. Lee, S. H. Lee,

H. Kang, H. S. Choi, D. H. Jeong, H. Chang, D.-E. Kim and B.-H. Jun, *J. Nanobiotechnol.*, 2022, **20**, 130.

509 O. E. Eremina, A. T. Czaja, A. Fernando, A. Aron, D. B. Eremin and C. Zavaleta, *ACS Nano*, 2022, **16**, 10341–10353.

510 G. Cutshaw, S. Uthaman, N. Hassan, S. Kothadiya, X. Wen and R. Bardhan, *Chem. Rev.*, 2023, **123**, 8297–8346.

511 J. Deal, S. Mayes, C. Browning, S. Hill, P. Rider, C. Boudreaux, T. C. Rich and S. J. Leavesley, *J. Biomed. Opt.*, 2018, **24**, 1.

512 J. Wang, D. Liang, J. Feng and X. Tang, *Anal. Chem.*, 2019, **91**, 11045–11054.

513 Y. Zou, S. Huang, Y. Liao, X. Zhu, Y. Chen, L. Chen, F. Liu, X. Hu, H. Tu, L. Zhang, Z. Liu, Z. Chen and W. Tan, *Chem. Sci.*, 2018, **9**, 2842–2849.

514 F. Nicolson, M. F. Kircher, N. Stone and P. Matousek, *Chem. Soc. Rev.*, 2021, **50**, 556–568.

515 F. Nicolson, B. Andreiuk, C. Andreou, H.-T. Hsu, S. Rudder and M. F. Kircher, *Theranostics*, 2019, **9**, 5899–5913.

516 P. Strobbia, V. Cupil-Garcia, B. M. Crawford, A. M. Fales, T. J. Pfefer, Y. Liu, M. Maiwald, B. Sumpf and T. Vo-Dinh, *Theranostics*, 2021, **11**, 4090–4102.

517 J. L. Rutter, D. B. Goldstein, A. Philippakis, J. W. Smoller, G. Jenkins, E. Dishman and J. C. Denny, *N. Engl. J. Med.*, 2019, **381**, 668.

518 A. P. Rao, N. Bokde and S. Sinha, *Appl. Sci.*, 2020, **10**, 767.

519 C. Zhang, Z. Xu, H. Di, E. Zeng, Y. Jiang and D. Liu, *Theranostics*, 2020, **10**, 6061–6071.

520 M. A. Wall, T. M. Shaffer, S. Harmsen, D.-F. Tschaharganeh, C.-H. Huang, S. W. Lowe, C. M. Drain and M. F. Kircher, *Theranostics*, 2017, **7**, 3068–3077.

521 B. Shi, D. Li, W. Yao, W. Wang, J. Jiang, R. Wang, F. Yan, H. Liu, H. Zhang and J. Ye, *Biomater. Sci.*, 2022, **10**, 2577–2589.

522 Y.-C. Ou, X. Wen, C. A. Johnson, D. Shae, O. D. Ayala, J. A. Webb, E. C. Lin, R. C. DeLapp, K. L. Boyd, A. Richmond, A. Mahadevan-Jansen, M. Rafat, J. T. Wilson, J. M. Balko, M. N. Tantawy, A. E. Vilgelm and R. Bardhan, *ACS Nano*, 2020, **14**, 651–663.

523 X. Chen, Z. Wu, Y. He, Z. Hao, Q. Wang, K. Zhou, W. Zhou, P. Wang, F. Shan, Z. Li, J. Ji, Y. Fan, Z. Li and S. Yue, *Adv. Sci.*, 2023, **10**(21), e2300961.

524 H. G. Lee, W. Choi, S. Y. Yang, D.-H. Kim, S.-G. Park, M.-Y. Lee and H. S. Jung, *Sens. Actuators, B*, 2021, **326**, 128802.

525 J. C. Denny, *N. Engl. J. Med.*, 2019, **381**, 668–676.

526 R. T. Busch, F. Karim, J. Weis, Y. Sun, C. Zhao and E. S. Vasquez, *ACS Omega*, 2019, **4**, 15269–15279.

527 Y. Liu, L. Zhan, Z. Qin, J. Sackrison and J. C. Bischof, *ACS Nano*, 2021, **15**, 3593–3611.

528 S. Yadav, M. A. Sadique, P. Ranjan, N. Kumar, A. Singhal, A. K. Srivastava and R. Khan, *ACS Appl. Bio Mater.*, 2021, **4**, 2974–2995.

529 M. Muhammad, C. Shao and Q. Huang, *Spectrochim. Acta, Part A*, 2019, **223**, 117282.

530 M. R. Willner, K. S. McMillan, D. Graham, P. J. Vikesland and M. Zagnoni, *Anal. Chem.*, 2018, **90**, 12004–12010.

531 R. Chen, X. Du, Y. Cui, X. Zhang, Q. Ge, J. Dong and X. Zhao, *Small*, 2020, **16**, 2002801.

532 X. Wen, Y. Ou, H. F. Zarick, X. Zhang, A. B. Hmelo, Q. J. Victor, E. P. Paul, J. M. Slocik, R. R. Naik, L. M. Bellan, E. C. Lin and R. Bardhan, *Bioeng. Transl. Med.*, 2020, **5**, e10165.

533 Y. Su, S. Xu, J. Zhang, X. Chen, L.-P. Jiang, T. Zheng and J.-J. Zhu, *Anal. Chem.*, 2019, **91**, 864–872.

534 J. Wang, A. Wuethrich, A. A. I. Sina, R. E. Lane, L. L. Lin, Y. Wang, J. Cebon, A. Behren and M. Trau, *Sci. Adv.*, 2020, **6**, eaax3223.

535 U. Mogera, H. Guo, M. Namkoong, M. S. Rahman, T. Nguyen and L. Tian, *Sci. Adv.*, 2022, **8**, 1736.

536 R. Alder, L. Xiao and S. Fu, *Drug Test. Anal.*, 2021, **13**, 944–952.

537 A. Azziz, W. Safar, Y. Xiang, M. Edely and M. Lamy de la Chapelle, *J. Mol. Struct.*, 2022, **1248**, 131519.

538 S. Abalde-Cela, L. Wu, A. Teixeira, K. Oliveira and L. Diéguez, *Adv. Opt. Mater.*, 2021, **9**, 2001171.

539 A. N. Ramya, M. M. Joseph, J. B. Nair, V. Karunakaran, N. Narayanan and K. K. Maiti, *ACS Appl. Mater. Interfaces*, 2016, **8**, 10220–10225.

540 Y. Pang, C. Wang, R. Xiao and Z. Sun, *Chem. – Eur. J.*, 2018, **24**, 7060–7067.

541 X. Wu, Y. Xia, Y. Huang, J. Li, H. Ruan, T. Chen, L. Luo, Z. Shen and A. Wu, *ACS Appl. Mater. Interfaces*, 2016, **8**, 19928–19938.

542 J. Wang, R. Zhang, X. Ji, P. Wang and C. Ding, *Anal. Chim. Acta*, 2021, **1141**, 206–213.

543 K. Oliveira, A. Teixeira, J. M. Fernandes, C. Lopes, A. Chícharo, P. Piairo, L. Wu, L. Rodríguez-Lorenzo, L. Diéguez and S. Abalde-Cela, *Adv. Opt. Mater.*, 2023, **11**, 2201500.

544 Y. Chen, X. Bai, L. Su, Z. Du, A. Shen, A. Materny and J. Hu, *Sci. Rep.*, 2016, **6**, 19173.

545 W. Nam, X. Ren, S. A. S. Tali, P. Ghassemi, I. Kim, M. Agah and W. Zhou, *Nano Lett.*, 2019, **19**, 7273–7281.

546 G. Kuku, M. Altunbek and M. Culha, *Anal. Chem.*, 2017, **89**, 11160–11166.

547 A. Kamińska, T. Szymborski, E. Witkowska, E. Kijeńska-Gawrońska, W. Świeszkowski, K. Niciński, J. Trzcińska-Danielewicz and A. Girstun, *Nanomaterials*, 2019, **9**, 366.

548 D. Wu, Y. Chen, S. Hou, W. Fang and H. Duan, *ChemBioChem*, 2019, **20**, 2432–2441.

549 Y. Zhang, X. Ye, G. Xu, X. Jin, M. Luan, J. Lou, L. Wang, C. Huang and J. Ye, *RSC Adv.*, 2016, **6**, 5401–5407.

550 J. Plou, I. García, M. Charconnet, I. Astobiza, C. García-Astrain, C. Matricardi, A. Mihi, A. Carracedo and L. M. Liz-Marzán, *Adv. Funct. Mater.*, 2020, **30**(17), 1910335.

551 J. Plou, P. S. Valera, I. García, D. Vila-Liarte, C. Renero-Lecuna, J. Ruiz-Cabello, A. Carracedo and L. M. Liz-Marzán, *Small*, 2023, 2207658.

552 M. Tavakkoli Yaraki, A. Tukova and Y. Wang, *Nanoscale*, 2022, **14**, 15242–15268.

553 J. Wang, Y.-C. Kao, Q. Zhou, A. Wuethrich, M. S. Stark, H. Schaider, H. P. Soyer, L. L. Lin and M. Trau, *Adv. Funct. Mater.*, 2022, **32**, 2010296.

554 A. Teixeira, J. Hernández-Rodríguez, L. Wu, K. Oliveira, K. Kant, P. Piairo, L. Diéguez and S. Abalde-Cela, *Appl. Sci.*, 2019, **9**, 1387.

555 Z. Du, Y. Qi, J. He, D. Zhong and M. Zhou, *WIREs Nanomed. Nanobiotechnol.*, 2021, **13**, e1672.

556 A. F. Palonpon, J. Ando, H. Yamakoshi, K. Dodo, M. Sodeoka, S. Kawata and K. Fujita, *Nat. Protoc.*, 2013, **8**, 677.

557 E. Lenzi, D. Jimenez de Aberasturi and L. M. Liz-Marzán, *ACS Sens.*, 2019, **4**, 1126–1137.

558 F. Lussier, T. Brulé,Brulé, M. Vishwakarma, T. Das, J. P. Spatz and J.-F. O. Masson, *Nano Lett.*, 2016, **16**(6), 3866–3871.

559 A. Y. F. Mahmoud, A. Teixeira, M. Aranda, M. S. Relvas, S. Quintero, M. Sousa-Silva, A. Chícharo, M. Chen, M. Hashemi, J. B. King, J. W. Tunnell, C. Morasso, F. Piccotti, F. Corsi, M. Henriksen-Lacey, D. J. de Aberasturi, D. M. Merino, A. Rodríguez-Patón, S. Abalde-Cela and L. Diéguez, *TrAC, Trends Anal. Chem.*, 2023, 117311.

560 G. Ramachandran, *Virulence*, 2014, **5**, 213–218.

561 M. McKee and D. Stuckler, *Nat. Med.*, 2020, **26**, 640–642.

562 G. Bonaccorsi, F. Pierri, M. Cinelli, A. Flori, A. Galeazzi, F. Porcelli, A. L. Schmidt, C. M. Valensise, A. Scala, W. Quattrociocchi and F. Pammolli, *Proc. Natl. Acad. Sci.*, 2020, **117**, 15530–15535.

563 V. M. Corman, O. Landt, M. Kaiser, R. Molenkamp, A. Meijer, D. K. Chu, T. Bleicker, S. Brünink, J. Schneider, M. L. Schmidt, D. G. Mulders, B. L. Haagmans, B. van der Veer, S. van den Brink, L. Wijsman, G. Goderski, J.-L. Romette, J. Ellis, M. Zambon, M. Peiris, H. Goossens, C. Reusken, M. P. Koopmans and C. Drosten, *Eurosurveillance*, 2020, **25**, 2000045.

564 M. Shen, Y. Zhou, J. Ye, A. A. Abdullah AL-maskri, Y. Kang, S. Zeng and S. Cai, *J. Pharm. Anal.*, 2020, **10**, 97–101.

565 K. Dighe, P. Moitra, M. Alafeef, N. Gunaseelan and D. Pan, *Biosens. Bioelectron.*, 2022, **200**, 113900.

566 H. Harpaldas, S. Arumugam, C. Campillo Rodriguez, B. A. Kumar, V. Shi and S. K. Sia, *Lab Chip*, 2021, **21**, 4517–4548.

567 Z. Cheng, N. Choi, R. Wang, S. Lee, K. C. Moon, S.-Y. Yoon, L. Chen and J. Choo, *ACS Nano*, 2017, **11**, 4926–4933.

568 X. Wang, S. Park, J. Ko, X. Xiao, V. Giannini, S. A. Maier, D. Kim and J. Choo, *Small*, 2018, **14**, 1801623.

569 S. H. Lee, J. Hwang, K. Kim, J. Jeon, S. Lee, J. Ko, J. Lee, M. Kang, D. R. Chung and J. Choo, *Anal. Chem.*, 2019, **91**, 12275–12282.

570 Y. Joung, K. Kim, S. Lee, B.-S. Chun, S. Lee, J. Hwang, S. Choi, T. Kang, M.-K. Lee, L. Chen and J. Choo, *ACS Sens.*, 2022, **7**, 3470–3480.

571 Q. Yu, H. D. Trinh, Y. Lee, T. Kang, L. Chen, S. Yoon and J. Choo, *Sens. Actuators, B*, 2023, **382**, 133521.

572 P. Mandal and B. S. Tewari, *Surf. Interfaces*, 2022, **28**, 101655.

573 I. V. Chernyshova, P. Somasundaran and S. Ponnurangam, *Proc. Natl. Acad. Sci.*, 2018, **115**, E9261–E9270.

574 G. Zheng, L. Polavarapu, L. M. Liz-Marzán, I. Pastoriza-Santos and J. Pérez-Juste, *Chem. Commun.*, 2015, **51**, 4572–4575.

575 P. Taladriz-Blanco, L. Rodríguez-Lorenzo, M. Sanles-Sobrido, P. Hervés, M. A. Correa-Duarte, R. A. Álvarez-Puebla and L. M. Liz-Marzán, *ACS Appl. Mater. Interfaces*, 2009, **1**, 56–59.

576 D. Devasia, A. J. Wilson, J. Heo, V. Mohan and P. K. Jain, *Nat. Commun.*, 2021, **12**, 2612.

577 G. Kumari, X. Zhang, D. Devasia, J. Heo and P. K. Jain, *ACS Nano*, 2018, **12**, 8330–8340.

578 S. Rodal-Cedeira, V. Montes-García, L. Polavarapu, D. M. Solís, H. Heidari, A. La Porta, M. Angiola, A. Martucci, J. M. Taboada, F. Obelleiro, S. Bals, J. Pérez-Juste and I. Pastoriza-Santos, *Chem. Mater.*, 2016, **28**, 9169–9180.

579 J. Li, J. Liu, Y. Yang and D. Qin, *J. Am. Chem. Soc.*, 2015, **137**, 7039–7042.

580 P. Li, B. Ma, L. Yang and J. Liu, *Chem. Commun.*, 2015, **51**, 11394–11397.

581 W. Xie, R. Grzeschik and S. Schlücker, *Angew. Chem., Int. Ed.*, 2016, **55**, 13729–13733.

582 H. Zhang, J. Wei, X.-G. Zhang, Y.-J. Zhang, P. M. Radjenovica, D.-Y. Wu, F. Pan, Z.-Q. Tian and J.-F. Li, *Chemistry*, 2020, **6**, 689–702.

583 J.-C. Dong, X.-G. Zhang, V. Briega-Martos, X. Jin, J. Yang, S. Chen, Z.-L. Yang, D.-Y. Wu, J. M. Feliu, C. T. Williams, Z.-Q. Tian and J.-F. Li, *Nat. Energy*, 2018, **4**, 60–67.

584 Samriti, V. Rajput, R. K. Gupta and J. Prakash, *J. Mater. Chem. C*, 2022, **10**, 73–95.

585 Y. Cao and M. Sun, *Rev. Phys.*, 2022, **8**, 100067.

586 J. Ma, Y. Cheng and M. Sun, *Nanoscale*, 2021, **13**, 10712–10725.

587 N. Kumar, B. M. Weckhuysen, A. J. Wain and A. J. Pollard, *Nat. Protoc.*, 2019, **14**, 1169–1193.

588 R. M. Stöckle, Y. D. Suh, V. Deckert and R. Zenobi, *Chem. Phys. Lett.*, 2000, **318**, 131–136.

589 B. Pettinger, B. Ren, G. Picardi, R. Schuster and G. Ertl, *Phys. Rev. Lett.*, 2004, **92**, 096101.

590 M. Sun, Z. Zhang, H. Zheng and H. Xu, *Sci. Rep.*, 2012, **2**, 647.

591 Y. Fang, Z. Zhang and M. Sun, *Rev. Sci. Instrum.*, 2022, **7**(1), 1165–1172.

592 G. Binnig, C. F. Quate and C. Gerber, *Phys. Rev. Lett.*, 1986, **56**, 930–933.

593 S. Sheng, W. Li, J. Gou, P. Cheng, L. Chen and K. Wu, *Rev. Sci. Instrum.*, 2018, **89**, 053107.

594 S. Sheng, J. Wu, X. Cong, W. Li, J. Gou, Q. Zhong, P. Cheng, P. Tan, L. Chen and K. Wu, *Phys. Rev. Lett.*, 2017, **119**, 196803.

595 E. M. van Schrojenstein Lantman, T. Deckert-Gaudig, A. J. G. Mank, V. Deckert and B. M. Weckhuysen, *Nat. Nanotechnol.*, 2012, **7**, 583–586.

596 R. Zhang, Y. Zhang, Z. C. Dong, S. Jiang, C. Zhang, L. G. Chen, L. Zhang, Y. Liao, J. Aizpurua, Y. Luo, J. L. Yang and J. G. Hou, *Nature*, 2013, **498**, 82–86.

597 Y. Cao, Y. Feng, Y. Cheng, L. Meng and M. Sun, *Appl. Phys. Lett.*, 2023, **122**, 231601.

598 J.-F. Masson, J. S. Biggins and E. Ringe, *Nat. Nanotechnol.*, 2023, **18**, 111–123.

599 Y. X. Leong, E. X. Tan, S. X. Leong, C. S. Lin Koh, L. B. Thanh Nguyen, J. R. Ting Chen, K. Xia and X. Y. Ling, *ACS Nano*, 2022, **16**, 13279–13293.

600 F. Cui, Y. Yue, Y. Zhang, Z. Zhang and H. S. Zhou, *ACS Sens.*, 2020, **5**, 3346–3364.

601 R. Beeram, K. R. Vepa and V. R. Soma, *Biosensors*, 2023, **13**, 328.

602 C. Liu, D. Xu, X. Dong and Q. Huang, *Trends Food Sci. Technol.*, 2022, **128**, 90–101.

603 S. X. Leong, Y. X. Leong, C. S. L. Koh, E. X. Tan, L. B. T. Nguyen, J. R. T. Chen, C. Chong, D. W. C. Pang, H. Y. F. Sim, X. Liang, N. S. Tan and X. Y. Ling, *Chem. Sci.*, 2022, **13**, 11009–11029.

604 J. Perumal, Y. Wang, A. B. E. Attia, U. S. Dinish and M. Olivo, *Nanoscale*, 2021, **13**, 553–580.

605 J. Hua, Z. Xiong, J. Lowey, E. Suh and E. R. Dougherty, *Bioinformatics*, 2005, **21**, 1509–1515.

606 R. Gautam, S. Vanga, F. Ariese and S. Umapathy, *EPJ Tech. Instrum.*, 2015, **2**, 8.

607 S. Nanga, A. T. Bawah, B. A. Acquaye, M.-I. Billa, F. D. Baeta, N. A. Odai, S. K. Obeng and A. D. Nsiah, *J. Data Anal. Inform. Process.*, 2021, **09**, 189–231.

608 S. X. Leong, C. S. L. Koh, H. Y. F. Sim, Y. H. Lee, X. Han, G. C. Phan-Quang and X. Y. Ling, *ACS Nano*, 2021, **15**, 1817–1825.

609 Y. Yang, B. Xu, J. Haverstick, N. Ibtehaz, A. Muszyński, X. Chen, M. E. H. Chowdhury, S. M. Zughaier and Y. Zhao, *Nanoscale*, 2022, **14**, 8806–8817.

610 K. Yang, F. Xu, L. Zhu, H. Li, Q. Sun, A. Yan, B. Ren, Y. Zhu and L. Cui, *Angew. Chem., Int. Ed.*, 2023, **62**, e202217412.

611 M. Sugiyama, *Statistical Reinforcement Learning*, Chapman and Hall/CRC, 2015.

612 A. L. Tarca, V. J. Carey, X. Chen, R. Romero and S. Drăghici, *PLoS Comput. Biol.*, 2007, **3**, e116.

613 F. Safir, N. Vu, L. F. Tadesse, K. Firouzi, N. Banaei, S. S. Jeffrey, A. A. E. Saleh, B. P. T. Khuri-Yakub and J. A. Dionne, *Nano Lett.*, 2023, **23**, 2065–2073.

614 L. J. P. van der Maaten and G. E. Hinton, *J. Mach. Learn. Res.*, 2008, **9**, 2579–2605.

615 L. McInnes, J. Healy and J. Melville.

616 H. Shin, B. H. Choi, O. Shim, J. Kim, Y. Park, S. K. Cho, H. K. Kim and Y. Choi, *Nat. Commun.*, 2023, **14**, 1644.

617 H. K. Lee, Y. H. Lee, C. S. L. Koh, G. C. Phan-Quang, X. Han, C. L. Lay, H. Y. F. Sim, Y.-C. Kao, Q. An and X. Y. Ling, *Chem. Soc. Rev.*, 2019, **48**, 731–756.

618 M. T. Ribeiro, S. Singh and C. Guestrin, *Proceedings of the 22nd ACM SIGKDD International Conference on Knowledge Discovery and Data Mining*, ACM, New York, NY, USA, 2016, vol. 13–17, 1135–1144.

619 S. M. Lundberg and S.-I. Lee, *Adv. Neural Inf. Process Syst.*, 2017, **30**, 3149–3157.

620 A. Dhurandhar, P.-Y. Chen, R. Luss, C.-C. Tu, P. Ting, K. Shanmugam and P. Das, *Adv. Neural Inf. Process Syst.*, 2018, 590–601.

621 V. Živanović, S. Seifert, D. Drescher, P. Schrade, S. Werner, P. Guttmann, G. P. Szekeres, S. Bachmann, G. Schneider, C. Arenz and J. Kneipp, *ACS Nano*, 2019, **13**, 9363–9375.

622 R. L. Woodbury, S. M. Varnum and R. C. Zangar, *J. Proteome Res.*, 2002, **1**, 233–237.

623 B. Schweitzer, S. Roberts, B. Grimwade, W. Shao, M. Wang, Q. Fu, Q. Shu, I. Laroche, Z. Zhou and V. T. Tchernev, *Nat. Biotechnol.*, 2002, **20**, 359–365.

624 M. M. Ali, F. Li, Z. Zhang, K. Zhang, D.-K. Kang, J. A. Ankrum, X. C. Le and W. Zhao, *Chem. Soc. Rev.*, 2014, **43**, 3324–3341.

625 N. Ganesh, W. Zhang, P. C. Mathias, E. Chow, J. Soares, V. Malyarchuk, A. D. Smith and B. T. Cunningham, *Nat. Nanotechnol.*, 2007, **2**, 515–520.

626 V. Flauraud, R. Regmi, P. M. Winkler, D. T. L. Alexander, H. Rigneault, N. F. Van Hulst, M. F. García-Parajo, J. Wenger and J. Brugger, *Nano Lett.*, 2017, **17**, 1703–1710.

627 F. Tam, G. P. Goodrich, B. R. Johnson and N. J. Halas, *Nano Lett.*, 2007, **7**, 496–501.

628 A. Kinkhabwala, Z. Yu, S. Fan, Y. Avlasevich, K. Müllen and W. E. Moerner, *Nat. Photonics*, 2009, **3**, 654–657.

629 S. M. Tabakman, L. Lau, J. T. Robinson, J. Price, S. P. Sherlock, H. Wang, B. Zhang, Z. Chen, S. Tangsombatvisit, J. A. Jarrell, P. J. Utz and H. Dai, *Nat. Commun.*, 2011, **2**, 466.

630 B. Zhang, R. B. Kumar, H. Dai and B. J. Feldman, *Nat. Med.*, 2014, **20**, 948–953.

631 B. Zhang, B. A. Pinsky, J. S. Ananta, S. Zhao, S. Arulkumar, H. Wan, M. K. Sahoo, J. Abeynayake, J. J. Waggoner and C. Hopes, *Nat. Med.*, 2017, **23**, 548–550.

632 B. Liu, Y. Li, H. Wan, L. Wang, W. Xu, S. Zhu, Y. Liang, B. Zhang, J. Lou, H. Dai and K. Qian, *Adv. Funct. Mater.*, 2016, **26**, 7994–8002.

633 K. M. Mayer and J. H. Hafner, *Chem. Rev.*, 2011, **111**, 3828–3857.

634 A. J. Haes, L. Chang, W. L. Klein and R. P. Van Duyne, *J. Am. Chem. Soc.*, 2005, **127**, 2264–2271.

635 R. Bardhan, N. K. Grady, J. R. Cole, A. Joshi and N. J. Halas, *ACS Nano*, 2009, **3**, 744–752.

636 H. Li, C.-Y. Chen, X. Wei, W. Qiang, Z. Li, Q. Cheng and D. Xu, *Anal. Chem.*, 2012, **84**, 8656–8662.

637 K.-X. Xie, S.-H. Cao, Z.-C. Wang, Y.-H. Weng, S.-X. Huo, Y.-Y. Zhai, M. Chen, X.-H. Pan and Y.-Q. Li, *Sens. Actuators, B*, 2017, **253**, 804–808.

638 Z. A. R. Jawad, I. G. Theodorou, L. R. Jiao and F. Xie, *Sci. Rep.*, 2017, **7**, 14309.

639 J. Lee, S. R. Ahmed, S. Oh, J. Kim, T. Suzuki, K. Parmar, S. S. Park, J. Lee and E. Y. Park, *Biosens. Bioelectron.*, 2015, **64**, 311–317.

640 K. Ray, H. Szmacinski and J. R. Lakowicz, *Anal. Chem.*, 2009, **81**, 6049–6054.

641 Y. Liu, Y. Yang, G. Wang, D. Wang, P.-L. Shao, J. Tang, T. He, J. Zheng, R. Hu, Y. Liu, Z. Xu, D. Niu, J. Lv, J. Yang, H. Xiao, S. Wu, S. He, Z. Tang, Y. Liu, M. Tang, X. Jiang, J. Yuan, H. Dai and B. Zhang, *Nat. Biomed. Eng.*, 2023, **7**(12), 1636–1648.

642 C. R. Sabanayagam and J. R. Lakowicz, *Nucleic Acids Res.*, 2006, **35**, e13–e13.

643 W. Hu, Y. Liu, H. Yang, X. Zhou and C. M. Li, *Biosens. Bioelectron.*, 2011, **26**, 3683–3687.

644 J. Zhang, E. Matveeva, I. Gryczynski, Z. Leonenko and J. R. Lakowicz, *J. Phys. Chem. B*, 2005, **109**, 7969–7975.

645 E. G. Matveeva, I. Gryczynski, A. Barnett, Z. Leonenko, J. R. Lakowicz and Z. Gryczynski, *Anal. Biochem.*, 2007, **363**, 239–245.

646 T. W. Ebbesen, H. J. Lezec, H. F. Ghaemi, T. Thio and P. A. Wolff, *Nature*, 1998, **391**, 667–669.

647 G. Hawa, L. Sonnleitner, A. Missbichler, A. Prinz, G. Bauer and C. Mauracher, *Anal. Biochem.*, 2018, **549**, 39–44.

648 P. P. Pompa, L. Martiradonna, A. Della Torre, F. Della Sala, L. Manna, M. De Vittorio, F. Calabi, R. Cingolani and R. Rinaldi, *Nat. Nanotechnol.*, 2006, **1**, 126–130.

649 L. Zhou, F. Ding, H. Chen, W. Ding, W. Zhang and S. Y. Chou, *Anal. Chem.*, 2012, **84**, 4489–4495.

650 C. Wang, S. Tadepalli, J. Luan, K. Liu, J. J. Morrissey, E. D. Kharasch, R. R. Naik and S. Singamaneni, *Adv. Mater.*, 2018, **3**(2), 342–351.

651 D. F. Cruz, C. M. Fontes, D. Semeniak, J. Huang, A. Hucknall, A. Chilkoti and M. H. Mikkelsen, *Nano Lett.*, 2020, **20**, 4330–4336.

652 D. Y. Joh, A. M. Hucknall, Q. Wei, K. A. Mason, M. L. Lund, C. M. Fontes, R. T. Hill, R. Blair, Z. Zimmers, R. K. Achar, D. Tseng, R. Gordan, M. Freemark, A. Ozcan and A. Chilkoti, *Proc. Natl. Acad. Sci. U. S. A.*, 2017, **114**, E7054–e7062.

653 J. Luan, J. J. Morrissey, Z. Wang, H. G. Derami, K.-K. Liu, S. Cao, Q. Jiang, C. Wang, E. D. Kharasch, R. R. Naik and S. Singamaneni, *Light: Sci. Appl.*, 2018, **7**, 29.

654 C. Liang, J. Luan, Z. Wang, Q. Jiang, R. Gupta, S. Cao, K.-K. Liu, J. J. Morrissey, E. D. Kharasch, R. R. Naik and S. Singamaneni, *ACS Appl. Mater. Interfaces*, 2021, **13**, 11414–11423.

655 J. Luan, A. Seth, R. Gupta, Z. Wang, P. Rathi, S. Cao, H. Gholami Derami, R. Tang, B. Xu, S. Achilefu, J. J. Morrissey and S. Singamaneni, *Nat. Biomed. Eng.*, 2020, **4**, 518–530.

656 Z. Wang, Q. Zhou, A. Seth, S. Kolla, J. Luan, Q. Jiang, P. Rathi, P. Gupta, J. J. Morrissey, R. R. Naik and S. Singamaneni, *Biosens. Bioelectron.*, 2022, **200**, 113918.

657 Y. Kim, Z. Wang, C. Li, K. Kidd, Y. Wang, B. G. Johnson, S. Kmoch, J. J. Morrissey, A. J. Bleyer, J. S. Duffield, S. Singamaneni and Y. M. Chen, *Am. J. Physiol.: Renal Physiol.*, 2021, **321**, F236–F244.

658 Y. Wang, J. J. Morrissey, P. Gupta, P. Chauhan, R. K. Pachynski, P. K. Harris, A. Chaudhuri and S. Singamaneni, *ACS Appl. Mater. Interfaces*, 2023, **15**, 18598–18607.

659 L. Liu, Z. Wang, Y. Wang, J. Luan, J. J. Morrissey, R. R. Naik and S. Singamaneni, *Adv. Healthcare Mater.*, 2021, **10**, 2100956.

660 Z. Wang, J. J. Morrissey, L. Liu, Y. Wang, Q. Zhou, R. R. Naik and S. Singamaneni, *Anal. Chem.*, 2022, **94**, 909–917.

661 Z. Wang, J. Luan, A. Seth, L. Liu, M. You, P. Gupta, P. Rathi, Y. Wang, S. Cao, Q. Jiang, X. Zhang, R. Gupta, Q. Zhou, J. J. Morrissey, E. L. Scheller, J. S. Rudra and S. Singamaneni, *Nat. Biomed. Eng.*, 2021, **5**, 64–76.

662 R. Gupta, P. Gupta, S. Wang, A. Melnykov, Q. Jiang, A. Seth, Z. Wang, J. J. Morrissey, I. George, S. Gandra, P. Sinha, G. A. Storch, B. A. Parikh, G. M. Genin and S. Singamaneni, *Nat. Biomed. Eng.*, 2023, **7**, 1556–1570.

663 A. Seth, E. Mittal, J. Luan, S. Kolla, M. B. Mazer, H. Joshi, R. Gupta, P. Rathi, Z. Wang, J. J. Morrissey, J. D. Ernst, C. Portal-Celhay, S. C. Morley, J. A. Philips and S. Singamaneni, *Cells Rep. Methods*, 2022, **2**, 100267.

664 E. Mittal, A. T. Roth, A. Seth, S. Singamaneni, W. Beatty and J. A. Philips, *eLife*, 2023, **12**, e85416.

665 H. Joshi, A. Almgren-Bell, E. P. Anaya, E. M. Todd, S. J. Van Dyken, A. Seth, K. M. McIntire, S. Singamaneni, F. Sutterwala and S. C. Morley, *Cell Rep.*, 2022, **38**, 110507.

666 H. Guo, R. Gupta, D. Sharma, E. Zhanov, C. Malone, R. Jada, Y. Liu, M. Garg, S. Singamaneni, F. Zhao and L. Tian, *Nano Lett.*, 2023, **23**, 10171–10178.

667 A. Seth, Y. Liu, R. Gupta, Z. Wang, E. Mittal, S. Kolla, P. Rathi, P. Gupta, B. A. Parikh, G. M. Genin, S. Gandra, G. A. Storch, J. A. Philips, I. A. George and S. Singamaneni, *Nano Lett.*, 2024, **24**(1), 229–237.

668 P. Gupta, P. Rathi, R. Gupta, H. Baldi, Q. Coquerel, A. Debnath, H. G. Derami, B. Raman and S. Singamaneni, *Nanoscale Horiz.*, 2023, **8**, 1537–1555.

669 P. Rathi, P. Gupta, A. Debnath, H. Baldi, Y. Wang, R. Gupta, B. Raman and S. Singamaneni, *Nano Lett.*, 2023, **23**, 5654–5662.

670 P. Barya, Y. Xiong, S. Shepherd, R. Gupta, L. D. Akin, J. Tibbs, H. Lee, S. Singamaneni and B. T. Cunningham, *Small*, 2023, **19**, 2207239.

671 N. G. Khlebtsov and L. A. Dykman, *J. Quant. Spectrosc. Radiat. Transfer*, 2010, **111**, 1–35.

672 U. Guler, V. M. Shalaev and A. Boltasseva, *Mater. Today*, 2015, **18**, 227–237.

673 K. M. Mayer and J. H. Hafner, *Chem. Rev.*, 2011, **111**(6), 3828–3857.

674 J. Katyal and R. K. Soni, *Plasmonics*, 2015, **10**, 1729–1740.

675 V. Devaraj, J. M. Lee and J. W. Oh, *Curr. Appl. Phys.*, 2020, **20**, 1335–1341.

676 A. Yuksel, M. Cullinan, E. T. Yu and J. Murthy, *J. Quant. Spectrosc. Radiat. Transfer*, 2020, **254**, 107207.

677 E. R. Encina and E. A. Coronado, *J. Phys. Chem. C*, 2007, **111**, 16796–16801.

678 K. Ueno, S. Juodkazis, M. Mino, V. Mizeikis and H. Misawa, *J. Phys. Chem. C*, 2007, **111**, 4180–4184.

679 J. Jatschka, A. Dathe, A. Csáki, W. Fritzsche and O. Stranik, *Sens. Biosens. Res.*, 2016, **7**, 62–70.

680 W. Cui, A. Xiao, J. Zheng, P. Chen, J. Liang, Y. Huang and B. O. Guan, *ACS Appl. Nano Mater.*, 2023, **6**, 6345–6353.

681 C. Goldmann, M. De Frutos, E. H. Hill, D. Constantin and C. Hamon, *Chem. Mater.*, 2021, **33**, 2948–2956.

682 A. Sa, X. Zhuo, W. Albrecht, S. Bals and L. M. Liz-Marza, *ACS Mater. Lett.*, 2020, **2**(9), 1246–1250.

683 Y. Koike and K. Koike, *J. Polym. Sci., Part B: Polym. Phys.*, 2011, **49**, 2–17.

684 M. Arumugam, *Pramana*, 2001, **57**, 849–869.

685 M. Chauhan and V. K. Singh, *Opt. Fiber Technol.*, 2021, **64**, 102580.

686 L. Tian, E. Chen, N. Gandra, A. Abbas and S. Singamaneni, *Langmuir*, 2012, **28**, 17435–17442.

687 J. Cao, E. K. Galbraith, T. Sun and K. T. V. Grattan, *IEEE Sens. J.*, 2012, **12**(7), 2355–2361.

688 B. Kaur and A. K. Sharma II, *Proc. SPIE*, 2019, **11028**, 405–410.

689 C. Christopher, A. Subrahmanyam and V. V. R. Sai, *Plasmonics*, 2018, **13**, 493–502.

690 J. Boehm, A. François, H. Ebendorff-Heidepriem and T. M. Monro, *Plasmonics*, 2011, **6**, 133–136.

691 V. Myroshnychenko, J. Rodríguez-Fernández, I. Pastoriza-Santos, A. M. Funston, C. Novo, P. Mulvaney, L. M. Liz-Marzán and F. J. García de Abajo, *Chem. Soc. Rev.*, 2008, **37**, 1792–1805.

692 R. K. Harrison and A. Ben-Yakar, *Opt. Express*, 2010, **18**, 22556–22571.

693 M. Hu, A. Ghoshal, M. Marquez and P. G. Kik, *J. Phys. Chem. C*, 2010, **114**, 7509–7514.

694 R. E. Armstrong, J. C. Van Liempt and P. Zijlstra, *J. Phys. Chem. C*, 2019, **123**, 25801–25808.

695 K. Hei Willis Ho, A. Shang, F. Shi, T. Wing Lo, P. Hong Yeung, Y. Sing Yu, X. Zhang, K. Wong, D. Yuan Lei, K. H. W. Ho, A. Shang, F. Shi, T. W. Lo, P. H. Yeung, Y. S. Yu, X. Zhang, D. Y. Lei and K. Wong, *Adv. Funct. Mater.*, 2018, **28**, 1800383.

696 H. Sugimoto, S. Yashima and M. Fujii, *ACS Photonics*, 2018, **5**, 3421–3427.

697 R. Chikkaraddy and J. J. Baumberg, *ACS Photonics*, 2021, **8**, 2811–2817.

698 F. Xia, H. Song, Y. Zhao, W. M. Zhao, Q. Wang, X. Z. Wang, B. T. Wang and Z. X. Dai, *Measurement*, 2020, **164**, 108083.

699 H. Sugimoto, S. Yashima and M. Fujii, *ACS Photonics*, 2018, **5**, 3421–3427.

700 Q. Wang, L. Hou, C. Li, H. Zhou, X. Gan, K. Liu, F. Xiao and J. Zhao, *Nanoscale*, 2022, **14**, 10773–10779.

701 M. A. Otte, M. C. Estévez, D. Regatos, L. M. Lechuga and B. Sepúlveda, *ACS Nano*, 2011, **5**, 9179–9186.

702 L. Y. Niu, Q. Wang, J. Y. Jing and W. M. Zhao, *Opt. Commun.*, 2019, **450**, 287–295.

703 X. Jiang and Q. Wang, *Opt. Fiber Technol.*, 2019, **51**, 118–124.

704 Q. Wang, X. Li, W. M. Zhao and S. Jin, *Appl. Surf. Sci.*, 2019, **492**, 374–381.

705 B. T. Wang and Q. Wang, *IEEE Sens. J.*, 2018, **18**, 8303–8310.

706 V. A. Markel, *J. Opt. Soc. Am. A*, 2016, **33**, 1244.

707 Z. Wang, X. Jia, H. Wu, F. Peng, Y. Fu and Y. Rao, 25th International Conference, *Opt. Fiber Sens.*, 2017, **10323**, 103230.

708 L. Liu, S. Deng, J. Zheng, L. Yuan, H. Deng and C. Teng, *Sensors*, 2021, **21**, 1516.

709 C. Caucheteur, T. Guo and J. Albert, *Anal. Bioanal. Chem.*, 2015, **407**, 3883–3897.

710 J. H. Qu, B. Peeters, F. Delport, K. Vanhoorelbeke, J. Lammertyn and D. Spasic, *Biosens. Bioelectron.*, 2021, **192**, 113549.

711 S. Jiang, Z. Li, C. Zhang, S. Gao, Z. Li, H. Qiu, C. Li, C. Yang, M. Liu and Y. Liu, *J. Phys. D: Appl. Phys.*, 2017, **50**, 165105.

712 T. J. Ray, A. Wang, X. Jia, W. Zhou and Y. Zhu, *Virgina Tech.*, 2019.

713 H. Dong, L. Chen, J. Zhou, J. Yu, H. Guan, W. Qiu, J. Dong, H. Lu, J. Tang, W. Zhu, Z. Cai, Y. I. Xiao, J. Zhang and Z. Chen, *Opt. Express*, 2017, **25**(5), 5352–5365.

714 L. Zhuo, J. Tang, W. Zhu, H. Zheng, H. Guan, H. Lu, Y. Chen, Y. Luo, J. Zhang, Y. Zhong, J. Yu and Z. Chen, *Photonic Sens.*, 2022, **13**, 1–24.

715 W. Udos, K. S. Lim, C. L. Tan, M. N. S. M. Ismail, C. W. Ooi, R. Zakaria and H. Ahmad, *Optics*, 2020, **219**, 164970.

716 J. A. García, D. Monzón-Hernández, J. Manríquez and E. Bustos, *Opt. Mater.*, 2016, **51**, 208–212.

717 J. L. Tang, S. F. Cheng, W. T. Hsu, T. Y. Chiang and L. K. Chau, *Sens. Actuators, B*, 2006, **119**, 105–109.

718 S. Jia, C. Bian, J. Sun, J. Tong and S. Xia, *Biosens. Bioelectron.*, 2018, **114**, 15–21.

719 E. Martinsson, B. Sepulveda, P. Chen, A. Elfwing, B. Liedberg and D. Aili, *Plasmonics*, 2014, **9**, 773–780.

720 M. Lin, M. Lu, Y. Liang, L. Yu and W. Peng, *ACS Appl. Nano Mater.*, 2022, **5**, 6171–6180.

721 K. C. Chen, Y. Le Li, C. W. Wu and C. C. Chiang, *Sensors*, 2018, **18**, 1217.

722 S. Jiang, Z. Li, C. Zhang, S. Gao, Z. Li, H. Qiu, C. Li, C. Yang, M. Liu and Y. Liu, *J. Phys. D: Appl. Phys.*, 2017, **50**, 165105.

723 J. Cao, M. H. Tu, T. Sun and K. T. V. Grattan, *Sens. Actuators, B*, 2013, **181**, 611–619.

724 J. Wang, H. Zhang, Y. Tang, M. Wen, B. Yao, S. Yuan, W. Zhang and H. Lei, *ACS Biomater. Sci. Eng.*, 2022, 1060–1066.

725 J. Feng, J. Gao, W. Yang, R. Liu, M. Shafi, Z. Zha, C. Liu, S. Xu, T. Ning, T. Ning, S. Jiang and S. Jiang, *Opt. Express*, 2022, **30**, 10187–10198.

726 M. H. Tu, T. Sun and K. T. V. Grattan, *Sens. Actuators, B*, 2014, **191**, 37–44.

727 N. Cennamo, G. D'Agostino, A. Donà, G. Dacarro, P. Pallavicini, M. Pesavento and L. Zeni, *Sensors*, 2013, **13**, 14676–14686.

728 C. Zhang, Z. Li, S. Z. Jiang, C. H. Li, S. C. Xu, J. Yu, Z. Li, M. H. Wang, A. H. Liu and B. Y. Man, *Sens. Actuators, B*, 2017, **251**, 127–133.

729 B. Sciacca and T. M. Monro, *Langmuir*, 2014, **30**, 946–954.

730 J. Chen, S. Shi, R. Su, W. Qi, R. Huang, M. Wang, L. Wang and Z. He, *Sensors*, 2015, **15**, 12205–12217.

731 C. Zhou, *Opt. Lasers Eng.*, 2012, **50**, 1592–1595.

732 S. Rodal-Cedeira, V. Montes-García, L. Polavarapu, D. M. Solís, H. Heidari, A. La Porta, M. Angiola, A. Martucci, J. M. Taboada, F. Obelleiro, S. Bals, J. Pérez-Juste and I. Pastoriza-Santos, *Chem. Mater.*, 2016, **28**, 9169–9180.

733 S. Barbosa, A. Agrawal, L. Rodríguez-Lorenzo, I. Pastoriza-Santos, R. A. Alvarez-Puebla, A. Kornowski, H. Weller and L. M. Liz-Marzán, *Langmuir*, 2010, **26**, 14943–14950.

734 E. Martinsson, M. A. Otte, M. M. Shahjamali, B. Sepulveda and D. Aili, *J. Phys. Chem. C*, 2014, **118**, 24680–24687.

735 C. L. Nehl, H. Liao and J. H. Hafner, *Nano Lett.*, 2006, **6**, 683–688.

736 H. Chen, X. Kou, Z. Yang, W. Ni and J. Wang, *Langmuir*, 2008, **24**, 5233–5237.

737 R. Bukasov and J. S. Shumaker-Parry, *Nano Lett.*, 2007, **7**, 1113–1118.

738 H. R. Hegde, S. Chidangil and R. K. Sinha, *J. Mater. Sci.: Mater. Electron.*, 2022, **33**, 4011–4024.

739 W. Te Wu, C. H. Chen, C. Y. Chiang and L. K. Chau, *Sensors*, 2018, **18**, 23–30.
740 S. M. Marinakos, S. Chen and A. Chilkoti, *Anal. Chem.*, 2007, **79**, 5278–5283.
741 C. A. Barrios, T. Mirea and M. H. Represa, *Sensors*, 2023, **1**, 66.
742 Y. Khalavka, J. Becker and C. Sönnichsen, *J. Am. Chem. Soc.*, 2009, **131**, 1871–1875.
743 N. Nath and A. Chilkoti, *Anal. Chem.*, 2002, **74**, 504–509.
744 M. Lu, H. Zhu, M. Lin, F. Wang, L. Hong, J. F. Masson and W. Peng, *Sens. Actuators, B*, 2021, **329**, 129094.
745 X. Zhuo, X. Zhu, Q. Li, Z. Yang and J. Wang, *ACS Nano*, 2015, **9**(7), 7523–7535.
746 C. D. Chen, S. F. Cheng, L. K. Chau and C. R. C. Wang, *Biosens. Bioelectron.*, 2007, **22**, 926–932.
747 J. Cao, M. H. Tu, T. Sun and K. T. V. Grattan, *Sens. Actuators, B*, 2013, **181**, 611–619.
748 C. Zhuang, Y. Xu, N. Xu, J. Wen, H. Chen and S. Deng, *Sensors*, 2018, **18**(10), 3458.
749 A. Sánchez-Iglesias, N. Winckelmans, T. Altantzis, S. Bals, M. Grzelczak and L. M. Liz-Marzán, *J. Am. Chem. Soc.*, 2016, **139**, 107–110.
750 C. Zhang, B. Man, Z. Li, X. Xiu, L. Hou, J. Yu, S. Jiang, X. Zhao, Q. Peng, S. Qiu and C. Li, *Nanophotonics*, 2021, **10**, 1529–1540.
751 J. K. Nayak and R. Jha, *IEEE Photonics Technol. Lett.*, 2018, **30**, 1667–1670.
752 G. C. Li, Q. Zhang, S. A. Maier and D. Lei, *Nanophotonics*, 2018, **7**, 1865–1889.
753 A. Moreau, C. Ciracì, J. J. Mock, D. R. Smith, R. T. Hill, A. Chilkoti, Q. Wang and B. J. Wiley, *Nature*, 2012, **492**(7427), 86–89.
754 J. Feng, J. Gao, W. Yang, R. Liu, M. Shafi, Z. Zha, C. Liu, S. Xu, T. Ning, T. Ning, S. Jiang and S. Jiang, *Opt. Express*, 2022, **30**(6), 10187–10198.
755 W. S. Mokrzycki and M. Tatol, *Mach. Graphics Vision Int. J.*, 2011, **20**, 383–411.
756 G. Sharma, W. Wu and E. N. Dalal, *Color Res. Appl.*, 2005, **30**, 21–30.
757 N. S. King, L. Liu, X. Yang, B. Cerjan, H. O. Everitt, P. Nordlander and N. J. Halas, *ACS Nano*, 2015, **9**, 10628–10636.
758 I. Reinhard, K. Miller, G. Diepenheim, K. Cantrell and W. P. Hall, *ACS Appl. Nano Mater.*, 2020, **3**, 4342–4350.
759 M. Toma, Y. Itakura, S. Namihara and K. Kajikawa, *Adv. Eng. Mater.*, 2023, **25**, 2200912.
760 A. Choe, J. Yeom, R. Shanker, M. P. Kim, S. Kang and H. Ko, *NPG Asia Mater.*, 2018, **10**, 912–922.
761 P. Cencillo-Abad, P. Mastranzo-Ortega, D. Appavoo, T. Guo, L. Zhai, J. Sanchez-Mondragon and D. Chanda, *Adv. Opt. Mater.*, 2023, **11**, 2300300.
762 T. M. Nguyen, J. H. Chung, G.-H. Bak, Y. H. Kim, M. Kim, Y.-J. Kim, R. J. Kwon, E.-J. Choi, K. H. Kim, Y. S. Kim and J.-W. Oh, *ACS Sens.*, 2023, **8**, 167–175.
763 M. Sanromán-Iglesias, V. Garrido, Y. Gil-Ramírez, J. Aizpurua, M. Grzelczak and M.-J. Grilló, *Sens. Actuators, B*, 2021, **349**, 130780.
764 J. L. Montaño-Priede, M. Sanromán-Iglesias, N. Zabala, M. Grzelczak and J. Aizpurua, *ACS Sens.*, 2023, **8**, 1827–1834.
765 T. H. Talukdar, B. McCoy, S. K. Timmins, T. Khan and J. D. Ryckman, *Proc. Natl. Acad. Sci.*, 2020, **117**, 30107–30117.
766 K. Saha, S. S. Agasti, C. Kim, X. Li and V. M. Rotello, *Chem. Rev.*, 2012, **112**, 2739–2779.
767 W. Zhou, X. Gao, D. Liu and X. Chen, *Chem. Rev.*, 2015, **115**, 10575–10636.
768 S. K. Ghosh and T. Pal, *Chem. Rev.*, 2007, **107**, 4797–4862.
769 L. Tang and J. Li, *ACS Sens.*, 2017, **2**, 857–875.
770 Z. Zhang, H. Wang, Z. Chen, X. Wang, J. Choo and L. Chen, *Biosens. Bioelectron.*, 2018, **114**, 52–65.
771 E. Mauriz, *Sensors*, 2020, **20**(21), 6214.
772 N. Gandra, A. Abbas, L. Tian and S. Singamaneni, *Nano Lett.*, 2012, **12**, 2645–2651.
773 A. Abbas, R. Kattumenu, L. Tian and S. Singamaneni, *Langmuir*, 2013, **29**, 56–64.
774 M. Zayats, R. Baron, I. Popov and I. Willner, *Nano Lett.*, 2005, **5**, 21–25.
775 Y. Guo, J. Wu, J. Li and H. Ju, *Biosens. Bioelectron.*, 2016, **78**, 267–273.
776 R. de la Rica and M. M. Stevens, *Nat. Nanotechnol.*, 2012, **7**, 821–824.
777 R. Huang, X. Cai, J. Du, J. Lian, P. Hui, M. Gu, F. Li, J. Wang and W. Chen, *ACS Nano*, 2022, **16**, 19229–19239.
778 S. Xu, W. Ouyang, P. Xie, Y. Lin, B. Qiu, Z. Lin, G. Chen and L. Guo, *Anal. Chem.*, 2017, **89**, 1617–1623.
779 R. Baron, M. Zayats and I. Willner, *Anal. Chem.*, 2005, **77**, 1566–1571.
780 G. Wang, Z. Chen and L. Chen, *Nanoscale*, 2011, **3**, 1756–1759.
781 X. Ma, Y. Lin, L. Guo, B. Qiu, G. Chen, H. H. Yang and Z. Lin, *Biosens. Bioelectron.*, 2017, **87**, 122–128.
782 H. Ye, C. Nowak, Y. Liu, Y. Li, T. Zhang, L. Bleris and Z. Qin, *Small*, 2022, **18**, e2107832.
783 M. N. Creyer, Z. Jin, M. Retout, W. Yim, J. Zhou and J. V. Jokerst, *Langmuir*, 2022, **38**, 14200–14207.
784 Y.-Y. Chen, H.-T. Chang, Y.-C. Shiang, Y.-L. Hung, C.-K. Chiang and C.-C. Huang, *Anal. Chem.*, 2009, **81**, 9433–9439.
785 Y. Xia, J. Ye, K. Tan, J. Wang and G. Yang, *Anal. Chem.*, 2013, **85**, 6241–6247.
786 D. Wang, Y. Zhang, X. Zhao and Z. Xu, *Sens. Actuators, B*, 2019, **296**, 126646.
787 J. Zeng, Y. Cao, J. Chen, X. Wang, J. Yu, B. Yu, Z. Yan and X. Chen, *Nanoscale*, 2014, **6**, 9939–9943.
788 Z. Chen, Z. Zhang, C. Qu, D. Pan and L. Chen, *Analyst*, 2012, **137**, 5197–5200.
789 X. Yang, Y. Yu and Z. Gao, *ACS Nano*, 2014, **8**, 4902–4907.
790 Y. Zhang, J. Jiao, Y. Wei, D. Wang, C. Yang and Z. Xu, *Anal. Chem.*, 2020, **92**, 15244–15252.
791 S. K. Tripathy, J. Y. Woo and C.-S. Han, *Anal. Chem.*, 2011, **83**, 9206–9212.
792 L. Tian, E. Chen, N. Gandra, A. Abbas and S. Singamaneni, *Langmuir*, 2012, **28**, 17435–17442.
793 F.-M. Li, J.-M. Liu, X.-X. Wang, L.-P. Lin, W.-L. Cai, X. Lin, Y.-N. Zeng, Z.-M. Li and S.-Q. Lin, *Sens. Actuators, B*, 2011, **155**, 817–822.

794 Z. Zhang, Z. Chen, C. Qu and L. Chen, *Langmuir*, 2014, **30**, 3625–3630.

795 Z. Zhang, Z. Chen, F. Cheng, Y. Zhang and L. Chen, *Biosens. Bioelectron.*, 2017, **89**, 932–936.

796 Y. Xianyu, Y. Chen and X. Jiang, *Anal. Chem.*, 2015, **87**, 10688–10692.

797 L. Lu and Y. Xia, *Anal. Chem.*, 2015, **87**, 8584–8591.

798 C.-H. Lu, Y.-W. Wang, S.-L. Ye, G.-N. Chen and H.-H. Yang, *NPG Asia Mater.*, 2012, **4**, e10–e10.

799 P. Valentini and P. P. Pompa, *Angew. Chem., Int. Ed.*, 2016, **55**, 2157–2160.

800 M.-P. N. Bui, S. Ahmed and A. Abbas, *Nano Lett.*, 2015, **15**, 6239–6246.

801 K. Zagorovsky and W. C. W. Chan, *Angew. Chem., Int. Ed.*, 2013, **52**, 3168–3171.

802 S. Kim, J.-M. Kim, J.-E. Park and J.-M. Nam, *Adv. Mater.*, 2018, **30**, 1704528.

803 C. H. Lee, L. Tian and S. Singamaneni, *ACS Appl. Mater. Interfaces*, 2010, **2**, 3429–3435.

804 C. H. Lee, M. E. Hankus, L. Tian, P. M. Pellegrino and S. Singamaneni, *Anal. Chem.*, 2011, **83**, 8953–8958.

805 L. Tian, J. Luan, K.-K. Liu, Q. Jiang, S. Tadepalli, M. K. Gupta, R. R. Naik and S. Singamaneni, *Nano Lett.*, 2016, **16**, 609–616.

806 L. Tian, J. J. Morrissey, R. Kattumenu, N. Gandra, E. D. Kharasch and S. Singamaneni, *Anal. Chem.*, 2012, **84**, 9928–9934.

807 L. Tian, Q. Jiang, K.-K. Liu, J. Luan, R. R. Naik and S. Singamaneni, *Adv. Mater. Interfaces*, 2016, **3**, 1600214.

808 U. Mogera, H. Guo, M. Namkoong, M. S. Rahman, T. Nguyen and L. Tian, *Sci. Adv.*, 2022, **8**(12), eabn1736.

809 S. Z. Nergiz, N. Gandra, M. E. Farrell, L. M. Tian, P. M. Pellegrino and S. Singamaneni, *J. Mater. Chem. A*, 2013, **1**, 6543–6549.

810 L. M. Tian, S. Tadepalli, M. E. Farrell, K. K. Liu, N. Gandra, P. M. Pellegrino and S. Singamaneni, *J. Mater. Chem. C*, 2014, **2**, 5438–5446.

811 L. Tian, S. Tadepalli, S. Hyun Park, K.-K. Liu, J. J. Morrissey, E. D. Kharasch, R. R. Naik and S. Singamaneni, *Biosens. Bioelectron.*, 2014, **59**, 208–215.

812 D. Tu, A. Holderby, H. Guo, S. Mabbott, L. Tian and G. L. Coté, *Anal. Chim. Acta*, 2022, **1198**, 339562.

813 H. Guo, Z. Yin, M. Namkoong, Y. Li, T. Nguyen, E. Salcedo, I. Arizpe and L. Tian, *ACS Appl. Mater. Interfaces*, 2022, **14**, 10729–10737.

814 S. Song, L. Wang, J. Li, C. Fan and J. Zhao, *TrAC, Trends Anal. Chem.*, 2008, **27**, 108–117.

815 A. Abbas, L. Tian, J. J. Morrissey, E. D. Kharasch and S. Singamaneni, *Adv. Funct. Mater.*, 2013, **23**, 1789–1797.

816 L. M. Tian, K. K. Liu, J. J. Morrissey, N. Gandra, E. D. Kharasch and S. Singamaneni, *J. Mater. Chem. B*, 2014, **2**, 167–170.

817 Z. Yin, H. Guo, Y. Li, J. Chiu and L. Tian, *ACS Appl. Mater. Interfaces*, 2020, **12**, 35977–35985.

818 Y. Li, H. Guo, Z. Yin, K. Lyle and L. Tian, *ACS Appl. Mater. Interfaces*, 2021, **13**, 5564–5573.

819 C. Wang, J. Luan, S. Tadepalli, K.-K. Liu, J. J. Morrissey, E. D. Kharasch, R. R. Naik and S. Singamaneni, *ACS Appl. Mater. Interfaces*, 2016, **8**, 26493–26500.

820 D. Quesada-González and A. Merkoçi, *Biosens. Bioelectron.*, 2015, **73**, 47–63.

821 V.-T. Nguyen, S. Song, S. Park and C. Joo, *Biosens. Bioelectron.*, 2020, **152**, 112015.

822 D. Quesada-González and A. Merkoçi, *Lateral Flow Biosensors, Sensor Technology Directory (eBook)*, Sensor100, 2023.

823 David E. Charlton, *US Pat.*, US6485982B1, 1988.

824 *Lateral Flow Immunoassay*, ed. R. Wong and H. Tse, Humana Press, Totowa, NJ, 2009.

825 C. Parolo, A. Sena-Torralba, J. F. Bergua, E. Calucho, C. Fuentes-Chust, L. Hu, L. Rivas, R. Álvarez-Diduk, E. P. Nguyen, S. Cinti, D. Quesada-González and A. Merkoçi, *Nat. Protoc.*, 2020, **15**, 3788–3816.

826 Whatman Fusion 5|Cytiva, **https://www.cytivalifesciences.com/en/es/shop/lab-filtration/immunodiagnostics/lateral-flow-pads/fusion-5-p-00787**, (accessed 22 May 2024).

827 A. Chamorro-Garcia, A. de la Escosura-Muñiz, M. Espinoza-Castañeda, C. J. Rodriguez-Hernandez, C. de Torres and A. Merkoçi, *Nanomedicine*, 2016, **12**, 53–61.

828 A. Sena-Torralba, J. Gabaldón-Atienza, A. Cubells-Gómez, P. Casino, Á. Maquieira and S. Morais, *Biosensors*, 2022, **12**, 980.

829 M. A. V. Ngu, J. H. Bergantin and J. D. A. Ramos, *Protein Pept. Lett.*, 2019, **26**, 357–363.

830 A. Rubio-Monterde, A. Génova-Tesoro, B. Contreras-Repiso, R. Monaghan, R. Merriman, B. Teixeira-Dias, L. Rivas, J. Escudero-Garcia, M. Gallegos, L. Ainsworth, S. Daniels and D. Quesada-González, A. Rubio-Monterde, *31st ECCMID*.

831 T. Wang, L. Chen, A. Chikkanna, S. Chen, I. Brusius, N. Sbuh and R. N. Veedu, *Theranostics*, 2021, **11**, 5174–5196.

832 M. Oliveira-Rodríguez, S. López-Cobo, H. T. Reyburn, A. Costa-García, S. López-Martín, M. Yáñez-Mó, E. Cernuda-Morollón, A. Paschen, M. Valés-Gómez and M. C. Blanco-López, *J. Extracell. Vesicles*, 2016, **5**(1), 31803.

833 D. Quesada-González, G. A. Jairo, R. C. Blake, D. A. Blake and A. Merkoçi, *Sci. Rep.*, 2018, **8**, 16157.

834 N. A. Taranova, N. A. Byzova, V. V. Zaiko, T. A. Starovoitova, Y. Y. Vengerov, A. V. Zherdev and B. B. Dzantiev, *Microchim. Acta*, 2013, **180**, 1165–1172.

835 L. Anfossi, F. Di Nardo, S. Cavalera, C. Giovannoli and C. Baggiani, *Biosensors*, 2018, **9**, 2.

836 D. Quesada-González and A. Merkoçi, *Biosens. Bioelectron.*, 2017, **92**, 549–562.

837 Using Portable SPR to Speed Up Your Lateral Flow Assay Development, **https://www.affiniteinstruments.com/post/spr-in-aiding-the-development-of-lateral-flow-assays**, (accessed 12 October 2023).

838 J. Kimling, M. Maier, B. Okenve, V. Kotaidis, H. Ballot and A. Plech, *J. Phys. Chem. B*, 2006, **110**, 15700–15707.

839 M. H. Jazayeri, H. Amani, A. A. Pourfatollah, H. Pazoki-Toroudi and B. Sedighimoghaddam, *Sens. Biosens. Res.*, 2016, **9**, 17–22.

840 K. Tripathi and J. D. Driskell, *ACS Omega*, 2018, **3**, 8253–8259.

841 Gold Nanoparticle Covalent Conjugation—Fortis Life Sciences, https://www.fortislife.com/lateral-flow-covalent-conjugation, (accessed 12 October 2023).

842 Y. Deng, H. Jiang, X. Li and X. Lv, *Microchim. Acta*, 2021, **188**, 379.

843 D. Quesada González, *Universitat Autònoma de Barcelona. Departament de Química.*, TDX (Tesis Doctorals en Xarxa).

844 Y. Shen and G. Shen, *ACS Omega*, 2019, **4**, 5083–5087.

845 E. Garrido, E. Climent, M. D. Marcos, F. Sancenón, K. Rurack and R. Martínez-Máñez, *Nanoscale*, 2022, **14**, 13505–13513.

846 D. Quesada and M. Gallegos, *EU Pat.*, EP4070105A1/WO2021110958, 2020.

847 G. Ross, M. Bremer, J. Wichers, A. van Amerongen and M. Nielen, *Biosensors*, 2018, **8**, 130.

848 D. Quesada-González, A. Sena-Torralba, W. P. Wicaksono, A. de la Escosura-Muñiz, T. A. Ivandini and A. Merkoçi, *Biosens. Bioelectron.*, 2019, **132**, 132–135.

849 B. Zhang, W. Ma, F. Li, W. Gao, Q. Zhao, W. Peng, J. Piao, X. Wu, H. Wang, X. Gong and J. Chang, *Nanoscale*, 2017, **9**, 18711–18722.

850 D. Quesada-González, C. Stefani, I. González, A. de la Escosura-Muñiz, N. Domingo, P. Mutjé and A. Merkoçi, *Biosens. Bioelectron.*, 2019, **141**, 111407.

851 T. You, W. Jeong, H. Lee, Y. S. Huh, S. M. Kim and T.-J. Jeon, *Microchim. Acta*, 2021, **188**, 364.

852 E. Renzi, A. Piper, F. Nastri, A. Merkoçi and A. Lombardi, *Small*, 2023, **19**, 2207949.

853 A. Scarsi, D. Pedone and P. P. Pompa, *Nanoscale Adv.*, 2023, **5**, 2167–2174.

854 I. N. Katis, P. J. W. He, R. W. Eason and C. L. Sones, *Biosens. Bioelectron.*, 2018, **113**, 95–100.

855 M. Díaz-González and A. de la Escosura-Muñiz, *Anal. Bioanal. Chem.*, 2021, **413**, 4111–4117.

856 T. Trakoolwilaiwan, Y. Takeuchi, T. S. Leung, M. Sebek, L. Storozhuk, L. Nguyen, L. D. Tung and N. T. K. Thanh, *Nanoscale*, 2023, **15**, 12915–12925.

857 H.-K. Oh, K. Kim, J. Park, H. Im, S. Maher and M.-G. Kim, *Biosens. Bioelectron.*, 2022, **205**, 114094.

858 D. A. Armbruster and T. Pry, *Clin. Biochem. Rev.*, 2008, **29**(Suppl 1), S49–S52.

859 A. H. A. Hassan, J. F. Bergua, E. Morales-Narváez and A. Mekoçi, *Food Chem.*, 2019, **297**, 124965.

860 X. Y. Wong, D. Quesada-González, S. Manickam and K. Muthoosamy, *Anal. Chim. Acta*, 2021, **1175**, 338745.

861 E. Morales-Narváez, T. Naghdi, E. Zor and A. Merkoçi, *Anal. Chem.*, 2015, **87**, 8573–8577.

862 ESEQuant Lateral Flow System-QIAGEN, https://www.qiagen.com/us/resources/resourcedetail?id=60ed2e10-7c42-464b-a805-08a6f9eacc22&lang=en, (accessed 12 October 2023).

863 E. coli E. coli O157:H7 ELISA Kit (ABIN5650391), https://www.antibodies-online.com/kit/5650391/Escherichia+Coli,+O157H7+ELISA+Kit/, (accessed 12 October 2023).

864 A. M. Ashrafi, Z. Bytesnikova, J. Barek, L. Richtera and V. Adam, *Biosens. Bioelectron.*, 2021, **192**, 113494.

865 Y. Wang, Z. Qin, D. R. Boulware, B. S. Pritt, L. M. Sloan, I. J. González, D. Bell, R. R. Rees-Channer, P. Chiodini, W. C. W. Chan and J. C. Bischof, *Anal. Chem.*, 2016, **88**, 11774–11782.

866 N. K. Bakirhan, B. D. Topal, G. Ozcelikay, L. Karadurmus and S. A. Ozkan, *Crit. Rev. Anal. Chem.*, 2022, **52**, 519–534.

867 J. Cheng, G. Yang, J. Guo, S. Liu and J. Guo, *Analyst*, 2022, **147**, 554–570.

868 A. Sena-Torralba, R. Álvarez-Diduk, C. Parolo, A. Piper and A. Merkoçi, *Chem. Rev.*, 2022, **122**, 14881–14910.

869 A. Sena-Torralba, Y. D. Banguera-Ordoñez, L. Mira-Pascual, Á. Maquieira and S. Morais, *Trends Biotechnol.*, 2023, **41**, 1299–1313.

870 Z. Wang, Z. Zhang, W. Luo, L. Wang, X. Han, R. Zhao, X. Liu, J. Zhang, W. Yu, J. Li, Y. Yang, C. Zuo and G. Xie, *Nanoscale*, 2023, **15**, 12660–12669.

871 A. Rubio-Monterde, D. Quesada-González and A. Merkoçi, *Anal. Chem.*, 2023, **95**, 468–489.

872 Y. Wang, J. Niu, M. Sun, Z. Li, X. Wang, Y. He and J. Qi, *Int. J. Mol. Sci.*, 2023, **24**, 7733.

873 M. S. Cordray and R. R. Richards-Kortum, *Malar. J.*, 2015, **14**, 472.

874 A. Salazar, F. M. Ochoa-Corona, J. L. Talley and B. H. Noden, *Sci. Rep.*, 2021, **11**, 15962.

875 M. Jauset-Rubio, M. Svobodová, T. Mairal, C. McNeil, N. Keegan, M. S. El-Shahawi, A. S. Bashammakh, A. O. Alyoubi and C. K. O'Sullivan, *Anal. Chem.*, 2016, **88**, 10701–10709.

876 J. Kumar, K. G. Thomas and L. M. Liz-Marzán, *Chem. Commun.*, 2016, **52**, 12555–12569.

877 J. Kumar and L. M. Liz-Marzán, *Bull. Chem. Soc. Jpn.*, 2019, **92**, 30–37.

878 Q. Zhang, T. Hernandez, K. W. Smith, S. A. H. Jebeli, A. X. Dai, L. Warning, R. Baiyasi, L. A. McCarthy, H. Guo, D. H. Chen, J. A. Dionne, C. F. Landes and S. Link, *Science*, 2019, **365**, 1475–1478.

879 W. Ma, H. Kuang, L. Xu, L. Ding, C. Xu, L. Wang and N. A. Kotov, *Nat. Commun.*, 2013, **4**, 2689.

880 Y. Zhao, A. N. Askarpour, L. Sun, J. Shi, X. Li and A. Alù, *Nat. Commun.*, 2017, **8**, 6–13.

881 P. Mulvaney, *Langmuir*, 1996, **12**, 788–800.

882 R. Thomas, J. Kumar, R. S. Swathi and K. G. George Thomas, *Curr. Sci.*, 2012, **102**, 85–96.

883 L. A. Warning, A. R. Miandashti, L. A. McCarthy, Q. Zhang, C. F. Landes and S. Link, *ACS Nano*, 2021, **15**, 15538–15566.

884 W. Ma, L. Xu, A. F. De Moura, X. Wu, H. Kuang, C. Xu and N. A. Kotov, *Chem. Rev.*, 2017, **117**, 8041–8093.

885 S. Maniappan, C. Dutta, D. M. Solís, J. M. Taboada and J. Kumar, *Angew. Chem., Int. Ed.*, 2023, **62**, e202300461.

886 G. Shemer, O. Krichevski, G. Markovich, T. Molotsky, I. Lubitz and A. B. Kotlyar, *J. Am. Chem. Soc.*, 2006, **128**, 11006–11007.

887 J. George and K. G. Thomas, *J. Am. Chem. Soc.*, 2010, **132**, 2502–2503.

888 J. Cai, C. Hao, M. Sun, W. Ma, C. Xu and H. Kuang, *Small*, 2018, **14**, 1–8.

889 T. Funck, F. Nicoli, A. Kuzyk and T. Liedl, *Angew. Chem., Int. Ed.*, 2018, **57**, 13495–13498.

890 L. Xu, Y. Gao, H. Kuang, L. M. Liz-Marzán and C. Xu, *Angew. Chem., Int. Ed.*, 2018, **57**, 10544–10548.
891 S. Dominguez-Medina, L. Kisley, L. J. Tauzin, A. Hoggard, B. Shuang, A. S. D. S. Indrasekara, S. Chen, L. Y. Wang, P. J. Derry, A. Liopo, E. R. Zubarev, C. F. Landes and S. Link, *ACS Nano*, 2016, **10**, 2103–2112.
892 M. Sun, L. Xu, J. H. Banhg, H. Kuang, S. Alben, N. A. Kotov and C. Xu, *Nat. Commun.*, 2017, **8**, 1–10.
893 X. T. Kong, L. V. Besteiro, Z. Wang and A. O. Govorov, *Adv. Mater.*, 2020, **32**, 1–14.
894 A. O. Govorov, Z. Fan, P. Hernandez, J. M. Slocik and R. R. Naik, *Nano Lett.*, 2010, **10**, 1374–1382.
895 B. M. Maoz, Y. Chaikin, A. B. Tesler, O. Bar Elli, Z. Fan, A. O. Govorov and G. Markovich, *Nano Lett.*, 2013, **13**, 1203–1209.
896 H. Zhang and A. O. Govorov, *Phys. Rev. B: Condens. Matter Mater. Phys.*, 2013, **87**, 1–8.
897 L. M. Kneer, E. M. Roller, L. V. Besteiro, R. Schreiber, A. O. Govorov and T. Liedl, *ACS Nano*, 2018, **12**, 9110–9115.
898 E. Severoni, S. Maniappan, L. M. Liz-Marzán, J. Kumar, F. J. Garciá De Abajo and L. Galantini, *ACS Nano*, 2020, **14**, 16712–16722.
899 F. Lu, Y. Tian, M. Liu, D. Su, H. Zhang, A. O. Govorov and O. Gang, *Nano Lett.*, 2013, **13**, 3145–3151.